Durham E-Theses

Current Transport across the Grain Boundaries of High-Field High-Temperature Micro- and Nanocrystalline Superconductors

WANG, GUANMEI

How to cite:

WANG, GUANMEI (2017) *Current Transport across the Grain Boundaries of High-Field High-Temperature Micro- and Nanocrystalline Superconductors*, Durham theses, Durham University. Available at Durham E-Theses Online: http://etheses.dur.ac.uk/12436/

Current Transport across the Grain Boundaries of High-Field High-Temperature Micro- and Nanocrystalline Superconductors

Guanmei Wang

A thesis submitted in partial fulfillment

of the requirements for the degree of

Doctor of Philosophy

Department of Physics,

Durham University

2017

Abstract

We have fabricated micro- and nanocrystalline $YBa_2Cu_3O_7$, $Bi_2Sr_2CaCu_2O_8$ and $Bi_2Sr_2Ca_2Cu_3O_{10}$ superconductors using mechanical ball milling, hot isostatic pressing and oxygen annealing. The fabricated materials were characterised using powder x-ray diffraction, differential scanning calorimetry, thermogravimetry, resistivity, $V - I$ traces, a.c. magnetic susceptibility and d.c. magnetic hysteresis. A new approach for measuring the resistivity of grain boundaries in polycrystalline materials is presented. The average resistivities of the grain boundaries (ρ_{GB}) in micro- and nanocrystalline $YBa_2Cu_3O_7$ are much higher than that of the grains (ρ_G) which leads to huge ρ_{GB}/ρ_G values of 2×10^3 and 1.6×10^5 respectively. For nanocrystalline $Bi_2Sr_2CaCu_2O_8$ and both micro- and nanocrystalline $Bi_2Sr_2Ca_2Cu_3O_{10}$ samples, ρ_{GB}/ρ_G is at least 10^3. Only microcrystalline $Bi_2Sr_2CaCu_2O_8$ has a very low ρ_{GB} that is similar to ρ_G such that $\rho_{GB}/\rho_G \approx 1$. The values of grain boundary resistivity measured in our samples were used in conjunction with a theoretical framework developed in Durham, to quantitatively calculate how high grain boundary resistivities must be to account for the decrease by several orders of magnitude in transport critical current density (J_c) in polycrystalline $YBa_2Cu_3O_7$ and $Bi_2Sr_2Ca_2Cu_3O_{10}$. We conclude that the significant effort made by the research community in texturing samples and removing the grain boundaries is well-founded. For low-temperature superconducting intermetallics such as Nb_3Sn, we demonstrate that increases in J_c by two orders of magnitude is still possible by completely removing the grain boundaries from these materials and incorporating additional artificial pinning. Only large-grained polycrystalline $Bi_2Sr_2CaCu_2O_8$ has sufficiently low grain boundary resistivity, that cost constraints for applications may yet lead to high J_c polycrystalline materials that have artificial pinning sites or pinning produced by irradiation.

Publications

G. Wang, M.J. Raine, and D.P. Hampshire, "How Resistive Must Grain Boundaries in Polycrystalline Superconductors be, to Limit J_c?", *Superconductor Science and Technology*, vol. 30, pp. 104001, 2017.

G. Wang, M.J. Raine, and D.P. Hampshire, "The Cause of 'Weak-Link' Grain Boundary Behaviour in Polycrystalline $Bi_2Sr_2CaCu_2O_8$ and $Bi_2Sr_2Ca_2Cu_3O_{10}$ Superconductors", submitted for publication to *Superconductor Science and Technology,* September 2017.

Table of Contents

Variables

a	Grain size
b	$b = B_{\mathrm{app}}/B_{\mathrm{c2}}$, reduced field
B_{app}	Applied magnetic field
B_{c1}	Lower critical field
B_{c2}	Upper critical field
B_{Irr}	Irreversibility field
C	Pinning force fitting parameter
d	Grain boundary thickness
D_{N}	Diffusivity in the normal layer
D_{S}	Diffusivity in the superconducting layer
e	Electron charge
E_{c}	Condensation energy
F_{P}	Pinning force
J_{c}	Critical current density
$J_{\mathrm{c}}^{\mathrm{G}}$	Grain critical current density
$J_{\mathrm{c}}^{\mathrm{GB}}$	Grain boundary critical current density
$J_{\mathrm{c}}^{\mathrm{m}}$	Magnetisation critical current density
$J_{\mathrm{c}}^{\mathrm{t}}$	Transport critical current density
J_{D}	Depairing current density
J_{DN}	Depairing current density of the normal layer
$\langle J_{\mathrm{DN}} \rangle$	Angular averaged depairing current across the normal layer
J_{DSc}	Depairing current density of the superconducting layer
$\langle J_{\mathrm{DSc}} \rangle$	Angular averaged depairing current across the superconducting layer
J_{DSc}^{ab}	Depairing current along the ab-plane
J_{DSc}^{c}	Depairing current along the c-axis direction
J_{P}	Current density associated with flux pinning
J_{PN}	Current density associated with flux pinning in the normal layer
l	Mean free path
m	Electron mass
n	Number of valence electrons per unit volume

$N(0)$ Energy density of states at $T = 0$

R Sample radius

r_{min} Minimum radius required to support superconductivity

p Pinning force fitting parameter

q Pinning force fitting parameter

T Temperature

t $t = T/T_{\mathrm{c}}$, reduced temperature

T_{c} Critical temperature

T_{cN} Critical temperature of the normal layer

T_{cS} Critical temperature of the superconducting layer

V Sample volume

V_{min} Minimum volume required to support superconductivity

k_{B} Boltzmann constant

k_{F} Fermi wavevector

v_{F} Fermi velocity

α Order parameter decay fitting parameter

β Order parameter decay fitting parameter

γ Sommerfeld constant

Γ Mass anisotropy ratio

δ Quasi-particle energy level separation

Δ BCS energy gap

ΔM Magnetisation hysteresis loop width

Δm Magnetic moment hysteresis loop width

η Exponent from the empirical temperature dependence of B_{c1}

θ Angle of current with respect to the c-axis direction

$\kappa(\theta)$ Angular dependence of Ginzburg-Landau parameter

$\lambda(\theta)$ Angular dependence of penetration depth

λ_{ab} Penetration depth along the ab-plane

λ_c Penetration depth along the c-axis direction

λ_{F} Fermi wavelength

μ_0 Permeability of free space

$\mu_0 \Delta M/\Delta B$ Field reversal gradient

ν Exponent from the empirical temperature dependence of B_{c2}

$\xi(\theta)$ Angular dependence of coherence length

ξ_0 BCS coherence length

ξ_{ab} Coherence length along the ab-plane

$\xi_{B_{\mathrm{c2(0)}}}$ Coherence length calculated from $B_{\mathrm{c2}}(0)$

ξ_c Coherence length along the c-axis direction

ξ_{N} Delay length of the order parameter in the normal layer

ξ_{NClean} Coherence length in the normal layer, in the clean limit

ξ_{NDirty} Coherence length in the normal layer, in the dirty limit

ξ_{NPippard} Pippard coherence length in the normal layer

ξ_{S} Coherence length of the superconducting layer

ξ_{SClean} Coherence length in the superconducting layer, in the clean limit

ξ_{SDirty} Coherence length in the superconducting layer, in the dirty limit

ξ_{SPippard} Pippard coherence length in the superconducting layer

ρ_{ab} Resistivity along the ab-plane

ρ_c Resistivity along the c-axis direction

ρ_{G} Grain resistivity

ρ_{GB} Grain boundary resistivity

ρ_{N} Resistivity of the normal layer

$\langle \rho_{\mathrm{N}} \rangle$ Angular averaged normal state resistivity

ρ_{S} Resistivity of the superconducting layer

Φ_0 Flux quantum

χ A.c. magnetic susceptibility

χ'_g/χ'_b Ratio of granular and bulk susceptibility

Ψ Ginzburg-Landau order parameter

Declaration and Copyright

I hereby declare that this thesis is my own work and has not previously been submitted for a degree in any university. If material has been generated through joint work, my independent contribution has been clearly indicated. Any material from work of others has been acknowledged and referenced.

Guanmei Wang

August 2017

Acknowledgements

I would like to begin by giving special thanks to my supervisor, Professor Damian Hampshire, for his guidance, support and encouragement, and without whom this work would not have been possible. I would also like to thank Dr Douglas Halliday for welcoming me as a member to the interdisciplinary energy CDT, which I greatly enjoyed and benefitted from. I would also like to thank everyone in the superconductivity group, Mark Raine, Yeekin Tsui, Prapaiwan Sunwong, Peter Byrne, Paul Branch, Francis Ridgeon, Alexander Blair, Andy Smith and Jack Greenwood, all of whom have helped me in many ways, and have all made the last few years more enjoyable. I would like to extend my thanks to the fusion reference laboratory technicians, Andrea Dawson, Michael McBreen, Emily Roe, Matthew Plumb and Craig Robinson for their assistance in the labs and teaching me some of the practical skills I needed especially in the early years.

Thanks go to all the support groups in the department, especially the technicians and the mechanical workshop for their assistance and excellent workmanship. I would also like to thank our collaborators in Cambridge for their advice. I would like to thank Professor John Evans and Gary Oswald from the Department of Chemistry for use of their XRD equipment; Dr Buddhika Mendis and Leon Bowen for use of their SEM facilities; Mike Glynn and Professor Moataz Attallah at Birmingham University for their support and use of their HIP facilities. I would also like to acknowledge the Engineering and Physical Sciences Research Council for funding this research.

On a more personal level, I would like to thank Penelope Lawton and Michael Copley-May for their companionship and emotional support over the years. Finally, I would like to give special, heartfelt thanks to my parents for all their love and support, and for always being there.

Chapter 1

Introduction

The concept of nuclear fusion energy – the energy released by the bonding of nuclei – first surfaced in the 1930s. Clean, safe and with virtually limitless fuel, it was heralded as the ultimate solution to the energy problem that is looming over the world. By the 1950s, various reactor designs emerged in a race towards harnessing fusion energy. The most promising reactor concept was magnetic confinement, in which the fuel, burning at ten times the core temperature of the sun, is held in the reactor by magnetic fields. However, even though fusion itself can be achieved with (relative!) ease, producing an energy gain has proved difficult. Magnets built using conventional conductors cannot produce a net energy gain as the energy loss due to the resistance in the conductors outweighs the fusion energy output.

Fortunately, superconductors had already been discovered by this time [1]. This is a class of materials which have zero electrical resistance, and are capable of carrying extremely high currents and producing the very high magnetic fields required for fusion confinement, but with minimal energy loss. However, the traditional superconducting materials can only operate at very low temperatures of a few degrees Kelvin above absolute zero, and are known as low-temperature superconductors (LTS). They are also limited by two more factors: they can only carry currents up to a critical value known as the *critical current*, and can only produce high magnetic fields up to a limit known as the *upper critical field*. The research community is always actively working towards trying to increase these critical parameters, and to improve the current carrying capabilities and field tolerance. One very successful method is to introduce grain boundaries into the materials by reducing the grain

size down to nanometre scales to produce *nanocrystalline superconductors*. Studies have shown that nanocrystalline superconductors [2-5] have increased critical current and upper critical field compared to large grained materials. For example, nanocrystalline NbCN fabricated by Raine *et al.* [6, 7] saw an increase in the critical current by a factor of 40.

The advent of high-temperature superconductors (HTS), with their higher operating temperatures and far superior current carrying capabilities, was a Nobel prize-winning breakthrough. Particularly notable was the discovery of $YBa_2Cu_3O_7$ in 1987, the first superconductor that is capable of operating at above 77 K, the boiling temperature of liquid nitrogen [8]. The discovery of the $Bi_2Sr_2CaCu_2O_8$ and $Bi_2Sr_2Ca_2Cu_3O_{10}$ superconductors was made in the following year [9]. These three materials make up the bulk of the commercial HTS market due to their high critical currents. However, the excitement that surrounded HTS was short-lived. Despite their obvious advantages, the commercial superconductor market is still largely dominated by LTS materials such as NbTi and Nb_3Sn. This is due to the fact that there remain many unsolved obstacles to the application of HTS conductors, including the complexity involved in their fabrication, leading to high costs. The origin of the high cost lies within the so-called "weak-link problem". The presence of grain boundaries in HTS materials was demonstrated to reduce the critical current by several orders of magnitude [10]; such a significant reduction that manufacturers of HTS conductors chose to remove these grain boundaries by fabricating pseudo single crystal tapes [11], which contributes to the majority of the production cost. Polycrystalline HTS is much simpler and cheaper to produce, however it suffers from low critical currents due to the weak-link problem. If it were possible to increase the low critical currents in polycrystalline HTS, it would completely change the current landscape of commercial superconductors and even fusion reactor designs.

This work aims to answer two questions. First, can nanocrystalline HTS become a new class of useful, commercial material? Polycrystalline HTS have been widely studied, but systematic data on nanocrystalline HTS are rare. Even though grain boundaries are proven to be detrimental in HTS, is it possible that a different phenomenon could arise at the opposite extreme to pseudo single crystals, where a high density of grain boundaries may

lead to improvements in critical current and field as in LTS? Second, by studying nanocrystalline HTS and the nature of grain boundaries, can we gain any insights as to how to improve all classes of commercial superconductors?

This thesis is structured as follows: Chapter 2 provides an overview of the history, the basic underlying theory that governs the phenomenon of superconductivity, and the applications of superconductors. Chapter 3 is a literature review of the high-temperature superconductors of interest in this thesis – $YBa_2Cu_3O_7$, $Bi_2Sr_2CaCu_2O_8$ and $Bi_2Sr_2Ca_2Cu_3O_{10}$. This chapter also reviews their fabrication methods and the physics of grain boundaries and nanocrystalline materials. Chapter 4 describes the fabrication and measurements on micro- and nanocrystalline $YBa_2Cu_3O_7$ class of materials, and presents the new data and findings. Chapter 5 describes common mode currents – a dangerous pitfall that may lead to erroneous claims of superconductivity, which may occur in transport measurements of any high-resistance materials, including nanocrystalline materials. Chapter 6 is similar in structure to Chapter 4, and presents the new data on the $Bi_2Sr_2CaCu_2O_8$ and $Bi_2Sr_2Ca_2Cu_3O_{10}$ materials. Finally, the findings are summarized and conclusions are drawn in Chapter 7, along with suggestions for future work.

Chapter 2

Theory and Applications of Superconductors

This chapter serves as an introduction to the basics of superconductivity and is structured as follows: Section 2.1 gives a brief description of the history of superconductivity. Section 2.2 through Section 2.4 outlines the basics of the main theories within superconductivity – the Bardeen-Cooper-Schrieffer microscopic theory, the London equations and Ginzburg-Landau theory. Section 2.5 presents analysis on the most important superconductors for high field applications and shows that their critical current densities are still far below their potential. This section also outlines the basics of the flux pinning and irreversible magnetisation. Finally, Section 2.6 looks at some applications, many of which are enabled with superconductivity.

2.1   Brief History of Superconductivity

In 1908, H. Kamerlingh Onnes was the first person to liquefy helium at its boiling temperature of 4.2 K at 1 atmosphere pressure [12]. This work enabled the discovery of the first superconductor. Three years later in 1911, Onnes was experimenting with the low-temperature behaviour of mercury, when he observed a sudden drop of electrical resistance to zero below a critical temperature (T_c) of 4.2 K [1]. This was the first observation of superconductivity. Two more elemental superconductors were discovered in the next 20 years: Lead, with a T_c of 7.2 K, and niobium, with T_c of 9.2 K [13]. Zero electrical resistivity below T_c is one of the two defining properties of superconductors.

In 1933, Meissner and Ochsenfeld observed the second defining property of superconductors – perfect diamagnetism [14]. When a superconductor is cooled into the superconducting state, the superconductor excludes all magnetic flux from its bulk when cooled in field. This is unlike a perfect conductor, which would not expel flux from its bulk if an external magnetic field was applied prior to cooling.

In 1935, the brothers Fritz and Heinz London proposed two equations that described the two unique characteristics of superconductors [15]. In 1950, Ginzburg and Landau extended the London equations and proposed a phenomenological theory describing the behaviour of superconductors in magnetic fields with a complex order parameter [16]. They also proposed that there are two types of superconductors. A Type I superconductor exhibits the Meissner effect: it excludes and expels magnetic flux from the bulk of the sample up to the critical field (B_c), above which the material reverts back to its normal state. A Type II superconductor behaves the same as Type I below a lower critical field (B_{c1}), in which all magnetic flux is expelled from the bulk. However, as the applied magnetic field B_{app} is increased above B_{c1}, Type II superconductors exhibit a "mixed state" where magnetic flux penetrates the superconductor as fluxons, until the applied field reaches the upper critical field (B_{c2}) and the material reverts to the normal state. A microscopic theory of superconductivity was proposed by Bardeen, Cooper and Schrieffer in 1957, which assumed supercurrent is carried by pairs of electrons in bound states known as Cooper pairs [17]. BCS theory forms the basis of present microscopic theoretical understanding of superconductivity – although it provides no straightforward explanation of high-temperature superconductors.

The first high-temperature superconductor was reported by Bednorz and Müller in 1986. The material was lanthanum barium copper oxide with a transition temperature of 35 K [18]. Since then, many more materials with higher transition temperatures have been discovered and activity in the field of high-temperature superconductivity has risen. Yttrium barium copper oxide ($YBa_2Cu_3O_7$) was found in 1987, and was famously the first superconductor with a transition temperature of 95 K that exceeds the boiling temperature of liquid nitrogen [8].

For over 20 years since 1993, the superconductor with the highest transition temperature was a series of Hg compounds $HgBa_2Ca_nCu_{n+1}O_{2n+4}$ with $n = 1$, 2, these have transition temperatures of above 130 K, which further increases to 150 K at high pressures of tens of GPa [19, 20]. Most recently, this was trumped by the discovery of superconductivity in hydrogen sulphide H_2S, which has T_c of 203 K at 150 GPa [21].

2.2   Barden-Cooper-Schrieffer Theory

In 1950, Fröhlich was the first to propose the fundamental mechanism of superconductivity – the interaction between electrons and lattice vibrations, which leads to the pairing between electrons themselves [22]. This pairing was proven by the discovery of the isotope effect, also in 1950 [23]. The original experiment found that the critical temperature of mercury, and indeed most superconductors, is a function of nuclear mass. The relationship between critical temperature and nuclear mass is given by the empirical law

$$T_c \propto M^{-a}, \tag{2.1}$$

where the exponent a is 0.5 or less, depending on the superconductor. The isotope effect provided evidence that ions play an essential role in the mechanism for superconductivity.

In 1957, John Bardeen, Leon Cooper and Robert Schrieffer [17] proposed the Nobel prize winning microscopic theory of superconductors consistent with Ginzburg-Landau theory (section 2.4). The theory states that as an electron passes through an ion lattice, the electron causes ion lattice vibrations, i.e. emits a phonon, which can then be absorbed by another electron. This interaction can be seen as an exchange of a phonon between two electrons, with the interaction taking the form

$$V(\underline{k}, \underline{k}', \underline{q}) = \frac{g^2 \hbar \omega_q}{(\epsilon_{k+q} - \epsilon_k)^2 - (\hbar \omega_q)^2}, \tag{2.2}$$

where $\underline{k}$ and $\underline{k}'$ are the wavenumbers of the incoming electrons, and $\underline{q}$ is that of the phonon. g is the coupling constant between electrons and phonons, ϵ_k and ϵ_{k+q} are the energies of electrons with wavenumbers $\underline{k}$ and $\underline{k} + \underline{q}$, and $\hbar \omega_q$ is the energy of the phonon with wavenumber $\underline{q}$.

It can be seen from equation (2.2) that the interaction is attractive for $|\epsilon_{k+q} - \epsilon_k| < \hbar\omega_q$. Depending on the relative strengths of this electron-phonon interaction and the repulsive Coulomb interaction between electrons, the net force between the electrons can either be attractive or repulsive. If the net force is attractive, superconductivity prevails. The strength of the electron-phonon interaction is given by the coupling constant g^2, and superconductivity is "stronger" when this value is large. However, a large electron-phonon coupling constant in the normal state increases scattering, and hence resistivity. This result is consistent with the general trend that good superconductors are poor conductors at room temperature.

The indirect attraction between two electrons via a phonon exchange described above causes the two electrons to form a "bound" state in what is known as a "Cooper pair". The energy of a Cooper pair lies below the Fermi surface, and therefore the formation of a Cooper pair is energetically favourable. The difference between the Cooper pair energy and the Fermi energy is given by the energy gap Δ:

$$\Delta = 2\hbar\omega_{\mathrm{D}}\exp\left(\frac{-1}{N(0)V}\right),\tag{2.3}$$

where $\hbar\omega_{\mathrm{D}}$ is the Debye energy of lattice phonons, $N(0)$ is the energy density of states at the Fermi energy and V is the interaction potential. The energy required to break a Cooper pair is 2Δ. The radius of a bound electron pair is given by

$$\xi_0 = \frac{\hbar v_{\mathrm{F}}}{\pi\Delta}.\tag{2.4}$$

While BCS theory was very successful at describing classic superconductors, it was less successful with high-temperature superconductivity. Most conventional superconductors have isotropic attractive interactions, thus the Cooper pairs have orbital angular momentum $l = 0$, this is known as s-wave pairing. However, for anisotropic high-temperature superconductors, the orbital angular moment is non-zero which could result in p-wave or d-wave pairing. There are a number of theories based on BCS theory which attempted to describe a pairing mechanism for high-temperature superconductors. For cuprate materials, the interlayer tunneling theory [24] hypothesizes that Cooper pairs behave as described by BCS theory within CuO layers, but are also able to tunnel between

layers of CuO. Calculations by Monthoux and Pines [25] showed it is possible that spin fluctuation gives rise to high-temperature superconductivity. Interest in strong coupling has renewed and grown significantly thanks to the discovery of H_2S with T_c of 203 K, though currently there is no consensus within the community on the pairing mechanism of HTS.

2.3 London Equations

In 1935, the London brothers proposed two phenomenological equations that described the behaviour of Type I superconductors [15]. The first equation is

$$\underline{\boldsymbol{E}} = \mu_0 \lambda_L^2 \frac{\mathrm{d}\underline{\boldsymbol{J}}}{\mathrm{d}t},$$
(2.5)

where μ_0 is the permeability of free space, $\underline{\boldsymbol{J}}$ is the current density and $\lambda_L^2 = \frac{m}{\mu_0 n_s e^2}$ is the London penetration depth in which m is the electron mass and n_s is the density of superelectrons. This equation embodies perfect conductivity: an electric field will cause current to accelerate, and a constant current will generate no electric field and hence zero resistance. The second London equation is given by:

$$\underline{\boldsymbol{B}} = -\mu_0 \lambda_L^2 \underline{\boldsymbol{\nabla}} \times \underline{\boldsymbol{J}}.$$
(2.6)

By combining equation (2.6) with two of Maxwell's equations, we arrive at

$$\nabla^2 \underline{\boldsymbol{B}} = \frac{\underline{\boldsymbol{B}}}{\lambda_L^2},$$
(2.7)

which has solution

$$B(x) = B_0 \exp\left(-\frac{x}{\lambda_L}\right).$$
(2.8)

This solution shows that an applied magnetic field will decrease exponentially as it penetrates into the superconductor with a characteristic distance of λ_L.

2.4 Ginzburg-Landau Theory

Ginzburg-Landau theory can be seen as an extension of the London theory described in the previous section. It begins by assuming a complex order parameter, ϕ. The order

parameter is zero above T_c, and increases below T_c until zero temperature. The physical significance of the order parameter is that its modulus squared is equal to the density of superconducting electrons,

$$n_s^* = |\phi|^2. \tag{2.9}$$

Ginzburg-Landau theory argued that the free energy density (f) of a superconductor near the superconducting state/normal state transition is given by

$$f = f_n + \alpha|\phi|^2 + \frac{\beta}{2}|\phi|^4 + \frac{1}{2m}|(-i\hbar\underline{\boldsymbol{\nabla}} - 2e\underline{\boldsymbol{A}})\phi|^2 + \frac{|B|^2}{2\mu_0}, \tag{2.10}$$

where f_n is the free energy density of the normal state, α and β are phenomenological parameters, and $\underline{\boldsymbol{A}}$ is the electromagnetic vector potential. Minimizing the free energy density with respect to ϕ and applying the equilibrium condition gives the first Ginzburg-Landau equation:

$$\alpha\phi + \beta|\phi|^2\phi + \frac{1}{2m}(-i\hbar\underline{\boldsymbol{\nabla}} - 2e\underline{\boldsymbol{A}})^2\phi = 0. \tag{2.11}$$

The second Ginzburg-Landau equation can be obtained by minimizing the free energy density with respect to $\underline{\boldsymbol{A}}$ and using Maxwell's equations. The second Ginzburg-Landau equation is given by

$$\underline{\boldsymbol{J}} = -\frac{i\hbar e}{m}(\phi^*\underline{\boldsymbol{\nabla}}\phi - \phi\underline{\boldsymbol{\nabla}}\phi^*) - \frac{4e^2}{m}\underline{\boldsymbol{A}}|\phi|^2. \tag{2.12}$$

Important superconducting parameters can be derived from the two Ginzburg-Landau equations and are presented in the following subsections.

2.4.1 Coherence Length

Consider first the one-dimensional, zero-field $(\underline{\boldsymbol{A}} = 0)$ case. The first Ginzburg-Landau equation can be written as

$$-\frac{\hbar^2}{2m}\frac{d^2\phi}{dx^2} + \alpha\phi + \beta|\phi|^2\phi = 0. \tag{2.13}$$

The solution is given by

$$\phi(x) = \phi_0\tanh\left(\frac{x}{\sqrt{2}\xi}\right), \tag{2.14}$$

where ξ is the coherence length, defined as the characteristic length over which ϕ can vary appreciably:

$$\xi = \left(\frac{\hbar^2}{2m|\alpha|}\right)^{1/2}. \tag{2.15}$$

2.4.2 Penetration Depth

The London results can be derived from Ginzburg-Landau theory. Given that ϕ is constant within a Type I superconductor, the second Ginzburg-Landau equation reduces to

$$\underline{\boldsymbol{J}} = -\frac{4e^2}{m}|\phi|^2\underline{\boldsymbol{A}}. \tag{2.16}$$

Combining this with Maxwell's equations, we arrive at

$$\nabla^2\underline{\boldsymbol{B}} = \frac{\underline{\boldsymbol{B}}}{\lambda_{\mathrm{GL}}^2}, \tag{2.17}$$

where

$$\lambda_{\mathrm{GL}} = \left(\frac{m}{e^2\mu_0 n_{\mathrm{s}}}\right)^{1/2} \tag{2.18}$$

is the Ginzburg-Landau penetration depth. The significance of λ_{GL} is that it is the characteristic length over which an external applied magnetic field will decay as it penetrates into the superconductor.

2.4.3 Ginzburg-Landau Parameter

A third parameter, the Ginzburg-Landau parameter κ, is the ratio of the penetration depth and coherence length

$$\kappa = \lambda_{\mathrm{GL}}/\xi. \tag{2.19}$$

Ginzburg-Landau theory predicts that a superconductor is Type I if $\kappa \leq 1/\sqrt{2}$ and Type II if $\kappa > 1/\sqrt{2}$.

2.4.4 Critical Fields – Type I

In the presence of an externally applied magnetic field, a bulk Type I superconductor excludes and expels magnetic flux from the bulk of the sample. The Cooper pairs in the

material create a supercurrent on the surface which in turn creates its own magnetic field equal and opposite to the applied field, cancelling the magnetic field inside the superconductor. This cancellation is maintained up to the critical field B_c, above which the material reverts back to its normal state. This can be expressed as:

$$\mu_0 M = -B_{\mathrm{app}} \text{ when } B_{\mathrm{app}} < B_c, \tag{2.20}$$

where M is the magnetisation.

In Type I superconductors, the critical field is defined as the field at which the transition from the superconducting state to the normal state occurs at $T = 0$. For a bulk Type I superconductor, ϕ is constant and the internal magnetic field is zero. Substituting this into equations (2.10) and (2.11) gives the Gibbs free energy of the superconducting state:

$$G_s = V \left(f_n - \frac{|\alpha|^2}{2\beta} + \frac{1}{2}\mu_0 H_0^2 \right), \tag{2.21}$$

where $H_0 = B_0/\mu_0$ is the magnetic field strength. In the normal state, the order parameter is zero, which leads to a Gibbs free energy of

$$G_n = V f_n. \tag{2.22}$$

At critical field, the two energies are equal. Therefore by equating and rearranging the above equations, we obtain

$$H_c^2 = \frac{|\alpha|^2}{\mu_0 \beta}. \tag{2.23}$$

2.4.5 Critical Fields – Type II

Similar to Type I superconductors, Type II superconductors also exhibit the Meissner effect when the external applied field is below a lower critical field (B_{c1}). However, as the external field is increased above this point, Type II superconductors allow quantized flux, each with magnetic flux of one flux quantum Φ_0, to enter the sample as vortices which form a lattice known as the Abrikosov vortex lattice. The vortices have a core radius of ξ and are surrounded by screening currents of radius λ. The density of vortices increases with external field until the separation between fluxons reaches ξ. At this point, the fluxons overlap and the material is driven normal. The field at which this occurs is defined as the

upper critical field (B_{c2}). The state between the lower and the upper critical field is referred to as the "mixed state" or the "vortex state". In Ginzburg-Landau theory, the lower and upper critical fields of Type II superconductors are given by

$$B_{c1} = \frac{\Phi_0}{4\pi\lambda^2}\ln\kappa, \tag{2.24}$$

and

$$B_{c2} = \frac{\Phi_0}{2\pi\xi^2} \tag{2.25}$$

respectively.

2.4.6 Reversible Magnetisation Near B_{c2}

As the applied magnetic field approaches B_{c2}, the density of fluxons increases and forms a flux line lattice until the separation between fluxons is equal to ξ. Abrikosov [26] demonstrated that in the limit of $B_{app} \to B_{c2}$, the reversible magnetisation is given by:

$$M = -\frac{H_{c2} - H}{(2\kappa^2 - 1)\beta_A}, \tag{2.26}$$

where $\beta_A = \langle\phi^4\rangle/\langle\phi^2\rangle^2 \geq 1$ is dependent on the configuration of the vortex lattice. The Ginzburg-Landau equations in this regime was precisely solved in 1997 by Brandt [27], who published an iterative method which determined the order parameter and field profile in the entire field range $0 \leq B \leq B_{c2}$. Combined with the virial theorem [28], the reversible magnetisation curves was obtained which confirmed the previous predictions.

2.4.7 Depairing Current Density

The depairing current density (J_D) is the theoretical maximum current density of any given superconductor. The depairing current density is found by maximizing the current density by differentiation with respect to $|\phi|^2$ to obtain:

$$J_D = \frac{\Phi_0}{3\sqrt{3}\pi\mu_0\lambda^2\xi}. \tag{2.27}$$

The field dependence of J_D is given by:

$$J_D(B) = J_D(0)(1 - B/B_{c2}), \tag{2.28}$$

where $J_D(0)$ is the depairing current density at zero temperature and field.

2.5 High Field Superconductors

The most technologically useful aspect of superconductors is their ability to produce high magnetic fields. This is not only limited by the upper critical field, but also by the maximum current density that can be put through a material before energy dissipation occurs. This is known as the critical current density J_c, and is often the most important figure of merit to consider when fabricating materials or choosing a material for applications. Figure 2.1 shows the ratio of $J_c/J_D(0\text{ T}, 4.2\text{ K})$ as a function of B_{app}/B_{c2} of the most important superconductors for high field applications. The details of the $J_D(0\text{ T}, 4.2\text{ K})$ calculations can be found in Chapter 4. It can be seen that even the current state-of-the-art materials are $1-5$ orders of magnitude below their theoretical maximum. Evidently there is much room for improvement, even in materials where the fabrication technologies are considered to be mature. The rest of this section describes some aspects of the critical current density.
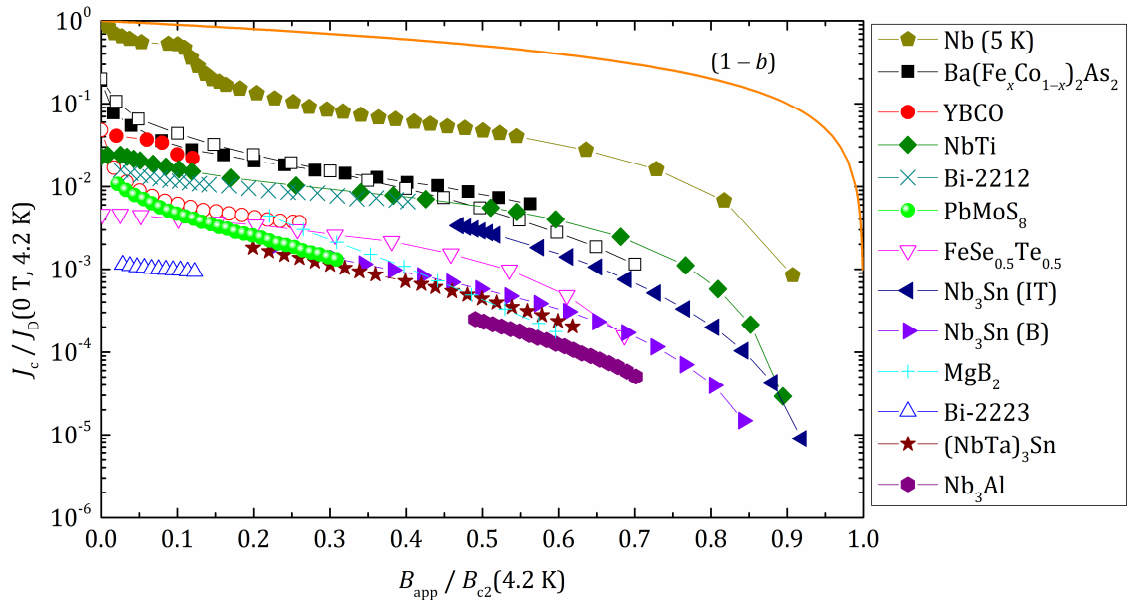
Figure 2.1: $J_c/J_D(0\text{ T}, 4.2\text{ K})$ as a function of $b = B_{app}/B_{c2}$ for the most important superconductors for high field applications, where J_c is the critical current density, J_D is the depairing current density, B_{app} is the applied field and B_{c2} is the upper critical field. The $(1-b)$ curve gives the field dependence of J_D. Closed and open symbols signify that B_{app} is parallel and perpendicular to the ab-plane respectively in anisotropic materials.

2.5.1 Flux Pinning

In the mixed state, the transport current density $\underline{\boldsymbol{J}}$ interacts with the flux vortices through the Lorentz force $\underline{\boldsymbol{F}}_\mathrm{L} = \underline{\boldsymbol{J}} \times \underline{\boldsymbol{B}}$. This causes the flux vortices to move and thereby dissipate energy. Therefore, it is impossible to carry current without dissipation in a perfectly homogeneous superconductor. Any useful superconductor must contain pinning sites – these are regions of inhomogeneity in the material, such as dislocations and grain boundaries, which may be non-superconducting or have different T_c or κ compared to the bulk. These pinning sites exert a pinning force ($\underline{\boldsymbol{F}}_\mathrm{p}$) on the flux vortices. As it is energetically favourable for flux vortices to occupy pinning centres, they are pinned in place thus preventing energy dissipation. The critical current density can then be defined as the current density at which the Lorentz force is equal to the pinning force, and the vortices are on the verge of moving, i.e.:

$$\underline{\boldsymbol{F}}_\mathrm{p} = \underline{\boldsymbol{J}}_\mathrm{c} \times \underline{\boldsymbol{B}}. \tag{2.29}$$

2.5.2 Bean's Model

In 1964, Charles Bean proposed a model which explained the irreversible magnetisation of Type II superconductors [29]. Bean's model states that the current density J within the sample is always equal to one of three critical values: $\pm J_\mathrm{c}$ or zero, where J_c is proportional to the gradient of the internal field profile and $\frac{\mathrm{d}B}{\mathrm{d}x} = \mu_0 J_\mathrm{c}$. Consider a slab of superconductor in an applied field. As the field is increased from zero, flux vortices penetrate into the sample from the surface. In the Bean model, the density of the flux vortices decreases linearly towards the centre of the sample, due to the presence of pinning centres. The applied field at which the internal field penetrates into the centre of the sample is defined as B^*. As the applied field is further raised above B^*, the shape of the internal field profile remains the same but the offset increases with the applied field. The internal field is on average less than external field, and thus flux is considered to be "shielded".

As the external applied field is decreased, it is again the vortices nearest the sample surface that start leaving first, accordingly it is the internal field near the surface that starts decreasing first. The field profile is completely reversed from the high field case when the

applied field decreases by $2B^*$. The field inside the sample is now on average greater than outside, and the flux is considered to be "trapped".

2.6 Applications

Since their discovery, the applications of superconductors have expanded from within research laboratory to broader areas in engineering. They are used in everything from ITER [30] and CERN [31] to d.c. motors [32] and energy storage [33]. This section looks at some of the important applications of superconductors.

2.6.1 Magnetically Confined Fusion

The magnetically confined fusion of a deuterium-tritium plasma is currently the most promising technology for achieving commercial fusion energy production. Though nuclear fusion is possible with conventional magnets, it is impossible to achieve a Q-value (the ratio power out to power in), of greater than 1. The ITER project (International Thermonuclear Experimental Reactor) is an international collaboration between 35 countries to build the world's largest tokamak. It sets out to demonstrate that commercial fusion is possible by achieving $Q > 10$. In the face of the global energy crisis looming ever closer, this is arguably the most important experiment in the world. In the design of the ITER tokamak [30, 34], the central solenoid and the toroidal field coils are to operate at peak fields of 13.0 T and 11.8 T respectively. Both field coils use Nb_3Sn, a low temperature superconductor with $T_c = 18$ K. The poloidal field coils use NbTi alloy, with $T_c = 9.2$ K.

The scale and ambition of ITER means it dominates the spotlight in the eyes of the public, and it is often easy to overlook smaller but successful projects. For example, Wendelstein 7-X, a stellarator built by the Max Planck Institute of Plasma Physics in Germany. The W7-X reactor uses NbTi to produce a magnetic field of 3 T. The first helium plasma was achieved on 10 December 2015 and reached 1 million °C.

2.6.2 MRI

Despite the grandness of ITER, the superconductor industry is actually dominated by Magnetic Resonance Imaging technology, saving lives in hospitals world-wide. If the magnet systems were made entirely from conventional, dissipative electromagnets, the energy losses would make MRIs impractical. On top of this, the resolution of MRIs increase with magnetic field and therefore higher fields are desirable. For example, the ISEULT-INUMAC project is an 11.75 T whole-body MRI magnet built for the NeuroSpin Research Centre at CEA Life Science Division in Saclay, France [35]. The magnet uses NbTi superconducting coils cooled by a He-II bath at 1.8 K.

2.6.3 Research

To quote a report from CERN, superconductivity has become a key enabling technologies for high-energy physics [36]. In small research laboratories, superconductors are used whenever high magnetic fields above 2 T are required as they are often less costly and much more compact compared to conventional electromagnets. In large scale high-energy physics research, such as the Big European Bubble Chamber at CERN [31] (in operation from the early 1970s to 1985), NbTi was used to produce the magnetic field with which particle trajectories can be tracked. The chamber required a peak field of 5.1 T. The power needed to provide this field with conventional magnets was ~ 60 MW. However, a superconducting system requires less than 10 W, with an additional 1.1 MW consumed by the cooling plant. The Large Hadron Collider at CERN also uses NbTi, operating in superfluid helium at 1.9 K. Hypothetically, if the LHC was built with conventional magnets, it would require 900 MW of electrical power, instead of the 40 MW power which is currently consumed by the cryogenic system of the superconducting magnets.

2.6.4 Magnetic Levitation

Magnetically levitated vehicles (maglevs) have many advantages over conventional trains in that they have higher speed, lower noise, and suffer negligible wear-and-tear due to their non-contact nature. Most designs involve either the train wrapped around the track or vice versa, making the train much safer as derailment is impossible. The JR-Maglev trains in

Japan [37, 38] contains superconducting magnets on the trains which are levitated and guided by levitation and propulsion coils in the track. The maglev employs an electrodynamic suspension system for levitation and linear synchronous motor for propulsion. The first tests began in 1977 on the Miyazaki test track. The Yamanashi Test Line began in 1997 and have broken the world speed records several times, once in 2003 at 581 km h^{-1} and again in 2015 at 603 km h^{-1}. The Yamanashi test track is a part of the 9 trillion JPY Chuo Shinkansen line – a maglev line currently under construction, which will extend between Tokyo and Osaka and is expected to be finished in 2045.

Chapter 3

Review of HTS and Nanocrystalline Materials

This chapter reviews the literature on the three materials of interest in this thesis – $YBa_2Cu_3O_7$, $Bi_2Sr_2CaCu_2O_8$ and $Bi_2Sr_2Ca_2Cu_3O_{10}$. The chemistry and structure of the materials are covered in Section 3.1. Section 3.2 discusses some superconducting properties of these materials. Section 3.3 provides the evidence for weak-links and section 3.4 reviews the origin of weak-links from the literature. Section 3.5 briefly describes the fabrication methods (including those used in this thesis) to make of various types of high temperature superconductors. A review of nanocrystalline materials is given in Section 3.6, including the motivation for fabricating such materials. A summary is presented in 3.7, where the existing gaps in the literature are outlined, showing some possible directions for work that are still required in this field.

3.1 Crystal Structure

Superconductivity in $YBa_2Cu_3O_{7-x}$ (YBCO, or Y123) was discovered by Wu *et al.* in 1987. With a T_c of 93 K, it is notable for being the first superconductor with a T_c greater than the boiling point of liquid nitrogen [8]. The discovery of the Bi-Sr-Ca-Cu-O (BiSCCO) family of superconductors soon followed in 1988, by Maeda *et al.* [9]. The general formula for these materials is $Bi_2Sr_2Ca_{n-1}Cu_nO_{2n+4}$ where $n = 1, 2, 3$. The most significant members of the BiSCCO family are $Bi_2Sr_2CaCu_2O_8$ (Bi-2212) and $Bi_2Sr_2Ca_2Cu_3O_{10}$ (Bi-2223).

The structure of all three materials is perovskite. The unit cells are highly anisotropic and show a layered structure. YBCO has a central layer containing a single Y atom, above this is a layer of puckered CuO_2 plane, then a layer of BaO_2 and finally a layer of CuO chains on top. The structure possesses a mirror plane symmetry about the central Y layer, as shown in Figure 3.1 (a). The BaO_2 and CuO chains are the charge reservoir layers, which supply charge carriers to the CuO_2 conduction layer. Oxygen vacancies are key to the structure of the unit cell and the electronic properties of YBCO. For $x = 0 - 0.6$, YBCO is orthorhombic and superconducting, with the greatest T_c occurring at $x = 0.07$. On decreasing the oxygen content (increasing x), the structure becomes tetragonal and non-superconducting. The unit cells of Bi-2201, Bi-2212 and Bi-2223 are shown in Figure 3.1 (b), (c) and (d) respectively. Bi-2201 ($Bi_2Sr_2CuO_5$) and Bi-2212 are orthorhombic [39, 40], whereas Bi-2223 is tetragonal [41]. The unit cells of BiSCCO are similar to that of YBCO. Again, the CuO_2 planes serve as conduction layers. The c-axis lattice parameter increases and the unit cell dimensions become more anisotropic for increasing n. Stacking in Bi-Sr-Ca-Cu-O system is shifted diagonally, as shown in Figure 3.1 (b), (c) and (d). The XRD diffraction patterns of YBCO and the BiSCCO family [42] are shown in Figure 3.2 and Figure 3.3.
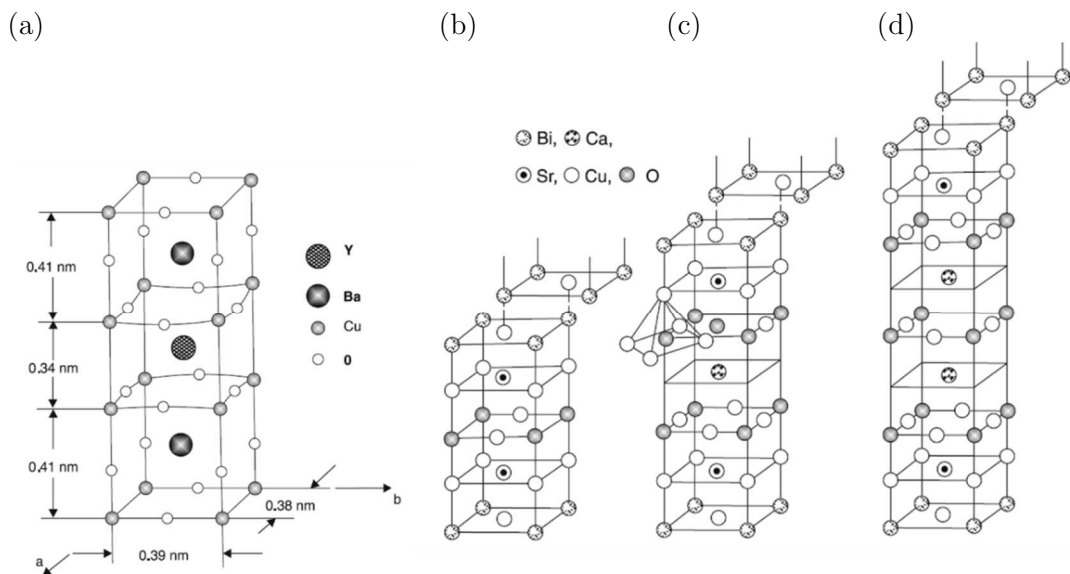
Figure 3.1: The unit cells of (a) $YBa_2Cu_3O_{7-x}$, (b) $Bi_2Sr_2CuO_5$, (c) $Bi_2Sr_2CaCu_2O_8$, (d) $Bi_2Sr_2Ca_2Cu_3O_{10}$ [43].
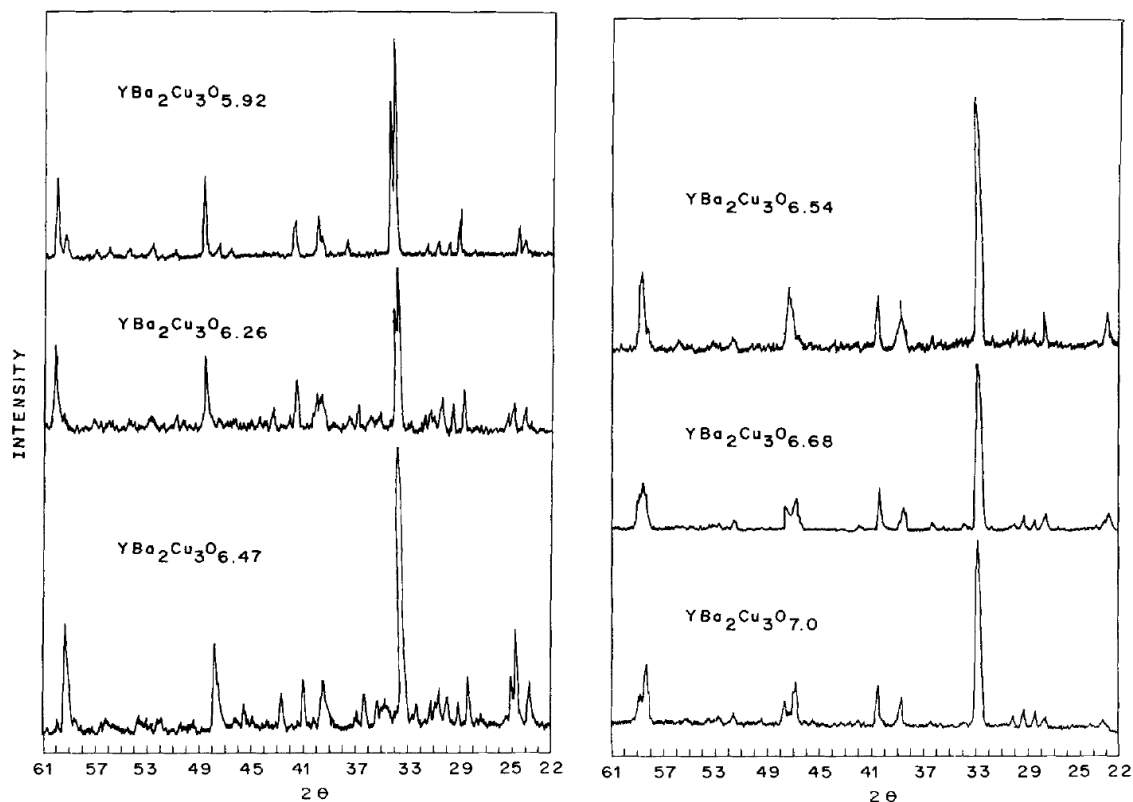
Figure 3.2: XRD of YBa$_2$Cu$_3$O$_{7-x}$ with various oxygen content [44].
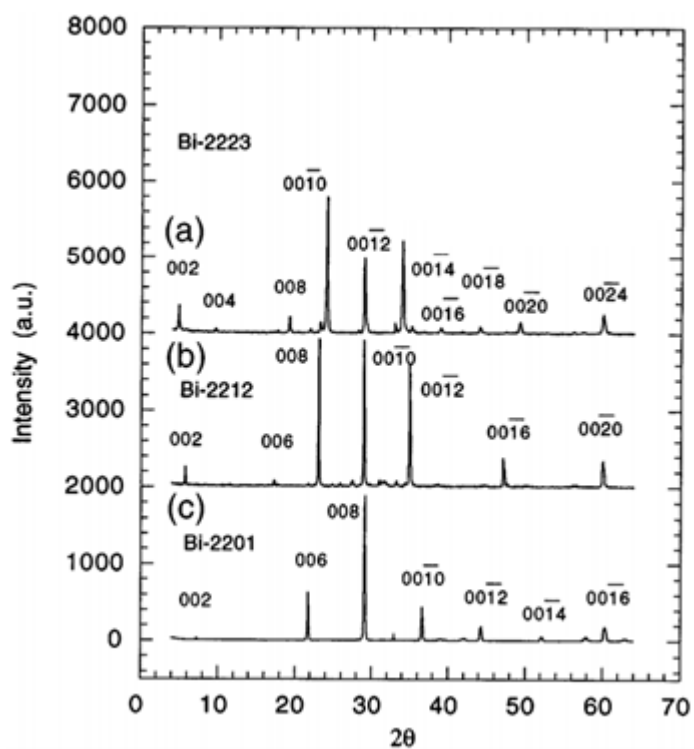
Figure 3.3: XRD of Bi$_2$Sr$_2$CuO$_6$, Bi$_2$Sr$_2$CaCu$_2$O$_8$ and Bi$_2$Sr$_2$Ca$_2$Cu$_3$O$_{10}$ [42].

Both classes of materials are sensitive to water or moisture in the air, YBCO more so than BiSCCO. Several studies [45, 46] have shown that in the presence of water YBCO can undergo chemical decomposition via:

$$3H_2O + 2YBa_2Cu_3O_7 \rightarrow Y_2BaCuO_5 + 3Ba(OH)_2 + 5CuO + 0.5O_2 \qquad (3.1)$$
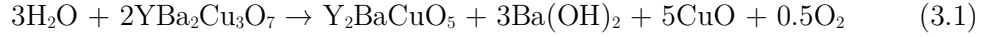
Here, YBCO decomposes into the non-superconducting phase Y_2BaCuO_5 (Y211), commonly known as the "green phase", and oxygen is lost. As such, the handling of YBCO, particularly in powder form, is often done in a low moisture, glovebox environment. The BiSCCO class of materials are more resistant to water or a humid atmosphere [43].

3.2 Superconducting Properties

YBCO, Bi-2212 and Bi-2223 are all sensitive to the oxygen content in the material. For example, in YBCO, oxygen atoms in the CuO_2 planes provide holes, which are the charge carriers, for the material. The hole doping, p, is usually characterised by the number of holes per Cu atom in the CuO_2 plane. Figure 3.4 shows the phase diagram of YBCO as a function of p [47]. It can be seen that superconductivity only exists for a range of p, with maximum T_c at $p \sim 0.16$. The oxygen content in the CuO_2 plane changes the charge in the plane, which can change the distance between CuO_2 planes and the oxygen atom above and below them, causing a change in the c lattice parameter. The relationship between T_c, the oxygen content, p, and the lattice parameter, c, offers a convenient way of calculating any one parameter given the others [48, 49].
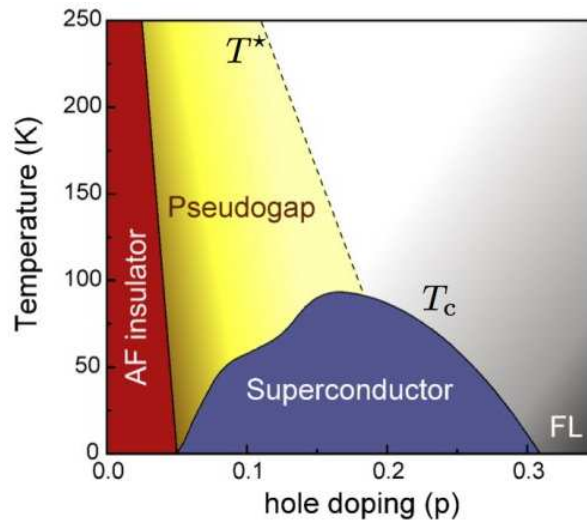
Figure 3.4: Phases of YBCO as a function of temperature and hole doping level [47].

The highly anisotropic structures of YBCO, Bi-2212 and Bi-2223 produce high anisotropy in the coherence length, penetration depth, lower and upper critical fields, and critical current density. The coherence lengths along the ab-plane are much higher than along the c-axis direction, and the opposite is true for the penetration depth. All three materials are highly conductive along the ab-plane, but are around 100 or more times less conductive along the c-axis direction. This can be seen in the resistivity of YBCO along the ab-plane and the c-axis direction as measured by Hagen $et\ al.$ [50], as shown in Figure 3.5. Similarly for Bi-2223, the resistivity along the c-axis direction is around 10^4 times more than along the ab-plane [51] as shown in Figure 3.6. For a current flowing through such an anisotropic material, the angular dependent resistivity is given by

$$\rho(\theta) = \rho_{ab} \sin^2 \theta + \rho_c \cos^2 \theta, \tag{3.2}$$

where θ is the angle between the direction of current flow and the c-axis [52].
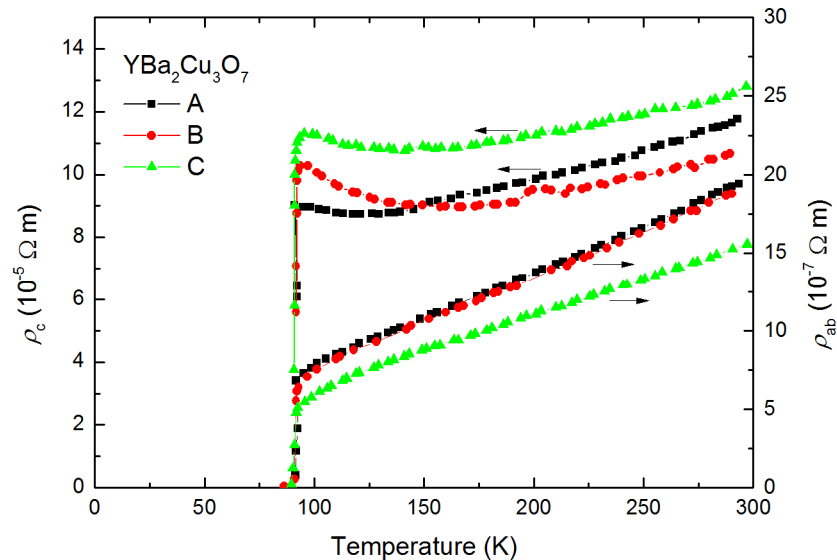
Figure 3.5: Resistivity of YBCO along the ab-plane (ρ_{ab}) and the c-axis direction (ρ_c) [50].

(a)   (b)
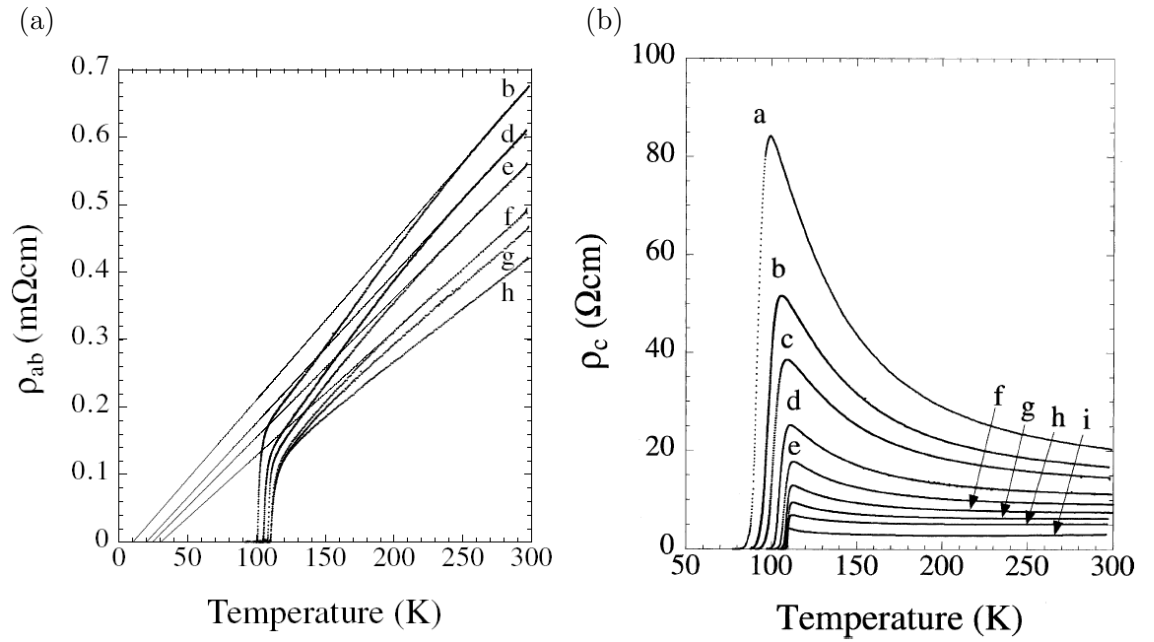
Figure 3.6: Resistivity of $Bi_2Sr_2Ca_2Cu_3O_{10}$ (a) along the ab-plane (ρ_{ab}) and (b) along the c-axis direction (ρ_c) [51].

3.3 Evidence for Weak-Links in Grain Boundaries

Grain boundaries in polycrystalline HTS are often described as "weak-links", which are regions of weakened superconductivity, with a depressed order parameter and possibly weakened flux pinning. Weak-links are very important in the context of this thesis in which we research into how current crosses grain boundaries. This section reviews the literature about the nature of grain boundaries, particularly in HTS.

In 1988, Chaudhari *et al.* [53] made the first direct measurement of J_c across a grain boundary of YBCO and demonstrated that the grain boundary J_c was always less than that of the grains, and significantly further depressed in the presence of a magnetic field. This work was expanded by Dimos *et al.* in their work on YBCO bicrystals [10, 54]. Measurements of the grain boundary critical current density, J_c^{GB} showed that it was substantially less than that in either adjacent grains, J_c^{G}:

$$J_c^{GB} / J_c^{G} < 0.1, \qquad (3.3)$$

except for low-angle grain boundaries with a misorientation angle (θ_{mis}) of less than 2°, this is shown in Figure 3.7. In general, the transition from strongly coupled low-angle

boundaries to high-angle weak-link behavior occurs over an angular range of $\theta_{\text{mis}} \sim 5 - 10°$, above which J_c^{GB} decreased very rapidly with increased θ_{mis} until saturation is reached. J_c^{GB} is also extremely sensitive to small applied magnetic fields whereas J_c^{G} is independent of applied fields up to 0.03 T. These observations demonstrate that the magnetic field penetrates preferentially at the grain boundary and that the grain boundary is a region of weakened superconductivity. The contact resistivity of the grain boundary is in the range of 10^{-14} Ωm^2 to 10^{-12} Ωm^2. Dimos' work concluded that all grain boundaries in HTS (except low-angle grain boundaries) are Josephson junctions [55] responsible for the field dependence of J_c and that weak-link behavior is an intrinsic property of these grain boundaries.

Magnetisation measurements have also confirmed the detrimental effect of grain boundaries on J_c. In 1989, Shimizu and Ito [56] measured the magnetisation loop of YBCO as a function of particle size. Their results showed that the loop width, ΔM, increased linearly with the particle diameter between 0 to 20 µm, and plateaued at above 20 µm, as shown in Figure 3.8. TEM and estimates of grain size showed that particles smaller than 20 µm were single grains, therefore the increase in ΔM was simply due to particle size. Particles larger than 20 µm were made of several grains, therefore the saturation of ΔM was
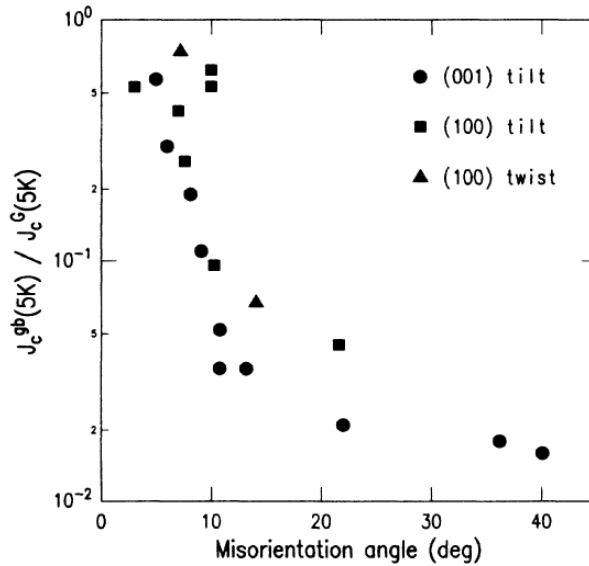
Figure 3.7: The ratio of grain boundary and grain current density at 5 K for three different misorientation types in bicrystals of YBCO, showing an exponential decrease with misorientation angle [10].
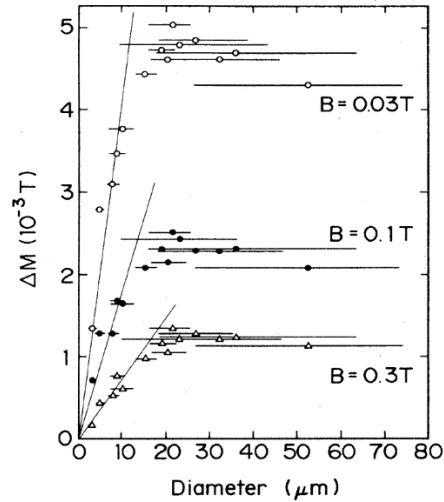
Figure 3.8: Magnetisation loop width as a function of particle diameter in YBCO, measured at 0.03 T, 0.1 T and 0.3 T and 77 K [56].

considered to be due to currents limited by grain boundaries, providing further evidence for the weak-link nature of grain boundaries.

3.4 The Origin of Weak-Links in Grain Boundaries

3.4.1 Structural Distortion and Strain Fields

Grain boundaries are often classed by the type of misorientation between the two neighbouring grains on either side. Three types of boundaries: the [001] tilt boundary, the [100] twist boundary and the [010] tilt boundary, are shown in Figure 3.9. Twist and tilt boundaries can combine to produce mixed boundaries, and translational boundaries can occur from a translation between neighbouring grains. The structural distortion leads to a strain field around the grain boundary, which can cause bonds to stretch or break [57], alter the local charge distribution [58] and even drive the superconductor into an insulating antiferromagnetic phase [59]. Thus the effective grain boundary thickness is often larger than just the region of structural distortion. Electron microscopy carried out by Browning *et al.* showed that some parts of the grain boundaries become completely non-superconducting and that the effective thickness of the non-superconducting region increased linearly from 0.2 to 0.9 nm for misorientation angles from 11° to 45° [60].
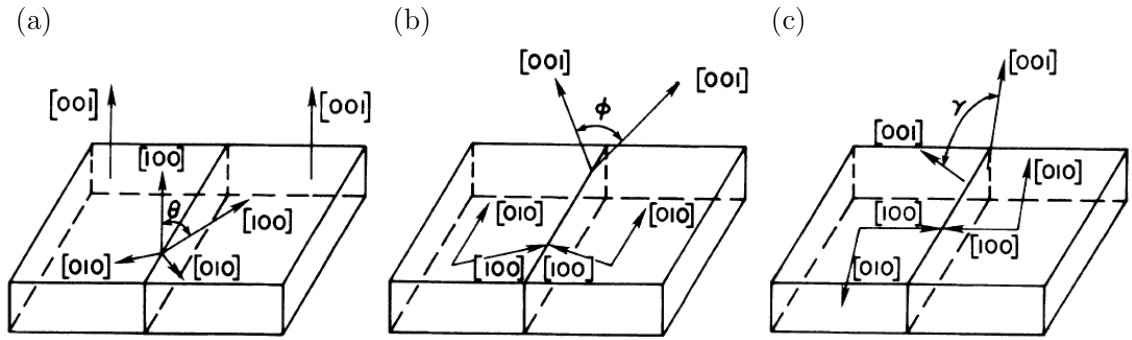
Figure 3.9: Three types of grain boundary geometries: (a) [001] tilt boundary (b) [100] tilt boundary (c) [100] twist boundary [10].

In 2010, Deutscher [57] published an explanation for the reduction of J_c due to grain boundaries based on the bond contraction pairing model [61], where pairing requires contraction of the Cu-O bond in the CuO_2 planes. Tensile strain generated by dislocations at grain boundaries causes stretching or breaking of the in-plane Cu-O bonds [62], and thus prevents superconducting pairing according to the bond contraction pairing model. This work showed that strain is sufficiently large to destroy pairing when $\theta_{mis} \sim 5 - 10°$, which is in agreement with the experimental data of Dimos [10, 54].

3.4.2 Deviations in Stoichiometry

Structural distortion also leads to a non-stoichiometric region around the grain boundary although in very clean grain boundaries, the grain boundaries can still be stoichiometric. In a paper by Chisolm *et al.* in 1988, it was found that the energy dispersive x-ray spectroscopy spectra in the grain boundary region and in the bulk are identical for very clean, 7.5° [100] tilt boundary in YBCO [63]. However, grain boundaries that are non-stoichiometric, for example if there is a depletion in oxygen, can result in extremely high normal state resistivities (see section 3.4.5).

3.4.3 Depression of the Order Parameter

Variation in the crystal orientation on either side of a grain boundary also results in a difference in the relative orientation of the *d*-wave order parameter, as shown in Figure 3.10 [64]. This causes the order parameter to be depressed in the grain boundary region.
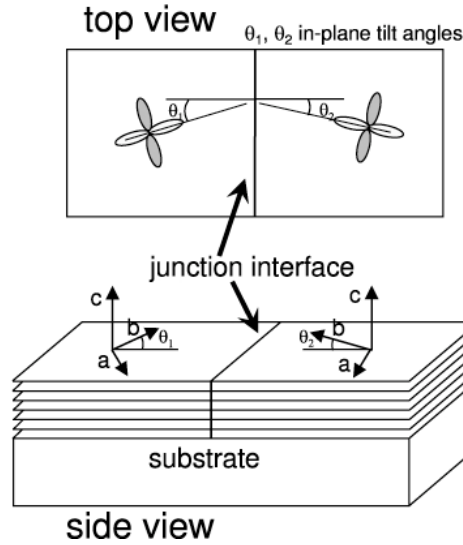
Figure 3.10: Orientation of the order parameter on either side of a [001] tilt grain boundary in YBCO [64].

This depression is dependent on the misorientation angle, and could lead to either enhanced flux pinning or lead to flux flow along grain boundary channels for low- and high-angle grain boundaries respectively [65-67]. Thus there is a crossover between properties of low- and high-angle grain boundaries. The works of Gurevich *et al.* have shown that the depression of order parameter cannot explain the exponential suppression of J_c over the full range of misorientation angles and therefore this is unlikely to be the dominant mechanism [59].

3.4.4 Band Bending and Charge Inhomogeneities

At interfaces between grains, bending of the electronic band structure can occur in a similar way to that of semiconductors. The structural distortion, order parameter depression and band bending at grain boundaries leads to a build-up or depletion of charge at grain boundaries. The build-up of charge at grain boundaries was computationally modelled by Graser *et al.* in 2010 [58] who simulated the structure of YBCO grain boundaries down to atomic scales. The contribution of charge at Cu and O sites around a (410) symmetric grain boundary is shown in Figure 3.11 (a). The charge contribution of copper is positive while the oxygen contribution is negative. Copper atoms are given by the yellow/green
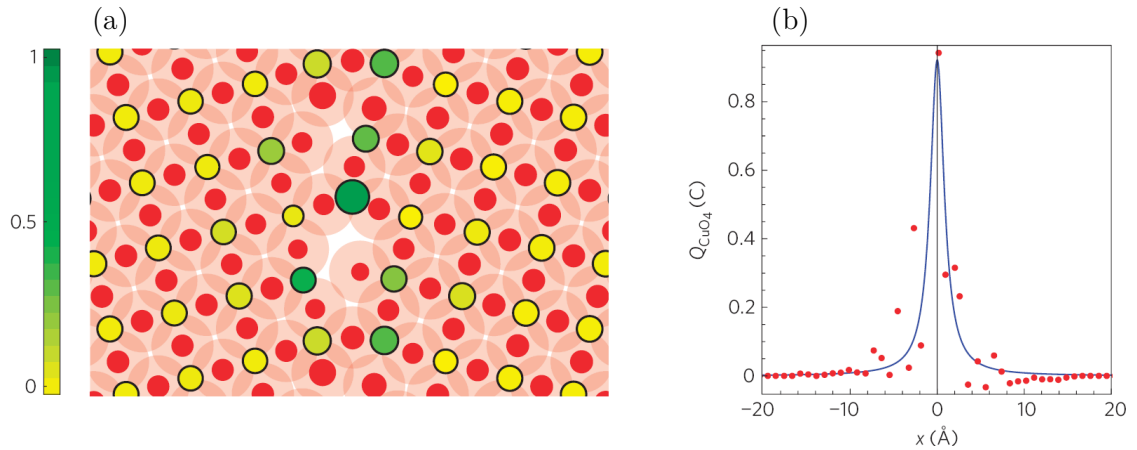
Figure 3.11: (a) Charge distribution at copper and oxygen sites at a (410) boundary in YBCO. Copper sites are yellow/green and oxygen sites are red. The diameter of the circles is a measure of the magnitude of charge. On the copper sites, the colour green indicates a positive charge compared to that of the bulk. Transparent pink circles show the charge contribution of oxygens site towards the charge of each CuO_4 square. (b) Profile of the average charge in each CuO_4 square as a function of distance from the grain boundary [58].

circles, in which green indicates a positive charge compared to that of the bulk. The presence of green circles, i.e. positive charge build up, at the centre of the grain boundary are due the lack of oxygen neighbours from broken Cu-O bonds. Figure 3.11 (b) shows the average charge of each CuO_4 square as a function of distance from the grain boundary, showing a sharp increase in charge close to the grain boundary. Using this information, a microscopic model was used to calculate J_c as a function of θ_{mis}. The results showed that J_c decreased exponentially with grain boundaries angle, in agreement with measurement data, with the dominant mechanism identified as the build-up of charge inhomogeneities at the grain boundaries.

3.4.5 Normal State Resistivity

Grain boundary regions can suffer from increased normal state resistivity, due to scattering from dislocations and structural imperfections [60, 68], from deviations in stoichiometry [69], and from band bending. The normal state interface resistivity of the grain boundary is defined as $R_n A$, where R_n is the resistance and A is the cross-sectional area of a grain
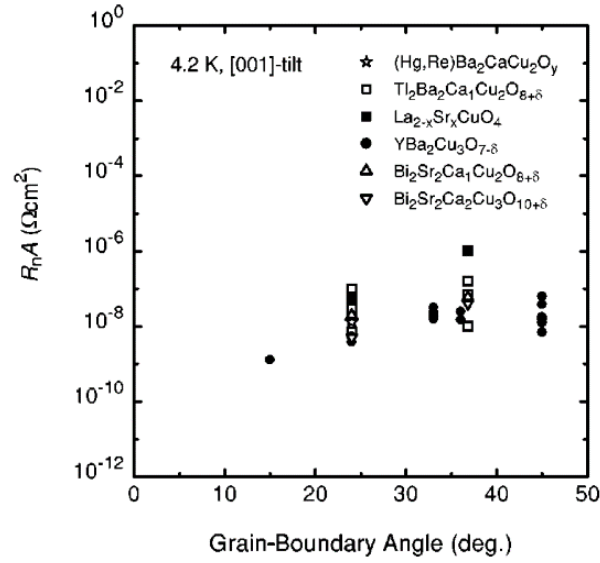
Figure 3.12: Interface resistivity as a function of misorientation angle for a [001] tilt grain boundary in various high temperature superconductors, measured at 4.2 K [70].

boundary, [69, 70]. The interface resistivity of a [001] tilt grain boundary in HTS films as a function of tilt angle is shown in Figure 3.12. These different materials have similar $R_n A$ values, possibly due to the common feature in their structure – the CuO_2 conduction planes. The structural distortion, deviation in stoichiometry and band bending effects in their CuO_2 planes are similar, leading to their $R_n A$ being within 2 orders of magnitude with each other. The interface resistivity of 10^{-7} Ωcm^2 correspond to a resistivity on the order of 10^{-2} Ωm (assuming 1 nm grain boundary thickness), several orders of magnitudes larger than the resistivity of the adjacent grains (10^{-6} Ωm – cf Figure 3.5). Such a high resistivity is partially responsible for the depression of J_c across a grain boundary. By considering band bending and the tunneling of Cooper pairs through the interfacial layer, Mannhart and Hilgenkamp [71] gave an order-of-magnitude estimate of $R_n A$ of 4×10^{-8} Ωcm^2 for a 30° [001] tilt boundary in YBCO, increasing by a factor of 20 from $\theta_{mis} = 15°$ to 45°. Similar band bending is expected for other interfaces, such as contact between superconductor and normal metal, therefore the changes in $R_n A$ also applies in other types of interfaces. Smilde *et al.* [72] fabricated a YBCO/Au/Nb junction in which the Au layer is 5-6 nm thick. They measured $R_n A = 8 \times 10^{-7}$ Ωcm^2, which is of the same order of magnitude as that of bicrystals.

3.4.6 Repairing Weak-Links

The effect of grain boundaries on J_c is so severe that the superconductor industry has resorted to make kilometre-length pseudo single crystal tapes of HTS [11], which is much more costly and less practical than the polycrystalline route, just to avoid these "weak-links". Such methods of fabrication are discussed in section 3.5. It has also lead to research into repairing the grain boundaries as discussed here. One method is to dope the grain boundaries. Cheng *et al.* [73-76] fabricated YBCO in which Ag, Ca and Ag + Ca were doped preferentially into the grain boundaries. Bicrystals were grown using the melt textured growth technique, in which opposite temperature gradients allow crystal nucleation from the outside towards the centre of the sample. The majority of the sample used a pure Y211 substrate, except the centre in which the nucleation fronts met, where the Y211 substrate also contained oxides of the desired dopant, e.g. CaO. This process formed a bicrystal with the dopant highly localized in the grain boundary, as shown in Figure 3.13. Ag, Ca and Ag + Ca doping all lead to an increase in J_c. The reason for the improvement in J_c from Ag doping is structural: the Cu-O bonds in the CuO_2 planes near the grain boundary are under tensile strain and significantly distorted, with the distortion extending several atomic layers from the grain boundary [62]. As Ag has a larger ionic size, the replacement of Cu with Ag in the grain boundary region reduces the geometric distortion and can turn the extended distortion region into a localized one, thus reducing the effective thickness of the grain boundary and reducing the weak-link effect. The mechanism of Ca doping is different to that of Ag: the structural distortion causes a reduced charge carrier concentration in the grain boundary region. Ca preferentially occupies the Y site, replacing Y^{3+} with Ca^{2+}, thus increasing the hole concentration in YBCO, compensating for the loss of hole concentration. Further improvements in J_c was seen when the sample was doped with Ag + Ca, showing that the two mechanisms are cooperative. The improvement in J_c was more significant at higher fields. At 77 K, J_c increased by 169 % at 0 T and 230 % at 77 K. At 60 K and 7 T, J_c increased more than 6 times. Schmehl [77] and Hammerl [78] also used preferential overdoping of Ca in the grain boundaries which resulted in an increase in J_c by a factor of seven compared to undoped materials.
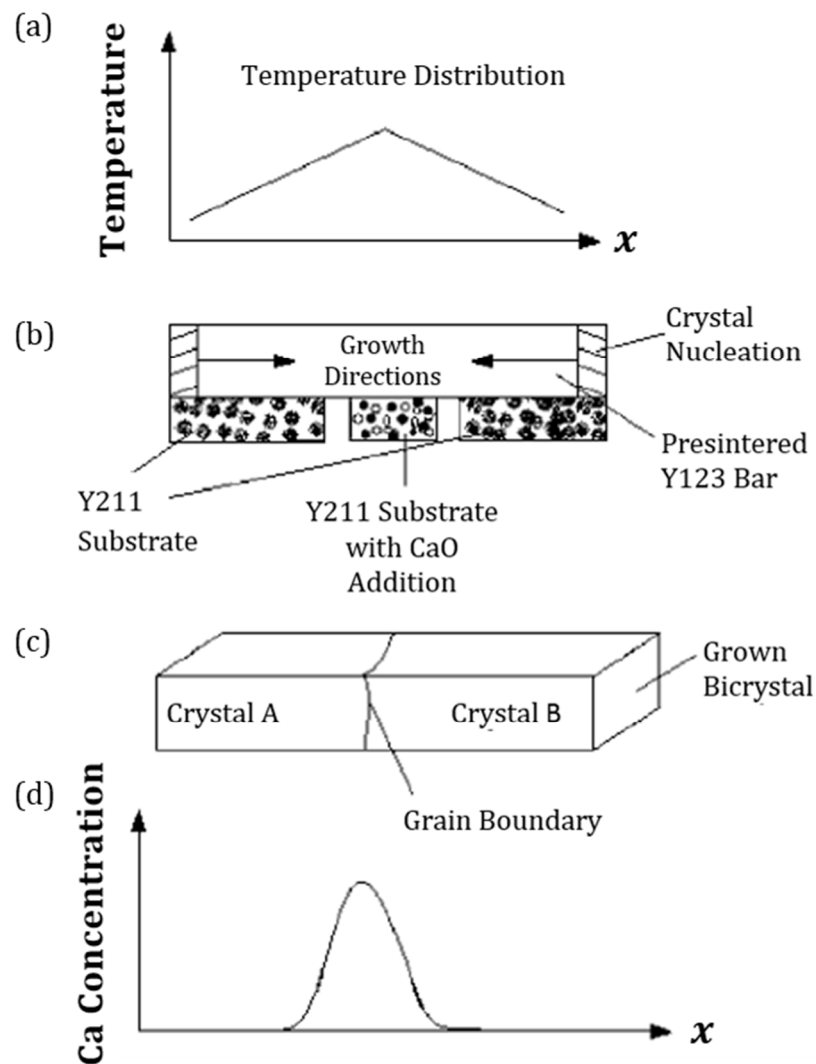
Figure 3.13: Fabrication method used to produce bicrystals of YBCO with doping localized in the grain boundaries [73] (a) Temperature profile of the melt textured growth process in order to produce bicrystals. (b) Schematic of the sample set up. The Y211 substrate was doped with oxides of the desired dopant (CaO in this example) at the peak of the temperature profile to produce (c) a bicrystal with doping localized in the grain boundary region. (d) Ca concentration across the length of the sample, clearly localized around the grain boundary.

3.5   Fabrication Methods

This section reviews the various forms that commercial conductors are supplied in, paying particular attention to the methods used in this thesis. Table 3.1 gives an overview of some

Manufacturer	Superconductor	Fabrication Method
American Superconductor Corporation	ReBCO	RABiTS + MOD
Bruker	YBCO	ABAD + PLD
	Nb_3Sn	PIT
Fujikura	ReBCO	IBAD + PLD
Oxford Instruments	Bi-2212	PIT/DIP
SuNAM	ReBCO	IBAD + RCE
Sumitomo	Bi-2223	PIT + CT-OP
SuperPower	ReBCO	IBAD + MOCVD

Table 3.1: A list of important superconductor manufacturers, their materials and fabrication methods, including Rolling Assisted Biaxially Textured Substrates (RABiTS), Metal Organic Deposition (MOD), Alternating Beam Assisted Deposition (ABAD), Pulsed Laser Deposition (PLD), Powder-in-Tube (PIT), Ion Beam Assisted Deposition (IBAD), Dip Coating (DIP), Reactive Co-Evaporation (RCE), Controlled Over Pressure (CT-OP) and Metal Organic Chemical Vapour Deposition (MOCVD).

prominent manufacturers of commercial superconductors and their fabrication methods, some of which are reviewed in this section.

3.5.1 Coated Conductors

Due to the anisotropy and the weak-link problem, most commercial YBCO and Bi-2223 conductors are fabricated in the form of tapes or "coated conductors". The material is deposited onto a substrate to form pseudo single crystals up to several kilometres in length, with ab-planes parallel to the tape surface and no high-angle grain boundaries in order to optimize J_c. There are two dominant technologies for fabricating coated conductors: Ion Beam Assisted Deposition (IBAD) and Rolling Assisted Biaxially Textured Substrates (RABiTS). In IBAD, the substrate (typically Hastealloy) is polycrystalline and untextured. Instead, texture is introduced in the buffer layers as they are grown, through ion bombardment which preferentially removes undesirable orientations. In RABiTs, texture is imparted on Nickel alloy substrates through repeated rolling and annealing. The texture of the substrate is then imparted on the buffer layers deposited above, through to the superconducting layer. The manufacturing process of IBAD and RABiTS can be seen in

Figure 3.14 and Figure 3.15 respectively. Figure 3.16 (a) shows the substrate layers of a typical IBAD sample. The structure of the layers of a RABiTS sample is shown in Figure 3.16 (b). A superconducting layer is deposited on the substrates, common methods include pulsed-laser deposition (PLD) and metal organic chemical vapour deposition (MOCVD). SuperPower, one of the dominant manufacturers of YBCO tape, use MOCVD on IBAD substrates. The complete layered structure of the SuperPower tape is shown in Figure 3.17, which includes a protective silver overlayer and the copper stabiliser, which protects the conductor during a sudden transition to the normal state by carrying away excess current. American Superconductor Corporation, another prominent manufacturer of YBCO tapes, uses the metal organic deposition (MOD) on RABiTS substrates.
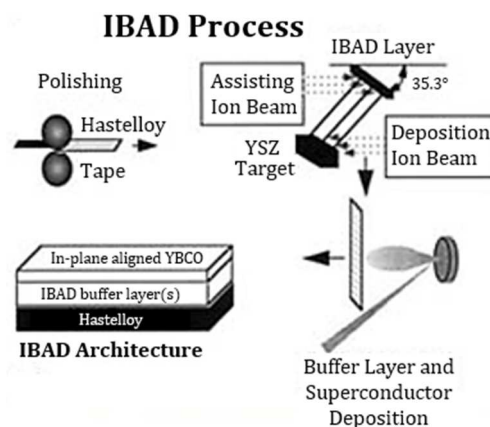
Figure 3.14: Ion Beam Assisted Deposition manufacturing process [79].
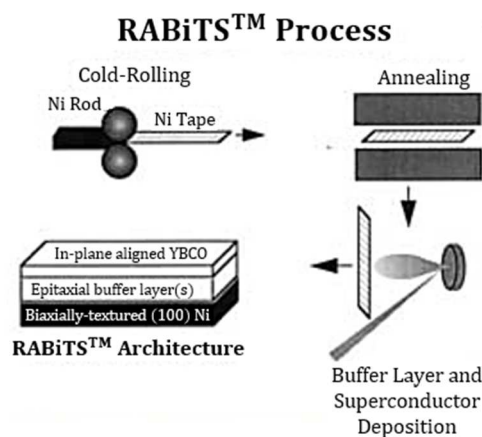
Figure 3.15: Rolling-Assisted Biaxially Textured Substrates manufacturing process [79].

(a)   (b)
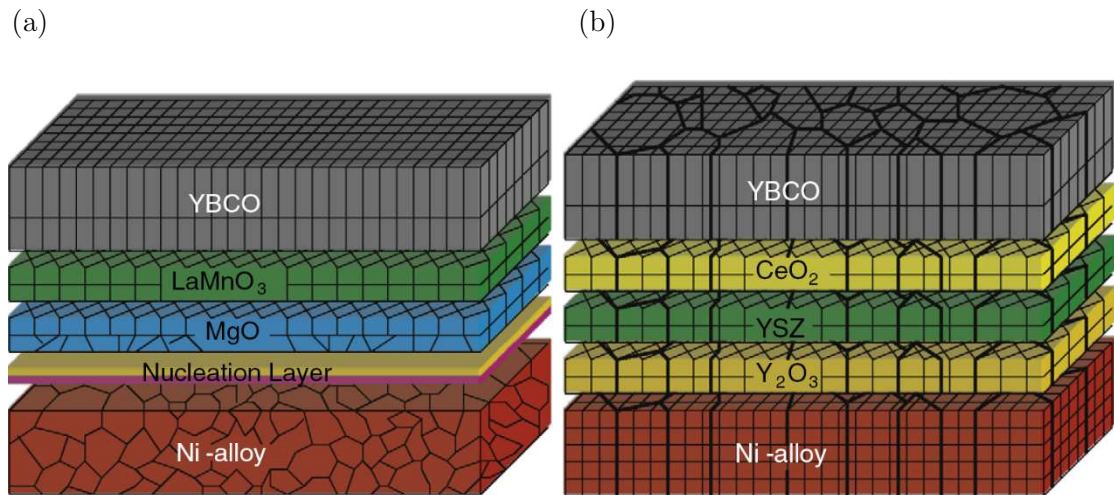
Figure 3.16: Structure of YBCO tapes fabricated through the (a) Ion Beam Assisted Deposition and (b) Rolling-Assisted Biaxially Textured Substrates [80].
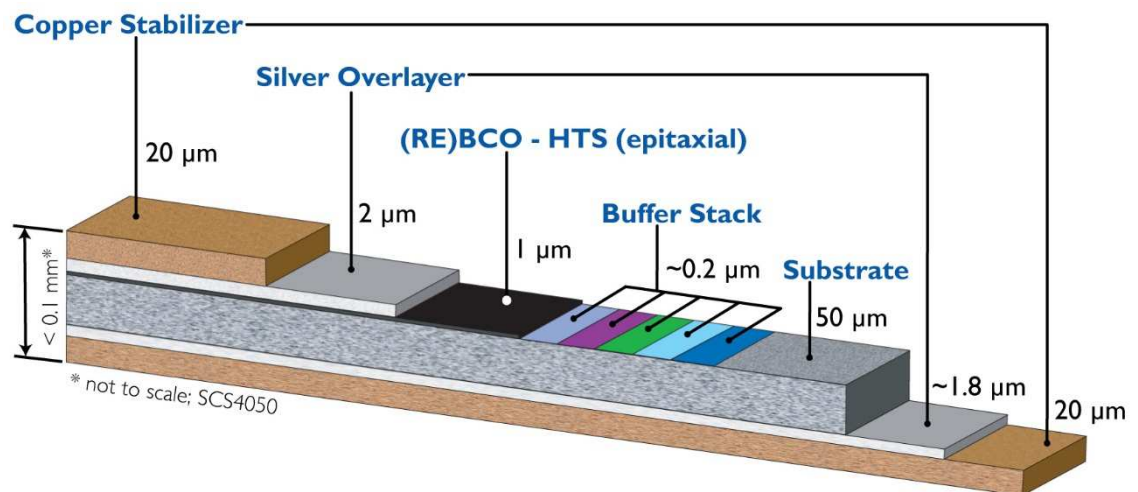
Figure 3.17: Layered structure of SuperPower (RE)BCO tape, in which the substrate, buffer stack and (RE)BCO layers were fabricated using the Ion Beam Assisted Deposition technique as shown in Figure 3.14. Image courtesy of SuperPower Inc., a Furukawa Company.

3.5.2 Wires

The Powder in Tube (PIT) is commonly used to manufacture LTS materials such as Nb_3Sn and MgB_2 [81, 82]. This method is also used to fabricate Bi-2212 wires and Bi-2223 tapes. The manufacture process is shown step-by-step in Figure 3.18. First, the material is

prepared in powder form, which is then packed into a billet, usually made of silver or silver alloy. This is then drawn into long wires or rolled into tapes. Afterwards, the wire or tape is annealed to form the superconducting phase. The larger anisotropy of BiSCCO meant that high grain alignment can be achieved through mechanically rolling alone. Bi-2223 wires are fabricated using this technique at Sumitomo Electric Industries [83]. However, as YBCO is less anisotropic, the PIT method is less suitable to producing highly aligned YBCO tapes.

The cross-section of typical Bi-2212 round wires before the heat treatment can be seen in Figure 3.19 [84]. The wires fabricated this way often suffer from bubbles of gas and voids within the filaments which occur during the heat treatment. This strongly degrades the connectivity of the wires. However, these bubbles can be avoided by applying very high pressures of up to 100 bar during the heat treatment. This increases the density of the
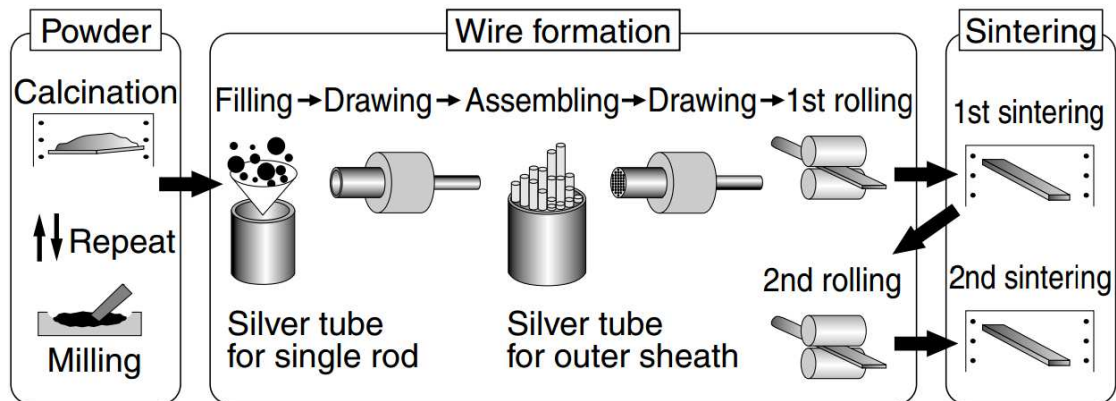
Figure 3.18: Example of the powder-in-tube manufacturing process [83].
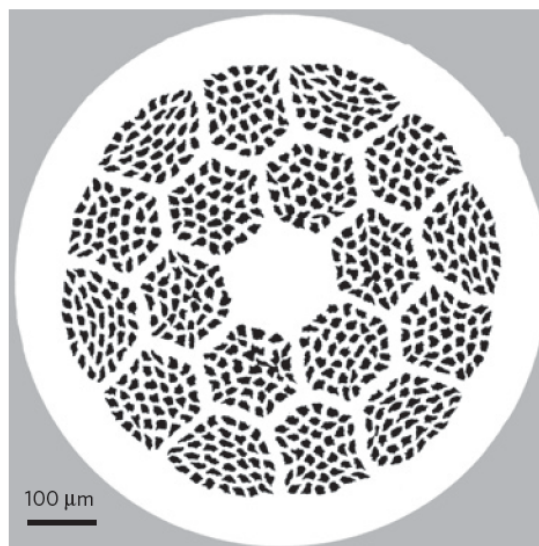
Figure 3.19: Cross-section of a $Bi_2Sr_2CaCu_2O_8$ round wire, before heat treatment [84].

wires and can improve the engineering critical current density (critical current density of the entire conductor cross-section) by a factor of 8.

3.5.3 Top Seed Melt Growth Bulks

The Top Seeded Melt Growth (TSMG) method is used by many laboratories world-wide to produce bulk superconductors such as YBCO [85-88]. The first step is mixing in which precursor powders are mixed in their nominal compositions, e.g. 70 wt% Y123 + 30 wt% Y211 + 0.1 wt% Pt. A small amount of Pt or CeO_2 are often added, this material allows the Y211 phase to distribute more uniformly inside the Y123. The mixed precursor is then poured into a die and pressed into the desired shape. A seed crystal is then placed on the top surface of the pressed sample. For example, for a YBCO bulk, an SmBCO or NdBCO seed is commonly used. The pressed material with seed are then heat treated in a furnace to produce a bulk superconductor. In 2014, Durrell *et al.* fabricated a stack of two Ag-doped GdBCO bulks using TSMG and reinforced with shrink-fit stainless steel, which had a trapped field of 17.6 T, breaking the previous world record by 0.4 T [89].

3.5.4 Ball Milling

Ball milling is a method used in this thesis work. It is commonly used for mixing, alloying, disordering and grinding materials. There are several factors to consider to optimize ball milling, including the material, milling media, duration, the miller, ball to powder mass ratio, sample yield, temperature considerations and conditioning [90]. The first few things to consider are the mechanical properties. For example, soft materials require shorter milling duration, and air sensitive materials may require an inert atmosphere and air-tight milling vials. This also affects the choice of milling media. For example, for superconductors, it is preferable to avoid magnetic materials such as stainless steel, as magnetic contamination in superconductors is extremely detrimental to its properties. However, softer milling media such as copper may produce higher amounts of contamination, and will require longer milling durations, which will again produce more contamination. During mechanical milling, the particle size decreases most drastically at the beginning. Eventually, an equilibrium will be reached in which larger particles are

fractured but smaller particles are welded, resulting in a saturation of grain size. There are two types of popular millers – planetary mills and shaker mills. The milling process in a planetary mill is shown in Figure 3.20. The motion is such that the balls roll along the sidewall of the vial which grinds the powder, and is then thrown towards the opposite sidewall which impacts the powder. In a shaker mill, for example, the high-energy SPEX 8000D shaker mill, the milling vial is shaken back-and-forth with an amplitude of 5.9 cm combined with lateral motion of amplitude 2.5 cm, such that the motion of the ends of the vial trace a figure "8". The vial is shaken approximately 1200 times per minute and the milling balls are subjected to a velocity of ~ 5 ms^{-1}. The milling balls hit the ends of the vial and impact the powder, and the shaking causes the balls to be mixed and dislodged. Ball to powder mass ratio (BPR) can be from as low as 1:1 or as high as 220:1. Higher BPR results in a greater collision rate and therefore lead to shorter milling times. However, very high BPR raises the temperature, leading to recrystallisation, as well as reducing the pot capacity and restricting the mobility of the milling balls. During ball-milling, the impact of balls on the vial causes the sample to become stuck on the vials walls, thus decreasing sample yield. To increase the yield, milling can be paused after set durations, the vial opened up and the inner walls and milling balls scraped to loosen the stuck powders. Depending on the sensitivity of the sample, this may also have to be done in an
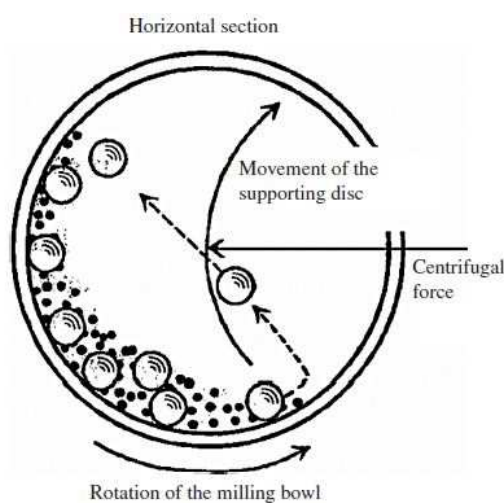
Figure 3.20: Schematic of planetary milling. The powder and milling balls roll along the sidewall of the vial which grinds the powder, and is then thrown towards the opposite sidewall which impacts the powder [91].

inert atmosphere. This also allows the powder and milling media to cool down. Prior to milling any material, the milling media should be conditioned to reduce contamination – a process in which all the surfaces of all milling media are covered with sample powder. Ideally this should be done using the same material, powder mass, BPR, scraping to ensure that the coating powder is the same as the desired product. Conditioning is usually repeated 2 or 3 times.

3.5.5 Hot Isostatic Pressing

Hot Isostatic Pressing (HIP) is a method used in this thesis work to prepare extremely dense bulk materials of YBCO, Bi-2212 and Bi-2223 [92-94]. The materials are sealed under vacuum inside a thin walled container such as stainless steel or pyrex glass, which is then subjected to high temperatures (400 – 900 °C) and extremely high pressures (up to 200 MPa). The canning material collapses under the pressure and compacts the sample inside. Higher HIP temperature, pressure and duration will produce higher density bulks, but increase the grain size of the materials. High pressures in the HIP process can also align the *ab*-planes of the crystals to form a *c*-axis oriented bulk [94]. After the HIP process, HTS can suffer from reduced oxygen content, which leads to a structural transition from orthorhombic to tetragonal, and ultimately reduces T_c, J_c and increases normal state resistivity. Therefore HTS are usually annealed in oxygen post-HIP to restore oxygen content and cause a tetragonal-to-orthorhombic transition, which restores T_c, J_c and reduces normal state resistivity [93-96].

3.6 Superconducting Properties of Nanocrystalline Materials

Much research has been devoted to fabricating large single crystal high temperature superconductors due to the suppression of the supercurrent that can cross high-angle grain boundaries [10]. This has lead to fabrication of quasi single crystalline coated conductors, which still remain very costly. However the assumption that grain boundaries are always weak-links in HTS materials is not supported by the most recent results on Bi-2212 polycrystalline wires which have many high-angle grain boundaries [84] and reopens the

question of using polycrystalline materials which are much easier and cheaper to fabricate. Furthermore, some nanocrystalline materials also exhibit improved physical properties of increased strength and improved ductility [97], as well as improved superconducting properties. In this section, the most important issues associated with changing superconducting properties using grain size reduction are discussed.

3.6.1 Upper Critical Field and Disorder

According to BCS theory, the upper critical field of a superconductor at zero temperature is related to its microscopic properties by [2]:

$$
\begin{aligned}
B_{c2}(0) = 0.973\mu_0^{\frac{1}{2}}\eta\kappa^*(0,\lambda_{\text{tr}})R(\lambda_{\text{tr}})^{-1} \\
\times \left[7.30\times10^{37}\left(\frac{\gamma T_{\text{c}}}{S}\right)^2 + 2.78\times10^6\gamma T_{\text{c}}\rho_{\text{n}}\right],
\end{aligned}
\tag{3.4}
$$

where η is the strong-coupling correction, $\kappa^*(0,\lambda_{\text{tr}})$ is the ratio of the Ginzburg-Landau parameter at $T=0$ and at critical temperature, $\kappa_{T=0}/\kappa_{T=T_{\text{c}}}$. $R(\lambda_{\text{tr}})$ is part of the Gor'kov function [98], $\lambda_{\text{tr}} = 3.81\times10^{-32}\,S^2\rho_{\text{n}}/\gamma T_{\text{c}}$ is the impurity parameter. S is the Fermi surface area, ρ_{n} is the normal state resistivity and γ is the Sommerfeld constant.

The important parameter here is ρ_{n}. It can be seen that $B_{c2}(0)$ increases with ρ_{n}. However, both γ and T_{c} are also indirectly dependent on ρ_{n}, further complicating the relationship between upper critical field and the normal state resistivity. The details of these dependences can be found in [2], where it was shown that both γ and T_{c} decrease with increasing ρ_{n}. An optimum ρ_{n} exists for which a maximum $B_{c2}(0)$ can be obtained. Below the optimum ρ_{n}, the effect of ρ_{n} dominates and $B_{c2}(0)$ decreases. Above the optimum ρ_{n}, the decrease in T_{c} and γ dominates and $B_{c2}(0)$ decreases again. The increase of ρ_{n} can be achieved through doping to introduce impurities in materials. Dislocations can also be introduced to increase ρ_{n}. A decrease in the grain size will increase the disorder and grain boundary density, and hence also increase ρ_{n}. As such, fabricating nanocrystalline materials with a high density of grain boundaries and disorder has the attractive potential of driving up the upper critical field.

3.6.2 Nanocrystalline LTS

In many low temperature superconductors, the reduction of grain size to nanometer scales, comparable to the coherence length, has led to significant increases in the upper critical field in LTS materials [2, 3]. However, this success has not been replicated for HTS [99]. This section reviews the work done on LTS nanocrystalline materials in Durham and in the broader literature. The fabrication methodology is included in this section as some were used as a reference for the work in this thesis.

The work on low temperature superconductors was completed in Durham on nanocrystalline $PbMo_6S_8$ and was published and patented in 2003 [3, 100]. The powdered microcrystalline material was ball-milled for 200 hours, the resulting material contained both amorphous phase and nanocrystalline phase of grain sizes ~ 10 nm [4]. The milled material was subsequently HIP'ed at a pressure of 2000 bars for 8 hours, then annealed at up to 1000 °C for up to 40 hours. The HIP and annealing process restored some crystalline order to the milled powder, which fine-tuned the grain size of the final product. Magnetisation and resistivity measurements showed that for the sample with grain size of 20 nm, T_c was decreased from 15.05 K to 12.30 K but $B_{c2}(0)$ was increased from the conventional value of 45 T to 110 T.

In a paper published by Taylor *et al.* in 2008 [2], niobium powder was mechanically ball milled under argon atmosphere for up to 69 hours, reducing the grain size from ~ 100 nm down to ~ 6 nm. The milled powder was then HIP'ed at a pressure of 2000 bar and at a range of different temperatures. A.c. magnetic susceptibility and specific heat capacity measurements were performed on the unmilled and milled samples to determine the critical temperature and critical fields. The results using a.c. susceptibility measurements, showing very large increases in $B_{c2}(0)$, are shown in Figure 3.21.
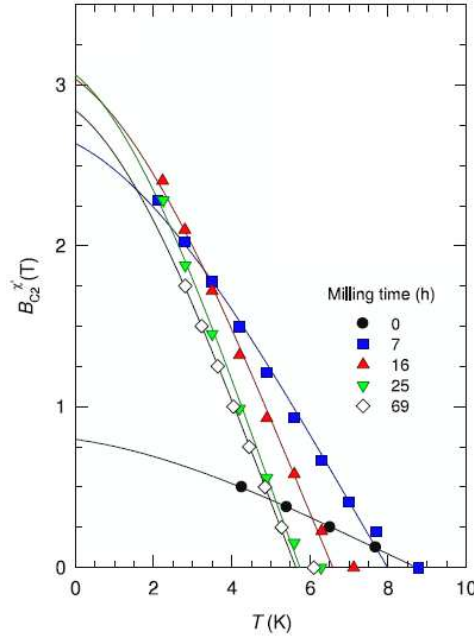
Figure 3.21: The upper critical field of Nb as a function of temperature at a range of milling times [2]. As the milling times increased, the grain size decreased which lead to a decrease in the critical temperature but an almost 4-fold increase in the upper critical field.

Raine *et al.* fabricated nanocrystalline NbCN with grain sizes of tens of nanometers. $B_{c2}(0)$ increased by a factor of 2, whereas J_c increased by an impressive factor of 40. These improvements have been made at a cost of 32% reduction in T_c [7].

MgB$_2$ does not suffer from the weak-link problem [101] and thus there is great interest in developing nanocrystalline MgB$_2$. In 2003, Gumbel *et al.* used WC ball milling and hot uniaxial pressing to fabricate nanocrystalline MgB$_2$ bulks [102]. A decrease in T_c with increasing milling time was observed. Both the irreversibility field and the magnetisation J_c were improved compared to that of thin films. In 2004, Li *et al.* [103] fabricated nanocrystalline MgB$_2$ through WC ball milling. Samples with grain sizes from 64.1 nm to 2.5 nm were obtained. T_c was 39.2 K at a grain size of 64.1 nm and was unchanged as the grain size decreased to 11.8 nm. Below 11.8 nm, T_c dropped dramatically. T_c was 13.2 K in 4 nm grains and superconductivity was completely lost in 2.5 nm grains. It was found that the contraction of the Mg-Mg bond as the grain size decreased caused the depression in T_c. In 2014, Sun *et al.* also fabricated nanocrystalline MgB$_2$ through WC ball milling and high pressure sintering. Samples with grain sizes of 10 nm gave very low T_c, J_c and

poor crystallinity. Samples with grain sizes of 20 nm showed magnetisation J_c that is competitive with that of thin films and higher than that of bulks [5].

As described above, the grain size can also affect T_c of superconductors. The dependence of critical temperature on grain size for several elemental superconductors can be found in a review by Sangita *et al.* [104], shown in Figure 3.22. In Al and Sn, T_c increased with decreasing grain size, until superconductivity is lost. Whereas in Nb and Pb, T_c decreased with decreasing grain size. The effect of grain size on the upper critical field are also measured and the data for Pb are shown in Figure 3.23 (a), in which a clear increase in H_{c2} can be seen as the grain size is decreased. Figure 3.23 (b) shows the H_{c2} of nanoparticles of Pb and Nb, normalized by their bulk values, for different grain sizes. A two-fold increase is seen in the H_{c2} of Nb and three-fold in Pb.

There has also been research into the intermetallic superconductor Nb$_3$Al, fabricated by gas-condensation method, showing that superconductivity vanished at grain sizes below 15 nm [105]. However, later studies showed that nanoparticles of Nb$_3$Al of grain size of 5 – 10 nm can be superconducting and can carry bulk critical current when embedded in a non-superconducting NbAl matrix [106]. The non-superconducting, metallic matrix was thought to provide coupling between nanocrystalline superconductors grains and thus it was able to overcome the size limit of 15 nm.
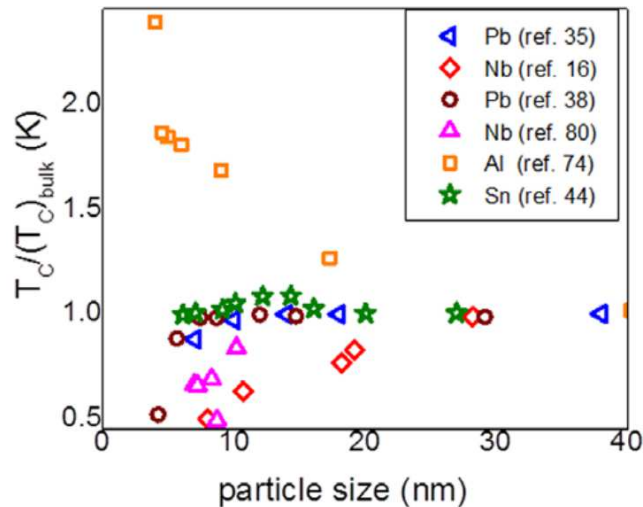
Figure 3.22: Particle size dependence of the normalized critical temperature for elemental superconductors Pb, Nb, Al and Sn, collated in [104].
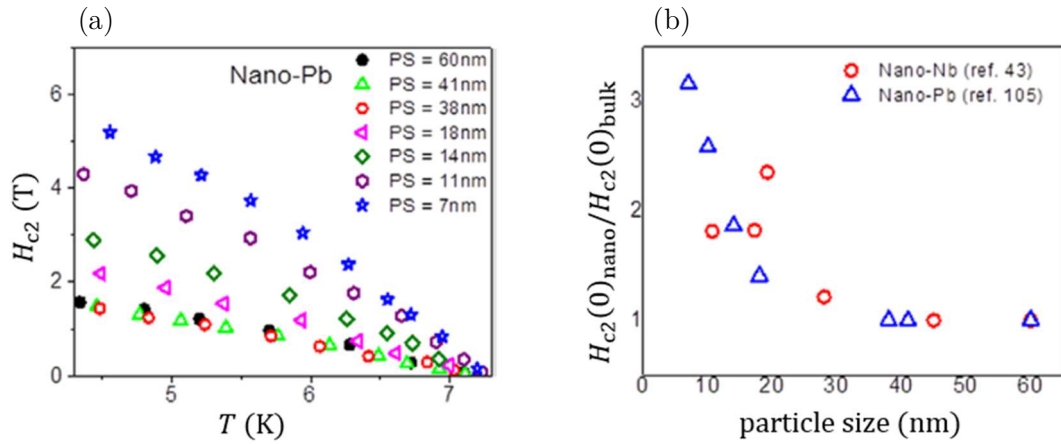
Figure 3.23: (a) Upper critical field of lead as a function of temperature for a range of particle sizes. (b) Upper critical field of nanoparticles of Pb and Nb normalized by the upper critical field of the bulk values, as a function of particle size [104].

3.6.3 Nanocrystalline HTS

In 2008, a pilot study on nanocrystalline YBCO was carried out in the Durham group [99]. In this work, commercial microcrystalline YBCO was milled using a Fritsch Pulverisette 6 planetary ball miller with copper milling media. As copper is a very soft material, the resulting milled powder suffered from high copper contamination. The material was milled in air, which affected the integrity of the YBCO. The material was milled for a maximum of 60 hours. XRD data had shown the grain size decreased most rapidly in the first 2 hours of milling. After 5 hours, the structure had transitions from orthorhombic to tetragonal, in agreement with Simonneau *et al.* [107]. After 30 hours, YBCO changes to a metastable cubic phase [108] (structure shown in Figure 3.24) and the grain size had reduced to ~ 4 nm, and there were no further changes in the XRD patterns after 30 hours. Thermogravimetry (TG) data of milled powder show increased mass loss below 140 °C for longer milling duration, associated with the loss of moisture. Differential scanning calorimetry (DSC) data showed that above 450 °C, the metastable cubic phase decomposes into YBCO, parent oxides, and oxygen. The powders milled for 30 hours were then HIP'ed at 2000 bar for 5 hours at various temperatures. XRD results showed that samples HIP'ed above 450 °C decomposed into parent oxides and suffered a higher loss of oxygen, whereas samples
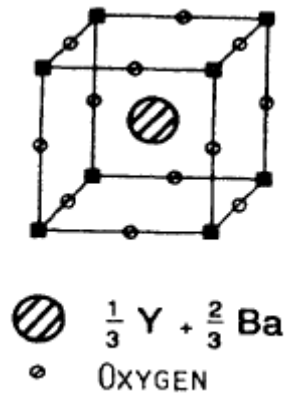
Figure 3.24: Structure of the metastable cubic phase $(Y_{0.33}Ba_{0.67})CuO_3$ [108].

HIP'ed at 400 °C avoided decomposition and oxygen loss while the grain size remained nanocrystalline. The milled and HIP'ed material was then annealed in oxygen at 750 °C to restore oxygen, which increased T_c of all samples. The milled, HIP'ed and annealed material has slightly higher dB_{c2}/dT near T_c compared to the unmilled, HIP'ed and annealed material, which may indicate an increase in B_{c2}. No magnetisation or transport J_c data were reported.

There are also several reports in which HTS were made nanocrystalline and paramagnetism was observed to coexist with superconductivity. Hasanain *et al.* [109] fabricated YBCO with grain size of 31 to 43 nm. T_c was found to decrease with decreasing grain size, similar to that in LTS. Room temperature ferromagnetism was observed in these nanoparticles, and a coexistence of paramagnetism and superconductivity was found at low temperatures. Hasanain *et al.* attributed the ferromagnetism to oxygen vacancies. Gomathi *et al.* [110] used the citrate gel method to fabricate nanoparticles of YBCO with 100 – 200 nm particle size, also observed similar room temperature ferromagnetism. Nanoparticles of YBCO was fabricated by Zhu *et al.* [111] using the citrate pyrolysis method [112]. The T_c of the air-annealed sample was 90 K showing that the grains were of good quality. They also observed room temperature ferromagnetism similar to that of [109]. The magnetisation curves also showed an increase in magnetisation at low temperatures below T_c which was interpreted as ferromagnetism and the cause was once again attributed to oxygen vacancies.

Nanocrystalline Bi-2212 has been fabricated by Jin *et al.* in 1997 through annealing amorphous plates [113] at various temperatures and durations. Grain sizes of between 9 nm and 120 nm were obtained depending on the annealing programme. A.c. magnetic susceptibility measurements showed that as the grain size was decreased, the samples underwent a transition from diamagnetic to paramagnetic, with an increase in the a.c. magnetic susceptibility at low temperatures, similar to that seen with YBCO [111]. T_c also decreased with grain size. A more extensive study was done by Zhao *et al.* in 1998 [114]. The samples were also fabricated through annealing amorphous plates of precursors to form nanometre or submicrometre-grained samples. At annealing temperatures of less than 550 °C, TEM images showed uniform, small grain size of several tens of nanometres. XRD data showed that the amorphous plates had crystallised into Bi-2201. The resistivity increased with decreasing temperature and was non-superconducting above 4.2 K – the lowest temperature measured. Between 550 and 650 °C, TEM showed that the grain size were between 10 and 100 nm. Bi-2201 and Bi-2212 were found to coexist in the XRD pattern, with sharper peaks corresponding to the grain size found in the TEM images. Annealing at 600 °C for 25 minutes produced mainly Bi-2201 phase, similar to the 550 °C sample, the resistivity increased as temperature decreased and no superconducting transition was observed. Annealing at 640 °C for 5 minutes produced mainly Bi-2212. A broad transition was seen in the resistivity data, with an onset T_c of 58 K. Between 650 °C and 750 °C, both nanocrystalline and coarse grains were obtained. The sample annealed at 650 °C for 64 hours contained only Bi-2212 phase according to XRD data. In this temperature range, two transitions were usually observed in the resistivity data in which the percentage of the low T_c phase decreased with prolonged annealing times. Two transitions were also seen in the a.c. magnetic susceptibility data and it was suggested that low T_c phase belonged to poor quality Bi-2212 grains.

3.7   Concluding Comments

The work on nanocrystalline LTS materials in Durham was a great success and provided a promising outlook for nanocrystalline superconductors. However, the literature on nanocrystalline HTS is few and limited. The studies so far have shown that nanocrystalline

HTS has been far less successful compared to LTS. There are still large gaps left in this area of research, understanding of the magnetisation and transport J_c data is particularly sorely lacking. A better understanding of nanocrystalline HTS may explain whether they have the potential to be useful technological superconductors and what role grain boundaries play in the low J_c values reported.

Chapter 4

Nanocrystalline YBCO

4.1 Introduction

The applied superconductivity research community is always trying to increase the critical current density $(J_c(B,T))$ of superconducting materials. There are two quite distinct requirements for achieving high J_c in practical materials. The local depairing current density $(J_D(B,T))$, which is the theoretical limit associated with the density of Cooper pairs, must be high enough throughout the entire material, and the current density associated with local flux pinning $(J_P(B,T))$ must be sufficiently high to stop flux motion. Thereafter many other issues, such as the strain and/or irradiation tolerance of J_c, or the thermal stability of the conductor, become important depending on the application. But, in most applications, high J_c in high magnetic fields is usually the primary technological and economic driver.

In the historical development of the low temperature superconductor (LTS) Nb_3Sn, reducing the grain size in polycrystalline material, significantly increased J_c in high magnetic fields [115]. It was reasonable to assume that in such an intermetallic superconductor, smaller grain size increased pinning and that the metallic bonding ensured that J_D was sufficiently high throughout the entire material that any depression in J_D in the grain boundaries was unimportant. However, over the last decade the progress in increasing J_c in Nb_3Sn has been relatively slow and the simple pinning approach that considers flux pinning alone (e.g. fluxons depinning themselves from isolated pinning sites) has not helped to produce any further significant increases in J_c. More recent

computational three-dimensional time-dependent-Ginzburg-Landau (TDGL) modelling [116] has shown that in polycrystalline superconductors, the dissipation mechanism can consist of fluxons moving along grain boundary channels past fluxons that are held stationary within the grains by strong surface pinning. The increase in pinning due to smaller grains is most likely caused by an increase in the density of triple points along the channels or by providing a more tortuous channel path along which the fluxons must flow. Hence, we suggest that in polycrystalline materials, it is useful to consider depairing and depinning separately and invoke separate values of J_D and J_P for both the grains and the grain boundary channels. This approach helps articulate the open question of whether further significant increases in J_c will be achieved, even in LTS polycrystalline materials, by increasing J_D or by increasing J_P along grain boundary channels. Since in practice we cannot completely decouple J_D and J_P and J_P cannot be larger than J_D, this approach becomes one of identifying whether or not J_D is sufficiently low (at the grain boundaries), that it is the barrier to achieving further increases in J_c.

In developing high temperature superconductors (HTS), the role of grain boundaries was found to be quite different to that of LTS [10, 117]. In the pioneering work of Dimos *et al.* [10], J_c was measured in $YBa_2Cu_3O_7$ (YBCO) bicrystals for different geometries and was found to decrease exponentially with increasing misorientation angle. This led to research into repairing the grain boundaries such as doping them to improve oxygen content or carrier concentration, with a view to increasing J_c [73, 118]. Experimental work was also supported by computational studies which included modelling the flow of current through a grain boundary at an atomic level [58] and modelling grain boundaries, both analytically [119] and using time-dependent Ginzburg-Landau theory [116, 120, 121]. Eventually, industry concluded that high-angle grain boundaries in HTS materials depressed J_c so severely that it committed itself to making kilometre-length pseudo single crystal 2G tapes of HTS [11] that were designed to completely exclude high-angle grain boundaries. In parallel with the development of 2G tapes, the language of "weak-links" was developed in the literature. It emphasized that although some materials have local regions of very high J_c, the practical limit for a material is usually determined by those regions of lowest J_c, although it does not make clear whether the "weak-link" is because of low J_D or low J_P.

Understanding and improving grain boundaries in both LTS and HTS materials is important because despite the huge applied superconductivity research effort, J_c in most materials is still far from its maximum theoretical value – the depairing current density of the superconductor (J_{DSc}) [122]. The first panel in Figure 4.1 shows the critical current density versus field at 4.2 K in the superconducting layer of many of the most important high field superconductors. There are other similar datasets in the literature, such as the excellent webpage produced and maintained by Lee [123]. Samples reported in Figure 4.1 were chosen by prioritising datasets providing a broad range of magnetic field data, and the quality of samples and measurements. The second panel in Figure 4.1 shows the data replotted as current density normalised by the depairing current density at zero field and 4.2 K ($J_c/J_{DSc}(0, 4.2)$), versus the applied magnetic field normalized by the upper critical field at 4.2 K ($B_{app}/B_{c2}(4.2)$). The temperature-dependent depairing current density in zero field has been calculated using

$$J_{DSc}(0, T) = \frac{\Phi_0}{3\sqrt{3}\pi\mu_0\lambda^2(T)\xi(T)}, \tag{4.1}$$

where for isotropic materials, Φ_0 is the flux quantum, $\lambda(T)$ is the Ginzburg-Landau (G-L) penetration depth and $\xi(T)$ is the G-L coherence length. The $(1 - b)$ curve shows the in-field theoretical limit derived from G-L theory where $J_{DSc}(B, 4.2) = J_{DSc}(0, 4.2)(1 - b)$, where $b = B_{app}/B_{c2}(4.2)$. The Appendix provides the method used for calculating the depairing current density in anisotropic materials and Table 4.1 lists the values of $J_{DSc}(0, 4.2)$ used to produce the second panel [98, 123-134]. We note that for YBCO, $Ba(FeCo)_2As_2$ and $FeSe_{0.5}Te_{0.5}$, there are small differences in the values of $\xi_{ab}\lambda_{ab}$ and $\xi_c\lambda_c$, due to the fact that B_{c2} and B_{c1} (or λ) were measured by different groups on different samples. We have neglected the differences between the upper critical field and the irreversibility field, which are generally only important at high temperatures for the high temperature superconductors (typically when ν values, as defined in the Appendix, are low) [84, 135, 136]. The second panel in Figure 4.1 shows that even in technologically mature materials such as NbTi, J_c values in high magnetic fields are still nearly two orders of magnitude below the theoretical upper limit of the depairing current density. The third

panel in Figure 4.1 shows J_c normalised to unity at $0.2B_{c2}$. One can globally fit these normalised data using the long-established standard flux pinning equation, of the form

$$F_P = J_c \times\ B = C\ b^p(1-b)^q, \tag{4.2}$$

where $p = 0.82$ and $q = 2.4$. The values of p and q vary considerably from one material to another when fitted individually. For example for NbTi, $p = 1$ and $q = 1$, whereas for the A15 compounds, $p = 0.5$ and $q = 2$ [137]. Nevertheless, the panel shows that to first order, the in-field behaviour of J_c is not very different across this range of quite different superconducting materials. Equally the data are reasonably well parameterised by an equation used for high temperature superconducting materials of the form [119, 138]

$$J_c =\ \alpha\left(1 - \frac{B}{B_{c2}(T)}\right)\exp\left(-\frac{B}{\beta(T)}\right), \tag{4.3}$$

where at $T = 4.2$ K, $\alpha = 2.9$ and $\beta(4.2) = 0.28\ B_{c2}(4.2)$. Equation (4.2) suggests flux pinning is important whereas the exponential in equation (4.3) suggests the decay of the order parameter across the grain boundaries is important. Hence, although the physical processes associated with these two equations are completely different, it is clear that fitting the data to one or other field dependence does not provide evidence for, or distinguish between, which mechanism operates [139].
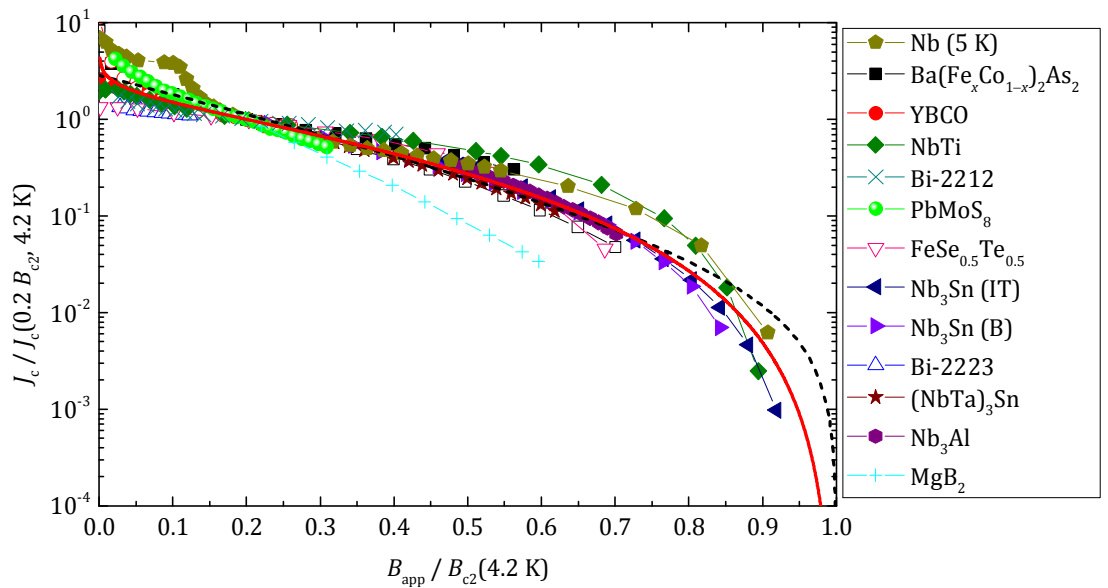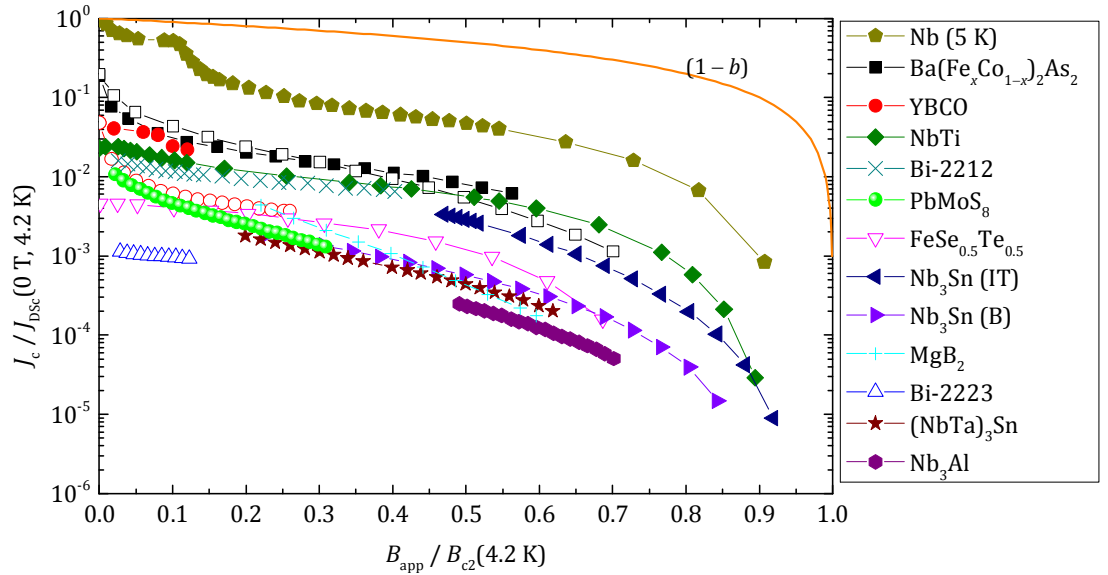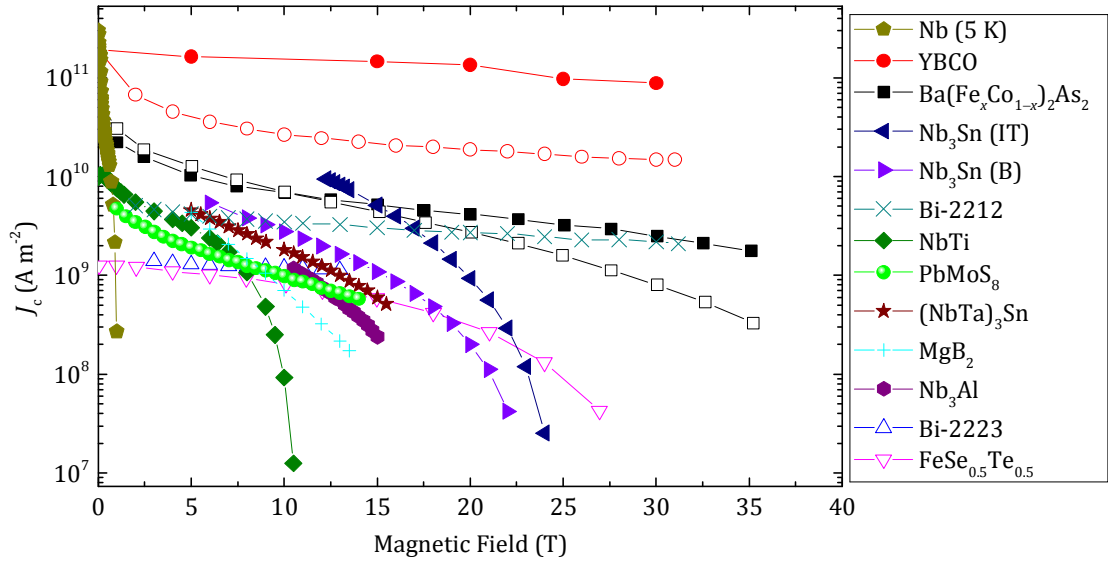
Figure 4.1: Upper panel: Critical current density of the superconducting layer J_c as a function of applied magnetic field B_{app}. The J_c data for YBCO (Superpower "Turbo" double layer tape), Bi-2212 (OST 2212 wire with 100 bar over-pressure) and Bi-2223 (Sumitomo Electric Industries "DI" BSCCO tape) are taken from [84]. J_c data for Nb (thin film with artificial nanoscale pores) [122] (measured at 5 K), Nb-47Ti ([140], 37% Superconductor Cross-Section Area (SCSA)), Nb_3Sn (Internal Sn RRP (IT), 12% SCSA [141] and High Sn Bronze-route (B), 11% SCSA [142]), Nb_3Al (jelly-roll strands, 32% SCSA) [143], $(NbTa)_3Sn$ (11% SCSA) [144], $PbMo_6S_8$ [145], MgB_2 (AIMI 18 Filament (39% Filament CS)) [146], $FeSe_{0.5}Te_{0.5}$ (thin film IBAD substrates) [147] and $Ba(FeCo)_2As_2$ (thin film on CaF_2 substrates) [148] are also included. Closed and open symbols are used for anisotropic materials and signify that the magnetic field is parallel and perpendicular to the ab-plane respectively. Middle panel: J_c normalised by the superconducting depairing current density $J_c/J_{DSc}(0\ \text{T}, 4.2\ \text{K})$ as a function of normalized field $B_{app}/B_{c2}(4.2\ \text{K})$ for the same materials as the upper panel. Values of $J_{DSc}(0\ \text{T}, 4.2\ \text{K})$ were calculated using the method outlined in the Appendix. In anisotropic materials, the $J_{DSc}(0\ \text{T}, 4.2\ \text{K})$ associated with the direction of current flow (i.e. $J_{DSc}^{ab}(0\ \text{T}, 4.2\ \text{K})$) were used. The $(1-b)$ curve shows the in-field theoretical limit derived from G-L theory where $J_{DSc}(B, 4.2) = J_{DSc}(0, 4.2)(1-b)$, where $b = B_{app}/B_{c2}(4.2)$. Lower panel: J_c normalised by its value at the $0.2B_{c2}(4.2\ \text{K})$ as a function of normalized field $B_{app}/B_{c2}(4.2\ \text{K})$ for the same materials as the upper panels. The solid red curve was fitted using equation (4.2), with $p = 0.82$ and $q = 2.4$, and the dashed black curve was fitted using equation (4.3) with $\alpha = 2.8$ and $\beta = 0.29B_{c2}(4.2\ \text{K})$. The fitting parameters were obtained without considering MgB_2.

Material	T_c (K)		ν	$B_{c2}(0)$ (T)	$B_{c1}(0)$ (mT)	$\xi(0)$ (nm)	$\lambda(0)$ (nm)	$J_{DSc}(0, 4.2)$ (10^{12} Am^{-2})
Nb (5 K)	7.50 [122]		1.4 [149]	2.61†	34.3*	9.67*	79.0† [124]	0.322*
NbTi	8.99 [125]		1.8 [125]	15.7 [125]	13.5*	3.40*	163 [124]	0.434*
PbMo$_6$S$_8$	13.7 [150]		1.7 [150]	56.0 [150]	6.40 [150]	1.89*	265*	0.441*
Nb$_3$Al	15.6 [143]		1.3 [143]	26.5 [143]	68.7*	3.15*	65.0 [151]	4.74*
(NbTa)$_3$Sn	16.8 [144]		1.1 [144]	32.0 [144]	38.0†	3.06*	91.9*	2.53*
Nb$_3$Sn	17.8 [152]		1.5 [139]	29.5 [152]	38.0 [153]	2.73*	93.5*	2.83*
MgB$_2$	38.6 [154]	ab:	0.75 [154]	25.5 [154]	38.4 [154]	7.07*	97.1*	1.27*
		c:	0.72 [154]	9.20 [154]	27.2 [154]	2.44*	282*	0.439*
		⟨ ⟩:				3.74*	129*	0.980*
Ba(FeCo)$_2$As$_2$	25.8 [155]	ab:	1.8 [155]	64.7 [155]	4.76*	2.18*	350 [156]	0.289*
		c:	1.2 [155]	56.4 [155]	3.75*	1.26*	605*	0.167*
		⟨ ⟩:				1.86*	413*	0.246*
FeSe$_{0.5}$Te$_{0.5}$	14.0 [157]	ab:	3.0 [157]	44.0 [157]	2.00 [158]	2.16*	317*	0.272*
		c:	1.5 [157]	47.0 [157]	4.50 [158]	1.15*	593*	0.145*
		⟨ ⟩:				1.80*	381*	0.228*
YBa$_2$Cu$_3$O$_7$	90.0 [129]	ab:	2.7 [129]	250 [129]	9.15*	1.29*	135 [128]	4.00*
		c:	1.7 [129]	120 [129]	23.3*	0.378*	894 [128]	0.604*
		⟨ ⟩:				0.969*	208*	2.65*
Bi$_2$Sr$_2$CaCu$_2$O$_8$	84.8 [159]	ab:				3.24*	300 [159]	0.321*
		c:	0.14 [135]	231 [135]	4.60*			
		⟨ ⟩:						
Bi$_2$Sr$_2$Ca$_2$Cu$_3$O$_{10}$	108 [132]	ab:				2.86*	165 [160]	1.22*
		c:	0.14†	297 [132]	13.8*			
		⟨ ⟩:						

Table 4.1: The depairing current density at zero magnetic field and 4.2 K, $J_{DSc}(0$ T, 4.2 K), and the parameters used to calculate it for important high-field superconductors. T_c is the critical temperature, ν is the exponent derived from the empirical equation $B_{c2}^c(T) = B_{c2}^c(0)(1 - (T/T_c)^\nu)$. The upper and lower critical fields B_{c1} and B_{c2} are given at 0 K and given for the magnetic field applied parallel to the ab-plane and parallel to the c-axis. For anisotropic materials, the G-L coherence length and G-L penetration depth are given parallel to the ab-plane, the c-axis as well as an angular average at 0 K. Anisotropic material parameters are taken from single crystals. Parameters for high-field isotropic superconductors were taken from wires. Parameters that were obtained from temperature dependent experiments in the literature have the relevant reference cited next to them. Calculated parameters are labelled with an uppercase star: *. For Nb†: critical values are at 5 K and B_{c2} were estimated from extrapolating critical current data to zero [122]. For (NbTa)$_3$Sn†: B_{c1} was taken to be the same as Nb$_3$Sn. For Bi$_2$Sr$_2$Ca$_2$Cu$_3$O$_{10}$†: ν was taken to be the same as Bi$_2$Sr$_2$CaCu$_2$O$_8$; The value of ν is small, determined from high temperature data.

It is long known that wide, insulating grain boundaries prevent supercurrent crossing them. In this chapter, we provide a quantitative description of when grain boundaries can be considered sufficiently resistive to limit J_c using our data on both microcrystalline and nanocrystalline YBCO. We have chosen these materials because: their fundamental properties in single crystal form are well known; the polycrystalline materials presented here provide a huge range of superconducting transport properties; and there is a huge commercial potential if cheap polycrystalline HTS materials can be fabricated with high J_c. In addition, our group has developed the expertise to make good nanocrystalline materials [2, 3, 99, 100]. The approach we have adopted is to try to make a sufficiently broad range of YBCO samples and measurements to enable us to identify whether J_D or J_P limits J_c. The structure of this chapter is as follows: Section 4.2 describes the sample fabrication process and the microstructure of the materials studied. The results from the transport and magnetic measurements used to characterise the samples are shown in section 4.3. Section 4.4 provides the theoretical considerations we have used to analyse our data and those of the literature. In section 4.5, we discuss our YBCO data and consider other high field superconductors, in particular Nb_3Sn. Finally, the conclusions are summarized in section 4.6.

4.2   Fabrication of Nanocrystalline Materials

4.2.1 Sample Milling and HIP'ing

Samples with two different compositions were made for this work – Y1: $YBa_2Cu_3O_7$ and Y2: 75 wt% $YBa_2Cu_3O_7$ + 25 wt% Y_2BaCuO_5 to which an additional 1 wt% CeO_2 was added to inhibit coarsening of the Y_2BaCuO_5 particles [88, 161]. Commercial $YBa_2Cu_3O_7$, Y_2BaCuO_5 (99.98%, Toshima) and CeO_2 powders (99.99%, Alfa Aesar) were used to fabricate the samples. The Y1 samples were produced from the commercial powders directly. The Y2 composition was chosen because of its high J_c in bulk single crystal form [162]. Powders were first mixed together by shaking the starting powders for 30 minutes in a stainless steel vial using a SPEX 8000D high-energy shaker mill. Next, samples were milled using the miller and tungsten carbide (WC 94/Co 6) milling media in an argon

atmosphere. In an earlier pilot study, we used copper milling media [99]. Although it is expected that copper is less detrimental to the superconducting properties of YBCO than WC or Co, we choose not to use Cu milling media in this work because it is too soft. The samples were milled in batches of 10 g, with a ball-to-powder mass ratio of 3:1, for a total of 30 hours. The milling vial and balls were scraped with a tungsten carbide rod regularly, in argon, to increase yield and improve homogeneity. The powders were placed into small niobium foil packets (0.025 mm thick, 99.8%, Alfa Aesar), which acted as a diffusion barrier and then consolidated using a hot isostatic press (HIP). The Nb packets were sealed into stainless steel tubes (type 316, 1 mm thickness) and HIP'ed at a temperature of 400 °C and pressure of 2000 atm for 5 hours. Many samples were subsequently annealed in pure flowing oxygen atmosphere in a dedicated oxygen furnace to optimize oxygen content and restore some crystallinity. In this chapter, the letters "P", "M", "H" and "A" denote that a sample has been processed through a combination of powder or pellet Pressing, Milling, HIP'ing, or Annealing respectively. The letters are added after the label for composition in the order that they occurred during processing.

Table 4.2 lists the microcrystalline and nanocrystalline samples where the superconducting properties have been studied in detail.

4.2.2 X-Ray Diffraction

The phases present and grain sizes of the samples were obtained using powder x-ray diffraction measurements (XRD). Figure 4.2 shows the evolution of the XRD spectra for the as-supplied powders with the compositions Y1 and Y2, after they were milled for up to 30 hours. Both compositions show similar behaviour, namely the peaks broadened with increased milling time. The associated decrease in the grain size of the $YBa_2Cu_3O_7$ was calculated using TOPAS Academic software and Rietveld refinement. Details of the refinement process can be found in the Appendix A.3. The insets show the grain size as a function of milling time. The grain size of the as-supplied materials is estimated to be 5 μm from SEM (not shown). Within the first 5 hours of milling, the grain size is drastically reduced by 3 orders of magnitude down to the nanometre scale. After 30 hours, the reduction in grain size saturates as it reaches <10 nm. Figure 4.3 shows the XRD spectra

Sample	Grain Size (nm) (±50%)	Annealed	T_c (K)	$B_{\mathrm{Irr}}(0)$ (T)	$\frac{\mu_0 \Delta M}{\Delta B}$ (±50%)	$J_c^{\mathrm{m}}(0,4.2)$ (A m⁻²)	J_c^{t} (A m⁻²)	$\rho_{\mathrm{N}}(300\ \mathrm{K})$ (Ω m)
Y1P	5000	-	81	140(7)	-2×10^{-1}	8.3×10^{10}	-	-
Y1H	5000	-	53	70(5)	-3×10^{-2}	4.1×10^{10}	-	-
Y1HA	5000	A	86	163(10)	-2×10^{-1}	2.9×10^{11}	1.2×10^{5} (0.1 T, 4.2 K)	7.1×10^{-5}
Y1MH	20	-	Para	-	-	-	-	62
Y1MHA(1)	100	A	Para	-	-4×10^{-4}	9.3×10^{9}	Resistive	2.5×10^{-2}
Y1MHA(2)	100	A*	Para	-	-6×10^{-4}	1.0×10^{10} (10 K)	Resistive	2.0×10^{-2}
Y1MHA(3)	100	B	70	66(5)	-3×10^{-3}	4.5×10^{10}	Resistive	8.9×10^{-3}
Y1MPA	25	A	73	40(1)	-2×10^{-3}	2.7×10^{10}	-	-
Y2P	5000	-	81	119(7)	-1×10^{-1}	5.1×10^{10}	-	-
Y2H	5000	-	53	62(3)	-2×10^{-2}	4.0×10^{10}	-	-
Y2HA	5000	A	83	132(5)	-2×10^{-1}	1.5×10^{11}	-	-
Y2MHA(1)	100	A	Para	-	-	-	-	1.0×10^{-2}
Y2MHA(2)	100	A×2	Para	-	-7×10^{-4}	1.7×10^{10} (10 K)	70 (0 T, 2 K)	5.2×10^{-3}
Y2MHA(3)	100	A×3	17	-	-	-	-	-

Table 4.2: The fabrication process, transport and magnetic properties of the microcrystalline and nanocrystalline samples in this chapter. "Y1" and "Y2" represent Y123 and Y123+Y211+CeO₂ compositions respectively. The letters "P", "M", "H", and "A" stand for Pressed powders, Milled, HIP'ed and Annealed respectively. Milled samples (M) were milled for 30 h. HIP processing (H) was at 400 °C and 2000 atm for 5 hours. Letter "A" denotes the standard annealing heat treatment used, which includes a dwell at 750 °C for 20 hours followed by 450 °C for 60 hours. Ramping between temperatures was completed at 600 °C hour⁻¹. A* denotes using heat treatment A, but with a ramp rate of 60 °C hour⁻¹. B denotes a dwell at 450 °C for 20 hours, followed by heat treatment A. A×2 and A×3 were heat treated using heat treatment A, twice and three times respectively. T_c was determined from the onset of ACMS data. "Para" indicates a sample behaves paramagnetically and that no T_c was measured. $B_{\mathrm{Irr}}(0)$ was determined by extrapolation from variable temperature susceptibility data (Figure 4.13) and equation (4.8). $J_c^{\mathrm{m}}(0,4.2)$ is the magnetisation critical current density at zero field and 4.2 K unless otherwise stated, calculated using the grain dimensions of the samples. J_c^{t} is the transport critical current density at a 1 mVm⁻¹ criterion. $\rho_{\mathrm{N}}(300\ \mathrm{K})$ is the normal state resistivity at 300 K. The symbol "-" denotes that the property was not measured.

of the MP, MH and MHA samples. The additional peaks at 30° in the Y1MHA(1) 30 h milled sample and at 24° in the Y2MHA(1) 30 h milled sample should be interpreted with care. We attribute these peaks predominantly to our samples being ground in air for and prior to XRD measurement itself, and the known high sensitivity of YBa₂Cu₃O₇ to decomposition to parent oxides and Y₂BaCuO₅ in the presence of water vapour in air, particularly in highly milled samples [45, 46, 107]. We do not expect such decomposition

to occur in our bulk HIP'ed samples that were not exposed to air. We have not identified the peak at 29° in the Y2MHA(1) sample. The grain size of the MHA samples is approximately 100 nm, with a relatively large uncertainty of $\pm 50\%$, due to the unidentified peaks and high strain in these materials that complicates the refinement process. Trace amounts of WC were found in the XRD and EDX (not reported here) in some milled materials of both Y1 and Y2 compositions. There exist methods in which the oxygen content of $YBa_2Cu_3O_7$ can be calculated using an analysis of the *c*-axis lattice parameter, however we were unable to apply such analysis to our samples because of the very high strain content in these milled materials [48].
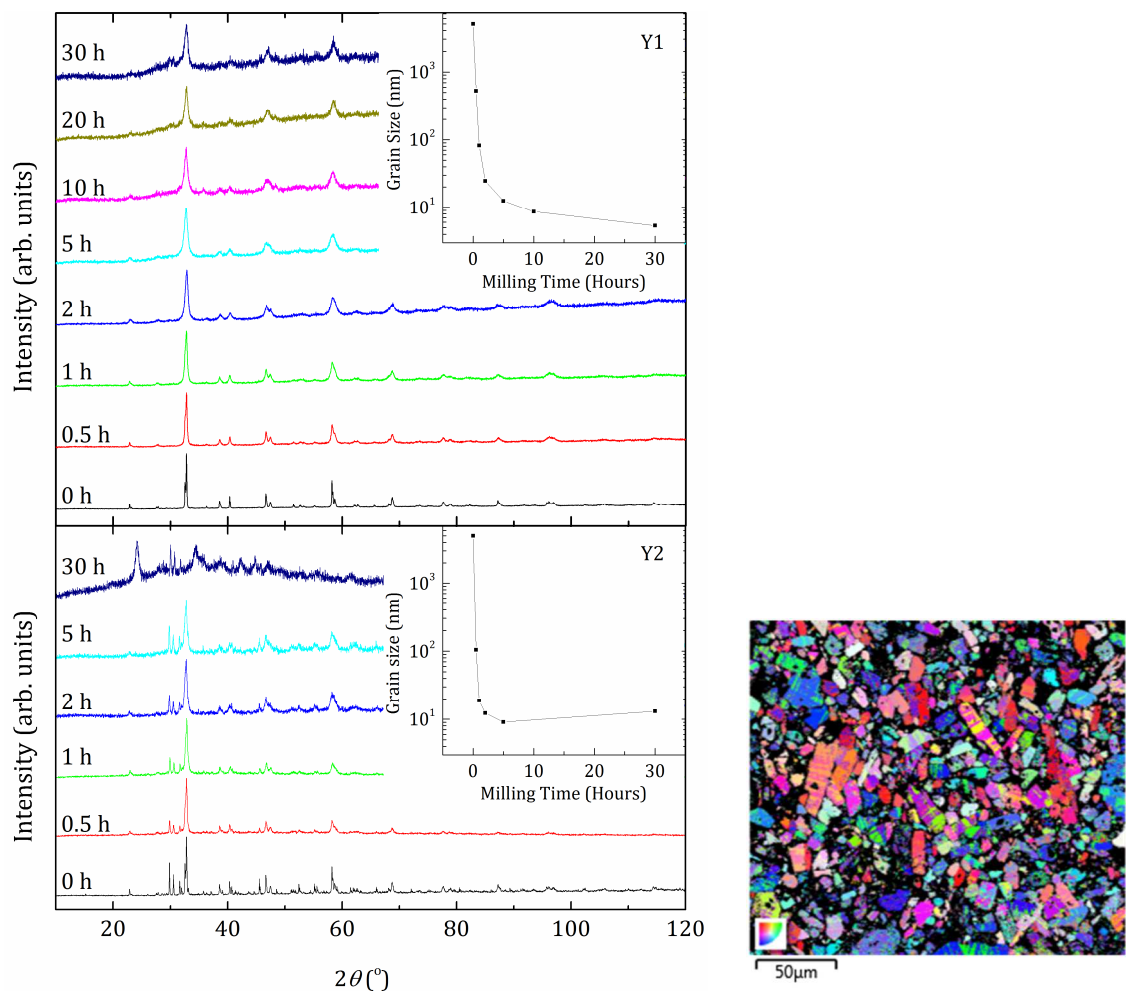
Figure 4.2: Left: X-ray diffraction patterns for the composition Y1 (upper panel) and the composition Y2 (lower panel) after milling for up to 30 hours. Inset: Grain size as a function of milling time. The 5 μm data point in the as-supplied material (at 0 h) is obtained from scanning electron microscopy. Right: Typical SEM image of microcrystalline samples.
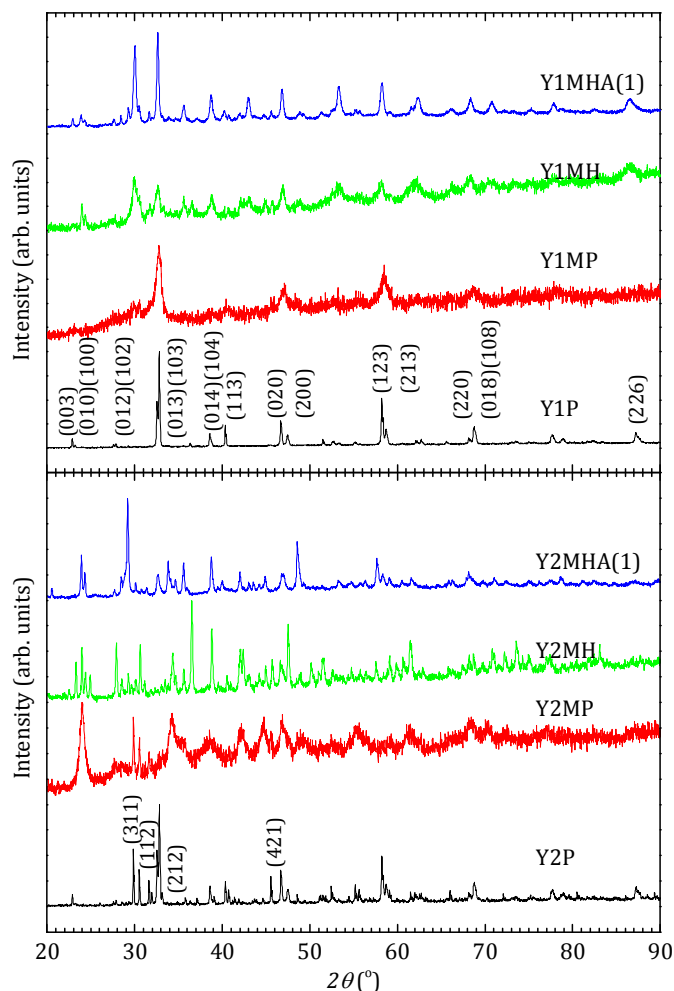
Figure 4.3: Upper panel: X-ray diffraction patterns for Y1P, Y1MP, Y1MH and Y1MHA(1). The main $YBa_2Cu_3O_7$ peaks are labelled. Lower panel: X-ray diffraction patterns for Y2P, Y2MP, Y2MH and Y2MHA(1). In addition to the $YBa_2Cu_3O_7$ peaks labelled in the upper panel, the main Y_2BaCuO_5 peaks are labelled in the lower panel.

4.2.3 Thermal Gravimetry and Differential Scanning Calorimetry

Figure 4.4 shows the thermal gravimetric (TG) and differential scanning calorimetry (DSC) data for the P, MP and MHA samples for both Y1 and Y2 compositions. Data were obtained over two cycles. In each cycle, samples were heated up to 1100 °C and cooled back to room temperature in a pure argon atmosphere at 10 °C min^{-1}. As was the case for the XRD data, one has to be careful interpreting the data for the highly milled samples. Although the DSC/TG samples were not powdered, they were exposed to air when they
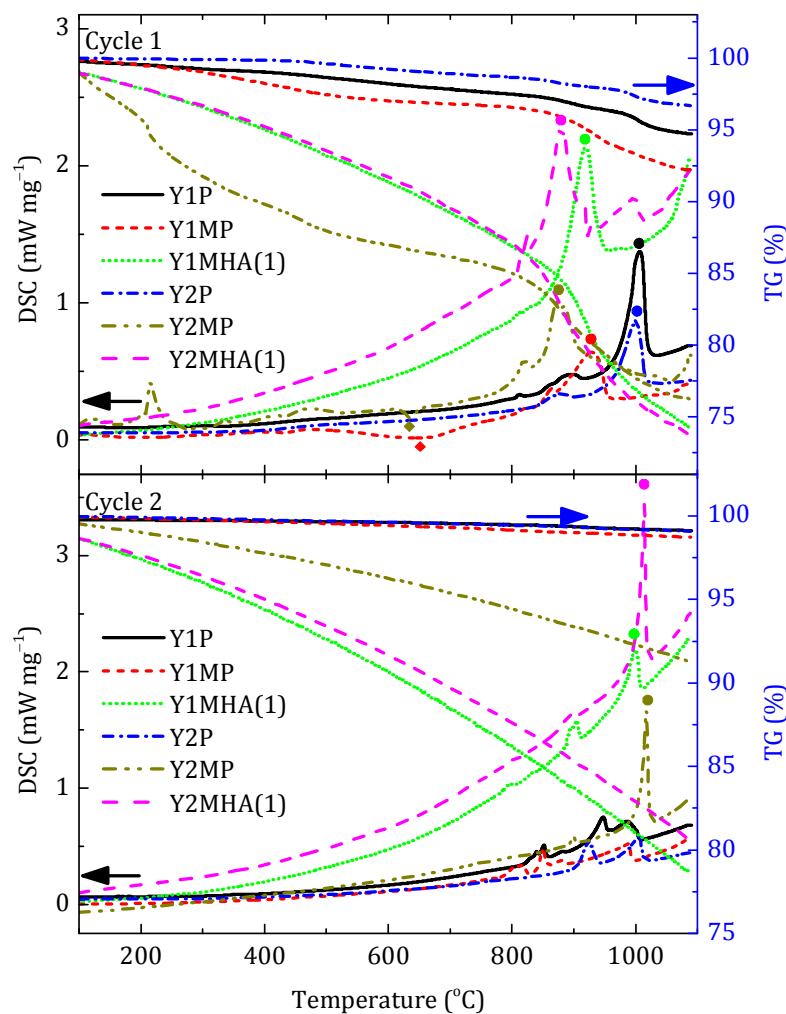
Figure 4.4: Differential scanning calorimetric signal and thermogravimetric signal (showing percentage mass change) for Y1P, Y1MP, Y1MHA(1), Y2P, Y2MP, Y2MHA(1) samples between 100 – 1100 °C, at 10 °C min^{-1}. Upper panel: the heating part of the first cycle. Lower panel: the heating part of the second cycle. Significant endothermic peaks, associated with melting are labelled with ● symbols and exothermic peaks, associated with the crystallisation of amorphous and recrystallisation of nanocrystalline phases, by the ♦ symbol.

were transferred into the DSC/TG sample holder cups prior to measurement. In particular, any significant mass loss or DSC peaks below 200 °C are usually associated with moisture.

Both TG and DSC data for the (as-supplied) Y1P and Y2P samples are in broad agreement with equivalent data from the literature [99]. The mass losses between 400 – 800 °C are

consistent with oxygen loss of $YBa_2Cu_3O_7$ phase from O_7 to O_6 and there are large endothermic melting peaks with onsets at 970 °C [99]. The Y1P, Y1MP and Y2P samples were most stable to mass loss during both cycles. The other three samples showed mass loss over the entire temperature range during both cycles. The only clear exothermic peaks were observed at about 630 °C as indicated by the ♦ symbols for the Y1MP and Y2MP milled samples in the first cycle. We associate these peaks at ~ 630 °C with crystallisation of amorphous, and recrystallisation of nanocrystalline phases, to produce larger grain sizes [163]. As expected, such peaks were not present in unmilled samples Y1P or Y2P nor in any of the second cycle data for any of the samples. These results led us to choose a HIP temperature of 400 °C to fabricate the YBCO materials in this work, to prevent excessive grain growth and follow an approach we have successfully used before to make other nanocrystalline materials [2, 3, 99, 100, 112, 164]. In the two samples that were milled, HIP'ed, and annealed (Y1MHA(1) and Y2MHA(1)), there was increased and significant mass loss near 850 °C in cycle 1 and coincident large endothermic peaks, both of which are absent in cycle 2. We attribute these peaks to melting and oxygen loss. At the highest temperatures of the cycles, we associate the large endothermic melting peaks in Figure 4.4 as follows: the peaks that occur in both panels near 1000 °C are due to melting of the $YBa_2Cu_3O_7$ phase – the exact melting temperature is dependent on oxygen content [165] and expected to be lower in argon atmosphere than in air [166]. The peaks with an onset near 993 °C are due to the reactions $Y_2BaCuO_5 + BaCuO_2 \rightarrow$ Liquid and $YBa_2Cu_3O_7 + BaCuO_2 \rightarrow Y_2BaCuO_5 +$ Liquid [167]. The peaks with an onset near 875 °C are due to the reaction $YBa_2Cu_3O_7 + BaCuO_2 + CuO \rightarrow$ Liquid [167]; and the peaks near 839 °C to melting of $BaCuO_2$ phase [99].

4.3 Experimental Results and Analysis

4.3.1 Transport Measurements – Resistivity and Critical Current Density

HIP'ed samples were shaped into cuboid bars for transport measurements with typical dimensions of $1 \times 1 \times 5$ mm. The samples were mounted onto a Physical Property

Measurement System (PPMS) resistivity puck [168]. Current and voltage leads were connected to the sample using silver paint for standard four-terminal measurements. The voltage taps were typically 2.5 mm apart. Control and measurement of the temperature and the magnetic field were made using the PPMS. To measure $V - I$ traces, the puck was connected to external high-precision voltmeter and current sources. The current was supplied by a Keithley 220 programmable current source. A resistor (typically 1 Ω) was added in series to the sample in order to confirm that the current through the sample was equal to the nominal output current in the range of 10 nA to 0.1 A. The voltage across the sample taps was measured with a Keithley 2100 6½ digit multimeter, with an additional $\times 50,000$ amplifier [169] when required, to measure extremely small voltages. Figure 4.5 shows a summary of the resistivity data for the samples in this chapter as a function of temperature, measured using excitation currents of typically 5 mA.
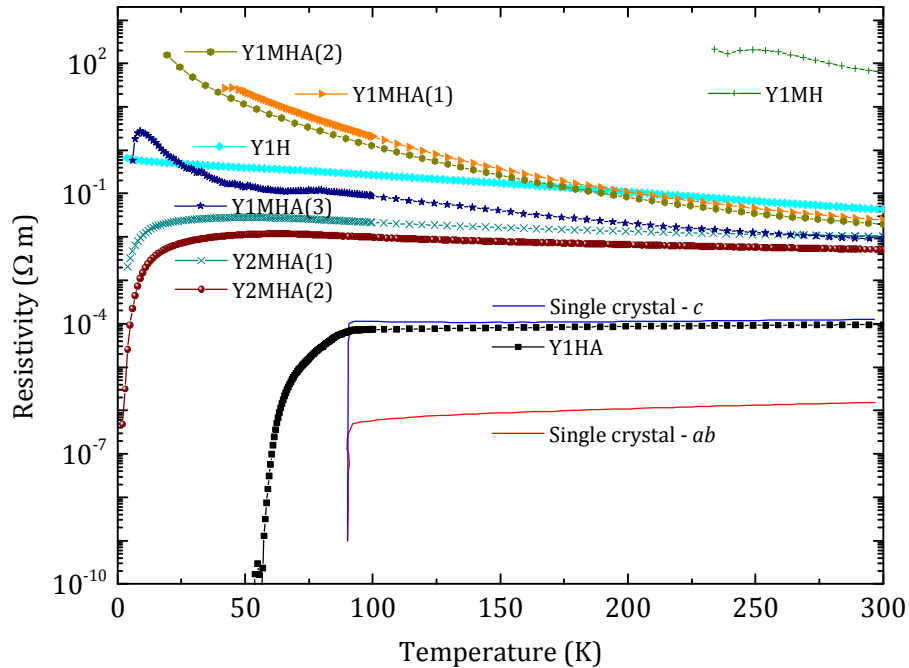
Figure 4.5: Resistivity as a function of temperature for all the materials of Y1 composition and the Y2MHA(1) and Y2MHA(2) samples. The strong effect of oxygen annealing can be seen in both micro- and nanocrystalline materials, decreasing $\rho_N(300\ \text{K})$ by a factor of $\sim 10^2$ and 10^3 respectively. However only three nanocrystalline materials showed a superconducting transition: Y1MHA(3), Y2MHA(1) and Y2MHA(2). Single crystal literature data were taken from [170].

The YBCO microcrystalline sample that was simply HIP'ed (Y1H) has a weak temperature dependent resistivity with no evidence of superconductivity. Oxygen annealing decreased $\rho_N(100\ K)$ by more than a factor of 10^3 and a superconducting transition was observed, which can be seen in the in-field data in the upper panel of Figure 4.6 for sample Y1HA. In zero magnetic field, the onset T_c is 92 K and zero-resistivity occurs at 60 K. Figure 4.6 shows that as the applied field was increased, the onset T_c, that we associate with the grains, does not vary significantly, whereas the zero-resistivity T_c, likely associated with
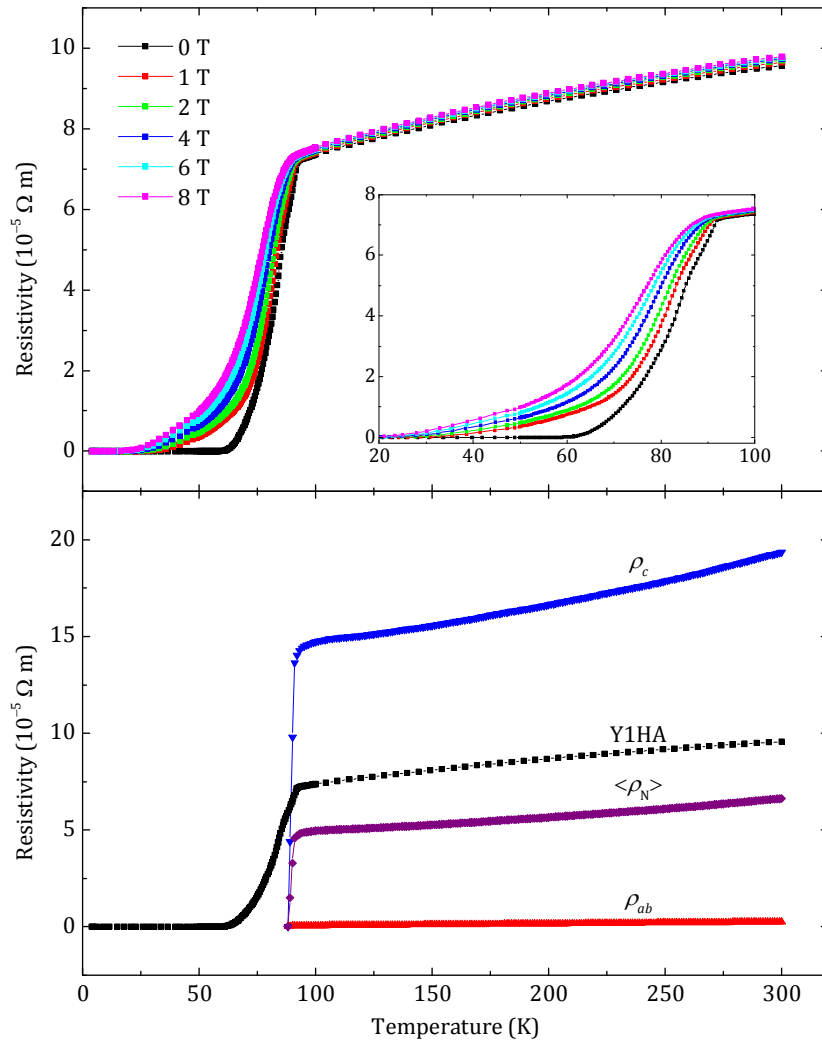
Figure 4.6: Upper panel: Resistivity of Y1HA sample measured in fields of 0 T – 8 T with a constant excitation current of 5 mA. Inset: Detail of the two-step transition. Lower panel: Resistivity of Y1HA in zero field compared to the resistivity of a single crystal of YBCO along the c-axis (ρ_c) and along the ab-planes (ρ_{ab}) [170] and the angular averaged resistivity $\langle \rho_N \rangle$ calculated using equation (4.16).

the grain boundaries, is very significantly decreased. These findings are consistent with those of Dimos *et al.* [54] where the largest suppression of superconductivity in relatively small fields occurs at the grain boundaries. The lower panel compares the values of ρ_N for Y1HA to those of single crystals in which current flows either along the c-axis direction or along the ab-plane. Figure 4.7 shows the equivalent $V - I$ traces for Y1HA. The $V - I$ traces show superconductivity between 0 and 8 T at 4.2 K. Zero field $V - I$ data were also obtained up to 120 K in steps of 10 K, and thereafter up to 300 K in steps 50 K. Using a criterion of when the $V - I$ curve intersects the 1 mVm^{-1} line, the transport J_c is 1.2×10^5 Am^{-2} at 0.1 T and 4.2 K. Figure 4.8 shows the transport J_c of Y1HA determined using the same criterion. The inset includes the zero field J_c from 40 and 60 K. As shown later in section 4.3.3, the intragranular magnetisation J_c in this sample is of the order of 10^{11} Am^{-2}. Hence the transport J_c values measured here are 6 orders of magnitude lower than the intragranular currents.

As can be seen in Figure 4.5, the nanocrystalline materials have resistivity values typically 3 or 4 orders of magnitude higher than microcrystalline materials. Y1MH sample has the highest ρ_N of all the samples – 60 Ωm at 300 K. For comparison, the values of the resistivity of a good metal like Cu and a good insulator like diamond are 10^{-8} Ωm and $10^{10} - 10^{11}$ Ωm [151]. After annealing, the resistivity decreased by a factor of approximately 10^3 at room temperature. A smaller, further reduction was found by repeating the annealing process as in the case for Y2MHA(1) and Y2MHA (2). The $V - I$ traces of nanocrystalline Y1MHA(1), (2) and (3) were entirely resistive with no signs of percolating supercurrents. Y1MHA(3) shows an inflection in ρ_N at 60 K which can also be seen in a.c. magnetic susceptibility discussed in section 4.3.2. We tried many different annealing procedures to produce supercurrents flowing across grain boundaries. A single nanocrystalline sample showed evidence that it could transport an intergranular supercurrent. Figure 4.9 shows the in-field resistivity of nanocrystalline materials of the Y2 composition. This sample was annealed twice. The data after the first annealing, Y2MHA(1), is given by solid symbols, and the data after the second annealing, Y2MHA(2), is given by the open symbols. The second annealing decreased the resistivity by at least a factor of 2 over the entire temperature range. The inset shows the $V - I$ trace of the sample after the second

annealing, measured at 2 K and 0 T. It provides evidence for very weak superconductivity. The transport J_c at 2 K and 0 T was very small, equivalent to about 70 Am^{-2} at an electric field criterion of 1 mVm^{-1}. This is at least 10^9 times lower than the transport J_c of commercial YBCO tapes.
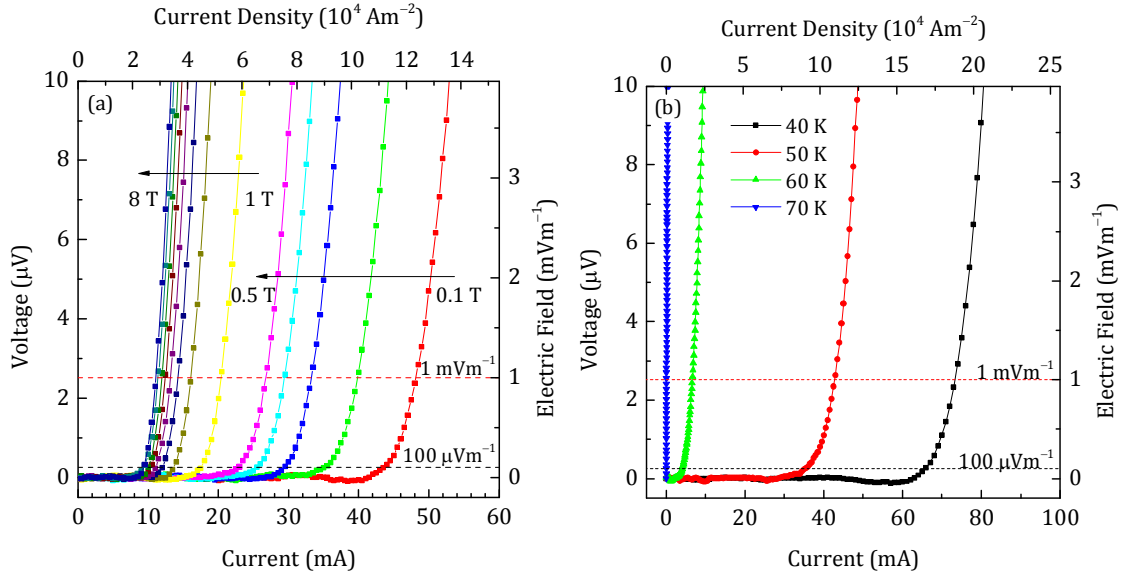
Figure 4.7: (a): Voltage as a function of current $(V - I)$ of Y1HA sample at 4.2 K and various magnetic fields. The dashed lines show the electric field criteria of 1 mVm^{-1} and 100 μVm^{-1}. (b): $V - I$ data from 40 K to 70 K at zero field.
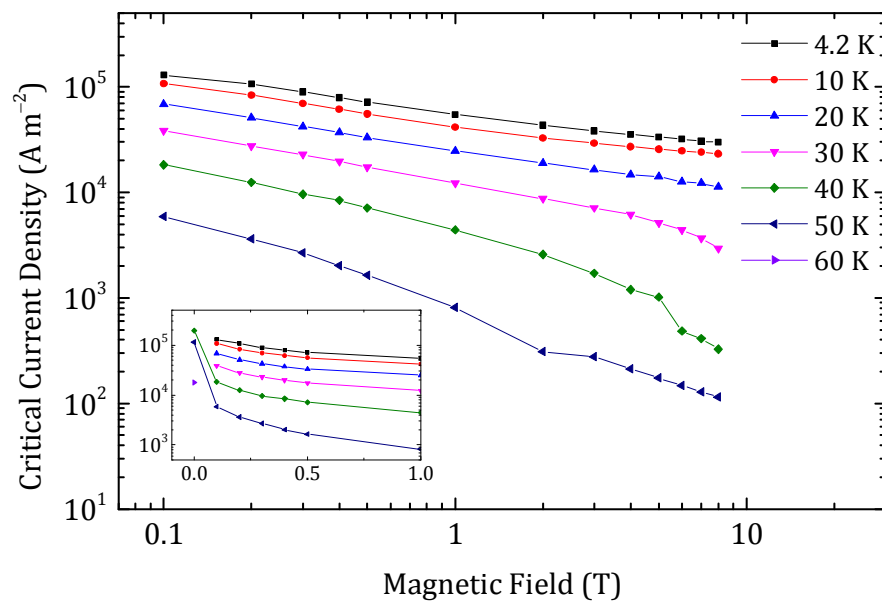
Figure 4.8: Transport J_c of Y1HA as a function of field and temperature using 1 mVm^{-1} criterion from 4.2 K to 60 K. The inset show the zero-field data obtained.
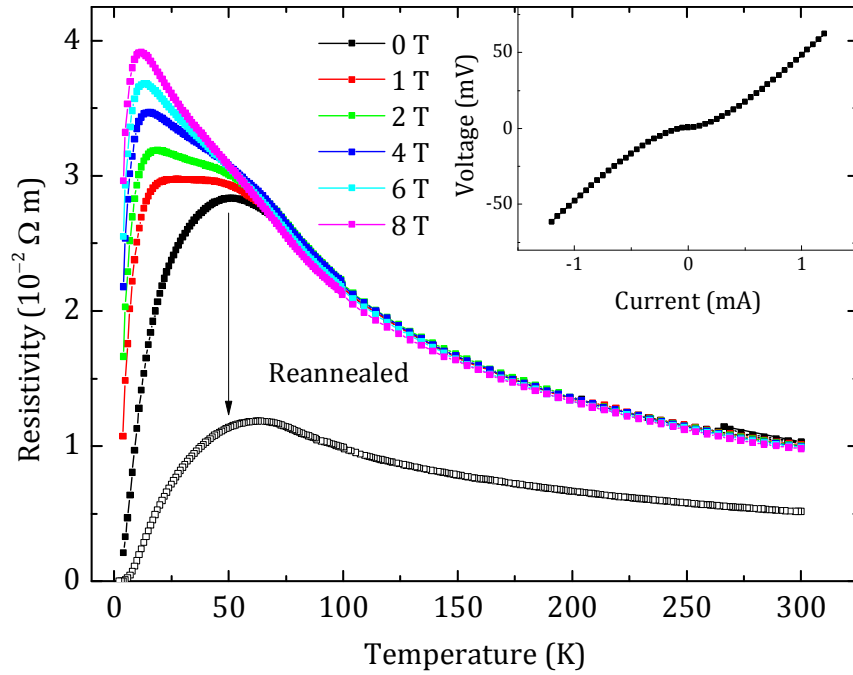
Figure 4.9: The resistivity of the Y2MHA(1) sample (solid symbols) as a function of temperature in fields of up to 8 T (measured with an excitation current of 10 μA). At zero field, the peak resistivity is at 52 K and the resistivity does not reach zero at 2 K. The Y2MHA(2) data at zero field is the open squares. The resistivity has decreased at all temperatures and the temperature at which peak resistivity has increased to 64 K. Inset: Voltage as a function of current of Y2MHA(2) at 2 K and 0 T, showing evidence for very weak superconductivity.

4.3.2 A.C. Magnetic Susceptibility

The a.c. magnetic susceptibility and d.c. magnetisation measurements were all taken in our Quantum Design PPMS system [171]. The non-HIP'ed samples were pressed into pellets with a typical size of 3 mm diameter and a height of 2 mm. The HIP'ed samples were shaped into cuboids with fine emery paper, with typical dimensions of $1 \times 1 \times 1$ mm. The a.c. magnetic susceptibility measurements were taken with an excitation field of 0.4 mT and 777 Hz (equivalent to 0.3 Ts^{-1}).

Figure 4.10 shows the a.c. magnetisation (and equivalent susceptibility) of the microcrystalline Y1P material with very broad transitions to the superconducting state. The inset shows the onset signal at 91 K, which shows an inflection at ∼ 80 K. There is a large signal with a second transition centred at ∼ 46 K. This granular sample is a pressed powder in which one can expect that the electronic powder-powder connections to be weak. We attribute the high temperature transition to the individual grains becoming superconducting and producing a large screening signal. The low temperature transition at 46 K is attributed to stronger coupling across the grains, allowing sufficiently large intergranular currents (flowing on the scale of the sample size) at low temperatures, to produce an additional signal. The signal of –115 Am^{-1} from this sample characterises full screening for our experimental conditions at the lowest temperature and is used to normalise susceptibility values to negative unity.
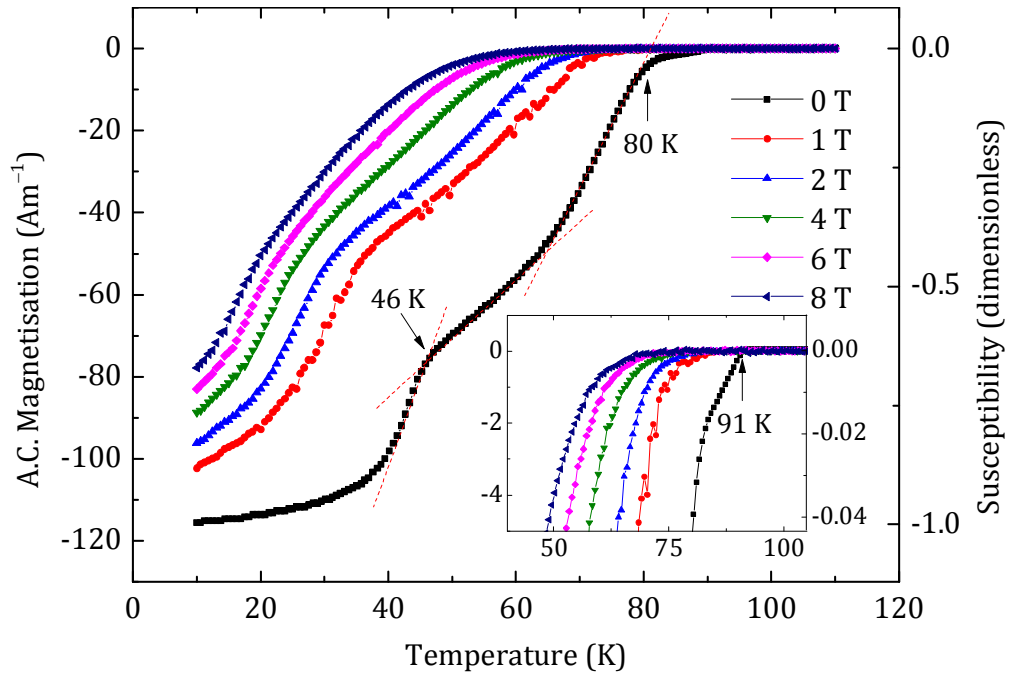
Figure 4.10: A.c. magnetisation and magnetic susceptibility as a function of temperature of Y1P sample. The dimensions of the sample were $1 \times 1 \times 1$ mm. Susceptibility is normalized to its value at 10 K. The noise in the 1 T data is due to field fluctuations. The red dashed lines were used to extrapolate T_c. Inset: Detail showing the small onset signal transition with $T_c = 91$ K at zero field. The data were taken with an excitation field of 0.4 mT at a frequency of 777 Hz.

However, for most of our HIP'ed nanocrystalline samples, large paramagnetic backgrounds with no superconducting transitions were found in the susceptibility data. A small superconducting signal was recovered in the Y1MHA(3) sample after oxygen annealing, as shown in Figure 4.11. This sample has a T_c of $\sim$ 70 K, but a low relative susceptibility of -4.0×10^{-2} at 4.2 K in zero field. Figure 4.12 shows typical data for nanocrystalline materials with Y2 composition, which show temperature dependent paramagnetic-like behaviour. The Y2MHA(3) data in the inset did show a superconducting transition at $\sim$ 17 K in zero field with a susceptibility of -1.5×10^{-2} at 4.2 K, although no signals associated with superconductivity were observed in the in-field data. Nevertheless, it is important to realise that while most nanocrystalline samples showed no superconducting a.c. screening signals (or more accurately, signals below our noise floor), they were in fact superconducting as demonstrated by the very sensitive d.c. magnetisation measurements shown in the next section. When screening currents are entirely within very small grains, the susceptibility is reduced by a factor χ'_g/χ'_b [172, 173] where

$$\frac{\chi'_g}{\chi'_b} = \frac{1}{15}\left(\frac{a^2}{\lambda^2}\right) f(a, \xi_0) \ \ \text{for} \ \ \lambda > a, \tag{4.4}$$

where χ'_g and χ'_b are the granular and bulk (intergranular) susceptibilities respectively and a is the grain size. The factor $f(a, \xi_0)$ accounts for non-local effects associated with the BCS coherence length (ξ_0). Low values of $f(a, \xi_0)$ occur when the grain size is much smaller than ξ_0 which is about 4 – 7 nm [174] for YBCO. It has a value of unity when $a \gg \xi_0$. The nanocrystalline samples in this work have grain sizes of 100 nm (cf. Table 4.2) so we assume $f(a, \xi_0) = 1$.

For an anisotropic superconductor, we can find an approximate value for the angular dependence of the G-L penetration depth $\big(\lambda(\theta)\big)$ from the angular dependence of the G-L coherence length $(\xi(\theta))$ derived from upper critical field, and the angular dependence of the Ginzburg Landau constant $(\kappa(\theta))$ where $\lambda(\theta) = \kappa(\theta)\xi(\theta)$ [175] so that

$$\xi^2(\theta) = \xi_{ab}(\xi_{ab}^2 \cos^2(\theta) + \xi_c^2 \sin^2(\theta))^{\frac{1}{2}}, \tag{4.5}$$

and

$$\lambda^2(\theta) = \lambda_{ab}^2 \lambda_c \; / (\lambda_c^2 \cos^2(\theta) + \lambda_{ab}^2 \sin^2(\theta))^{\frac{1}{2}}. \tag{4.6}$$

By integrating equation (4.5) or equation (4.6) over all solid angles, we obtain an angular average where for example $\langle 1/\lambda^2(\theta)\rangle$, the angular average of the inverse of the G-L penetration depth squared, for a collection of random oriented grains, is

$$\left\langle \frac{1}{\lambda^2(\theta)} \right\rangle = \frac{1}{2} \int_0^\pi \frac{1}{\lambda^2(\theta)} \; \sin\theta \, \mathrm{d}\theta. \tag{4.7}$$

Numerical integration of equation (4.7) with values of $\lambda_c = 916$ nm and $\lambda_{ab} = 138$ nm [128] and using an average grain size of 100 nm, gives $\langle \chi'_\mathrm{g}/\chi'_\mathrm{b} \rangle = 1.8 \times 10^{-2}$. This value is similar to that given in Figure 4.11 for Y1MHA(3) and Figure 4.12 inset for Y2MHA(3), consistent with a reversible a.c. signal entirely from within the nanocrystalline grains. We note that this calculation does not account for the induced moment and the applied field not being parallel or demagnetisation factors [176]. Figure 4.13 shows the irreversibility field $(B_\mathrm{Irr}(T))$ as a function of temperature for our samples, taken from the onset of the a.c. susceptibility data. The data were fitted using the equation [139]

$$B_\mathrm{Irr}(T) = B_\mathrm{Irr}(0)(1 - t^{0.5})^{2.1}, \tag{4.8}$$

where $t = T/T_\mathrm{c}$, the free parameters were $B_\mathrm{Irr}(0)$ and T_c. The grains in the Y1HA and Y2HA samples have the highest superconducting critical properties of our samples. Of the microcrystalline materials, Y1H and Y2H have among the lowest T_c and $B_\mathrm{Irr}(0)$, lower than Y1MHA (3) and Y1MPA, which demonstrates the severity of the oxygen loss that the samples suffered during the HIP process. The onset T_c and $B_\mathrm{Irr}(0)$ values derived using equation (4.8) are listed in Table 4.2.
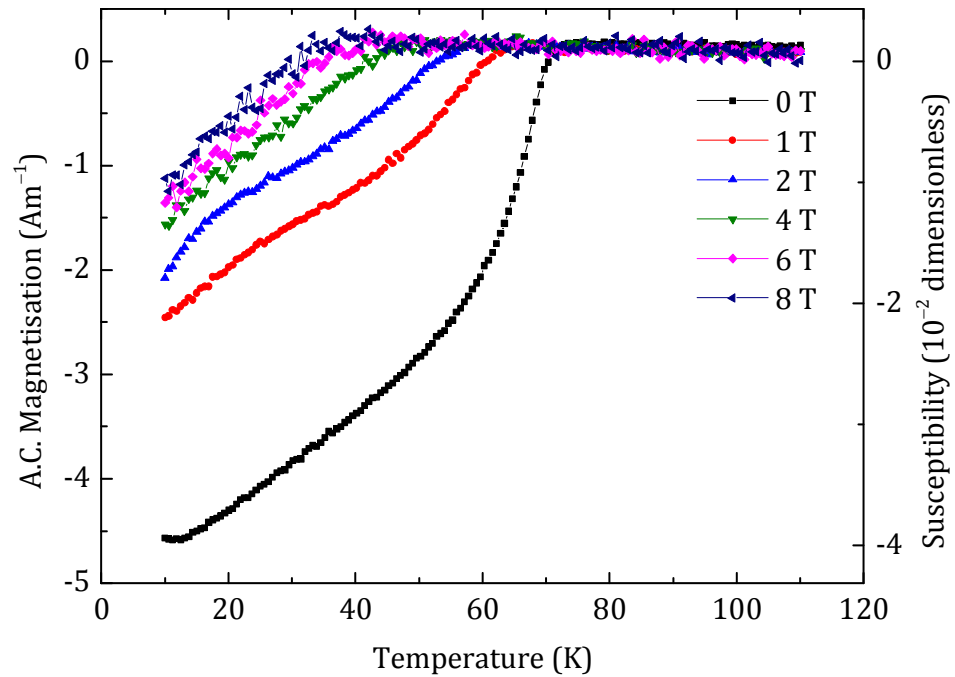
Figure 4.11: A.c. magnetisation and magnetic susceptibility as a function of temperature of Y1MHA(3) sample, the susceptibility was normalised with respect to the 0 T data of the Y1P sample in Figure 4.10. The data were taken with an excitation field of 0.4 mT and at a frequency of 777 Hz.
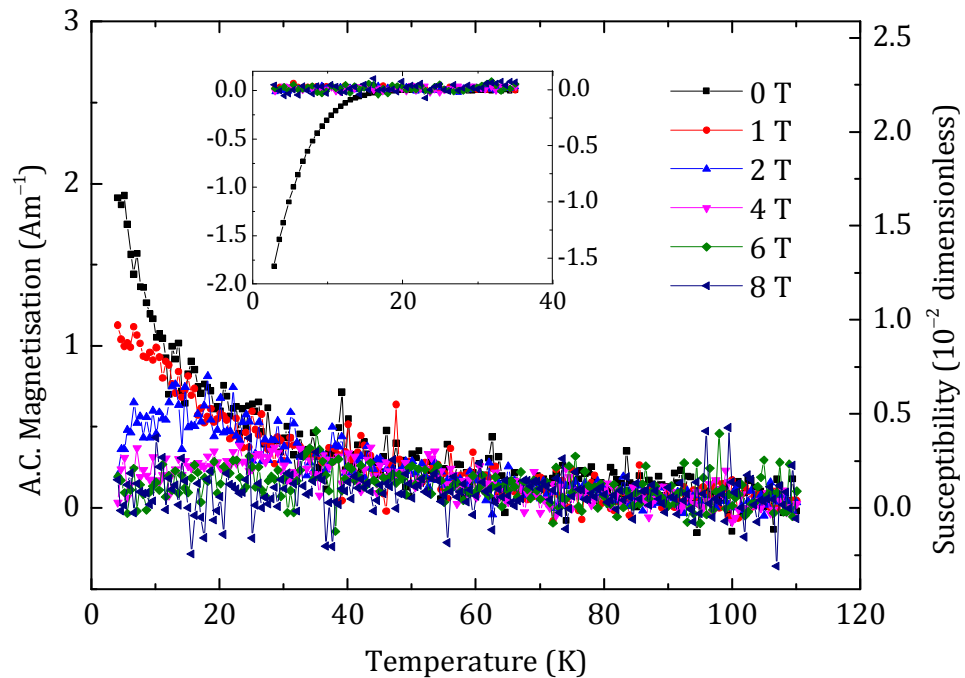
Figure 4.12: A.c. magnetisation and magnetic susceptibility as a function of temperature of Y2MHA(2) sample. No superconductivity is observed. Inset: A.c. magnetic susceptibility as a function of temperature of Y2MHA(3) sample which was annealed 3 times. The data were taken with an excitation field of 0.4 mT and at a frequency of 777 Hz.
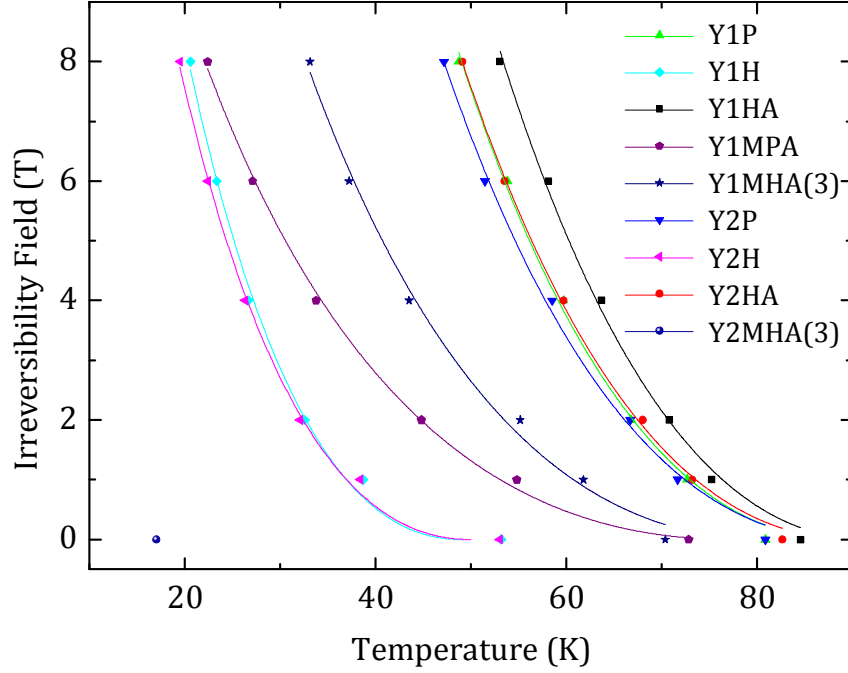
Figure 4.13: Irreversibility field as a function of temperature of all the micro- and nanocrystalline fabricated samples. B_{Irr} is defined as the onset in susceptibility measurements and the data fitted using an equation of the form of equation (4.8).

4.3.3 D.C. Magnetic Hysteresis

D.c. magnetisation hysteresis data were also taken with the PPMS. At each temperature, the field was swept from 0 T down to –1.5 T (or –2 T in some cases), then swept up to 8.5 T and back to –1.5 T. This approach meant we could extract values of $\mu_0 \Delta M / \Delta B$ as the magnetisation changed from the upper branch to the lower branch, as well as magnetisation J_{c} values calculated using Bean's model [177], as shown in Table 4.2. For pellets of radius R and volume V,

$$J_{\text{c}} = 3\frac{\Delta m}{RV}, \tag{4.9}$$

where Δm is the difference in magnetic moment between the increasing and decreasing field branches. For rectangular bars with length w and width b,

$$J_{\text{c}} = \frac{2\Delta m}{w\left(1 - \frac{w}{3b}\right)V}. \tag{4.10}$$

Typical hysteresis and J_c data for microcrystalline materials are shown in Figure 4.14 and Figure 4.15. In this work, we assume that the currents flowing are either entirely intergranular or intragranular, or both. We set aside the possibility of clusters of well-connected grains. Given that the measured transport J_c is only of the order of 10^5 Am^{-2} in microcrystalline materials, intergranular J_c contributes typically less than 1% of the total d.c. magnetisation signal in-field and can be ignored. Hence we conclude that the d.c. magnetisation signal comes predominantly from hysteretic screening currents flowing within grains. The typical response for nanocrystalline materials is shown in Figure 4.16. The data show a paramagnetic background with superconducting hysteresis which has been observed in a.c. susceptibility data in other granular materials in the literature [109, 110]. The paramagnetic background was estimated by finding the average magnetisation at each field. The lower panel of Figure 4.16 shows the data after the paramagnetic background has been subtracted, showing a typical Type II superconductor hysteresis curve. Straumal *et al.* [178, 179] have shown that in ZnO, a high density of grain boundaries leads to ferromagnetism even without doping, but also that the solubility of magnetic contaminants such as Co can significantly increase with the density of grain boundaries. To investigate
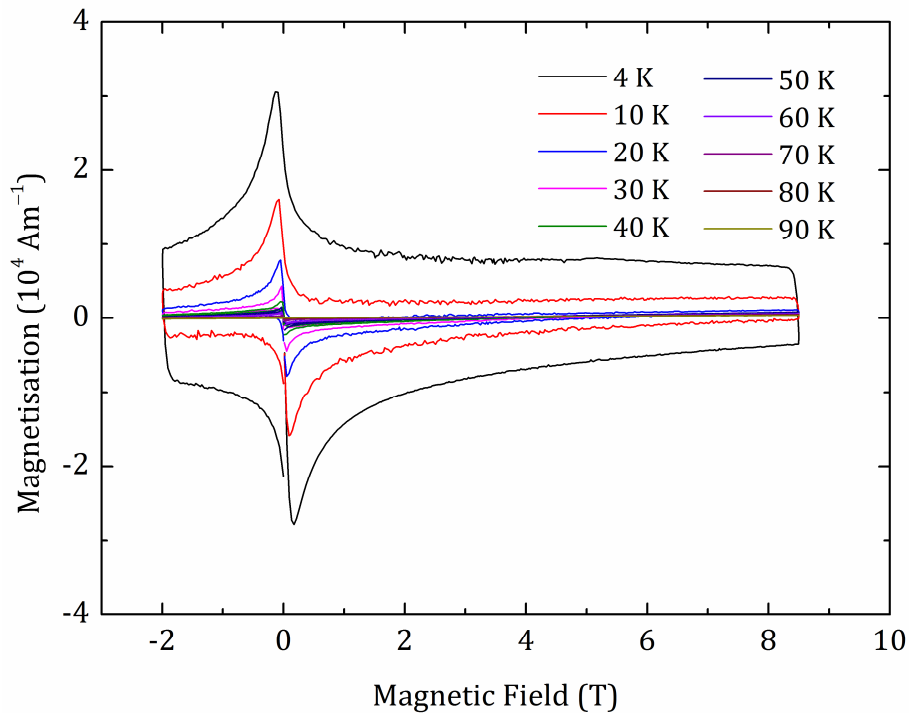
Figure 4.14: Magnetisation as a function of field for Y1P at temperatures from 4 to 90 K and between –2 and 8 T. The data at –2 T have a gradient of $\mu_0 \Delta M / \Delta B = -0.2$.
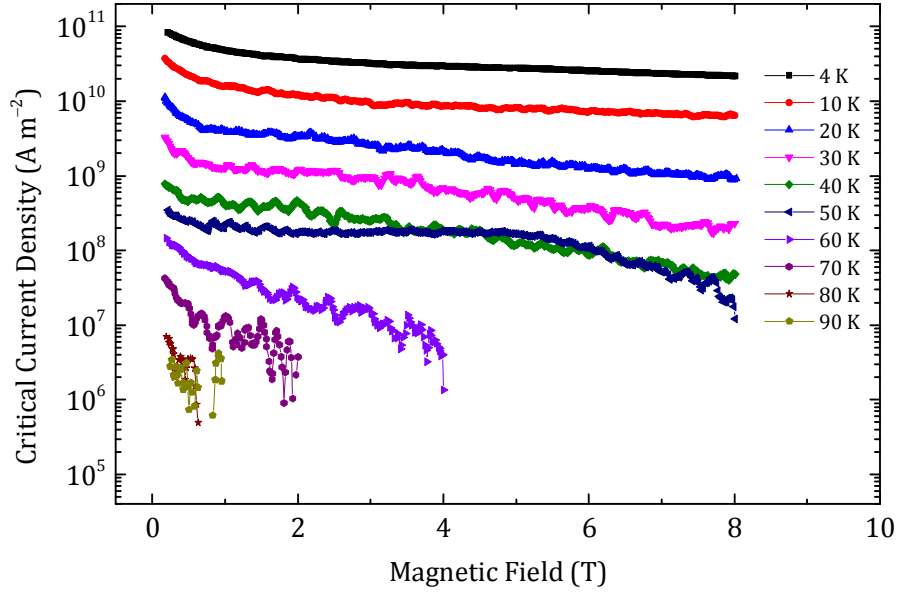
Figure 4.15: Critical current density as a function of field for Y1P, at temperatures from 4 to 90 K and between 0 and 8 T. Grain dimensions were used to calculate magnetisation J_c. Fluctuation in the data is representative of the uncertainty.

the effect of contamination, the WC/Co vial and balls were milled without any powder (except for that caked onto the surfaces) which yielded mainly WC/Co powder with small amounts of YBCO. The contaminants were pressed into a pellet and measured using the same method as the superconducting samples. These data are shown in the inset of Figure 4.16. The magnetisation of contaminants are temperature-independent around 0 T, which is different to the background from the sample, consistent with the expectation that the extent of WC/Co contamination and its ferromagnetic contribution to the magnetisation are low. Hence, as with the microcrystalline samples, the d.c. magnetisation signal from the nanocrystalline samples is almost entirely due to screening currents flowing within the grains. Figure 4.17 shows a compilation of the intragranular magnetisation J_c for both the microcrystalline and nanocrystalline samples (we note that the uncertainty in the grain size is typically about $\pm 50\%$) and also contains transport J_c values for commercial YBCO tape [123]. Given that in our polycrystalline samples the current flows both along the ab-planes and along the c-direction, whereas J_c values in commercial tapes only flows along the ab-plane for the two configurations given, Figure 4.17 shows that the intragranular J_c values in our polycrystalline samples are high. The best microcrystalline samples have

intragranular J_c comparable to that of tapes, and strikingly the field dependence for all the samples that have been annealed is very similar to the commercial tapes. The samples that were HIP'ed-only (Y1H and Y2H) show a more drastic decrease in J_c with magnetic
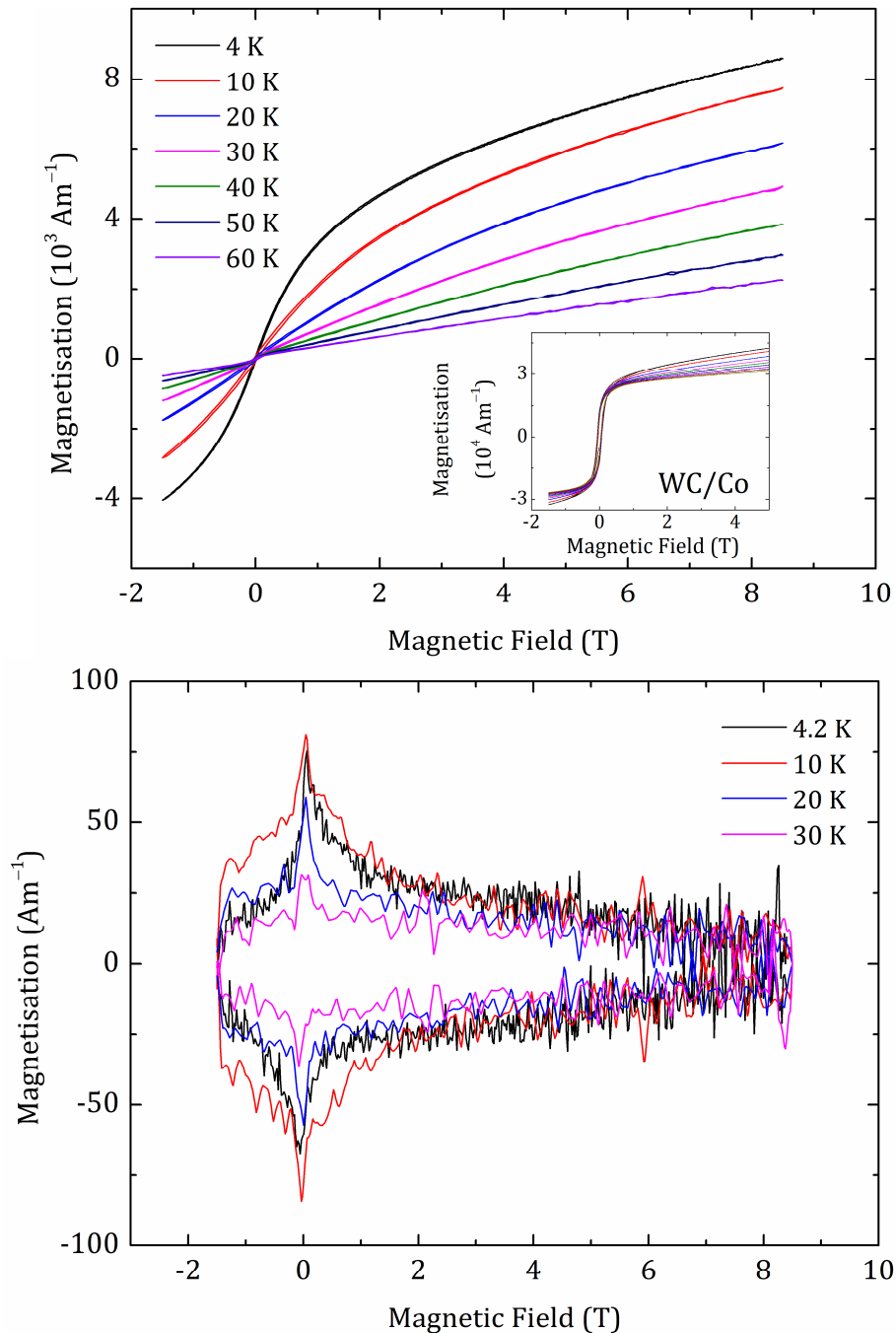
Figure 4.16: Upper panel: Hysteretic magnetisation of Y1MHA(1) sample. Inset: Magnetisation of the milling materials (that are potential contaminants in the samples). Lower panel: The same hysteretic magnetisation data as the upper panel, after subtracting the paramagnetic background, that show typical Type II hysteresis and temperature dependence.
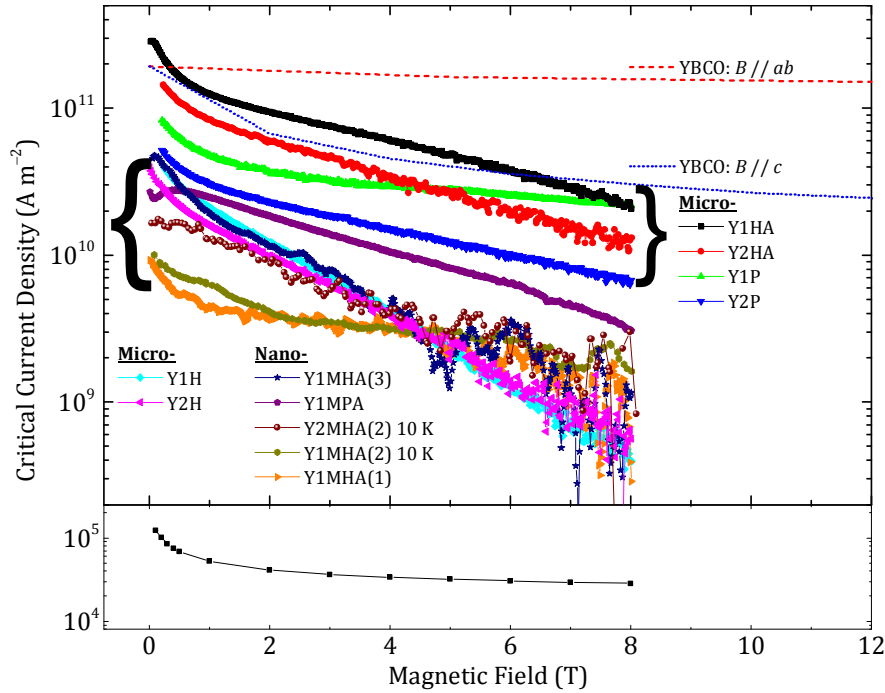
Figure 4.17: Magnetisation J_c as a function of field for fabricated samples at 4.2 K (unless otherwise labelled). Grain dimensions were used to calculate magnetisation J_c. Transport J_c of Y1HA sample (shown in the lower panel) and YBCO commercial tape data are also included for comparison [123]. The best microcrystalline samples have intragranular J_c comparable to that of tapes. Fluctuation in the data is representative of the uncertainty.

field compared to other microcrystalline samples, and at 8 T, have J_c comparable to that of the nanocrystalline group. We attribute the poorer in-field properties of some of our samples to the decrease in oxygen content during HIP'ing, consistent with the decrease in T_c and $B_{Irr}(0)$ seen in the a.c. susceptibility data. After annealing (Y1HA and Y2HA), T_c, $B_{Irr}(0)$ and J_c have all recovered. Compared to commercial YBCO tape, transport J_c of microcrystalline materials is 10^6 lower, and for nanocrystalline material Y2MHA(2) (not included on this graph) this difference increases to 10^9.

In addition to finding a clear intragranular signal associated with superconductivity for the nanocrystalline materials, not found using standard a.c. susceptibility measurements, we can use field reversal in the d.c. magnetisation measurements ($\mu_0 \Delta M / \Delta B$). With these data we can address the type of pinning. Using Bean's relation for a cylinder, $|\Delta B| = 2\mu_0 J_c R$ where $|\Delta B|$ is the magnitude of the field required to reverse the magnetisation, equation (4.9) gives [180]

$$\frac{\mu_0 \Delta M}{\Delta B} = -\frac{\frac{1}{3} J_c R}{2 J_c R} = -0.17, \qquad (4.11)$$

where the negative sign comes from Lenz's law. Figure 4.18 shows minor hysteresis loops taken at 10 K for Y1P. The inset of Figure 4.18 shows that $\mu_0 \Delta M/\Delta B$ is only weakly field dependent. At very low fields, $\mu_0 \Delta M/\Delta B$ increases, associated with the increased role of reversible screening currents flowing at the surface of the sample. The $\mu_0 \Delta M/\Delta B$ values in Table 4.2 were obtained from the field reversal data at –1.5 T or –2 T, calculated from the linear region during the initial field reversal. In most microcrystalline materials, typical values of $\mu_0 \Delta M/\Delta B$ are approximately –0.17, consistent with bulk pinning in Bean's model. For nanocrystalline materials, the values of $\mu_0 \Delta M/\Delta B$, derived from data similar to that in Figure 4.16 are typically 3 orders of magnitude smaller. These small values, compiled in Table 4.2, have been found in the work of Shimizu and Ito [56] and cannot be explained by bulk pinning using Bean's model. We attribute the low values to the surface pinning in the grains, consistent with d.c. magnetisation signals that are
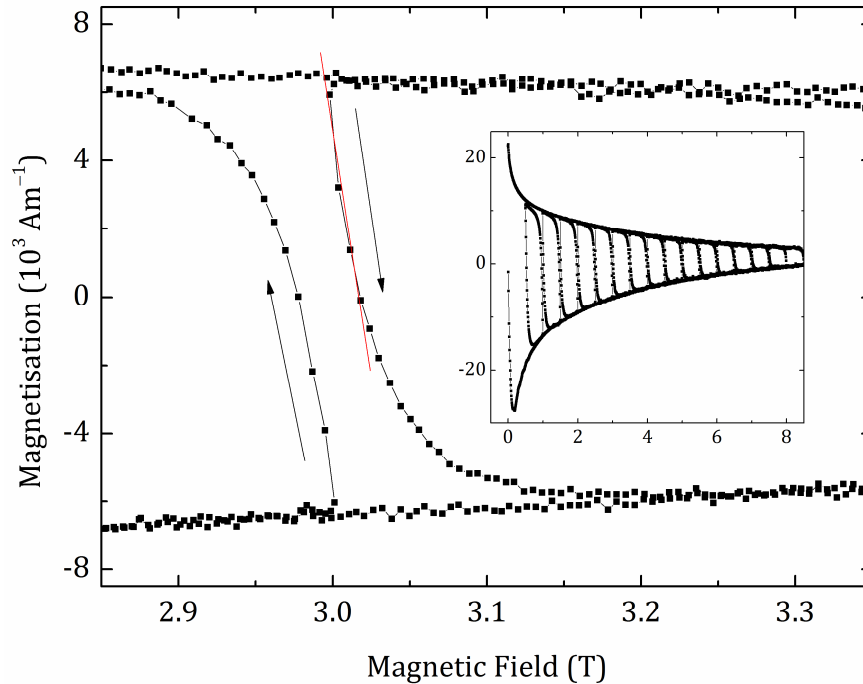
Figure 4.18: Magnetisation hysteresis as a function of magnetic field in order to study field reversal for the Y1P sample at 4.2 K. Starting from zero field, the field was repeatedly ramped +1 T then –0.5 T, up to 8.5 T. Inset: Field reversal data set showing the full range. The arrows show the direction of the hysteresis and have a gradient for $\mu_0 \Delta M/\Delta B = -0.2$ with an uncertainty of approximately $\pm 50\%$.

predominantly intragranular. Hence, the magnetisation J_c we have calculated using grain size dimensions, provides a lower bound for the grain's surface pinning J_c.

4.4 Theoretical Considerations

By using a combination of transport and a.c. magnetic susceptibility data, we can separately determine the magnitude of the intergranular current density and the intragranular current density. In this section we consider grain and grain boundary properties. We use our resistivity data and the theoretical considerations to explain why the transport current density is so low in our YBCO samples.

4.4.1 The Limiting Size for Superconductivity

While fabricating nanocrystalline materials, it is reasonable to ask first, how small grains can be before they can no longer be considered bulk material. Deutscher *et al.* [181] have provided three methods for calculating the minimum size required to sustain superconductivity in low temperature superconductors. The first is the condition that superconductivity is quenched when the fluctuations in the order parameter ($\delta\Psi$) are of the same order as the order parameter (Ψ_0), which leads to

$$\frac{\langle|\delta\Psi|^2\rangle}{|\Psi_0|^2} \approx \frac{k_\mathrm{B}T}{2E_\mathrm{c}V_\mathrm{min}}, \tag{4.12}$$

where E_c is the condensation energy density and V_min is the minimum volume of a grain that still sustains superconductivity. The second is when there is only one Cooper pair per grain so that

$$N(0)\Delta V_\mathrm{min} \approx 1, \tag{4.13}$$

where $N(0)$ is the energy density of states at $T = 0$ and Δ is the superconducting energy gap. The third is when the separation of quasi-particle energy levels δ is of the order of Δ, which leads to the equation

$$r_\mathrm{min} = \left(\frac{8\pi}{3 \times 0.18}\xi_0\lambda_\mathrm{F}^2\right)^{\frac{1}{3}}, \tag{4.14}$$

where r_{min} is the minimum radius and λ_F is the Fermi wavelength. Deutscher made assumptions that are only strictly justified for low temperature superconductors. However, if we naively apply these methods to YBCO, then we obtain $r_{\text{min}} = 0.3 - 1$ nm (using literature values of $E_c = 0.063\ k_B T_c$ per unit cell [182], $N(0) = 2.10 \times 10^{28}$ m^{-3}eV^{-1} [183], $\Delta = 30$ meV [177], $\lambda_F = 0.3$ nm [184] and $\xi_0 = 1.5$ nm [185]). These calculations suggest even the (100 nm) grains in our nanocrystalline YBCO are sufficiently large to be well within the bulk material regime.

4.4.2 The Resistivity of the Grain Boundaries

Without understanding why high-angle grain boundaries do not support high J_c, we cannot know why J_c is low in polycrystalline materials. The standard explanation for the Dimos results that showed J_c decreases with increased misorientation angle in [001] tilt boundaries is that grain boundaries act as "weak-links". However, this does not clarify whether the low J_c values found by Dimos were due to poor coupling across the grain boundaries or weak flux pinning in the grain boundaries. TDGL calculations suggest that the surface properties at the ends of any junction strongly affect the current the junction can carry as well as the interior of the junction, which undermines comparisons between single junctions and bulk properties. Other possible explanations for low J_c values could include the nature of the fundamental mechanism for superconductivity itself or perhaps the underlying symmetry of the d-wave order parameter. The low carrier density or specific electronic structure that leads to HTS or the phononic structure may also have been responsible. Despite the range of possibilities, a review of the literature shows that in S-N-S junctions, the effective resistivity of the normal layer in the junction can easily vary from a factor of 10^2 times higher than the bulk resistivity of normal material in the junction, as found for Pb/Cd/Pb [186], and up to a factor of 10^4 times higher, as is the case for Nb/Al/Nb [187] [188], Pb/Cu/Pb [189, 190], and YBCO/Au/YBCO [191]. Recent work in our group on YBCO tapes has shown that large interfacial resistances of 2.5×10^{-8} Ωcm^2 can even occur between a silver interface and a YBCO layer [192]. Given the potential for highly resistive interfaces and highly resistive grain boundaries in YBCO, in this work we try to quantify how much the high resistivity of the grain boundaries lowers the critical current density of

polycrystalline YBCO. We consider the most simple case, where the grain boundaries are modelled as a highly resistive N-component (i.e. where the normal layer has $T_c = 0$) of an S-N-S junction.

We first calculate the expected resistivity of a randomly aligned polycrystalline YBCO sample with completely transparent grain boundaries (i.e. normal grain boundaries with zero resistivity). The angular resistivity $\rho_N(\theta)$ of a YBCO single crystal when the transport current is at angle θ with the c-axis in spherical coordinates is given by [52]:

$$\rho_N(\theta) = \rho_c \cos^2 \theta + \rho_{ab} \sin^2 \theta, \tag{4.15}$$

where ρ_c is the resistivity along the c-axis and ρ_{ab} is the resistivity along the ab-plane. Integrating $\rho_N(\theta)$ through all solid angles, gives the angular averaged resistivity $\langle \rho_N \rangle$ where:

$$\langle \rho_N \rangle = \frac{1}{2} \int_0^\pi \rho_N(\theta) \sin \theta \ d\theta = \frac{1}{3} \ (2\rho_{ab} + \rho_c). \tag{4.16}$$

In equating $\langle \rho_N \rangle$ to the resistivity of a randomly aligned polycrystalline material, one is assuming that there is no redistribution or preferential percolation of the current along low resistivity paths. We can assess whether this approach is valid by considering polycrystalline graphite. Graphite is a good choice because it has very low resistivity grain boundaries. Single crystal resistivity values for graphite are: $\rho_{ab} = 6 \times 10^{-5}$ Ωm and $\rho_c = 6 \times 10^{-3}$ Ωm [193]. Polycrystalline graphite has a resistivity of 2×10^{-3} Ωm [194] which is consistent with the value of $\langle \rho_N \rangle$ from equation (4.16). A similar calculation for YBCO using the resistivity of single crystals, where $\rho_{ab} = 6 \times 10^{-7}$ Ωm and $\rho_c = 1.5 \times 10^{-4}$ Ωm at 100 K [170], gives $\langle \rho_N \rangle = 5.0 \times 10^{-5}$ Ωm. Figure 4.6 shows the resistivity of sample Y1HA and compares it to values for single crystals and $\langle \rho_N \rangle$. Sample Y1HA has a resistivity about 50% higher than $\langle \rho_N \rangle$. Given the very high values of critical parameters for the grains of this material (T_c, $B_{Irr}(0)$ and magnetisation J_c^m), we attribute the enhanced resistivity (2.4×10^{-5} Ωm) to the resistivity of grain boundaries. This contribution is then multiplied by the ratio of grain size to grain boundary thickness (approximately 1 nm [195]) to obtain a large grain boundary resistivity of $\rho_{GB} \approx 0.12$ Ωm. Using a similar approach to the resistivity data for the nanocrystalline materials in Table 4.2, a grain size

of 100 nm gives a very large grain boundary resistivity of $\rho_{\mathrm{GB}} = 8.2 \ \Omega\mathrm{m}$. In terms of contact (areal) resistivity, the micro and nanocrystalline grain boundary resistivities are $1.2 \times 10^{-10} \ \Omega\mathrm{m}^2$ and $8.2 \times 10^{-9} \ \Omega\mathrm{m}^2$ respectively. These values can be compared to the contact resistivities for some [001] tilt grain boundaries in thin-film oxide bicrystals (including YBCO) [70], which are generally lower and in the range of $10^{-14} \ \Omega\mathrm{m}^2$ to $10^{-11} \ \Omega\mathrm{m}^2$. We note that one can expect the resistivity of grain boundaries with misorientation angles that can include all possible angles to be higher than the [001] tilt, strain-free bicrystal grain boundaries. The resistivity data in Figure 4.6 for Y1HA also provide supporting evidence for the additional resistance of the grain boundaries being similar to that of the grains: after the initial onset of the superconducting transition of the grains at 92 K, there is an inflection at $\sim$ 83 K, which we attribute to the grain boundaries starting to carry significant current. It is unlikely that inflection is due to a secondary phase, since it would mean that the milling had not produced broadly homogenized polycrystalline material. It would also mean that $J_{\mathrm{c}}^{\mathrm{m}}$, associated with the magnitude of the small signals, have just by chance given values that are similar to optimum values from the literature. The lower temperature part of the transition is much more strongly depressed by the magnetic field than the onset transition which is similar to that observed elsewhere [164] and consistent with the in-field properties of grain boundaries [10].

4.4.3 Depairing Current Density of the Grain Boundaries

In this section we calculate the reduction in the local depairing current density (J_{DN}) in the boundary caused by its high resistivity. Recently the analytic solutions to the Ginzburg-Landau equations in zero field was found for the $J_{\mathrm{DN}}(T)$ in a 1D S-N-S junction in the clean and dirty limit [119] where:

$$
\begin{aligned}
J_{\mathrm{DN}}(T) \approx J_{\mathrm{DSc}}(T)\sqrt{2}\frac{\rho_{\mathrm{S}}\xi_{\mathrm{S}}}{\rho_{\mathrm{N}}\xi_{\mathrm{N}}} \\
\times \left\{ \sqrt{\left(\frac{\xi_{\mathrm{S}}\rho_{\mathrm{S}}}{\xi_{\mathrm{N}}\rho_{\mathrm{N}}\sqrt{2}}\right)^2 + 1} - \frac{\xi_{\mathrm{S}}\rho_{\mathrm{S}}}{\xi_{\mathrm{N}}\rho_{\mathrm{N}}\sqrt{2}} \right\}^2 \exp\left(\frac{-2d}{\xi_{\mathrm{N}}}\right),
\end{aligned} \tag{4.17}
$$

where $J_{\mathrm{DSc}}(T)$ is the depairing current density in the superconducting grain, $\rho_{\mathrm{S}}/\rho_{\mathrm{N}}$ is the ratio of the resistivity in the grain to the grain boundary, $\xi_{\mathrm{S}}/\xi_{\mathrm{N}}$ is the ratio of the G-L

coherence length in the superconductor to the decay length of the order parameter in the normal grain boundary, and d is the thickness of the grain boundary. Because equation (4.17) provides zero-field values, we use it to provide upper bound values for J_{DN} in the grain boundaries of polycrystalline YBCO (ξ_S values in Table 4.1 were used in these calculations). To simplify the analysis for the anisotropic materials, we have only considered angular averaged properties to calculate an angular average for J_{DN} (i.e. $\langle J_{DN} \rangle$) in Table 4.3, where we have used

$$\langle J_{DSc}(T) \rangle \approx \frac{\Phi_0}{3\sqrt{3}\pi\mu_0} \left\langle \frac{1}{\lambda^2(T)\xi(T)} \right\rangle, \tag{4.18}$$

where $\langle \lambda \rangle$ and $\langle \xi \rangle$ are the angular average G-L penetration depth and G-L coherence length and can be found in Table 4.1. The superconducting parameters in equation (4.17) are well established. Microscopic theory gives the clean coherence length as

$$\xi_{SClean}(T) \approx \frac{\hbar v_F}{1.76\pi k_B T_{cS}^{\frac{1}{2}}(T_{cS}-T)^{\frac{1}{2}}} \,, \tag{4.19}$$

and the dirty coherence length

$$\xi_{SDirty}(T) \approx \left(\frac{\pi\hbar D_S}{8k_B(T_{cS}-T)} \right)^{\frac{1}{2}}, \tag{4.20}$$

where T_{cS} is the critical temperature of the superconducting layer. We can use the relation for the diffusivity given by:

$$D_S \approx \frac{\pi^2 k_B^2}{3e^2\rho_S\gamma} = \frac{v_F l}{3} = \frac{m v_F^2}{3e^2\rho_S n}, \tag{4.21}$$

where the equivalent forms in equation (4.21) have been derived using standard relations [196] for resistivity and the Sommerfeld constant (γ), and also for the angular averaged Fermi velocity (v_F) and mean free path (l) in terms of number of valence electrons per unit volume (n). Accurate values of these microscopic parameters are critical to the calculation of J_{DN}. To test the validity of these values listed in Table 4.3, we used Pippard's approach to find a coherence length ($\xi_{SPippard}(0)$) from the clean and dirty values [119] using

$$\xi_{SPippard}(0) \approx \left(\frac{1}{\xi_{SClean}(0)} + \frac{1}{\xi_{SDirty}(0)} \right)^{-1}. \tag{4.22}$$

We suggest that the microscopic parameters are reasonable values since a comparison between $\xi_{\text{SPippard}}(0)$ and $\xi_{Bc2}(0)$ (cf Table 4.3), shows they are similar. We have used the Ginzburg-Landau relation (that is strictly only valid close to T_c) to define $\xi_{Bc2}(0)$ where

$$B_{\text{c2}}(0) \approx \frac{\Phi_0}{2\pi\xi_{Bc2}^2(0)}. \tag{4.23}$$

Within the context of the Ginzburg-Landau theory, the temperature dependence of $\xi_\text{N}(T)$ is given by

$$\xi_\text{N}(T) \approx \xi_\text{N}(T_\text{cS}) \left(\frac{T_\text{cS} - T_\text{cN}}{T - T_\text{cN}}\right)^{\frac{1}{2}}. \tag{4.24}$$

We have followed Pippard's approach and related $\xi_\text{NPippard}(T_\text{cS})$ to the microscopic clean and dirty limits [119] using

$$\xi_\text{NPippard}(T_\text{cS}) \approx \left(\frac{1}{\xi_\text{NClean}(T_\text{cS})} + \frac{1}{\xi_\text{NDirty}(T_\text{cS})}\right)^{-1}. \tag{4.25}$$

where

$$\xi_\text{NClean}(T_\text{cS}) \approx \frac{\hbar v_\text{F}}{1.76\pi k_\text{B} T_\text{cN}^{\frac{1}{2}}(T_\text{cS} - T_\text{cN})^{\frac{1}{2}}}, \tag{4.26}$$

$$\xi_\text{NDirty}(T_\text{cS}) \approx \left(\frac{\pi\hbar D_\text{N}}{8k_\text{B}(T_\text{cS} - T_\text{cN})}\right)^{\frac{1}{2}}, \tag{4.27}$$

in which D_N is the normal layer equivalent of D_S as given by equation (4.21) and T_cN is the critical temperature of the normal layer. The largest uncertainties in calculating J_DN are associated with the values of the microscopic properties of the grain boundaries. We have simplified the analysis by assuming that grain boundary structures are not superconducting (i.e. $T_\text{cN} = 0$) and that we can use resistivity to characterise the difference between the microscopic properties of the grains and the grain boundaries. Grain boundaries are complex structures and one can expect that when their resistivity changes, their carrier concentration, effective thickness and scattering time all change. Our assumptions lead to $\xi_\text{NPippard}(T_\text{cS}) = \xi_\text{NDirty}(T_\text{cS})$ and

$$\xi_\text{N}(T) \approx \xi_\text{NDirty}(T_\text{cS}) \left(\frac{T_\text{cS}}{T}\right)^{\frac{1}{2}} = \xi_\text{SDirty}(0) \left(\frac{\rho_\text{S}}{\rho_\text{N}} \frac{T_\text{cS}}{T}\right)^{\frac{1}{2}}. \tag{4.28}$$

As a starting point for calculating $\langle J_{\mathrm{DN}}(0) \rangle$, in Table 4.3 we have assumed that the grain boundary thicknesses in all the materials (i.e. d in equation (4.17)) is 1 nm. Equations (4.17) and (4.28) show that as the resistivity of the grain boundaries increases, ξ_{N} decreases and $\langle J_{\mathrm{DN}}(0) \rangle$ is severely depressed. In the microcrystalline YBCO materials of this work, the resistivity is more than three orders of magnitude higher than the grains, which by itself provides a straightforward explanation for the very low transport current densities we have experimentally measured. The calculations of $\langle J_{\mathrm{DN}}(0) \rangle$ are particularly sensitive to the values of d and ξ_{N}. Once ξ_{N} is smaller than d, the exponential term in equation (4.17) dominates. In this regime, small increases in d produce very large reductions in $\langle J_{\mathrm{DN}}(0) \rangle$. The resistivity of our nanocrystalline materials is even higher than the microcrystalline values and $\langle J_{\mathrm{DN}}(0) \rangle$ even lower. We note that these very high values of resistivity are beyond the Ioffe-Regel criterion (i.e. $k_{\mathrm{F}}l < 1$ [197]). However, we conclude that even the straightforward analysis provided here demonstrates that the values of grain boundary resistivity we have measured in microcrystalline and nanocrystalline materials are sufficient to explain the low values of our transport J_{c} data.

Material	$\rho_N(T_c)$ (±50%) (Ω m)	γ (J m^{-3} K^{-2})	v_F (10^5 m s^{-1})	$\xi_{SClean}(0)$ (nm)	$\xi_{SDirty}(0)$ (nm)	$\xi_{SPippard}(0)$ $\xi_{B_{c2}}(0)$ (nm)	D_N (±50%) (m^2 s^{-1})	ξ_N(4.2 K) (±25%) (nm)	$\dfrac{J_{DN}(4.2\ K)}{\langle J_{DSc}(4.2\ K)\rangle}$
NbTi	4.0×10^{-7} [198]	1.1×10^3 [198]	2.0 [177, 198]	31	4.3	3.8 4.6	5.7×10^{-5}	6.4	0.28
Nb$_3$Sn	8.8×10^{-8} [98]	1.2×10^3 [2]	0.60 [199]	4.6	6.3	2.7 3.3	2.4×10^{-4}	13	0.21
PbMo$_6$S$_8$	7.0×10^{-7} [3]	3.8×10^2 [3]	0.40 [199]	4.0	4.5	2.1 2.4	9.2×10^{-5}	8.1	0.21
MgB$_2$ (A.A.)	1.0×10^{-6} [200]	1.5×10^2 [201]	6.1 [202]	22	3.5	3.0 4.3	1.6×10^{-4}	10	0.28
YBa$_2$Cu$_3$O$_7$ (ab-plane)	5.0×10^{-7}	2.0×10^2 [203]	5.0 [174]	7.5	2.8	2.1 1.5	2.4×10^{-4}	13	0.16
YBa$_2$Cu$_3$O$_7$ (A.A., 5 µm)	5.0×10^{-5}	2.0×10^2 [203]	5.0 [174]	7.5	0.28	0.27 1.5	2.4×10^{-6}	1.3	0.077
YBa$_2$Cu$_3$O$_7$ (Micro, 5 µm)	1.2×10^{-1}	2.0×10^2 [203]	5.0 [174]	7.5	0.28	0.27 1.5	1.0×10^{-9}	0.027	10^{-35}
YBa$_2$Cu$_3$O$_7$ (Nano, 100 nm)	8.2	2.0×10^2 [203]	5.0 [174]	7.5	0.28	0.27 1.5	1.5×10^{-11}	0.0033	10^{-270}

Table 4.3: Resistivity of the normal layer ρ_N at T_c, Sommerfeld constant (γ), Fermi velocity (v_F), the superconducting layer coherence length in the clean and dirty limits (ξ_{SClean} and ξ_{SDirty}), comparison of the Pippard coherence length ($(\xi_{SPippard})^{-1} = (\xi_{SClean})^{-1} + (\xi_{SDirty})^{-1}$) with the $\xi_{B_{c2}}(0)$ coherence length calculated from B_{c2} where ($\xi_{B_{c2}}(0) = (\Phi_0/2\pi B_{c2}(0))^{\frac{1}{2}}$), the normal layer diffusivity (D_N) calculated using γ values, decay length of the normal layer in a Josephson junction (ξ_N), and the ratio of the local depairing current density of the grain boundary to the depairing current density of the superconductor: $J_{DN}/\langle J_{DSc}\rangle$, given by equation (4.17). For angular averaged (A.A.), microcrystalline and nanocrystalline YBCO, we have taken the resistivity values from measurements in this work and assumed that the grain boundaries are 1 nm thick. For all other materials, we have again assumed that the grain boundaries are 1 nm thick normal grain boundaries, but that the resistivity is equal to the resistivity of the grains. For all materials, we have assumed that the Sommerfeld constant and the Fermi velocity are an angular average in the calculation of $J_{DN}(4.2\ K)/\langle J_{DSc}(4.2\ K)\rangle$. Note that the extremely small ξ_N values for micro and nanocrystalline samples are of the order of picometres and simply suggest that the order parameter decays significantly near the boundary of the superconducting and normal layers.

4.5 Discussion

4.5.1 Micro- and Nanocrystalline YBCO

We have found, using a combination of transport measurements and a.c. magnetic susceptibility measurements, that our micro- and nanocrystalline YBCO can be considered to be high quality grains surrounded by non-superconducting highly resistive grain boundaries that limit transport J_c. The current densities within the grains are high and those across the grain boundaries low. We have adopted a pragmatic approach to the analysis of the grain boundaries in our samples and used angular averages for this strongly anisotropic material and ignored percolation (including percolation in the analysis would reduce calculated $\langle \rho_N \rangle$ values). We have also adopted a simple two-component description of our materials as grains and grain boundaries and used an S-N-S description that assumes that the pinning is sufficiently strong along the grain boundaries that J_c is determined by the local depairing current density in the grain boundaries themselves. One can expect in superconducting materials there are a range of different length scales for the variations in composition, strain and physical structure as well as electronic and phononic structure. Although it is reasonable for us to have assumed that grain boundary structures are not superconducting themselves in bulk form, finding the other characteristic microscopic properties of the grain boundaries (γ, v_F, l, n) will be a formidable challenge. Characterising bulk materials in thin film form proved difficult enough for the scientific community with the luxury of free-standing samples, or samples on insulators and data for parent bulk samples. Grain boundaries can be considered as internal surfaces. They bring the challenges of characterising a structure that is inhomogenous, is sandwiched between two grains, and is not available in bulk form [204]. Given the large effort it has taken to understand bulk materials, one can expect an even larger effort will be required for the local normal and superconducting properties of grain boundaries.

From a technological perspective, we would like to increase J_c in polycrystalline YBCO if at all possible. The [001] tilt boundaries in the literature have contact resistivities which vary from 2×10^{-14} Ωm^2 in the low-angle bicrystal data [10], up to 10^{-11} Ωm^2 for $40°$

boundaries [71]. The average contact resistivities in our microcrystalline samples were 10^{-10} Ωm^2 and in the nanocrystalline samples 10^{-8} Ωm^2. Higher average contact resistivity values are expected in the polycrystalline samples than bicrystals because the misorientation angles are not limited to [001] tilt grain boundaries. We have modelled grain boundaries, as simple non-superconducting resistive layers. This ignores complexities such as the possibility that very low-angle grain boundaries may have non-zero critical temperature and high-angle grain boundaries may be ferromagnetic [178, 179], which in the Ginzburg-Landau framework can be described using negative local critical temperatures. However, Table 4.3 shows that even if we just apply our simple model, and reduce the grain boundary resistivity to be the same as the grains, the value of J_{DN}/J_{DSc} along the ab-plane is still 0.16, which is similar to that in the best YBCO tapes. For bulk YBCO with equal grain and grain boundary resistivity, J_{DN}/J_{DSc} is further reduced to 0.077. We may hope that faceted grain boundaries [205] may help but given the high grain boundary resistivities found at high angles in bicrystal data, it seems unlikely that grain boundary engineering will enable high J_c in polycrystalline YBCO. Grain boundary engineering such as Ca doping has successfully reduced grain boundary contact resistivity by over an order of magnitude and increased J_c by a factor of 6-7, however these results were on bicrystals preferentially doped at grain boundaries [73], thin film bicrystals [77] or multilayer films [78]. We consider it unlikely that one can reduce the grain boundary resistivity in polycrystalline materials to be less than that of the grains themselves and therefore that grain boundary engineering is unlikely to be successful in increasing J_c to technologically useful values, in randomly aligned polycrystalline YBCO.

4.5.2 Improving J_c in LTS and HTS High-Field Superconductors

The data in the second panel of Figure 4.1 shows that in high fields, all technological superconductors have a large headroom for improvement. In applied fields of half $B_{c2}(4.2$ K$)$, NbTi is only a few percent of its theoretical limit, and Nb$_3$Sn(IT) produced using the internal tin route is only about 0.3% of its theoretical limit. Materials with the highest J_c/J_{DSc} values include commercial YBCO tape [84], thin film Ba(FeCo)$_2$As$_2$ [148]

and Nb [122] that have been fabricated with no high-angle grain boundaries. Hence one can expect high J_D throughout the entire material, and strong pinning to be effective. It is unclear whether adding even more pinning will lead to further improvements, or whether the low-angle grain boundaries or channels formed by contiguous strained and degraded material between pinning sites provide channels for flux flow and hence limit J_{DN}/J_{DSc} in these three materials. In addition to the thin film Ba-122 in Figure 4.1, Ba-122 thin films with artificially engineered superlattices with strong pinning along the ab–plane and c-axis and improved J_c over a wide angular range [206] have been developed. Although untextured polycrystalline bulks and wires have achieved J_c of 10^9 Am^{-2} at 0 T and 4.2 K, which is more than 10 times higher than other round untextured ferropnictide wires, it is still 10 times lower than the thin film materials [207]. The materials with markedly low J_c/J_{DSc} values include MgB$_2$ [146], FeSe$_{0.5}$Te$_{0.5}$ [147] and the A15 polycrystalline materials [141, 142]. Excellent polycrystalline, untextured MgB$_2$ can be produced cheaply through solid state reactions [101, 208-210], as can FeSe$_{0.5}$Te$_{0.5}$ through sintering [211] or powder-in-tube process [212]. However, such FeSe$_{0.5}$Te$_{0.5}$ materials achieve J_c values of 10^7 Am^{-2} at 0 T and 4.2 K, which are two orders of magnitude lower than the tape sample in Figure 4.1. After Nb$_3$Sn was discovered in 1954 [213], materials for magnets were fabricated with J_c values of 1.5×10^9 Am^{-2} at 8.8 T in 1961 [214]. By 1990, J_c values of 2.2×10^9 Am^{-2} at 11 T were achieved [81] and now state-of-the-art values are approximately 8×10^9 Am^{-2} at 11 T. Improvements in J_c are hard-earned and have enabled technological applications above 10 T including high-field MRI, particle accelerator magnets and fusion energy. However, an improvement in J_c by an order of magnitude over 50 years does not seem very large in the context of a headroom of nearly 3 orders of magnitude between J_c and the theoretical upper limit J_{DSc}. If flux flow along channels rather than pinning in the grains is the problem, equation (4.17) suggests high grain boundary resistivity and/or wide grain boundaries are responsible. The resistivity of Nb$_3$Sn and the other A15 intermetallics has been studied extensively. Very large changes in resistivity have been found in Nb$_3$Sn and V$_3$Si with relatively small changes in composition [215]. For binary Nb$_3$Sn, $\rho_N = 4 \times 10^{-8}$ Ωm for 25 at% Sn and $\rho_N = 4 \times 10^{-7}$ Ωm for 24.5 at% Sn. In a series of nanocrystalline HIP'ed Nb$_3$Sn fabricated in our group, materials with 120 nm grain size

and $T_c = 17.4$ K and $B_{c2}(0) = 30$ T, $J_c = 3 \times 10^9$ Am^{-2} at 0 T and 5 K, $J_c = 7 \times 10^8$ Am^{-2} at 6 T and 5 K, were found to have resistivity values of $\rho_N = 6 \times 10^{-7}$ Ωm [216]. When the grain size was reduced to 20 nm, T_c reduced to 10 K and ρ_N increased to 2×10^{-6} Ωm. When the grain size was below 10 nm, T_c was below 2 K and ρ_N increased to 4×10^{-6} Ωm [217]. These nanocrystalline results show that very high resistivity values can occur in Nb$_3$Sn and that a non-superconducting thickness for the grain boundaries of 3 nm in Nb$_3$Sn polycrystalline materials is not unreasonable. The quality of our nanocrystalline Nb$_3$Sn materials may simply have been poor, but the sustained low J_c/J_{DSc} values in state-of-the-art materials may point to a more fundamental grain boundary problem. There are other factors may also help explain why the effective thickness of non-superconducting grain boundaries are large in A15 compounds. Band structure calculations point to the density of states at the Fermi level being determined by the one-dimensional chains of Nb atoms [215, 218]. Variable strain measurements show that a strain as low as 1% significantly depresses T_c [142, 219, 220]. Calculations using equation (4.17) show that for Nb$_3$Sn, low values of $J_{DN}(4.2 \text{ K})/J_{DSc}(4.2 \text{ K})$ of just 0.2 % can occur, when the grain boundary thickness is 3 nm and $\rho_N = 4 \times 10^{-6}$ Ωm. It follows that improvement in the J_c of Nb$_3$Sn can be achieved if the grain boundaries are improved or removed. However, the properties of the grains and the grain boundaries cannot be considered completely decoupled. If we improve the connectivity by lowering the resistivity of the grain boundaries, although we increase the local depairing current in the grain boundaries, we can expect to decrease the surface pinning that restrains the fluxons within the superconducting grains. Hence, we may need to add strong pinning sites into the grains themselves. Whether the improvements would be commercially viable is beyond the scope of this thesis.

4.6   Concluding Comments

Micro- and nanocrystalline YBCO samples were fabricated in order to study the nature of grain boundaries. Detailed magnetic data enabled us to measure and distinguish hysteretic screening currents, limited to within the grains, from transport currents that cross grain boundaries and conclude that the magnetisation J_c is at least $10^5 - 10^6$ times larger than

transport J_c for both our micro- and nanocrystalline materials. Using resistivity data and considering the polycrystalline material as S-N-S junctions, we have shown that high resistivity in the grain boundaries is enough by itself to reduce the local depairing current density of the grain boundaries and hence limit the transport J_c. For microcrystalline materials, transport J_c on the order of 10^5 Am^{-2} was measured. In our nanocrystalline samples, we found there were no intergranular currents through our samples except for just one, in which J_c was reduced by at least 10^9 compared to commercial tapes. This work has provided a quantitative description of grain boundaries that we hope can help provide a framework to extend our characterisation of grain boundaries from those in model systems and bicrystals, to those in technologically-important high field superconducting materials that are used in commercial applications. It provides calculations that identify when grain boundaries are so resistive they limit J_c in polycrystalline materials. Grain boundaries in polycrystalline technological materials are complex and inhomogeneous. We expect a more complete treatment to consider percolative effects and to provide more sophisticated measurements of local grain boundary properties.

Chapter 5

Superconducting Objects and Experimental Artefacts

5.1 Introduction

Unusual hysteresis was found in the $V - I$ characteristics of two different nanocrystalline superconductors from cryogenic temperatures up to room temperature. The resemblance of the hysteresis to Josephson junction behaviour opened the possibility of its origin being superconducting in nature. Several months of work was invested before it was proven to be an experimental artefact associated with measuring extremely high resistances using the Keithley Digital Multimeter (DMM) 2100, a very popular multimeter used in many laboratories worldwide. The measurement circuit can be easily modified to circumvent this problem, however the solution is not obvious. The purpose of this chapter is to document this artefact so it can be identified quickly and easily in the future.

Section 5.2 gives an introduction to what is known as unidentified superconducting objects (USOs) in literature. The experimental data we found are presented in Section 5.3. Section 5.4 outlines the cause of the data and how the artefact may be avoided. Brief conclusions are drawn in Section 5.5.

5.2 USOs in Literature

The seductive draw of room temperature superconductivity is too tantalizing for any researcher in the field to ignore. It has long been sought after and often reported in vain

by the scientific community. Some reports have been experimentally proven to be false while many more have been left as open questions. Such materials are commonly known as Unidentified Superconducting Objects (USO), a term first coined by Paul Chu. In 1946, superconductivity was thought to have been found in solid metal-ammonia solutions with T_c of 180 K – 190 K [221]. Many laboratories attempted to duplicate the experiment without success and it was later proven to be high conductivity rather than superconductivity [222-224]. There are also many publications which claimed to have found YBCO with T_c in the range of 100 K – 240 K [225-227], some even up to 300 K [228]. In 1987, one group observed anomalous voltage excursions which were believed to be due to flux jumps within weakly connected superconducting grains, which has localized T_c of up to 167 K [225]. It is in the interest of the superconductivity community that when a USO is debunked, its true nature should be clearly documented to avoid repeating the same mistake.

In the following section we present data encountered in the study of nanocrystalline materials – initially considered as a potential USO but eventually found to be an experimental artefact of the highly resistive samples and the instruments used.

5.3 Hysteretic $V - I$ Characteristics in Nanocrystalline Superconductors

5.3.1 Hysteretic $V - I$ Data

Unusual hysteretic $V - I$ characteristics were found in two separate Y1MHA samples. The fabrication and experimental setup details are as described in Chapter 4. The magnetisation and transport data can also be seen in Chapter 4. However, during the initial stage of $V - I$ measurements, the typical raw data for nanocrystalline materials displayed the hysteresis shown in Figure 5.1. As the current was increased from zero, the differential resistance showed discrete changes. At 0.3 mA, the voltage stepped up abruptly and then followed the up-branch resistive line. On decreasing the current, the voltage followed a resistive line towards the origin but as the current approached zero, there is a small step down in voltage at approximately 0.05 mA. The negative currents showed similar behaviour which was
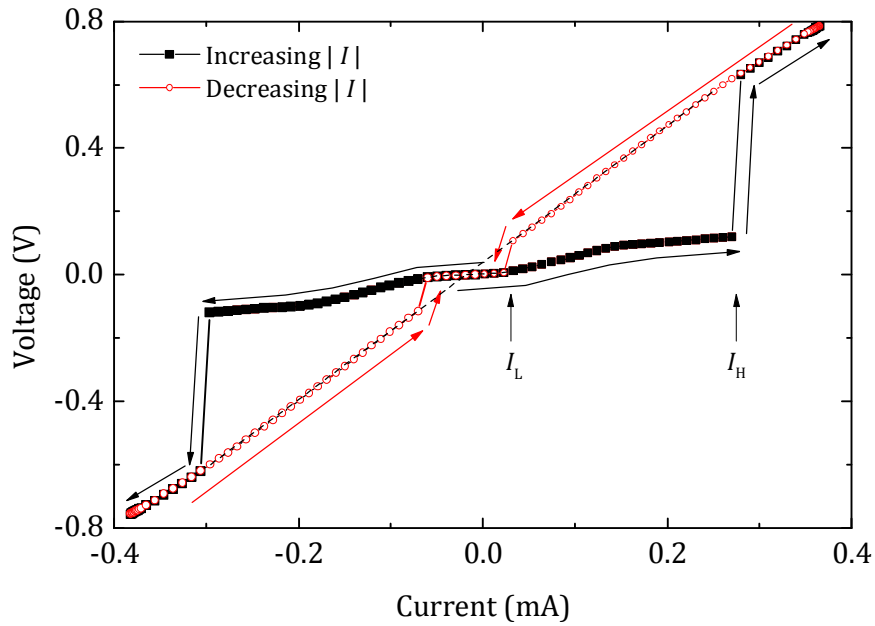
Figure 5.1: Voltage as a function of current at 100 K showing hysteresis. The steps which occurred at high and low currents are denoted I_H and I_L respectively.

antisymmetric about the origin (unipolar). The steps which occurred at high and low currents are denoted I_H and I_L respectively.

Other unusual properties of the nanocrystalline material are summarized in Figure 5.2 to Figure 5.4. Figure 5.2 shows the typical $V - I$ characteristics from 20 K – 300 K. At all temperatures, the hysteresis is as described above. To within the accuracy of our measurements, there were no zero voltage currents percolating through the sample. The temperature dependence of I_H and I_L up to 300 K is presented in Figure 5.3, which shows that I_H and I_L increased with temperature and the hysteresis may well continue above 300 K. An external magnetic field of up to 8 T was applied to the sample at a range of different temperatures, some of which are shown in Figure 5.4. The data showed that the external magnetic field had no effect on the $V - I$ hysteresis. The field independence, extensive temperature range up to room temperature and increase of I_H and I_L all suggest that this is unlikely be a superconducting effect.
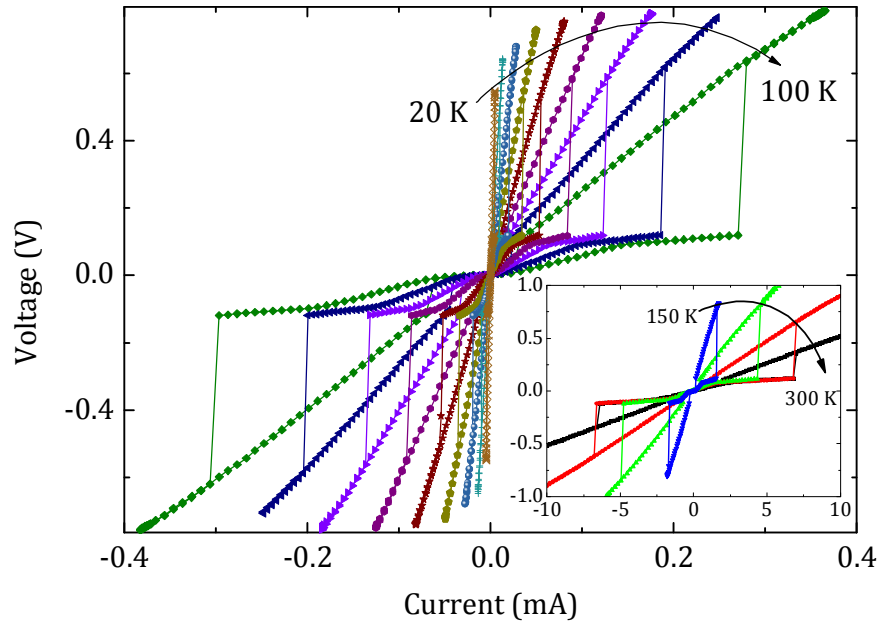
Figure 5.2: Voltage as a function of current between 20 – 100 K in steps of 10 K, and (inset) between 150 – 300 K in steps of 50 K.
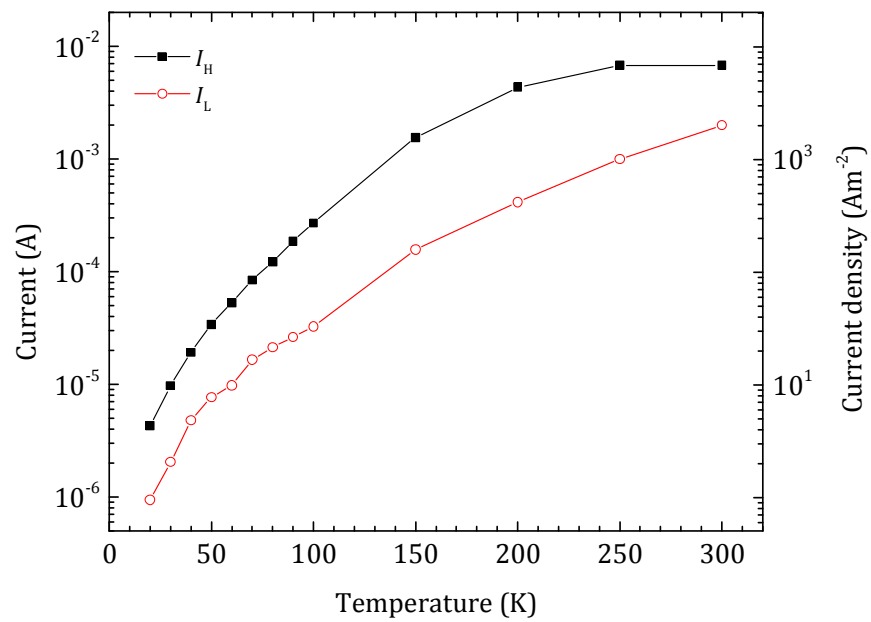

Figure 5.3: The current at which the small (I_L) and large (I_H) steps in voltage occur, as seen in Figure 5.2, as a function of temperature.
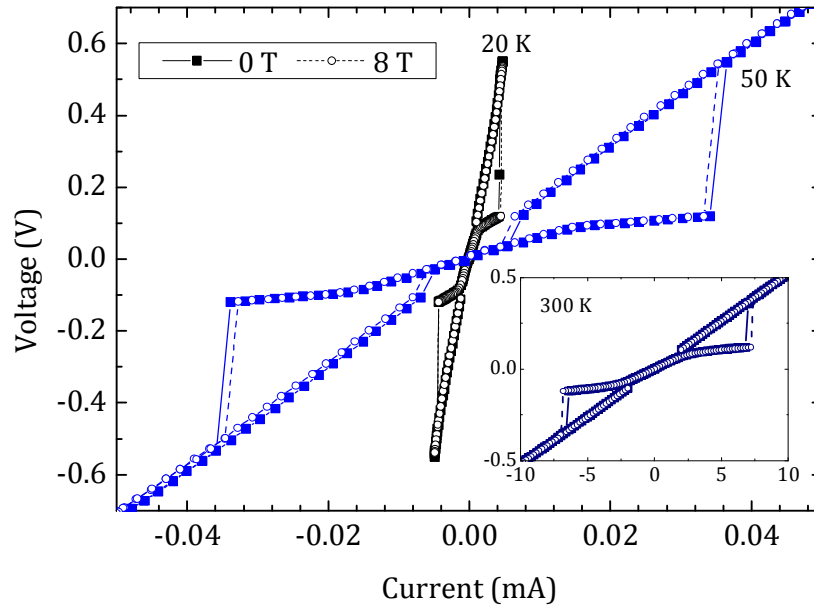
Figure 5.4: Voltage as a function of current at 20 K, 50 K and 300 K, in 0 T and 8 T, showing that the hysteresis is not affected by the external field. 0 T data is given by closed squares with solid lines and 8 T data is given by open circles with dashed lines.

Meticulous checks were done to ensure the hysteretic behaviour was indeed characteristic of the sample. Standard microcrystalline samples, which were HIP'ed and annealed without milling, were measured using exactly the same method and equipment. These microcrystalline samples showed standard results without hysteresis. The fact that the hysteresis occurred in two nanocrystalline samples with different fabrication processes increased confidence in the reliability of the data. Repeat measurements were also completed after stripping off the contacts, removing the surface layer of the samples with fine emery paper, and making fresh silver paint contacts. Measurements were repeated after the samples were thermally cycled between 4.2 K to 300 K. Heating at the contacts was unlikely as I_L and I_H were unaffected by varying the current ramp rate. Heating was also unlikely to produce the neat and sharp steps seen in Figure 5.1 to Figure 5.4. No minor hysteresis loops existed – increasing or decreasing the current at various voltages still mapped out the single "Josephson-like" hysteresis loop. Several different Keithley DMMs of the 2100 model were used to ensure the hysteresis was not due to a single faulty DMM. For all measurements, the internal resistance of the DMMs was set to > 10 GΩ, which is

several orders of magnitude higher than that of the sample, to eliminate the possibility of current shunting through the DMMs.

5.3.2 Colossal Electroresistance in Literature

At first glance, the data resembled the colossal electroresistance (CER) effects reported for a wide range of materials for more than a decade [229-233]. There are several possible mechanisms for resistive switching, including thermal effects, electronic effects and ionic effects [234]. However, in CER, the material switches from high to low resistance in the first quadrant measured, and either from high to low (unipolar) or from low to high (bipolar) in the opposite quadrant [234]. In contrast, for the materials reported here, the switching is always from low resistance to high resistance. The direction of the hysteresis is like that of a Josephson junction, be that for example in model Josephson junctions [235, 236], wires or nanowires [237]. The hysteresis was therefore given the name Josephson-Like Colossal Resistive Switching (JCRS). There was no precedence for the type of hysteresis observed in any type of material known to the author. However, there were a number of features of the data that mitigated against a superconducting explanation for the JCRS behaviour: In most superconducting materials, the critical current increases as the temperature reduces. However, Figure 5.3 shows that I_{H} and I_{L} that characterize the JCRS hysteresis both decrease with decreasing temperature. Nevertheless, the decrease may have been explained by the strong increase in resistivity at low temperatures (Figure 4.5), which can be interpreted as a reduction in carrier concentration or an increase in the penetration depth. Equally, applying a magnetic field usually depresses the superconducting phase in bulk materials. However, if the superconductivity is of reduced dimensionality, for example unconnected filaments or sheets, one could have expected extremely high $B_{\mathrm{c}2}$ where 8 T may not produce any measureable effects. Given these data, a superconducting explanation was unlikely but it was not ruled out until similar hysteresis was reproduced in a circuit which only used passive components including MΩ resistors.

5.4   Origin and Solution to Hysteresis

5.4.1 Auto Range Problem in Keithley DMM 2100

The true nature of the hysteresis only became apparent when a second pair of hysteresis loops was found at higher currents, as shown in Figure 5.5. It was noted that as the current was increased, the voltage prior to the second jump was 1.2 V, exactly 10 times that of the first jump at 120 mV. The factor of 10 lead to the realization that the hysteresis was an artefact of the experiment.

The measurement was done with the DMM set to auto range, and at each range, the Keithley DMM 2100 can measure up to 120 % of the range. It was noted that the jumps always coincided with the automatic switching of range at 120 %. At low currents, auto range selected the 100 mV option. When the measured voltage reached 120 % of this range, i.e. 120 mV, auto range switched to the 1 V range, this coincides with the step at I_{H}. As current is decreased, the auto range switched to the 100 mV range at 120 mV, at the same time as the step at I_{L} occured. A similar hysteresis can occur when auto range switched between 1 V and 10 V ranges, at 1.2 V, which lead to the second pair of hysteresis loops.
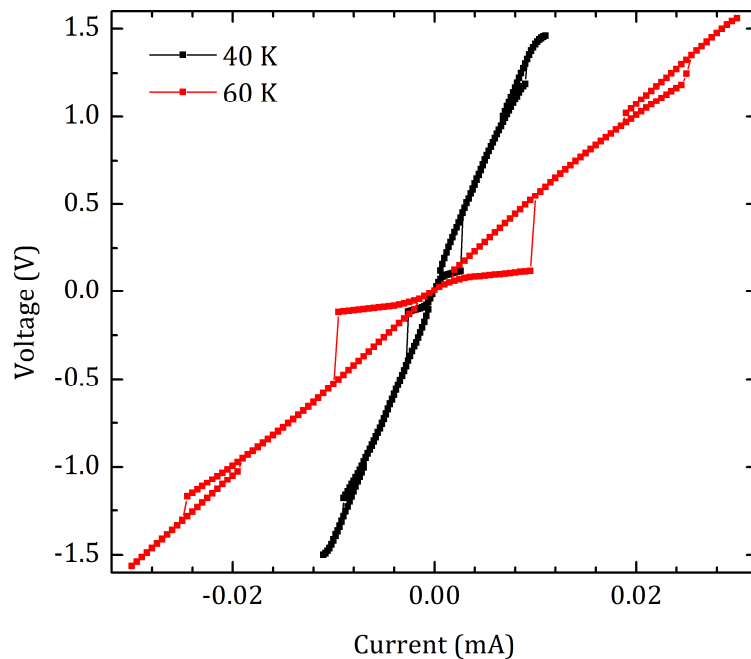

Figure 5.5: Voltage as a function of current at 40 K and 60 K, showing a second pair of hysteresis loops when the current was increased sufficiently high.

Tests showed that the problem of hysteretic $V - I$ characteristics can be circumvented by using a set range, e.g. 1 V, rather than relying on auto range.

The hysteretic behaviour was successfully reproduced with simple resistors. First, a circuit was built to simulate the highly resistive sample as shown in Figure 5.6 (a). A 10 kΩ resistor was chosen as it had similar resistance to the nanocrystalline samples. The $V - I$ characteristics of the 10 kΩ resistor was Ohmic as expected and shown in Figure 5.6 (b). However, this circuit neglects the high contact resistance between the sample and the voltage taps. Two 1 MΩ resistors, each representing one contact, were then added into the circuit as shown in Figure 5.7 (a), and the data (Figure 5.7 (b)) now shows the same hysteresis as that from the nanocrystalline materials. The problem appears to be exclusive to the 2100 model. When the DMM in Figure 5.7 (a) was replaced with a Keithley DMM 2000, the hysteresis was not seen on either auto range or manual range.
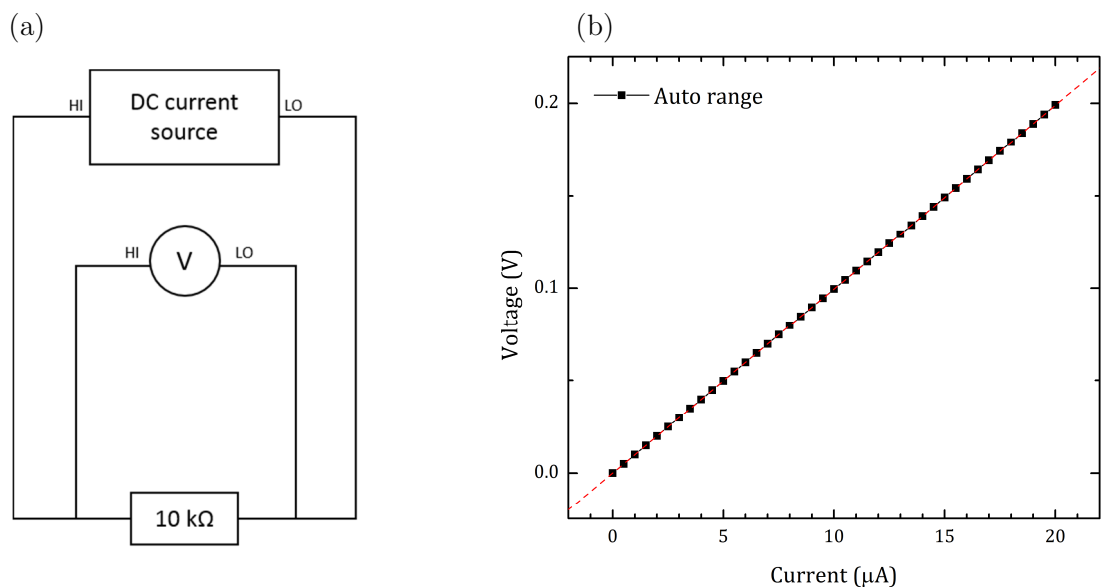

Figure 5.6: (a) Circuit used to attempt to reproduce the $V - I$ hysteresis in which the 10 kΩ resistor represents a nanocrystalline sample. (b) $V - I$ characteristics obtained with this circuit showed standard, Ohmic results.
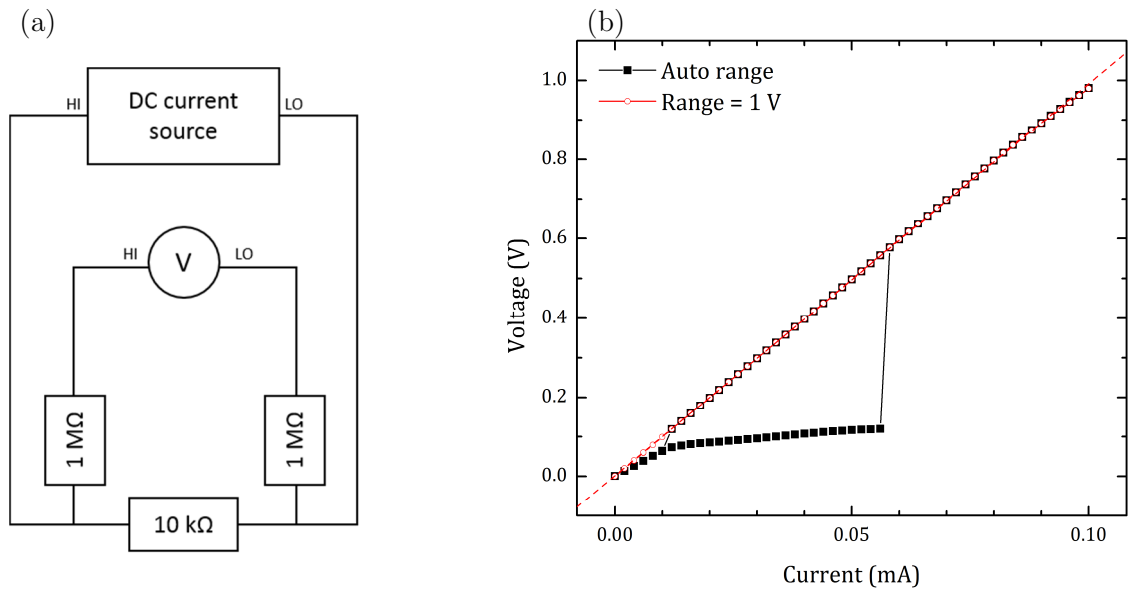
Figure 5.7: (a) Circuit used to reproduce the $V-I$ hysteresis in which a 10 kΩ resistor represents a nanocrystalline sample and the 1 MΩ resistors represent high contact resistances at the voltage taps. (b) $V-I$ characteristics obtained with this circuit. The hysteresis was seen when the Keithley DMM 2100 was set to auto range whereas the standard Ohmic behaviour was seen when range was set to 1 V.

5.4.2 Correcting for Common Mode Current

The origin of the deviation in the measured voltage lies with noise clipping and common mode currents, as shown in Figure 5.8. When the resistance of the sample and any contacts become comparable to the isolation resistance (R_{v}) of the DMM, a common mode current can flow [238]. These are a.c. currents that flow from the LO terminal of the current source through the sample and any contacts, into the LO terminal of the DMM, then back to ground. This is shown by the red arrow in Figure 5.8 (a). This common mode current has a 50 Hz noise due to external sources or ripple of the current supply, resulting in a 50 Hz noise in the LO terminal and hence the measured voltage. In the range of 100 mV, any peak in the signal greater than 120 mV is clipped, as shown in Figure 5.8 (b). The DMM measures an averaged voltage over a certain integration time, which is reduced from the true average voltage due to clipping. Auto range only switches to the next higher range when the clipped average is equal to 120 mV. After switching, in the range of 1 V, the
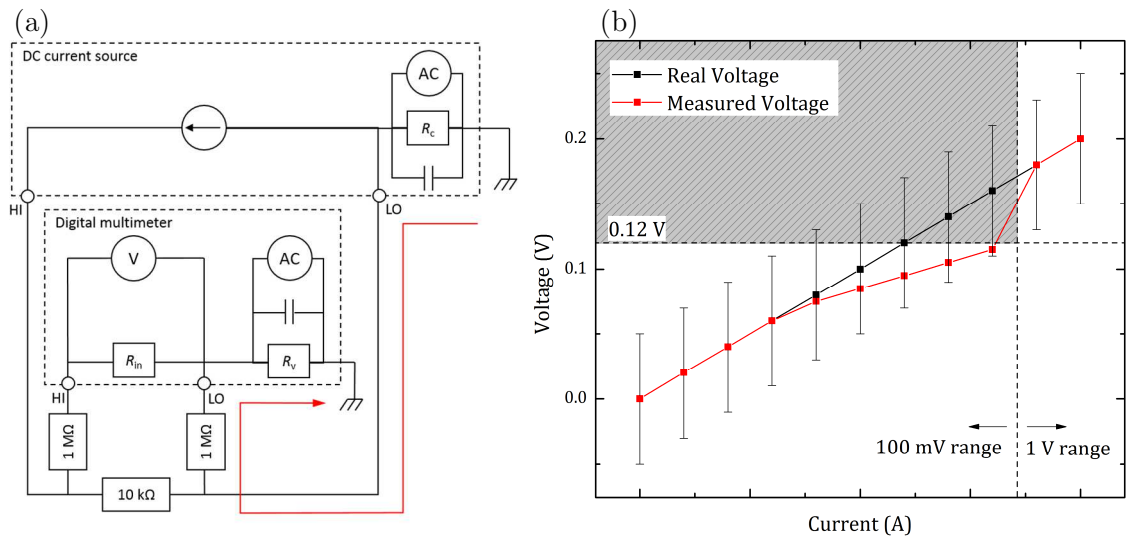
(a)

(b)

Figure 5.8: (a) Circuit diagram to show how common mode current can flow between the d.c. current source and the digital multimeter, given by the red arrow. R_{in} is the input resistance of the digital multimeter. R_{v} and R_{c} are the isolation resistance of the multimeter and the current supplier respectively. (b) Simulation of noise clipping as current is increased with artificial data. The noise on each data point is given by error bars. In the range of 100 mV, any signal above the range threshold of 120 mV (shaded region) is clipped. The resulting time averaged voltage measured by the Keithley is reduced from the real average. In the range of 1 V, all noise is within the measurable range and thus the measured voltage is the real voltage.

noise is now within the measurable range, no clipping occurs and thus the measured voltage is once again correct.

A method of removing common mode current is to use two DMMs, an example of this is shown in Figure 5.9 (a) [238]. The LO terminal of the original circuit is replaced with a second DMM, and the LO terminals of both DMMs are connected to the ground of the current source. This setup eliminates the use of LO terminals, which has a low isolation resistance (R_{v}), compared to the > 10 GΩ input resistance of the HI terminals (R_{in}). The voltage of the sample is given by the difference between the HI terminals of the two DMMs, which due to the high input resistance, is less prone to common mode currents. The result is shown in Figure 5.9 (b), in which the standard Ohmic result is recovered.
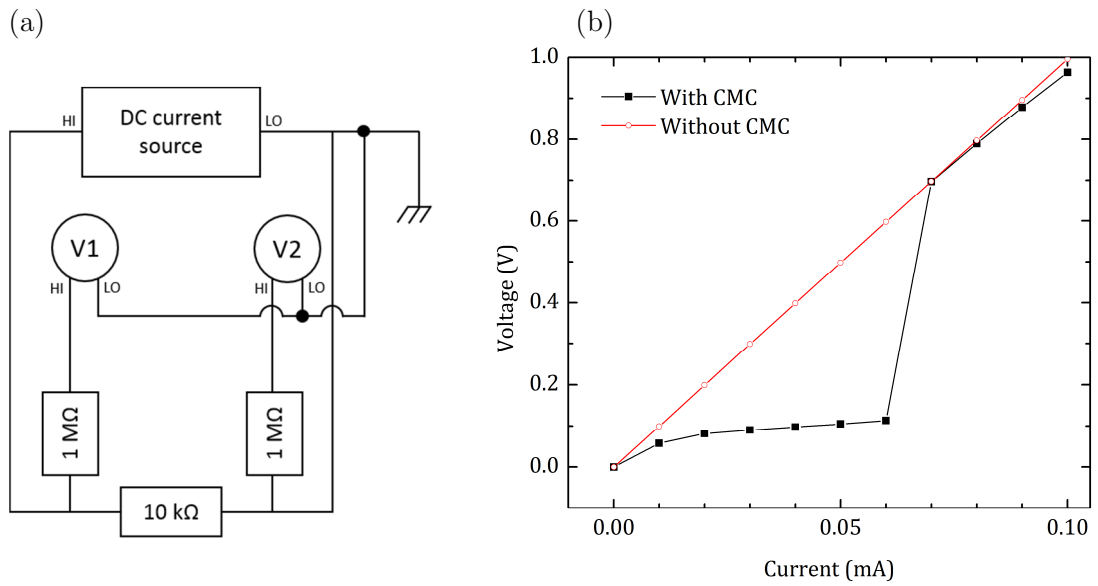
(a)   (b)

Figure 5.9: (a) Circuit in which a 10 kΩ resistor represents a nanocrystalline sample and the 1 MΩ resistors represent contact resistance. The LO terminals of each multimeter were connected to the ground of the DC current source to remove common mode currents (CMC). (b) $V - I$ characteristics obtained with the modified circuit showed Ohmic behaviour, without common mode currents.

5.5   Concluding Comments

Hysteretic $V - I$ characteristics are not uncommon in a range of materials. They can be found, for example, in colossal electroresistance and avalanche breakdown of diodes. However, such sharp and distinct unipolar hysteresis observed in the nanocrystalline materials is uncommon and only seen in Josephson junctions. Combined with the weak superconductivity found in the magnetic measurements, it is easy to misinterpret the transport data as superconducting. Through experimentation with equivalent circuits, the cause of the hysteresis was found to be due to the DMM incorrectly clipping the large noise in the common mode current. This problem is expected to be quite common in transport measurement of highly resistive nanocrystalline HTS and the work in this Chapter can be used to identify such artefacts or "USO"s in the literature and in future work. The hysteresis can be removed simply by selecting a range manually, or using a slightly modified circuit to remove clipped common mode currents.

Chapter 6

Nanocrystalline BiSCCO

6.1 Introduction

High critical current density (J_c) in superconducting materials is usually the most important technological figure of merit. In this field, this requires both a high current density associated with flux pinning (J_P) and a high depairing current density (J_{DSc}) throughout the entire material. A high J_P ensures that there are pinning forces preventing the fluxons from moving. In polycrystalline low temperature superconductors (LTS), such large pinning forces were often achieved by reducing the grain size. This increased the force necessary to drive the fluxons along the grain boundaries from one side of the sample to the other, by increasing the density of grain boundary triple points and the distortions of the fluxons required for them to move [115, 116]. In high temperature superconductors (HTS), the pinning force has often been increased by adding inclusions that pin each fluxon [239]. In properly optimised technological materials, in addition to high J_P, we must also ensure that J_{DSc}, which is the theoretical upper limit associated with density of Cooper pairs in a material, is high enough to ensure J_c does not cause the pairs to break. In HTS, it is well established that large angle grain boundaries can cause J_c to drop by several orders of magnitudes, depending on the misorientation angle [10, 240, 241]. This has become known as the "weak-link problem". Although historically, weak-links were uniquely identified by low J_c, it is important to identify why J_c is low – whether J_{DN} is low or if there is low J_{PN}. Although studying bicrystal systems has contributed to our understanding, because they provide a route to study grain boundaries with precisely

fabricated boundaries and misorientation angles [10, 240, 241] and can be considered the building blocks for polycrystalline materials, most measurements do not include reports of local values of J_{DN} and J_{PN}. Furthermore it is not straightforward to relate the behaviour of a bicrystal to the role of the equivalent grains or grain boundaries in a polycrystalline material. For example, we have long known that notches or flaws [242] as well as the surface conditions or coatings [243] in single crystals strongly affect their current carrying capacity as well as appreciating that the topology of (and hence the pinning by) grain boundaries in polycrystalline materials is very important and quite different to that found in the broadly planar grain boundaries in bicrystal studies.

Given the uncertainties in the potential for grain boundaries in HTS materials to carry high critical current densities in high fields and the importance of driving down the cost of HTS materials with high J_c for applications such as fusion [138], we have decided to investigate micro- and nanocrystalline HTS materials further. We have already presented results on polycrystalline $YBa_2Cu_3O_7$ (YBCO) with micro- and nano-sized grains that included measurements and calculations of angular averaged grain boundary resistivities in Chapter 4. Following work on S-N-S junctions that showed it was possible to relate the resistivity of junctions to the local depairing current density [119], we found that for most LTS, MgB_2, iron-based superconductors and YBCO, even if the grain boundaries are non-superconducting, if their resistivity is equal to that of the grains, they have a J_{DN} that is only about a factor of 5 lower than the depairing current density. Equally we found how resistive grain boundaries must be to depress the local current density severely (i.e. to produce low J_{DN}).

In this chapter, we look at the Bi-based materials that have the chemical formula $Bi_2Sr_2Ca_{n-1}Cu_nO_{2n+4}$ (BiSCCO) where $n = 1, 2, 3$ gives the first three members of this class: $Bi_2Sr_2CuO_6$, $Bi_2Sr_2CaCu_2O_8$ and $Bi_2Sr_2Ca_2Cu_3O_{10}$, with critical temperatures (T_c) of 20 K, 85 K and 110 K respectively. These materials have a layered structure such that the anisotropy of the unit cell lattice parameters increases with n. We consider in detail $Bi_2Sr_2CaCu_2O_8$ and $Bi_2Sr_2Ca_2Cu_3O_{10}$. They are complex materials with flux lines that can behave as vortex pancakes [244] and have vortex states including vortex liquids, glasses

and solids in their field-temperature phase diagram [136, 245, 246]. They have a much higher carrier mass anisotropy than YBCO, their flux-line lattices melt at fields and temperatures much lower than YBCO [247] and the irreversibility fields (B_{Irr}) in BiSCCO are significantly lower than YBCO at temperatures above 10 K [84]. Nevertheless, although an extrapolation of both upper critical field (B_{c2}) and B_{Irr} to 0 K for BiSCCO has a large uncertainty, the critical fields for $Bi_2Sr_2CaCu_2O_8$ and $Bi_2Sr_2Ca_2Cu_3O_{10}$ are estimated to be of the order of a few hundred Tesla which is clearly sufficiently high for high-field applications [84, 135, 136, 248].

In addition to high critical fields, potentially useful high-field technological superconductors must also have high J_{DSc}. Table 6.1 shows the J_{DSc} for $Bi_2Sr_2CaCu_2O_8$ and $Bi_2Sr_2Ca_2Cu_3O_{10}$, and the parameters used to calculate them [249]. The angular averaged depairing current densities ($\langle J_{\mathrm{DSc}}(0,T)\rangle$) were calculated using

$$\langle J_{\mathrm{DSc}}(0,T)\rangle = \frac{\Phi_0}{3\sqrt{3}\pi\mu_0}\left\langle \frac{1}{\lambda^2(T)\xi(T)}\right\rangle, \qquad (6.1)$$

where $\left\langle \frac{1}{\lambda^2(T)\xi(T)}\right\rangle$ can be calculated from the anisotropic λ and ξ values in Table 6.1. We have chosen to calculate the values of λ_{ab} and ξ_{ab} from B_{c2}^c and B_{c1}^c (see Appendix for derivations). The values of λ_c and ξ_c were then derived from the mass anisotropy ratio Γ, where we have used $\Gamma = \frac{\mathrm{d}B_{c2}^{ab}}{\mathrm{d}T}\big/\frac{\mathrm{d}B_{c2}^c}{\mathrm{d}T} \approx 10$ [250] and 7 [251]. Higher values of Γ have also been reported [247], but does not significantly change our calculated values for angular averages of any of the critical parameters. The large ratio of J_{DSc} along the ab-plane to the c-axis direction leads to the "railway switch" model which described current flowing preferentially along the ab-planes [252]. Useful J_c values have already been achieved in both $Bi_2Sr_2CaCu_2O_8$ and $Bi_2Sr_2Ca_2Cu_3O_{10}$ conductors. $Bi_2Sr_2CaCu_2O_8$ can produce high J_c in round wire form, due to its quasi-biaxial textured grain structure [248, 253, 254]. Bi-2223 tapes have a uniaxial c-axis texture with high J_c in tapes and wires [255-257]. It is clear that removing grain boundaries or producing materials that only incorporate low angle grain boundaries can produce high J_c. Nevertheless, at 0 T and 4.2 K, J_c/J_{DSc} is still approximately only 10^{-2} and 10^{-3} for Bi-2212 and Bi-2223 respectively, showing that further large increases in J_c are still possible in these materials. However in this thesis, our

Material	T_c (K)	ν		$B_{c2}(0)$ (T)	$B_{c1}(0)$ (mT)	$\xi(0)$ (nm)	$\lambda(0)$ (nm)	$J_{DSc}(0, 4.2)$ (Am^{-2})
Bi$_2$Sr$_2$CaCu$_2$O$_8$	84.8	ab:		2310*	1.34*	3.24*	300 [159]	3.21×10^{11}*
	[159]	c:	0.14 [135]	231 [135]	4.60*	0.324*	3000*	3.21×10^{10}*
		$\langle\ \rangle$:				2.28*	500*	2.21×10^{11}*
Bi$_2$Sr$_2$Ca$_2$Cu$_3$O$_{10}$	108	ab:		2080*	5.62*	2.86*	165 [160]	1.22×10^{12}*
	[132]	c:	0.14†	297 [132]	13.8*	0.408*	1160*	1.74×10^{11}*
		$\langle\ \rangle$:				2.04*	262*	8.56×10^{11}*

Table 6.1: The depairing current density at zero magnetic field and 4.2 K, $J_{DSc}(0$ T, 4.2 K$)$, and the parameters used to calculate it. T_c is the critical temperature, ν is the exponent derived from fitting the empirical equation for the temperature dependence of the upper critical field in $B_{c2}^c(T) = B_{c2}^c(0)(1 - (T/T_c)^\nu)$ to single crystal data along the c-axis. We have assumed a similar temperature dependence for fields applied along the ab-plane. We have used a mass anisotropy ratio $\Gamma = \frac{dB_{c2}^{ab}}{dT} / \frac{dB_{c2}^c}{dT} \approx 10$ [250] and 7 [251] for Bi$_2$Sr$_2$CaCu$_2$O$_8$ and Bi$_2$Sr$_2$Ca$_2$Cu$_3$O$_{10}$ respectively. The G-L coherence length and G-L penetration depth are given parallel to the ab-plane and parallel to the c-axis at 0 K and have been calculated using the temperature dependence of the critical fields close to T_c as described in the Appendix. Parameters that were obtained from temperature dependent experiments in the literature have the relevant reference cited next to them. Calculated parameters are labelled with *. For Bi$_2$Sr$_2$Ca$_2$Cu$_3$O$_{10}$†: we chose the value for ν to be the same as for Bi$_2$Sr$_2$CaCu$_2$O$_8$ (i.e. 0.14).

approach is quite different to that of eliminating high angle grain boundaries. We fabricate and measure bulk micro- and nanocrystalline Bi$_2$Sr$_2$CaCu$_2$O$_8$ and Bi$_2$Sr$_2$Ca$_2$Cu$_3$O$_{10}$ materials using well-established powder metallurgy techniques because of their significant potential for use in a conductor technology. Using our measurements and analysis, we try to identify the potential these polycrystalline materials have – more specifically what mechanism limits J_c and are there any approaches for producing relatively cheap high J_c randomly-aligned polycrystalline BiSCCO materials that will lead to conductors that make new high-field superconducting applications cost-effective.

The rest of the chapter is structured as follows: The fabrication process and microstructure characterisation is presented in section 6.2. The transport and magnetisation measurement results are shown in section 6.3. Section 6.4 presents some theoretical considerations and section 6.5 discusses the important results. Finally, our conclusions are summarised in section 6.6.

6.2   Fabrication of Nanocrystalline Materials

6.2.1   Sample Milling and HIP'ing

Commercial $Bi_2Sr_2CaCu_2O_8$ (B1) and $Bi_2Sr_2Ca_2Cu_3O_{10}$ (B2) powders (99.98%, purchased from Toshima) were used to fabricate the micro- and nanocrystalline samples. The powders were milled using a SPEX 8000D high-energy shaker mill, with tungsten carbide (WC 94/Co 6) milling media in an argon atmosphere. The samples were milled in batches of 10 g, with a ball-to-powder mass ratio of 3:1, for either 30 minutes or 60 minutes. The milling vial and balls were scraped with a tungsten carbide rod regularly, in an argon glovebox, to increase yield and improve homogeneity. After milling, magnetic separation [258] was employed to remove Co contamination in the milling media from the milled powdered samples, using a 0.7 T iron-core magnet. The powders were placed into niobium foil packets (0.025 mm thick, 99.8%, Alfa Aesar), which acted as diffusion barriers, sealed into stainless steel tubes (type 316, 1 mm thickness) and then consolidated using a hot isostatic press (HIP) at a temperature of 450 °C and pressure of 177 MPa for 5 hours. The pressure, 177 MPa, was the practical limit for the HIP. Samples were subsequently annealed in a pure flowing oxygen atmosphere in a dedicated oxygen furnace to optimise oxygen content and restore some crystallinity. We have chosen to anneal our samples at 750 °C, following Zhao *et al.* [114], and also at 500 °C and 800 °C. In this chapter, the letters "P", "M", "H" and "A" denote that a sample has been processed through a combination of pellet Pressing, Milling, HIP'ing or Annealing respectively. The magnetic separation process was used on all our milled samples. The numbers 30 and 60 following "M" indicate the milling time in minutes. The numbers following the letter "A" denote the annealing temperature in degrees Celsius. Table 6.2 lists the details of the fabrication process for all microcrystalline and nanocrystalline samples in this chapter. A full set of measurements was completed on four samples, which includes a micro- and a nanocrystalline samples for both B1 and B2, namely: B1HA750, B1M30HA750, B2HA750 and B2M30HA750.

Sample	Grain Size (nm) ($\pm 50\%$)	Annealed
B1P	5000	-
B1HA750	5000	750 °C for 20 hours then 450 °C for 60 hours
B1M30P	3.6	-
B1M60P	2.8	-
B1M30H	70	-
B1M30HA500	200†	500 °C for 5 hours then 500 °C for 20 hours
B1M30HA750	200†	750 °C for 20 hours then 450 °C for 60 hours
B1M60HA750	200†	750 °C for 20 hours then 450 °C for 60 hours
B1M60HA800	200†	800 °C for 20 hours then 450 °C for 60 hours
B2P	5000	-
B2HA750	5000	750 °C for 20 hours then 450 °C for 60 hours
B2M30P	9.8	-
B2M60P	3.6	-
B2M30H	70	-
B2M30HA500	200†	500 °C for 5 hours then 500 °C for 20 hours
B2M30HA750	200	750 °C for 20 hours then 450 °C for 60 hours
B2M60HA750	200†	750 °C for 20 hours then 450 °C for 60 hours
B2M60HA800	200†	800 °C for 20 hours then 450 °C for 60 hours

Table 6.2: The nanocrystalline samples in this chapter and their fabrication process. "B1" and "B2" represent Bi-2212 and Bi-2223 respectively. Letters "P", "M", "H", and "A" stand for Pressed, Milled, HIP'ed and Annealed respectively. The numbers following "M" shows the milling time in minutes. HIP processing was at 450 °C and 177 MPa for 5 hours. Letter "A" followed by a number denotes the maximum annealing temperature used, the details can be found in this table. The grain size of B2M30HA750 was 200 nm and has been taken as representative of all nanocrystalline materials and denoted using the symbol "†".

6.2.2 X-Ray Diffraction

The grain sizes of the samples were obtained using powder x-ray diffraction (XRD) measurements. Figure 6.1 shows the evolution of the XRD patterns for the as-supplied material, and after they were milled for 5, 10, 15, 20, 25, 30 and 60 minutes. The XRD peaks broadened with increased milling time in a similar way for both B1 and B2. The grain size was obtained using Rietveld refinement using TOPAS Academic software. The

Figure 6.1: XRD patterns of B1 (upper panel) and B2 (lower panel) samples. From the bottom to the top, the traces in each panel are: as-supplied material, milled 5, 10, 15, 20, 25, 30 and 60 minute samples. Inset: Grain size as a function of milling time for both B1 and B2.

inset shows the grain size as a function of milling time. After 30 minutes of milling, the grain size has reduced to < 10 nm. No decrease in grain size was observed for milling times greater than 3 hours.

Figure 6.2 shows the powder XRD spectra for both B1 and B2 of the as-supplied, M30H, M60H and M30HA750 samples. HA750 data are also shown for a solid flat piece of sample. The main $Bi_2Sr_2CuO_6$, $Bi_2Sr_2CaCu_2O_8$ and $Bi_2Sr_2Ca_2Cu_3O_{10}$ peaks are labelled with "▼", "∘" and "♦" symbols respectively. For both sets of samples, the peak positions of the HA750, M30H and M60H samples are still largely the same as the as-supplied material. Compared
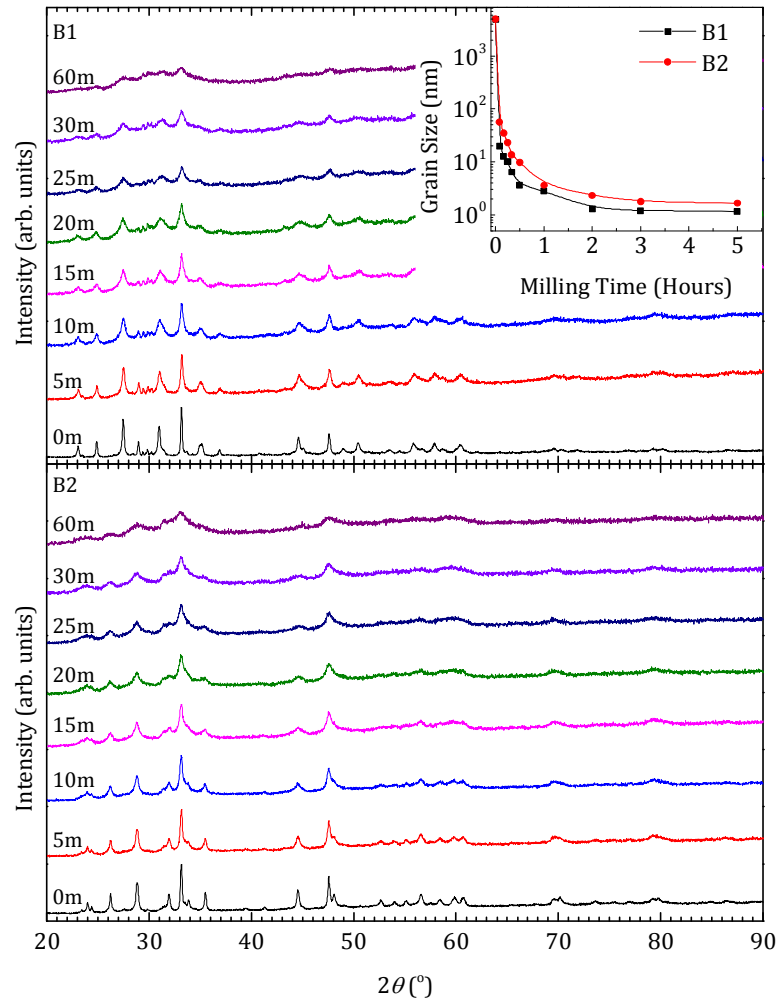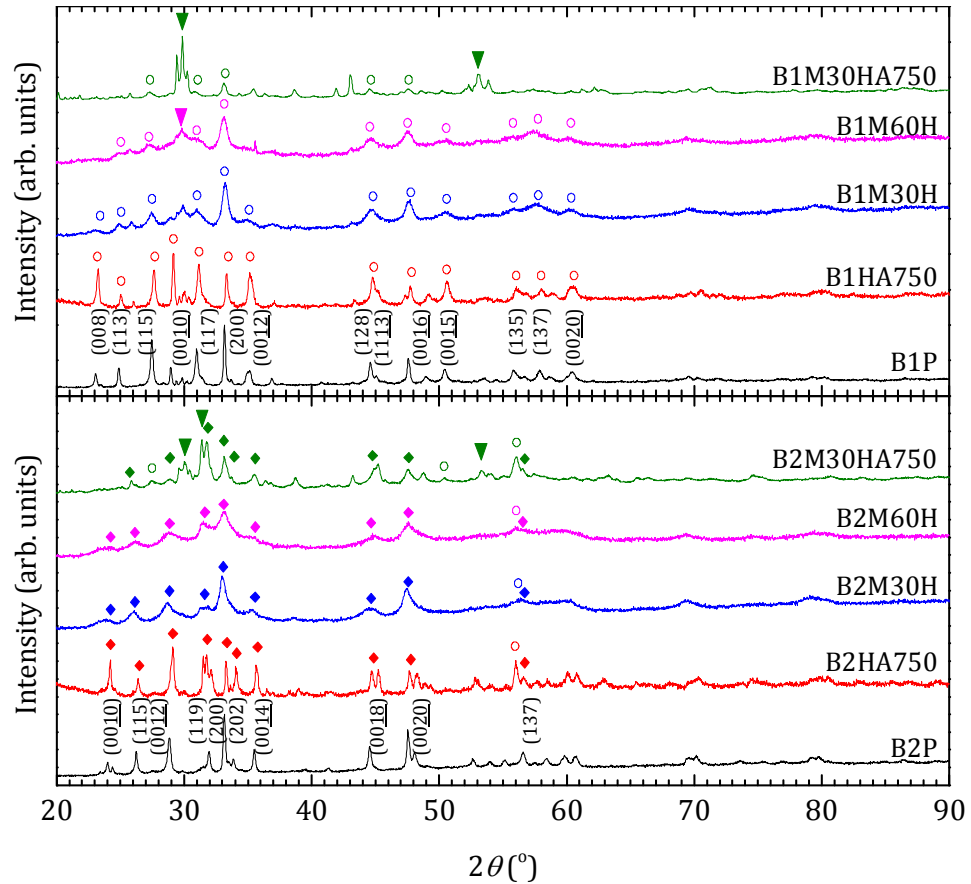
Figure 6.2: XRD of B1 (upper panel) and B2 (lower panel) samples. From the bottom to top, the traces in each panel are: as-supplied material, HA750, M30H, M60H and M30HA750 samples. The main $Bi_2Sr_2CuO_6$, $Bi_2Sr_2CaCu_2O_8$ and $Bi_2Sr_2Ca_2Cu_3O_{10}$ peaks are labelled with "▼", "○" and "♦" symbols respectively.

to the P samples, the HA750 samples have different relative peak intensities, which is indicative of texturing in the sample – that the grains are not randomly aligned but have a strong preferred orientation that was enhanced through the processing. A more complete study could include inverse pole figures in order to quantify the degree of texturing. The peaks of the milled samples were broad but some crystallinity was restored after annealing. The microcrystalline HA750 materials are predominantly single phase. The M30H and M60H materials are also predominantly single phase, but have low superconducting critical parameters. The annealed samples have superconductivity restored but are mixed $Bi_2Sr_2Ca_{n-1}Cu_nO_{2n+4}$ phases with some additional secondary phase material. The grain sizes of all samples are listed in Table 6.2. Accurate values for the nanocrystalline sample

B2M30HA750 were obtained and taken to be representative of all nanocrystalline samples because of the large uncertainties found for the other nanocrystalline materials.

6.2.3 Thermal Gravimetry and Differential Scanning Calorimetry

Figure 6.3 shows differential scanning calorimetry (DSC) and thermal gravimetric (TG) data for the P, M30P, M60P and M30HA750 samples for B1. The same data for B2 are shown in Figure 6.4. Data were obtained over two cycles. In each cycle, samples were heated up to 1100 °C and cooled back to room temperature in a pure argon atmosphere at 10 °C min^{-1}. We identify the main endothermic DSC peaks as follows: The peak near 890 °C in the B1P sample corresponds to the melting of the $Bi_2Sr_2CaCu_2O_8$ phase and the peaks near 940 °C in B1P corresponds to melting of the $(Sr,Ca)CuO_2$ and $(Sr,Ca)_2CuO_3$ phases that grew from the $Bi_2Sr_2CaCu_2O_8$ melt [259, 260]. After milling, these melting temperatures were lowered. In the case of B1M30HA750, the melting of the $Bi_2Sr_2CaCu_2O_8$ was lowered to $\sim$ 870 °C and the $(Sr,Ca)_xCuO_y$ phases was lowered to $\sim$ 890 °C. In the second cycle of B1 samples, the peak near 780 °C may be melting of Bi_2O_3 or the polymorphous transition of Bi_2O_3 $\alpha \rightarrow \beta$ [260]. In Figure 6.4, the peak near 875 °C in the B2P sample corresponds to melting of the $Bi_2Sr_2Ca_2Cu_3O_{10}$ phase [260-262], and the peak near 920 °C corresponds to melting of the $Bi_2Sr_2CuO_6$, $(Sr,Ca)CuO_2$ and Ca_2CuO_3 phases [263]. After milling, the melting temperature of the $Bi_2Sr_2Ca_2Cu_3O_{10}$ phase was lowered to 850 °C. The peaks at 650-680 °C in cycle 2 of the B2 materials may be $Bi_2Sr_2CuO_6$ + Ca_2CuO_3 + CuO $\rightarrow$ $Bi_2Sr_2CaCu_2O_8$ + Ca_2CuO_5 + CuO [263], and the peak near 780 °C is the same as cycle 2 of B1. Generally, in nanocrystalline or amorphous materials, small exothermic peaks are observed in the milled materials, which identifies the temperature at which crystallisation occurs [163, 249, 264]. B1 and B2 are very soft, thus the energy associated with crystallisation is expected to be small. Unfortunately, no exothermic crystallisation peaks are seen in Figure 6.3 and Figure 6.4 for the milled B1 and B2 materials. We confirm that annealing temperatures above 450 °C in oxygen were required to recover superconductivity in milled samples [114], and so chose this low temperature for HIP'ing to minimise crystal growth.
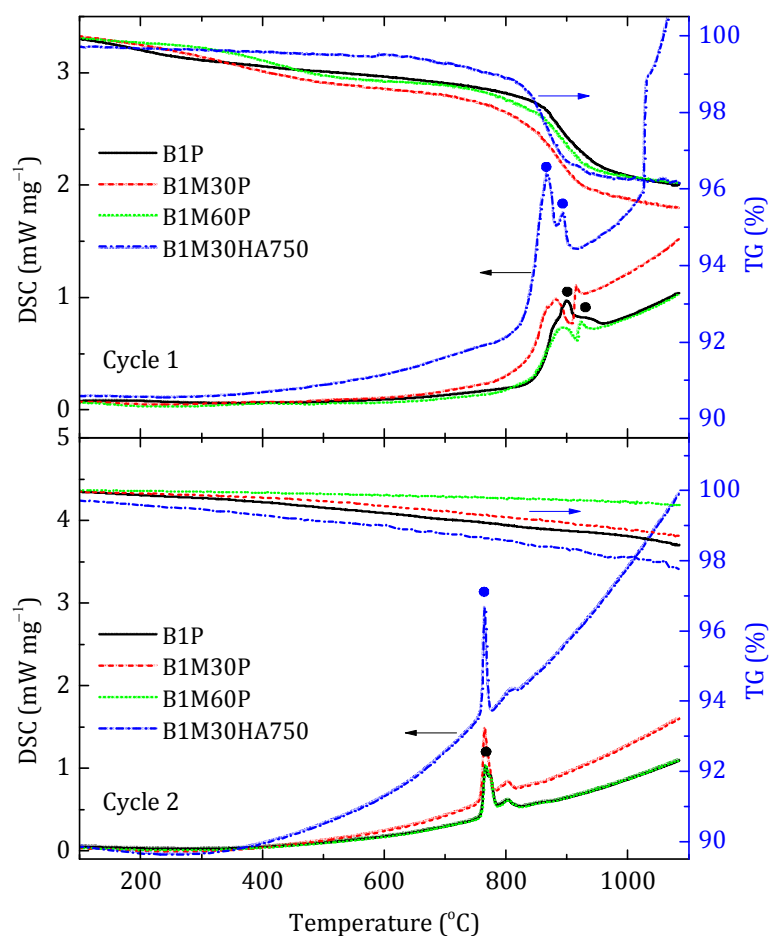
Figure 6.3: Differential Scanning Calorimetric (DSC) signal and Thermogravimetric (TG) signal of B1P, B1M30P, B1M60P and B1M30HA750 samples between 100 – 1100 °C, ramped at 10 °C min⁻¹. Top: first cycle, bottom: second cycle. Significant endothermic peaks, associated with melting are labelled with ● symbols. No crystallisation peaks are seen in the milled materials. The apparent drop in DSC signal near 900 °C for the milled samples in Cycle 1 are between two endothermic peaks and is likely to be due to the signal returning to the background value, rather than due to an exothermic peak.
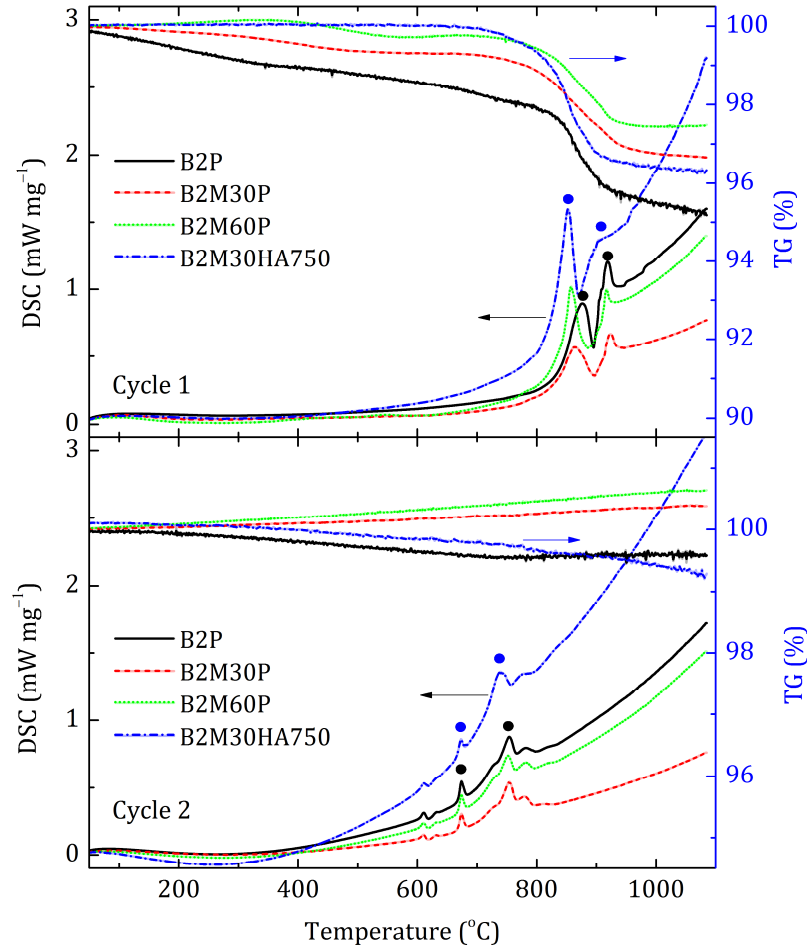
Figure 6.4: Differential Scanning Calorimetric (DSC) signal and Thermogravimetric (TG) signal of B2P, B2M30P, B2M60P and B2M30HA750 samples between 100 – 1100 °C, ramped at 10 °C min^{-1}. Top: first cycle, bottom: second cycle. Significant endothermic peaks, associated with melting are labelled with ● symbols. No crystallisation peaks are seen in the milled materials. TG values of >100% is due to an experimental artefact. The apparent drop in DSC signal near 900 °C for all samples in Cycle 1 are between two endothermic peaks and is likely to be due to the signal returning to the background value, rather than due to an exothermic peak.

6.3 Experimental Results and Analysis

6.3.1 Resistivity Measurements

HIP'ed samples were shaped into cuboid bars using fine emery paper for transport measurements with typical dimensions of $1 \times 1 \times 8$ mm. The samples were mounted onto a Physical Property Measurement System (PPMS) resistivity puck [168] in the same way

as described in Chapter 4. Current and voltage leads were attached to the samples using silver paint for standard four-terminal measurements. The voltage taps were typically 5 mm apart. The temperature and the magnetic field were controlled and measured using the PPMS.

Figure 6.5 shows the zero field resistivity as a function of temperature for the four most important samples, B1HA750, B1M30HA750, B2HA750 and B2M30HA750, measured using excitation currents of typically 5 mA. The single crystal resistivity of $Bi_2Sr_2CaCu_2O_8$ [265] and $Bi_2Sr_2Ca_2Cu_3O_{10}$ [51] along the ab-plane (ρ_{ab}) and c-axis (ρ_c) are also shown on each graph. The angular averaged resistivity ($\langle\rho_N\rangle$), calculated from the single crystal data and discussed below, are also shown. Figure 6.6 and Figure 6.7 show the in-field resistivity for each of the four samples and the irreversibility field derived using criteria of 90%, 50%, 10% and 0% of $\rho_N(T_c)$. Both the B1HA750 sample and the B1M30HA750 sample in Figure 6.6 shows similar superconducting transitions at 75 K due to the $Bi_2Sr_2CaCu_2O_8$ phase where the onset (cf 90% of $\rho_N(T_c)$) is only weakly sensitive to magnetic field. However the two materials reach zero resistivity at quite different fields and temperatures (cf 0% of $\rho_N(T_c)$). We associate these differences with the much poorer properties of the grain boundaries in the nanocrystalline material. Similar behaviour has been reported elsewhere in $Bi_2Sr_2CaCu_2O_8$ bicrystals and polycrystalline material [266, 267]. Figure 6.7 shows equivalent data for the B2HA750 and B2M30HA750 samples. Both materials show a transition at 110 K due to the optimally-doped $Bi_2Sr_2Ca_2Cu_3O_{10}$ phase which is also only weakly sensitive to field. A second superconducting transition at 75 K occurs in both materials due to $Bi_2Sr_2CaCu_2O_8$. In the B2M30HA750 sample, the reduction in resistivity between 110 K and 75 K is small in comparison to B2HA750, indicative of a much larger content of $Bi_2Sr_2CaCu_2O_8$ in the milled material.
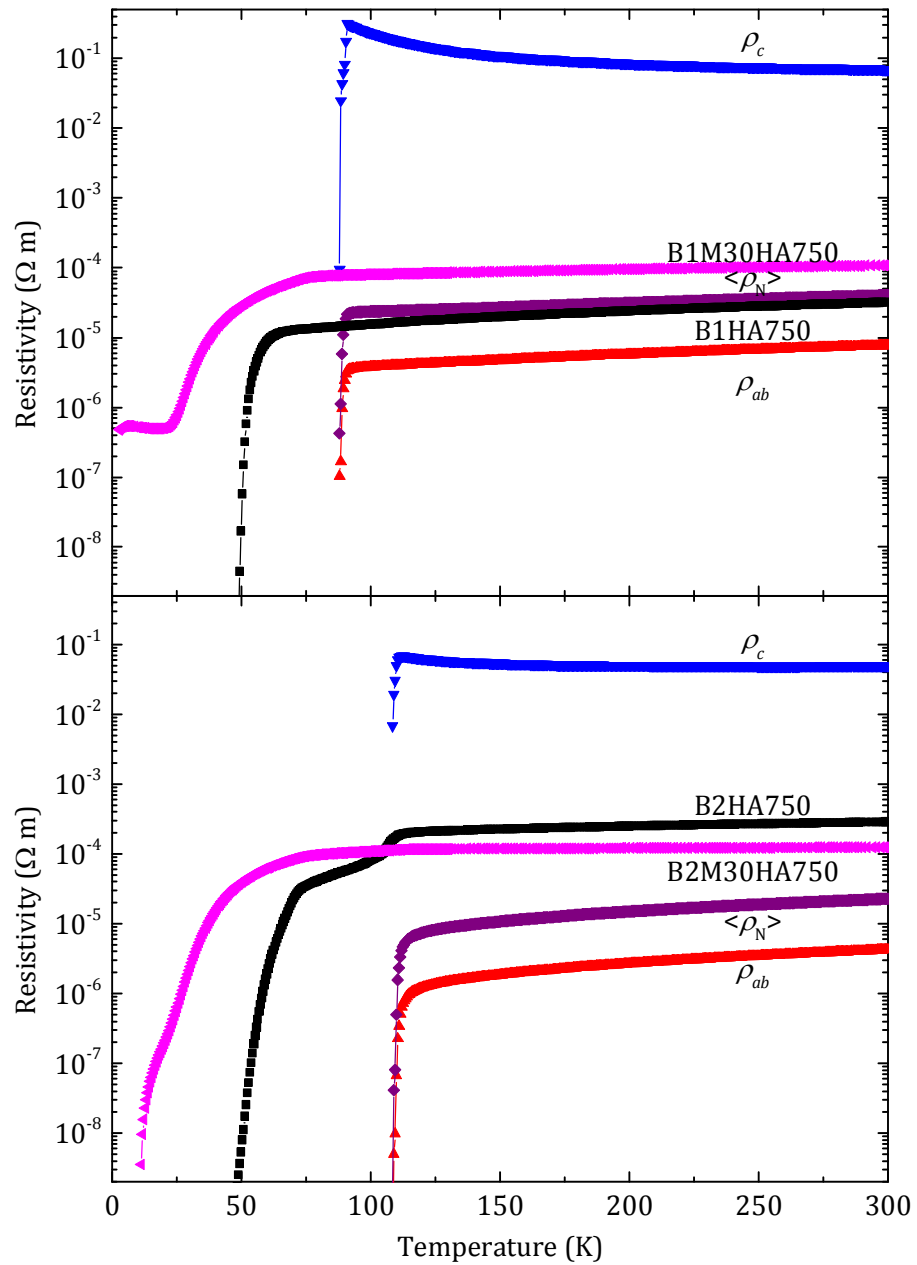
Figure 6.5: Resistivity as a function of temperature for $Bi_2Sr_2CaCu_2O_8$ (upper panel) and $Bi_2Sr_2Ca_2Cu_3O_{10}$ (lower panel) micro- (HA750) and nanocrystalline (M30HA750) materials in zero field.
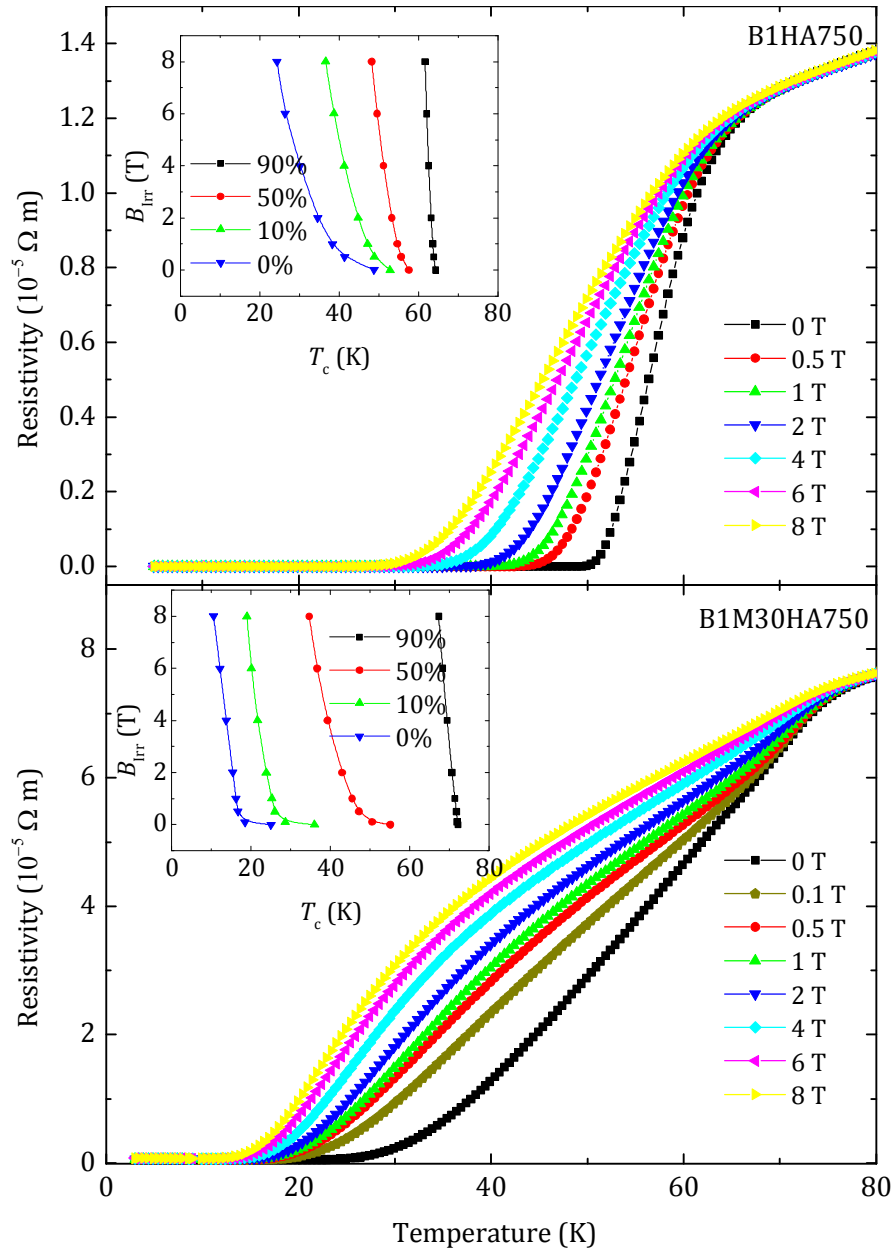
Figure 6.6: Upper panel: Resistivity of the B1HA750 sample measured in fields of 0 T – 8 T with a constant excitation current of 5 mA. Inset: B_{Irr} determined using the criteria of 90%, 50% and 10% of $\rho_N(0\,T, 70\,K)$, and onset of zero resistivity ($0\%\rho_N$). Lower panel: equivalent data for the B1M30HA750 sample.
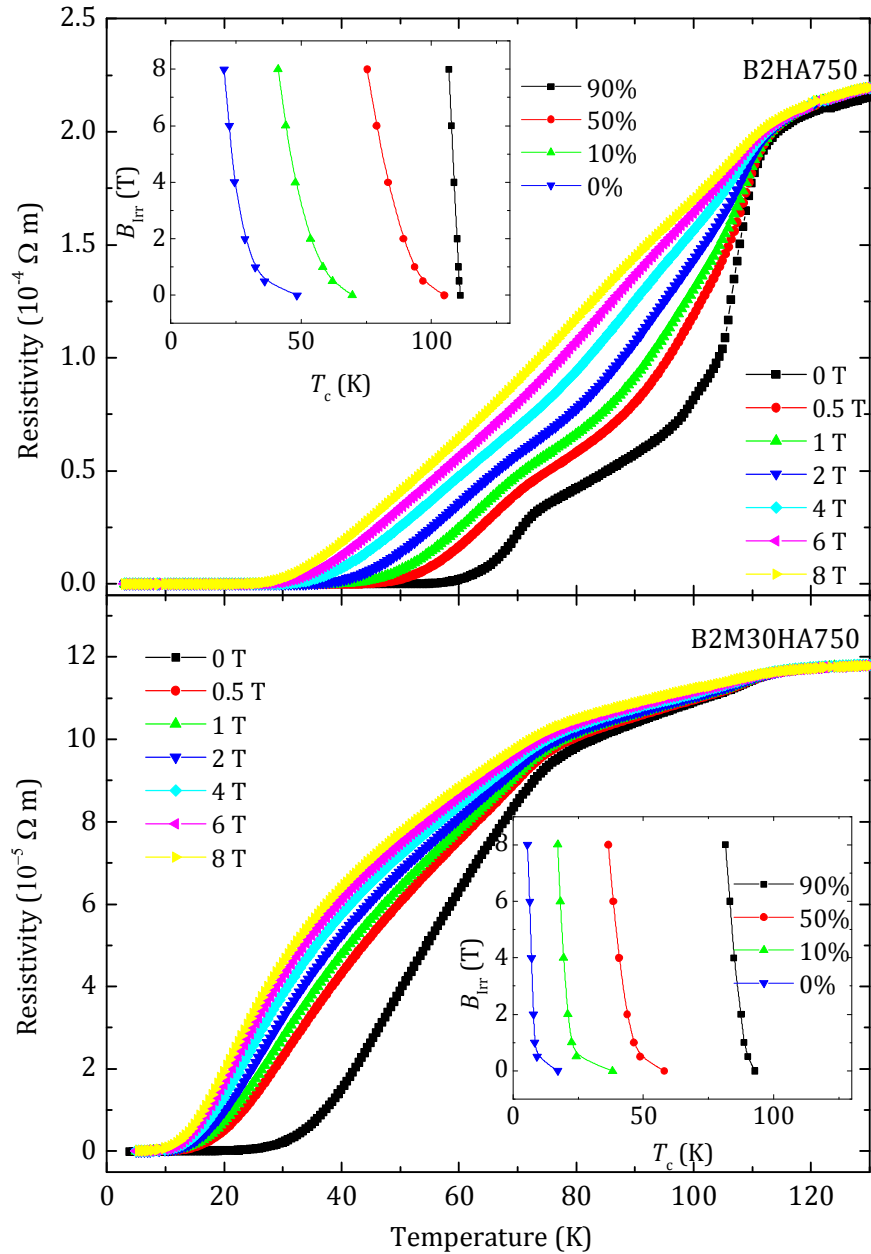
Figure 6.7: Upper panel: Resistivity of the B2HA750 sample measured in fields of 0 T –
8 T with a constant excitation current of 5 mA. Inset: B_{Irr} determined using the criteria
of 90%, 50% and 10% of $\rho_{\mathrm{N}}(0\ \mathrm{T}, 120\ \mathrm{K})$, and zero resistivity $(0\%\rho_{\mathrm{N}})$. Lower panel:
Equivalent data for the B2M30HA750 sample.

6.3.2 A.C. Magnetic Susceptibility

A.c. magnetic susceptibility measurements were taken using a Quantum Design PPMS system [171] as a function of field up to 8 T and temperature, with an excitation field of 0.4 mT operating at 777 Hz. The non-HIP'ed samples were pressed into pellets. HIP'ed samples were shaped into cuboids or bars using fine emery paper. A collation of all zero-field a.c. magnetic susceptibility for B1 samples is shown in Figure 6.8, where the onset transitions are shown in the main figure and the complete data sets are shown in the inset. We have also calculated T_c values by extrapolating the large signal data for which the magnitude of the susceptibility is typically a few percent of full screening and listed them in Table 6.3. The pressed sample and the B1HA750 sample were not of standard shape so we have set their susceptibility to be –1 at the lowest temperatures. The as-supplied material B1P and unmilled material B1HA750 contains significant $Bi_2Sr_2Ca_2Sr_3O_{10}$, as evidenced by their onset values close to 105 K. However, a large signal associated with the $Bi_2Sr_2CaSr_2O_8$ phase and bulk screening, leading to transmission of current across grain boundaries occurs below 75.2 K and 72.1 K respectively. The milling process almost completely removed all superconductivity. The milled, unannealed samples, B1M30P,

Figure 6.8: A.c. magnetisation and magnetic susceptibility of all B1 samples in zero field. The data were taken with an excitation field of 0.4 mT at a frequency of 777 Hz. Inset: Equivalent large signal data.

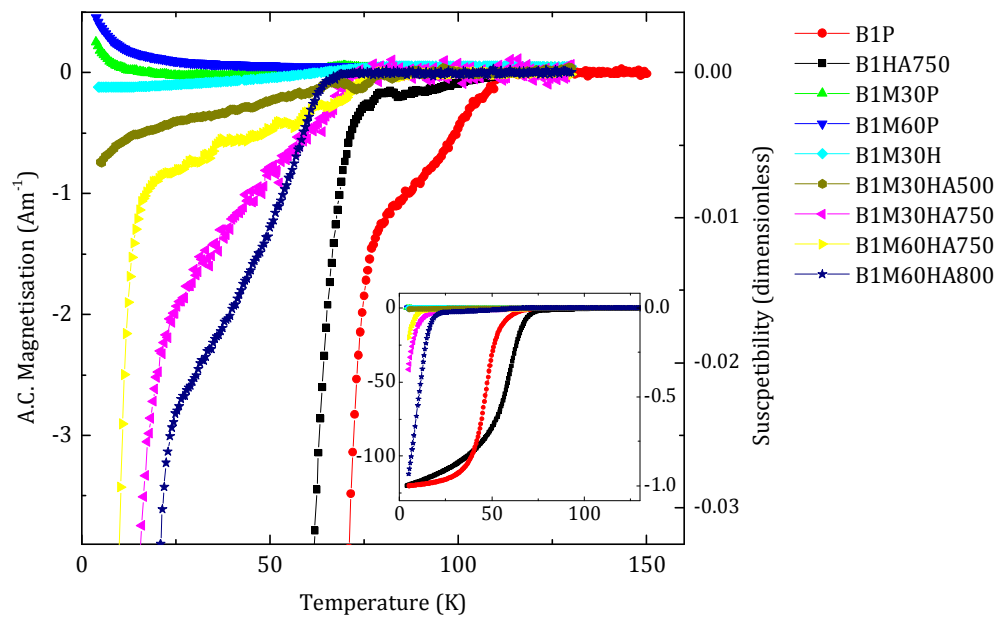| Sample	T_c (K) Onset/ Large signal	$B_{\mathrm{Irr}}(0)$ (T) Onset/ Large signal	χ'_g/χ'_b (0 T, 4.2 K)	$\mu_0\Delta M/\Delta B$ (−1.5 T) (±50%)	J_c^{m} (0 T, 4.2 K) (A m^{-2})	J_c^{t} (A m^{-2})	ρ_{N}(300 K) (Ω m^{-1}) (±50%)
B1P	105* 67.6	63(5) 49(9)	1	−0.1	1.6×10^{10}	-	-
B1HA750	105* 54.0	85(6) 79(6)	1	−0.2	1.5×10^{8}	7.8×10^{4} (4 T, 30 K)	3.2×10^{-5}
B1M30P	62.5 Para	- -	-	-	7.6×10^{8}	-	-
B1M60P	Para	-	-	-	1.8×10^{8}	-	-
B1M30H	70.1 -	- -	1.6×10^{-3}	-	7.6×10^{9}	-	-
B1M30HA500	76.4 -	75(9) -	6.2×10^{-3}	−6×10^{-4}	1.2×10^{10}	-	-
B1M30HA750	73.4 10.5	91(5) 34(8)†	0.34	−3×10^{-3}	2.8×10^{10}	7.2×10^{4} (0 T, 4.2 K)	1.1×10^{-4}
B1M60HA750	78.1 8.4	53(13) 48(10)†	0.17	−2×10^{-3}	1.4×10^{10}	-	-
B1M60HA800	64.5 16.7	61(4) 34(2)†	0.93	−5×10^{-3}	2.5×10^{10}	-	-
B2P	109.7 105.7	105(20) 95(16)	1	−0.4	5.1×10^{10}	-	-
B2HA750	107.3 107.1	57(5) 51(12)	0.97	−0.1	4.0×10^{10}	1.4×10^{4} (1 T, 30 K)	2.9×10^{-4}
B2M30P	106.9 Para	- -	-	-	2.7×10^{9}	-	-
B2M60P	Para	-	-	-	4.8×10^{8}	-	-
B2M30H	96.8 -	- -	1.8×10^{-3}	-	1.0×10^{10}	-	-
B2M30HA500	90.6 -	82(24) -	6.0×10^{-3}	−9×10^{-4}	1.9×10^{10}	-	-
B2M30HA750	85.2 13.5	50(4) 1.56†	0.30	−3×10^{-3}	4.0×10^{10}	9.1×10^{3} (0 T, 4.2 K)	1.2×10^{-4}
B2M60HA750	84.8 -	52(25) -	1.8×10^{-3}	−2×10^{-4}	4.8×10^{9}	-	-
B2M60HA800	61.9 58.9	54(3) 74(15)	0.95	−4×10^{-2}	2.3×10^{11}	-	-

Table 6.3: Summary of critical temperature (T_c), irreversibility field ($B_{\mathrm{Irr}}(0)$), magnetisation and transport critical current density (J_c^{m} and J_c^{t}) and room temperature normal state resistivity (ρ_{N}) of fabricated samples. "B1" and "B2" represent Bi-2212 and Bi-2223 respectively. Letters "P", "M", "H", and "A" stands for Pressed powders, Milled, HIP'ed and Annealed respectively. T_c was determined from the onset (typical ~10^{-4} of full screening) or large signal (typical ~10^{-2} of full screening) of ACMS data. The symbol * suggests that a minority phase denoted the onset. "Para" indicates a sample that behaved paramagnetically with no T_c found. $B_{\mathrm{Irr}}(0)$ was calculated using in-field susceptibility data and extrapolating to zero temperature using equation (6.2), whereas "$\dagger$" indicates a linear fit. χ'_g/χ'_b is the a.c. magnetic susceptibility data at 0 T and 4.2 K. $\mu_0\Delta M/\Delta B$ is from d.c. magnetisation hysteresis measurements. J_c^{m} is at 4.2 K, calculated using sample dimensions for B1HA750 and the grain size for all other samples. J_c^{t} used a 1 mVm^{-1} criterion.

B1M60P, B1M30H and the sample annealed at the lowest temperature, B1M30HA500, all showed similar behaviour – a weak or no diamagnetic signal generally followed by a paramagnetic temperature dependence, similar to that seen in Chapter 4 and in [109, 110, 249] for YBCO after milling. All the annealed samples show that superconductivity has been recovered with onset signals near 75 K associated with the grains. At lower temperatures eventually large signals occur as the grain boundaries support significant screening currents. Figure 6.9 shows the in-field susceptibility of the B1HA750 sample, and the equivalent data for the B1M30HA750 sample are shown in the inset. The B1HA750 sample shows an onset T_c at 70 K in zero field. At lower temperatures, the sample shows full-screening and most notably (as discussed in section 6.3.3), values of $\mu_0 \Delta M / \Delta B$ close to Bean values of –0.17, similar to a low temperature polycrystalline superconductor with well-connected grains or a single crystal superconductor. In contrast, the B1M30HA750 sample shows granular behaviour [172, 173, 249] and does not reach full screening. We have measured all the B1 samples in-field and used the onset and large signal data to produce irreversibility fields associated with each signal and provided them in Figure 6.10. The upper and lower panels show the onset and large signal B_{Irr} values respectively. In order to obtain estimates of $B_{\mathrm{Irr}}(0)$, the temperature dependence of the data were generally characterised using the equation [139]:

$$B_{\mathrm{Irr}}(T) = B_{\mathrm{Irr}}(0)(1 - t^{0.5})^{2.1}, \tag{6.2}$$

where $t = T/T_c$. Although for some large signal, nanocrystalline materials, a linear fit was used. Figure 6.10 shows that the irreversibility fields are high and similar to the upper critical field values along the c-axis for $Bi_2Sr_2CaCu_2O_8$ [84, 135]. Similar compilations for all the B2 samples are also provided. Figure 6.11 shows all zero-field a.c. magnetic susceptibility and Figure 6.12 shows the irreversibility fields. All onset and large signal values of T_c, and $B_{\mathrm{Irr}}(0)$ can be found in Table 6.3. The milled, unannealed materials were again either only weakly diamagnetic or paramagnetic. Annealing was required to recover superconductivity in these materials. Irreversibility fields were again high at low temperatures for some of these B2 materials [84]. Even though full screening is recovered in some samples, it is important to note that the full screening of a 0.4 mT signal is not indicative of well-connected grains with grain boundaries carrying high current densities.

The susceptibility data can be used to estimate whether the supercurrent screening path is inter- or intragranular. If the screening currents are entirely intragranular, the susceptibility is reduced by a factor χ'_g/χ'_b where [172, 173]:

$$\frac{\chi'_g}{\chi'_b} = \frac{1}{15}\left(\frac{a^2}{\lambda^2}\right)f(a,\xi_0) \quad \text{for} \quad \lambda > a, \tag{6.3}$$

where χ'_g and χ'_b are the granular and bulk (non-granular) susceptibilities respectively and a is the grain size as explained in section 4.3.2. If we use the values $a = 200$ nm from Table 6.2, and $\langle 1/\lambda^2 \rangle$ calculated using the data in Table 6.1, we find $\chi'_g/\chi'_b = 1.5 \times 10^{-2}$ and 5.0×10^{-2} for B1 and B2 respectively, with an uncertainty of $\pm 100\%$. The values of χ'_g/χ'_b for all samples can be found in Table 6.3. The calculated values are similar to the measured χ'_g/χ'_b for the samples where the grains are not well-connected. For those samples where $\chi'_g/\chi'_b \approx -1$, we find

$$\frac{\chi'_g}{\chi'_b} = 1 - \frac{3\lambda}{a} \quad \text{for} \quad \lambda < a. \tag{6.4}$$

This gives path size $a \approx 2$ μm and 1 μm for B1M30HA750 and B2M30HA750, suggesting that these very small screening currents are not strictly confined within grains of 200 nm, and may flow around clusters of grains.
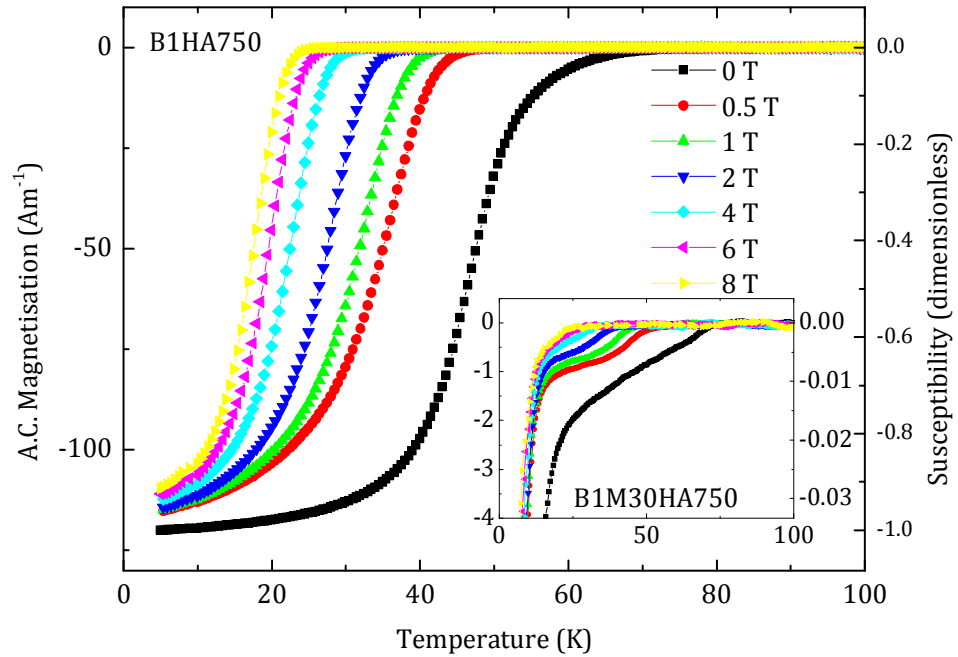
Figure 6.9: A.c. magnetic susceptibility as a function of temperature of the B1HA750 sample. The data were taken with an excitation field of 0.4 mT and at a frequency of 777 Hz. Inset: Equivalent data for the B1M30HA750 sample.
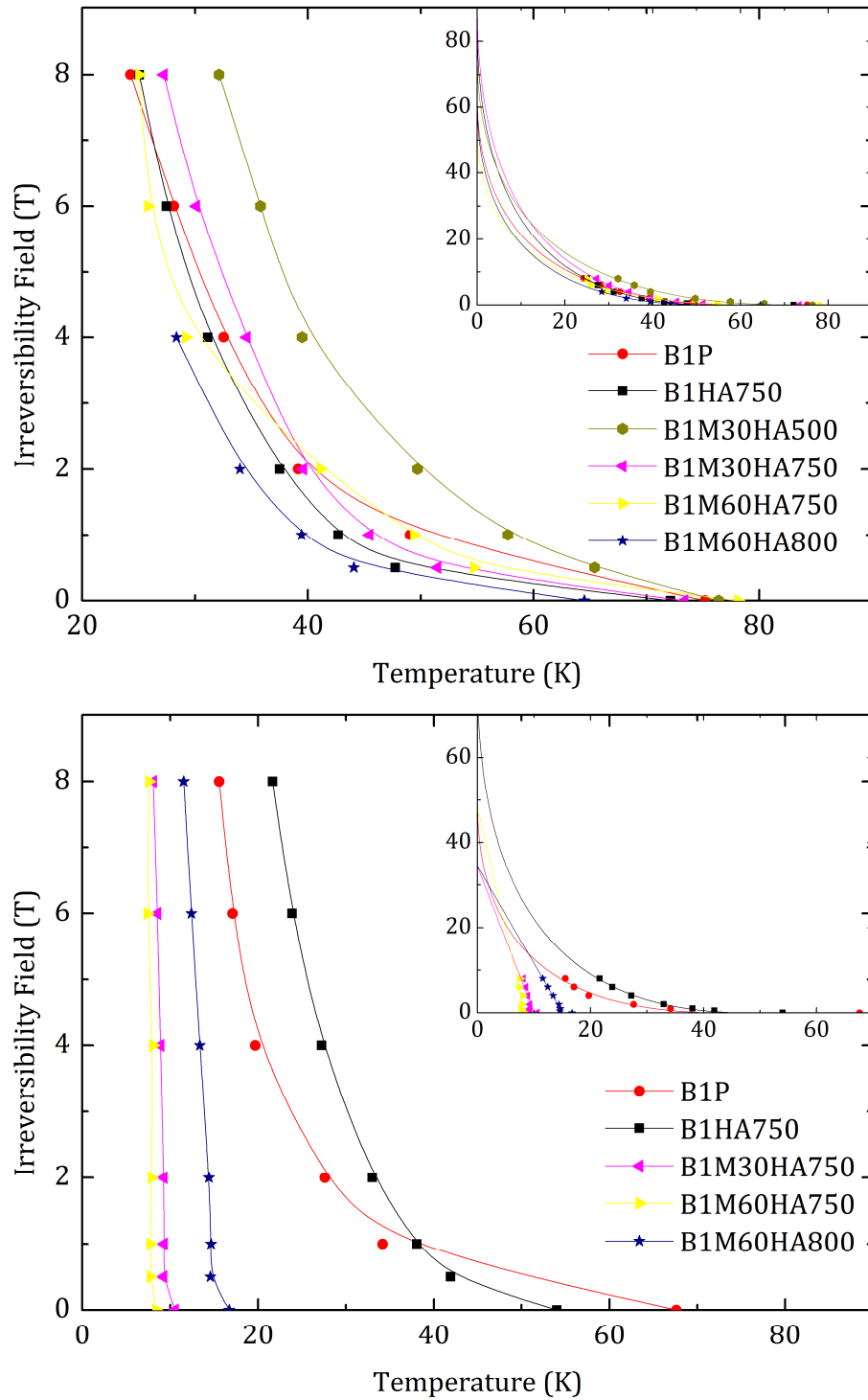
Figure 6.10: Irreversibility field as a function of temperature of all B1 samples. Upper panel: Onset B_{Irr}. Lower panel: Large signal B_{Irr} – obtained by extrapolating the large signal data for which the magnitude of the susceptibility is typically a few percent to zero signal. The data were fitted using equation (6.2) or linear fits to obtain values for $B_{\mathrm{Irr}}(0)$ as listed in Table 6.3. Insets show the fitted curves over the full temperature range.
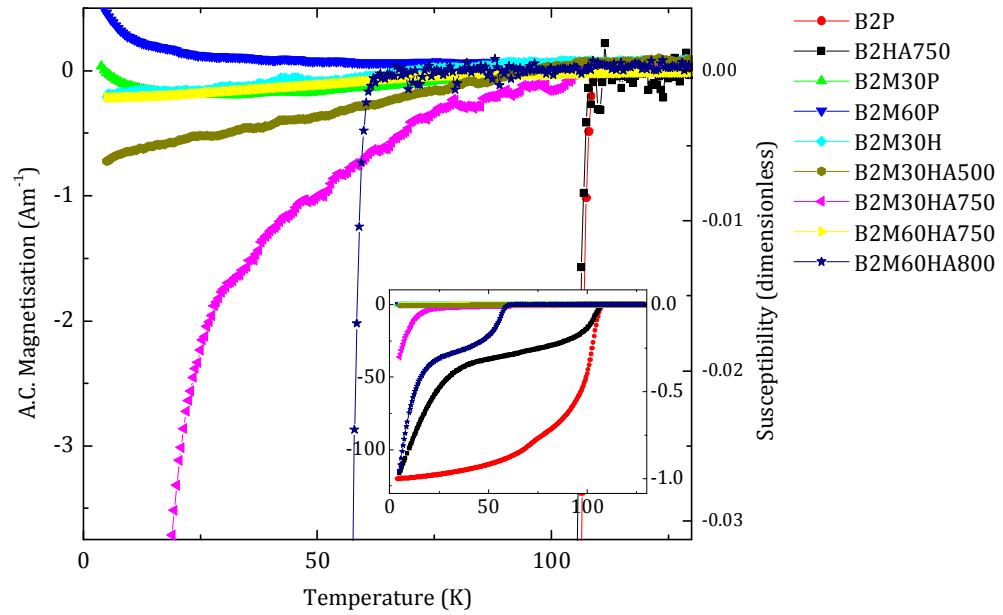
Figure 6.11: A.c. magnetisation and magnetic susceptibility of all B2 samples in zero field. The data were taken with an excitation field of 0.4 mT at a frequency of 777 Hz. Inset: Equivalent large signal data.
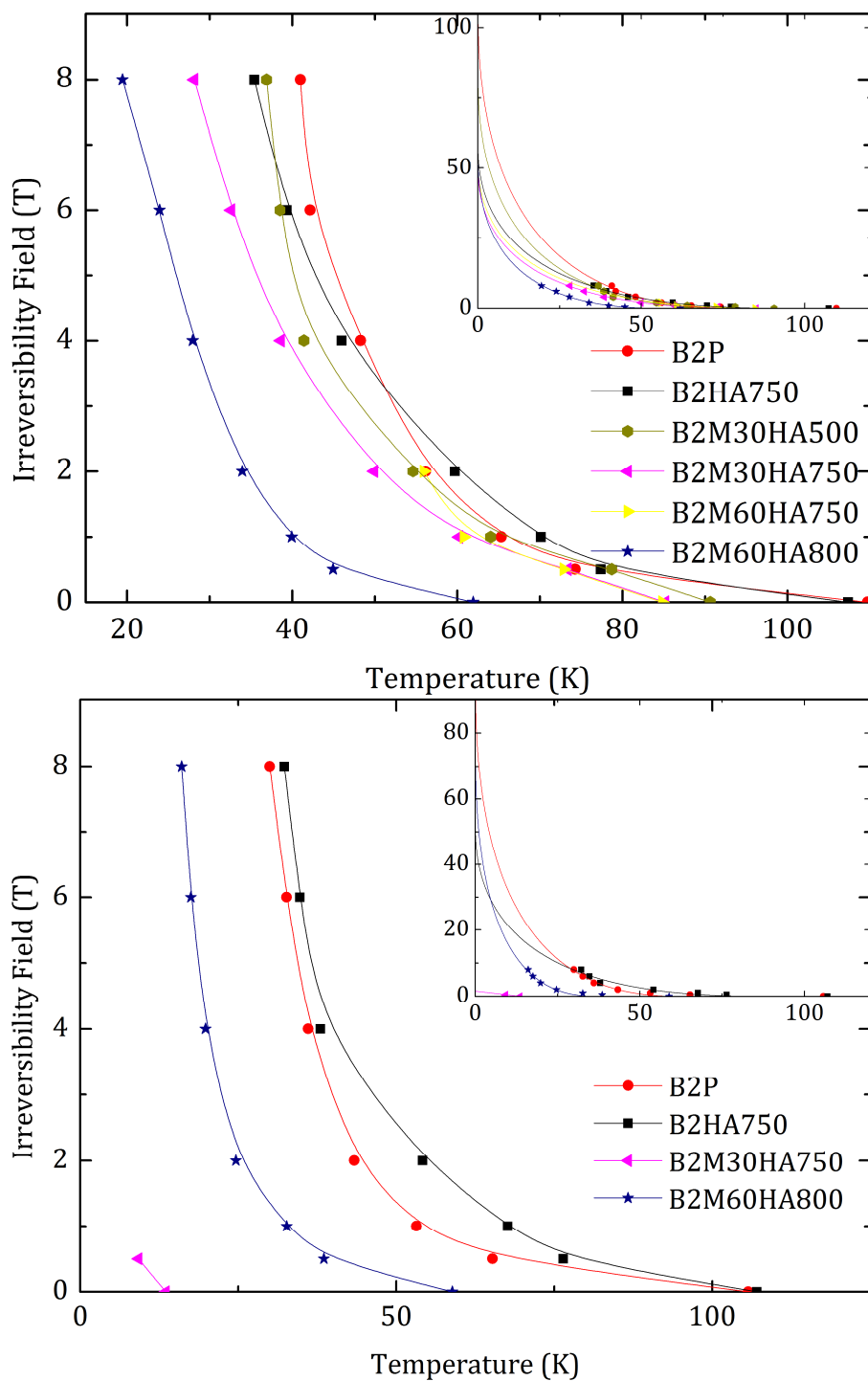
Figure 6.12: Irreversibility as a function of temperature of all B2 samples. Upper panel: Onset B_{Irr}. Lower panel: Large signal B_{Irr} – obtained by extrapolating the large signal data for which the magnitude of the susceptibility is typically a few percent to zero signal. The data were fitted using equation (6.2) or linear fits to obtain values for $B_{\mathrm{Irr}}(0)$ as listed in Table 6.3. Insets show the fitted curves over the full temperature range.

6.3.3 D.C. Magnetic Hysteresis

D.c. magnetisation hysteresis data were also taken with the PPMS. At each temperature, the field was swept from 0 T down to –1.5 T, then up to 8 T and back to –1.5 T. J_c values were calculated from these hysteresis data between 0 T and 8 T using standard Bean's model [29], i.e. for pellets of radius R and volume V [177],

$$J_c = 3\frac{\Delta m}{RV},\qquad(6.5)$$

where Δm is the difference in magnetic moment between the increasing and decreasing field branches. For cuboid bars with length w and width b [177],

$$J_c = \frac{2\Delta m}{w\left(1-\frac{w}{3b}\right)V}.\qquad(6.6)$$

Figure 6.13 and Figure 6.14 shows the hysteresis loops for B1HA750 and B1M30HA750 respectively. The microcrystalline B1HA750 sample shows textbook Type II behaviour for a polycrystalline sample with bulk pinning and well-connected grains. On the other hand, the nanocrystalline B1M30HA750 sample shows a strong asymmetry about the baseline,

Figure 6.13: Magnetisation as a function of field the B1HA750 sample between –1.5 and 8 T at temperatures from 4 and 90 K. The data at –1.5 T have a gradient $\mu_0\Delta M/\Delta B$ of –0.2.

with a large diamagnetic signal on increasing field and almost no signal on decreasing field. This behaviour has been reported in the literature and is associated with surface currents [268]. These asymmetric hysteresis loops were observed in all milled, HIP'ed and annealed materials. Figure 6.15 shows a compilation of the magnetisation J_c at 4.2 K for all the B1 samples and compares them with state-of-the-art Bi-2212 OP wires. The values shown for almost all the samples are intragranular values calculated using the grain size. The high intragranular values are in many cases higher than state-of the-art transport J_c in Bi-2212 OP wires. The only exception is the B1HA750 sample, where as we find in the next section, the magnetic signal is almost entirely due to intergranular currents flowing on the length scale of the sample, so we have used the sample dimensions to calculate J_c as shown in Figure 6.15. However the intergranular J_c values are still 2 orders of magnitude below Bi-2212 OP wires. Figure 6.16 shows the magnetisation J_c of B1HA750 and B1M30HA750, and compares them to the transport J_c and is discussed in section 6.3.4.

Figure 6.14: Magnetisation as a function of field the B1M30HA750 sample between −1.5 and 8 T at temperatures from 4 and 90 K. The data at −1.5 T have a gradient $\mu_0 \Delta M/\Delta B$ of -3×10^{-3}.

Figure 6.15: Magnetisation J_c as a function of field for fabricated B1 samples at 4.2 K. Grain dimensions were used to calculate magnetisation J_c, except for B1HA750, where sample dimension was used. Transport J_c of the OST NHMFL 100 bar OP sample [84] is also included for comparison. Fluctuation in the data is representative of the uncertainty.
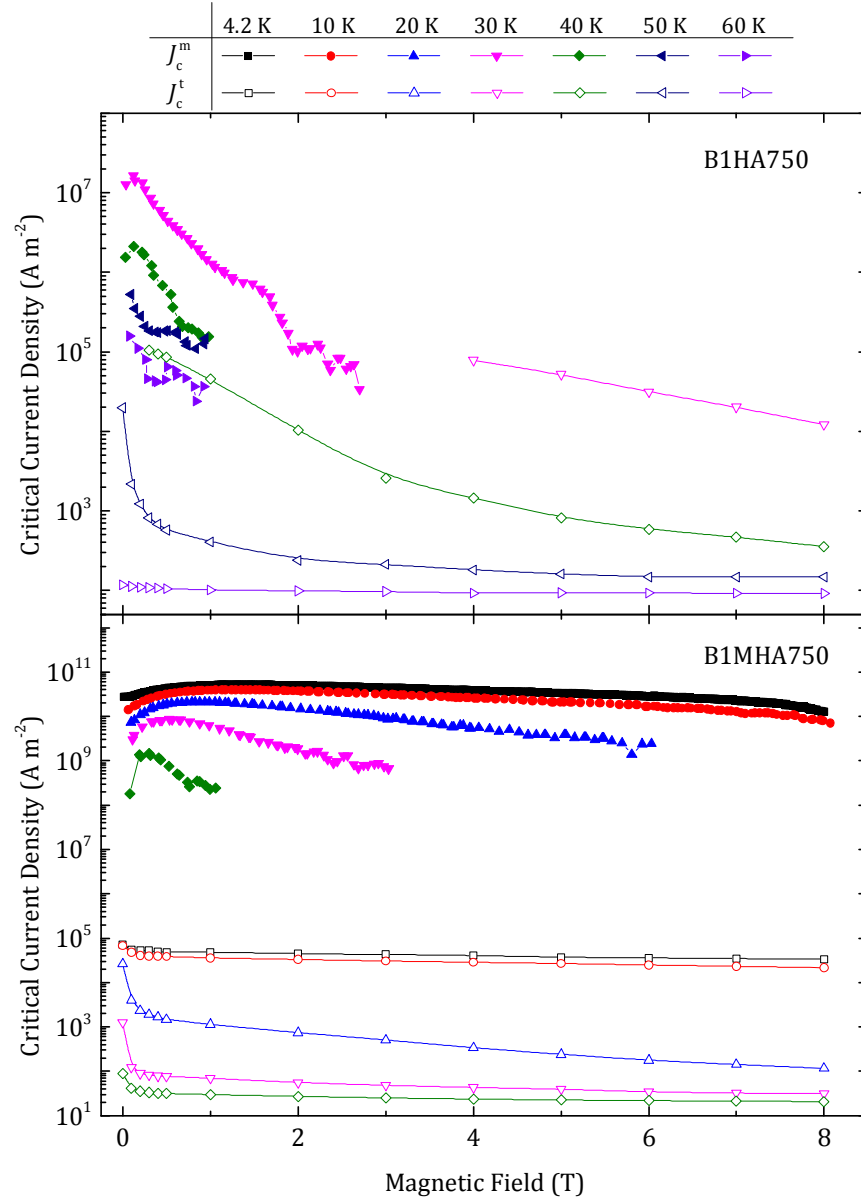
Figure 6.16: Transport J_c^t (open) and magnetisation J_c^m (closed) for B1 samples: Upper panel: B1HA750. At 30 K, the transport and magnetisation J_c are very similar. Lower panel: B1M30HA750. Fluctuation in the data is representative of the uncertainty.

Figure 6.17 and Figure 6.18 shows the hysteresis loops for B2HA750 and B2M30HA750 respectively. Similar to B1, the microcrystalline samples shows textbook, symmetric Type II loops, while the nanocrystalline sample has asymmetric loops, except at 4.2 K, where it is symmetric. Figure 6.19 compares the magnetisation J_c of all B2 samples with commercial Bi-2223 tape, where the grain size was used to calculate the intragranular J_c for all samples. Figure 6.20 shows the magnetisation J_c of B2HA750 and B2M30HA750, and compares them to their transport J_c.
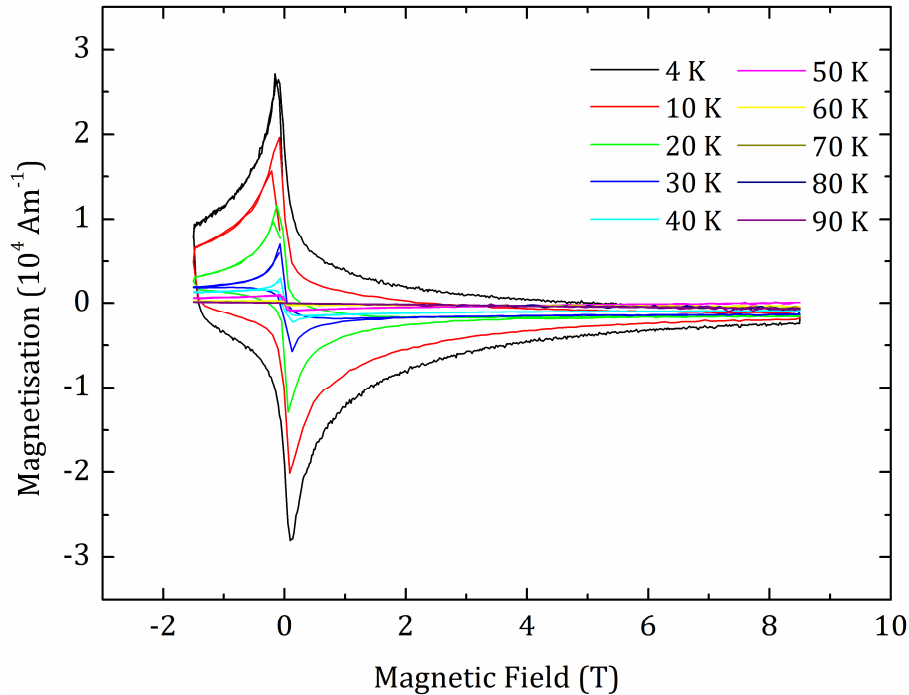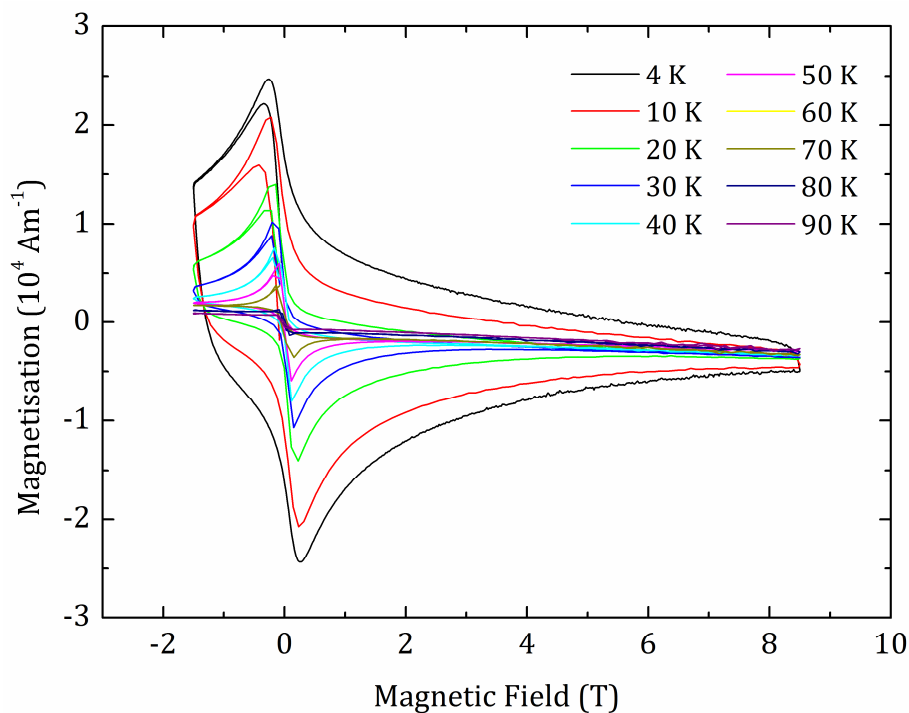
Figure 6.17: Magnetisation as a function of field for the B2HA750 sample between –1.5 and 8 T at temperatures from 4 and 90 K. The data at –1.5 T have a gradient $\mu_0 \Delta M/\Delta B$ of –0.1.
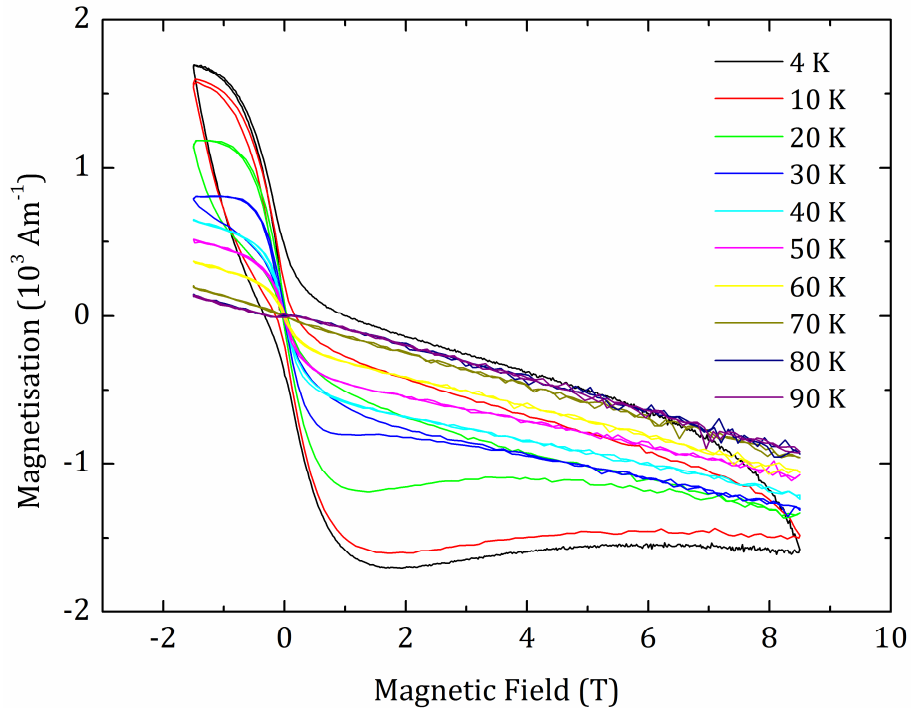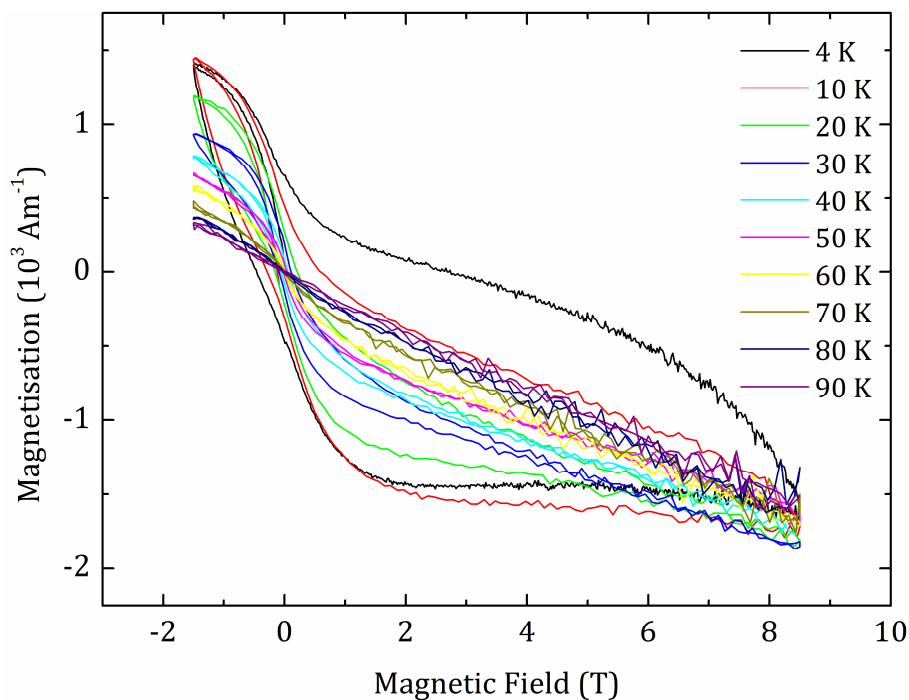

Figure 6.18: Magnetisation as a function of field for the B2M30HA750 sample between –1.5 and 8 T at temperatures from 4 and 90 K. The data at –1.5 T have a gradient $\mu_0 \Delta M/\Delta B$ of -3×10^{-3}.

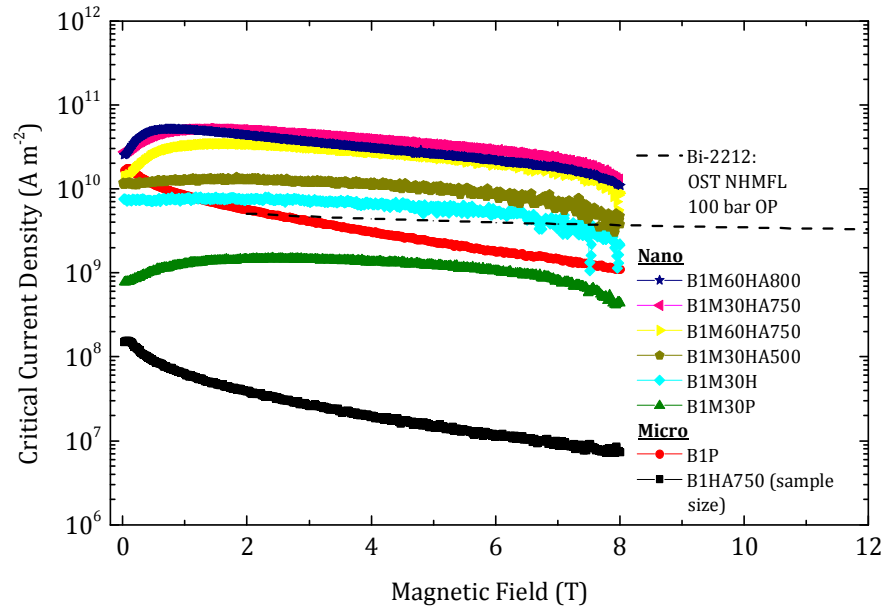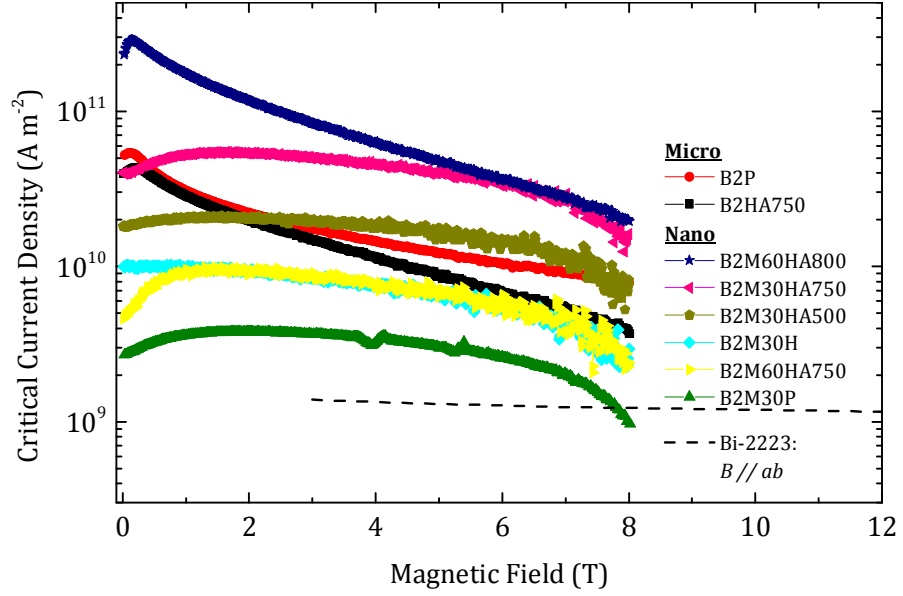Figure 6.19: Magnetisation J_c as a function of field for fabricated B2 samples at 4.2 K. Grain size was used in these calculations. Transport J_c of Bi-2223 tape with field applied along the ab-plane is also included for comparison [84]. Fluctuation in the data is representative of the uncertainty.

The sequence we have chosen for field sweeping ensured we can also extract values of $\mu_0 \Delta M / \Delta B$ at –1.5 T and are listed for all our samples in Table 6.3. Using Bean's relation for a cylinder $\Delta B = 2\mu_0 J_c R$ where ΔB is the field required to reverse the magnetisation and equation (6.5) gives [180]:

$$\frac{\mu_0 \Delta M}{\Delta B} = -\frac{\frac{1}{3} J_c R}{2 J_c R} = -0.17. \tag{6.7}$$

Microcrystalline samples have $\mu_0 \Delta M / \Delta B$ values similar to –0.17, which indicates that the pinning mechanism is Bean-like. However the pressed samples remind us that this does not guarantee good connectivity between the grains. The values in nanocrystalline materials of the order $10^{-4} - 10^{-3}$. Such decrease of $\mu_0 \Delta M / \Delta B$ has been reported in other small grained materials [56]. These values are outside the scope of Bean's model and can be indicative of surface pinning in the grains [268], consistent with the asymmetry of the hysteresis loops.
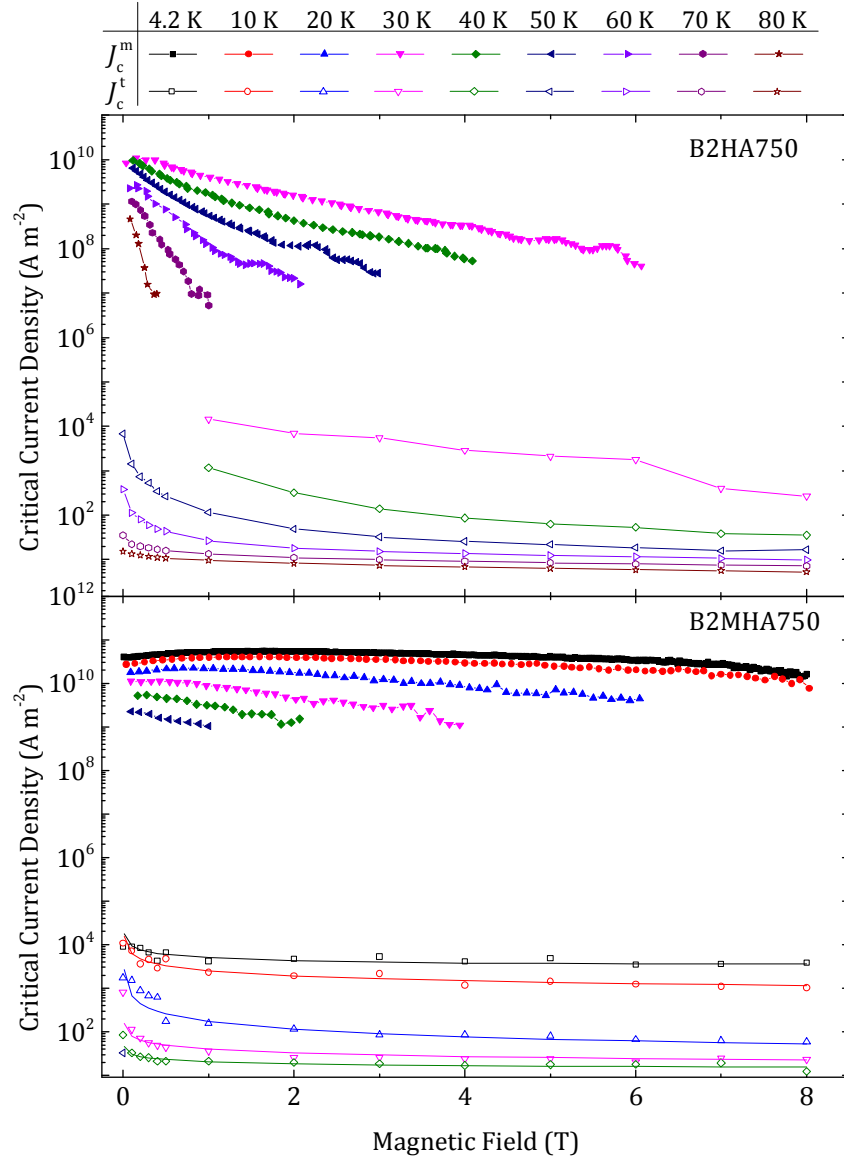
Figure 6.20: Transport J_c^t (open) and magnetisation J_c^m (closed) for B2 samples. Upper panel: B2HA750. Lower panel: B2M30HA750. Fluctuation in the data is representative of the uncertainty.

6.3.4 Transport Critical Current Density Measurements

After the resistivity measurements were completed in the PPMS, the PPMS circuitry was replaced with an external current supply and a multimeter for high precision four-terminal $V - I$ measurements in the same way as described in Chapter 4. The current was supplied by a Keithley 220 programmable current source. A resistor was added in series to the sample in order to confirm that the current through the sample was equal to the nominal output current in the range of 10 nA to 0.1 A. The voltage across the sample taps were

measured with a Keithley 2100 6½ digit multimeter. An additional $\times$ 50,000 amplifier [169] was also used when required to measure extremely small voltages.

$V - I$ traces of the B1HA750, B1M30HA750, B2HA750 and B2M30HA750 samples were measured. For the microcrystalline samples, data are only available above 30 K, as the high currents required at low temperatures were above the limit of the current supply. Figure 6.21 shows the $V - I$ traces for the B1M30HA750 sample. The red dashed line show the 1 mVm^{-1} criterion used to define J_c^t. The values of J_c^t obtained are given in the lower panel of Figure 6.16. The equivalent transport J_c^t data for B1HA750, B2HA750 and B2M30HA750 are given in the upper panel of Figure 6.16 and also in the two panels of Figure 6.20. We note that there is a large decrease in the transport J_c^t for the B1M30HA750 and B2M30HA750 samples, when temperature is increased from 10 K to 20 K that is discussed in section 6.5. Most importantly the transport J_c^t in B1HA750 is typically two orders of magnitude higher than any of our other samples and in fact at 30 K is similar to the magnetisation J_c^m. For all other materials, the magnetisation J_c^m is several orders of magnitude larger than transport J_c^t and this difference remains at least two orders of magnitude whether we use the grain dimensions or sample dimensions to calculate J_c^m, i.e. the transport current contribution to the magnetisation is less than 1%.
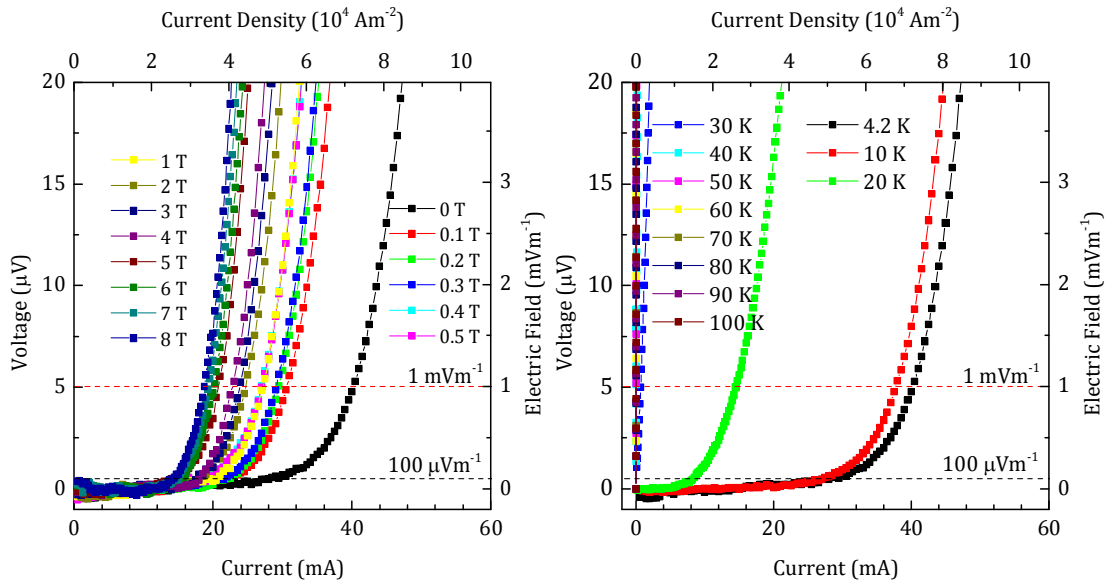
Figure 6.21: Left: Voltage as a function of current for the B1M30HA750 sample at 4.2 K. The dashed lines show the field criteria of 1 mVm^{-1} and 100 μVm^{-1}. Right: Voltage as a function of current at different temperatures in zero field.

6.4 Theoretical Considerations

6.4.1 The Resistivity of the Grain Boundaries

In this section, we present a method to calculate the grain boundary resistivity using polycrystalline bulk resistivity data, and single crystal resistivity as shown in Figure 6.5. In Table 6.4, we have listed the single crystal resistivity values of $Bi_2Sr_2CaCu_2O_8$ and $Bi_2Sr_2Ca_2Cu_3O_{10}$. Because of the very large $\rho_c/\rho_{ab} > 10^4$ [51, 265] and the evidence that these materials are strongly layered [247, 269], we have chosen to set aside the anisotropic mass description for the angular dependence of resistivity and consider these Bi-based materials as consisting of highly conductive ab-layers separated by highly resistive layers. This leads to an angular dependence for the resistivity given by [270]

$$\rho_N(\theta) = \frac{\rho_{ab}\rho_c}{\rho_{ab}\cos^2\theta + \rho_c\sin^2\theta} \, , \tag{6.8}$$

where θ is the angle between transport current and the c-axis direction. This equation was developed by Nagata and Nakajima [270] because in two dimensional layered materials, the angular averaged resistivity in polycrystalline materials tends to be similar to the resistivity along the ab-plane, a result which cannot be explained by the anisotropic mass model. Assuming perfectly transparent grain boundaries, the theoretical angular averaged resistivity due to collection of randomly oriented grains is then given by [270]

$$\langle\rho_N\rangle = \frac{1}{2}\int_0^\pi \rho_N(\theta)\sin\theta \, d\theta = \frac{\rho_{ab}\rho_c}{\sqrt{1-\frac{\rho_{ab}}{\rho_c}}}\ln\sqrt{\frac{\rho_c}{\rho_{ab}}}\left(1+\sqrt{1-\frac{\rho_{ab}}{\rho_c}}\right). \tag{6.9}$$

The angular averaged resistivity of the grains has been calculated using the temperature dependence of the single crystal data and is shown in Figure 6.5. We note that had we used the anisotropic mass model, the resistivity of all B1 and B2 samples would be several orders of magnitudes below $\langle\rho_N\rangle$, which is unphysical. The grain boundary resistivity was then calculated by subtracting $\langle\rho_N\rangle$ from the measured resistivity to obtain the contribution to the total resistivity from grain boundaries only ($\Delta\rho$). This contribution is then multiplied by the ratio of grain size (5 μm for micro-, 200 nm for nanocrystalline samples) to grain boundary thickness to obtain an estimate of the local resistivity of each grain boundary. Equally, we can calculate the contact (areal) resistivity by multiplying

Material	ρ_{N} (T_{c}) $(\pm 50\%)$ $(\Omega\,\mathrm{m})$	$\xi_{\mathrm{SPippard}}(0)$ $\xi_{B_{c2}}(0)$ (nm)	$\xi_{\mathrm{N}}(4.2\ \mathrm{K})$ $(\pm 25\%)$ (nm)	$\dfrac{J_{\mathrm{DN}}(4.2\ \mathrm{K})}{\langle J_{\mathrm{DSc}}(4.2\ \mathrm{K})\rangle}$
$Bi_2Sr_2CaCu_2O_8$ (ab-plane)	3.58×10^{-6}	2.1 1.2	14	0.21
$Bi_2Sr_2CaCu_2O_8$ (c-axis)	2.90×10^{-1}	0.010 0.0042	0.049	$\sim 10^{-19}$
$Bi_2Sr_2CaCu_2O_8$ (A.A.)	2.37×10^{-5}	0.98 0.79	5.4	0.23
B1HA750	1.55×10^{-5}	1.5 0.79	6.7	0.22
B1M30HA750	9.72×10^{-3}	1.43 0.79	0.27	10^{-5}
$Bi_2Sr_2Ca_2Cu_3O_{10}$ (ab-plane)	1.22×10^{-6}	0.86 1.1	21	0.15
$Bi_2Sr_2Ca_2Cu_3O_{10}$ (c-axis)	6.26×10^{-2}	0.017 0.0047	0.091	$\sim 10^{-11}$
$Bi_2Sr_2Ca_2Cu_3O_{10}$ (A.A.)	7.45×10^{-6}	0.66 0.70	8.3	0.19
B2HA750	1.01	0.66 0.70	0.023	$\sim 10^{-42}$
B2M30HA750	1.65×10^{-2}	0.66 0.70	0.18	$\sim 10^{-7}$

Table 6.4: The parameters required to calculate the ratio of the local depairing current density across a grain boundary ($J_{\mathrm{DN}}(4.2\ \mathrm{K})$) to the angular average (A.A.) of depairing current density of the superconducting grains $\langle J_{\mathrm{DSc}}(4.2\ \mathrm{K})\rangle$ using equation (6.10). The resistivity of the normal layer at T_{c} (ρ_{N}), the Sommerfeld constant (γ) and the Fermi velocity (v_{F}) have been used to calculate the Pippard coherence length (ξ_{SPippard}), and the decay length of the order parameter in the grain boundary (ξ_{N}) [249]. For Bi-2212 we have used $\gamma = 25.2\ \mathrm{Jm^{-3}K^{-2}}$ [271] and $v_{\mathrm{F}} = 4.50 \times 10^5\ \mathrm{ms^{-1}}$ [174] and for Bi-2223, we have used $\gamma = 33.8\ \mathrm{Jm^{-3}K^{-2}}$ [272] and $v_{\mathrm{F}} = 0.96 \times 10^5\ \mathrm{ms^{-1}}$ [273]. The $\xi_{B_{c2}}(0)$ coherence length has been calculated using $B_{c2}(0)$ from Table 6.1 where ($\xi_{B_{c2}}(0) = (\Phi_0/2\pi B_{c2}(0))^{\frac{1}{2}}$).

$\Delta\rho$ by the grain size. In this work, we have assumed grain boundary thicknesses are 1 nm to enable comparisons between areal and bulk resistivity values.

For B1HA750, $J_{\mathrm{c}}^{\mathrm{m}} = J_{\mathrm{c}}^{\mathrm{t}}$ as shown in Figure 6.16, and $\langle\rho_{\mathrm{N}}\rangle$ is similar to the measured resistivity. Thus our most striking result is that for the B1HA750 sample alone, the grain boundaries have a similar resistivity to the grains: $\rho_{\mathrm{GB}} = \rho_{\mathrm{S}} = 1.55 \times 10^{-5}\ \Omega\mathrm{m}$. Such low ρ_{GB} may be due texturing, as suggested by XRD data. For B1M30HA750, the grain boundary resistivity $\rho_{\mathrm{GB}} = 9.71 \times 10^{-3}\ \Omega\mathrm{m}$ with an uncertainty of $\pm 50\%$. These values are almost a thousand times larger than microcrystalline values, but are nevertheless

similar to Mayer's [274] grain boundary values of $(2.0 - 6.5) \times 10^{-3}$ Ωm on Bi-2212 bicrystals. For the B2 samples, the grain boundary resistivity in all our samples are large. For B2HA750, $\rho_{\mathrm{GB}} = 1.01$ Ωm, which is nearly 10^5 times large than equivalent numbers for B1HA750 and much higher than the bicrystal values of $(3.6 - 4.0) \times 10^{-3}$ Ωm, reported by Frey *et al.* [275] and Ohbayashi *et al.* [276]. B2M30HA750 has $\rho_{\mathrm{GB}} = 1.65 \times 10^{-2}$ Ωm, which is 10^2 times lower than microcrystalline B2HA750. Given the XRD, DSC and resistivity data for B2HA750, we attribute the value to some second phase $Bi_2Sr_2CaCu_2O_8$ appearing in the grain boundaries. The grain boundary resistivity values can be found in Table 6.4.

6.4.2 Depairing Current Density of the Grain Boundaries

In this section we follow the approach we used for YBCO in Chapter 4 to calculate the local depairing current density across a normal (i.e. non-superconducting) grain boundary (J_{DN}). If the transport current through a grain boundary is modelled as a 1D S-N-S junction, the analytic solution to the Ginzburg-Landau equations in zero field is given by [119]:

$$
\begin{aligned}
J_{\mathrm{DN}}(T) \approx J_{\mathrm{DSc}}(T)\sqrt{2}\frac{\rho_{\mathrm{S}}\xi_{\mathrm{S}}}{\rho_{\mathrm{N}}\xi_{\mathrm{N}}} \\
\times \left\{ \sqrt{\left(\frac{\xi_{\mathrm{S}}\rho_{\mathrm{S}}}{\xi_{\mathrm{N}}\rho_{\mathrm{N}}\sqrt{2}}\right)^2 + 1} - \frac{\xi_{\mathrm{S}}\rho_{\mathrm{S}}}{\xi_{\mathrm{N}}\rho_{\mathrm{N}}\sqrt{2}} \right\}^2 \exp\left(\frac{-2d}{\xi_{\mathrm{N}}}\right),
\end{aligned} \tag{6.10}
$$

where $J_{\mathrm{DSc}}(T)$ is the depairing current density in the superconducting grain, $\rho_{\mathrm{S}}/\rho_{\mathrm{N}}$ is the ratio of the resistivity in the grain to the grain boundary, $\xi_{\mathrm{S}}/\xi_{\mathrm{N}}$ is the ratio of the G-L coherence length in the superconductor to the decay length of the order parameter across the grain boundary, and d is the thickness of the grain boundary. In order to simplify the calculations, we have assumed the grain boundary T_{c} to be 0 K. We can expect this to break down in the case of very low-angle grain boundaries where the grain boundaries themselves may be considered as strained superconductors. We have also made the simplifying assumptions that we can use angular averages for each of the parameters, ignore the complexity associated with grains with different critical properties (with respect to the direction of current flow) on either side of a given grain boundary and ignore percolation.

In Table 6.4, we calculated $J_{DN}(T)$ at 4.2 K for both $Bi_2Sr_2CaCu_2O_8$ and $Bi_2Sr_2Ca_2Cu_3O_{10}$, along the ab-plane, and in the c-axis direction. All angular averaged values of $J_{DN}(T)$ in Table 6.4 were calculated using relevant resistivity values in equation (6.10). For the ab-plane and c-axis data, the grains and the grain boundaries were assumed to have the same resistivity, $\rho_N = \rho_S$, where ρ_S is simply the single crystal resistivity values from the literature. The resistivity of an angular averaged sample (A.A.) is calculated from the single crystal values. For the HA750 samples and the M30HA750 samples, we have assumed the resistivity of the grains is that calculated for the A.A. sample. The values of $\rho_N(T_c)$, the resistivity of the normal layer at T_c for each material considered, used in equation (6.10) are listed in Table 6.4. The superconductor layer coherence length ξ_S used in equation (6.10) was calculated at 4.2 K, following the approach used in Table 6.1 as shown in the Appendix. $\xi_{SPippard}(0)$ is the Pippard coherence length calculated from the Fermi velocity (v_F), resistivity (ρ_S), and the Sommerfeld constant (γ). $\xi_{B_{c2}}(0)$ is the superconductor coherence length calculated from $B_{c2}(0)$ as indicated in Table 6.4. We have produced the different angular averaged coherence lengths, $\xi_{SPippard}(0)$ and $\xi_{B_{c2}}(0)$ so we could check that they are similar values and hence have confidence that the microscopic values used to calculate $\xi_N(4.2$ K$)$ [119, 249] and J_{DN} are reasonable.

Table 6.4 shows for both $Bi_2Sr_2CaCu_2O_8$ and $Bi_2Sr_2Ca_2Cu_3O_{10}$, the single crystal samples along the ab-plane have $J_{DN}/\langle J_{DSc}\rangle$ values of near 0.2, whereas $J_{DN}/\langle J_{DSc}\rangle$ in the c-axis direction is more than 10 orders of magnitude smaller. The angular averaged $J_{DN}/\langle J_{DSc}\rangle$ are on the order of 0.2 consistent with most current transport occurring along the ab-plane. The values quoted in Table 6.4 that were derived using angular averages have uncertainties larger than $\pm 50\%$, associated with the simplifications we have made. Given the high resistivity anisotropy, it is reasonable to assume that $J_{DN}/\langle J_{DSc}\rangle$ of the theoretical angular average material is similar to that along the ab-plane. One of the important result in this work is that the B1HA750 sample has a low grain boundary resistivity and a value for $J_{DN}/\langle J_{DSc}\rangle \approx 0.22$, similar to the A.A. sample. The B1M30HA750, B2HA750 and B2M30HA750 samples have grain boundary resistivities that are so high that ξ_N decreases to below the thickness of the grain boundaries (i.e. $d = 1$ nm), the exponential term in

equation (6.10) dominates and $J_{\mathrm{DN}}/\langle J_{\mathrm{DSc}}\rangle$ is severely suppressed to the very small values shown in Table 6.4.

6.5   Discussion

DSC data show that both B1 and B2 samples, micro- or nanocrystalline, consist mainly of their nominal $\mathrm{Bi_2Sr_2CaCu_2O_8}$ or $\mathrm{Bi_2Sr_2Ca_2Cu_3O_{10}}$ phases. However XRD data show that significant secondary phase signals appear in XRD after a combination of milling, HIP and annealing. These latter processes were unavoidable in order to restore superconductivity to the nanocrystalline samples. We note that XRD measurements produce large peaks for ordered crystalline material and is much less sensitive to detecting amorphous or nanocrystalline phases. Hence, consistent with the lower magnitude of the signals observed for the nanocrystalline samples, the XRD data preferentially identifies ordered second phase material. In contrast, the DSC data which shows largely Bi-based superconducting phases and relatively small amounts of second phase material, is volumetric.

We have used complementary transport and magnetic measurements to distinguish intergranular currents from intragranular, and infer the properties of the grain boundaries. For B1HA750, the resistivity of the grain boundaries are low. Such low grain boundary resistivity may be due to texturing in the sample, as suggested by XRD data. The transport and magnetisation in this sample are similar, $J_{\mathrm{c}}^{\mathrm{t}}$ is 7.8×10^4 $\mathrm{Am^{-2}}$ at 4 T and 30 K, and we observed a Bean-like value for $\mu_0\Delta M/\Delta B\approx-0.2$. These results are typical of a well-connected LTS material. Nevertheless $J_{\mathrm{c}}^{\mathrm{t}}$ is about two orders of magnitude lower than J_{DN}. We note that in samples with well-connected grains, one can expect the surface pinning in the grains to be reduced. We interpret our data and theoretical considerations, as evidence that this sample has well-connected grains that could carry critical current densities up to 20 % of J_{DSc} but that weak pinning is the limiting factor for the suppression of J_{c}. Like LTS materials, the low $J_{\mathrm{c}}^{\mathrm{t}}$ values are consistent with large grains [142, 143] but unlike LTS, we have found in nanocrystalline materials that reducing the grain size decreased $J_{\mathrm{c}}^{\mathrm{t}}$ because the grains become highly resistive. Increasing grain boundary pinning by adding

artificial pinning sites or perhaps irradiation may provide a solution. For example, Kumakura *et al.* [277, 278] reported irradiated Nb$_3$Al tape with increased $J_c = 2 \times 10^8$ Am^{-2} at 23 T and 4.2 K. Proton irradiation of MgB$_2$ by Bugoslavsky *et al.* [279] and neutron irradiation of A15 materials by Bauer *et al.* [280] also showed an enhancement in pinning and increase in J_c. However, the results reported in the literature can be mixed, depending on the irradiation particle, energy, duration and type of defects created. Nishimura *et al.* [281] found neutron irradiation increased J_c in Nb$_3$Sn at low fields, but had no effect on NbTi and Nb$_3$Al wires, or on Bi$_2$Sr$_2$Ca$_2$Cu$_3$O$_{10}$ tapes. An improvement in flux pinning was seen in proton irradiated sintered ceramic pellets of YBCO and Bi$_2$Sr$_2$Ca$_2$Cu$_3$O$_{10}$ by Mezzetti *et al.* [282], and in ion irradiated melt-textured YBCO with a high concentration of discontinuous columnar defects by Fuchs *et al.* [283]. However, Behera *et al.* [284] found that swift heavy ion irradiation of YBCO granular thick films damaged grain boundaries, and Eisterer *et al.* [285] found that neutron irradiation of YBCO coated conductors made no improvements. Irradiation is a promising route but the parameter space is vast and systematic studies with good information about values of J_{DN} and J_{PN} will be required to optimise J_c.

For the B1M30HA750 sample, the resistivity of the grain boundaries is high, $\rho_N(T_c) = 9.30 \times 10^{-3}$ Ωm with an uncertainty of ±50%, consistent with literature bicrystal values [274], $J_c^t \ll J_c^m$, and the values of $\mu_0 \Delta M / \Delta B$ are small. We note that the grain boundary resistivity is much higher than the microcrystalline counterpart. J_{DN} is five orders of magnitude below J_{DSc}. Poor pinx` ning can cause transport J_c^t across the grain boundaries to decrease even further, and the measured J_c^t is another factor of 30 below J_{DN}. However, the literature for Bi$_2$Sr$_2$CaCu$_2$O$_8$ bicrystals gives grain boundary resistivities of $(2 - 6.5) \times 10^{-3}$ Ωm with transport critical current densities of $J_c^{GB}(0 \text{ T}, 4.2 \text{ K}) = (0.2 - 1.5) \times 10^8$ Am^{-2} [274]. This is consistent with J_{DN} calculated using equation (6.10), and shows that it is possible to increase pinning across grain boundaries. We attribute the large decrease in J_c^t between 10 K and 20 K either to a large reduction in the irreversibility field in this temperature range or to regions near the grain boundaries becoming superconducting below 20 K (possibly associated with Bi$_2$Sr$_2$CuO$_6$ at the grain boundaries), evidenced by the field dependence of resistivity, initially increasing as temperature drops

below T_c, then decreasing as the temperature approaches 20 K, as well as the rapid increase in screening shown in the a.c. magnetic susceptibility data. The magnetisation J_c^m is high in this material, associated with high intragranular current densities. We consider this sample to be a collection of high quality grains that are poorly connected.

For the B2HA750 sample, the angular average grain boundary resistivity is 1.01 Ωm, even higher than the resistivity in the c-axis direction of single crystal $Bi_2Sr_2Ca_2Cu_3O_{10}$. Without considering pinning, the high grain boundary resistivities alone is enough to cause J_{DN} to be very small as seen in Table 6.4, and is the limiting factor for the suppression of J_c. The measured, non-zero J_c^t is likely due to the existence of a percolative path. Again, we consider this sample to be high quality grains separated by highly resistive grain boundaries.

B2M30HA750 has an extremely high grain boundary resistivity of 1.65×10^{-2} Ωm, much higher than literature bicrystal values on the order of 10^{-3} Ωm [275, 276]. $J_c^t \ll J_c^m$, and the values of $\mu_0 \Delta M / \Delta B$ are small. The measured $J_c^t(0\text{ T}, 4.2\text{ K}) = 9.1 \times 10^3$ Am^{-2}, an order of magnitude below J_{DN}, thus the limiting factor for the suppression of J_c is due to the high grain boundary resistivity. Similar to B1M30HA750, there is the large decrease in J_c^t between 10 K and 20 K. We consider the B2M30HA750 sample to be similar to the B1M30HA750 sample and as such to be a highly granular sample.

There is very limited literature on the resistivity of high angle grain boundaries. This prevents us from assessing whether the angular averaged values calculated and measured in this work can be considered typical or intrinsic. Much more work is needed before one can make general statements about grain boundaries and how effective grain boundary engineering may be in manipulating their properties. Among our materials, microcrystalline $Bi_2Sr_2CaCu_2O_8$ is the only material for which grain boundary engineering could yet produce useful commercial materials, when combined with improvements in pinning. For nanocrystalline B1 and micro- or nanocrystalline B2, reducing the grain boundary resistivity is a prerequisite for improving J_c.

6.6 Concluding Comments

Both micro- and nanocrystalline $Bi_2Sr_2CaCu_2O_8$ and $Bi_2Sr_2Ca_2Cu_3O_{10}$ samples were fabricated and measured. A complementary set of a.c. magnetic susceptibility, d.c. magnetisation and transport measurements allowed us to distinguish intergranular currents from intragranular currents. We have calculated the grain boundary resistivity for these materials and combined this with the 1D S-N-S junction model for polycrystalline materials to calculate the suppression of J_c due to grain boundaries. The most interesting sample we have studied is polycrystalline $Bi_2Sr_2CaCu_2O_8$ with grain sizes on the order of microns. Whilst grain boundary resistivity does decrease the local depairing current density by an order of magnitude, this sample alone has the potential for very high J_c if strong pinning centres can be introduced. The theoretical calculations for $Bi_2Sr_2CaCu_2O_8$ and $Bi_2Sr_2Ca_2Cu_3O_{10}$ have similarities with other commercial superconductors including YBCO, LTS and Fe-based superconductors in that there is an intrinsic loss in depairing current density by about a factor of 5 simply by the presence of grain boundaries in polycrystalline materials. Furthermore the materials with the highest J_c/J_{DSc} [249], whether it is the cuprate material YBCO [84], Fe-based material $Ba(FeCo)_2As_2$ [148] or the elemental material Nb [122], are tapes with no high-angle grain boundaries and with strong pinning. The materials with the lowest J_c/J_{DSc} are polycrystalline materials, including MgB_2 [146] and A15 materials [141-144]. Although removing high angle grain boundaries from technological polycrystalline materials is the favoured route to increase J_c, thus far, this approach has proven very expensive. We suggest that cost constraint may yet lead to use of broadly untextured polycrystalline $Bi_2Sr_2CaCu_2O_8$ materials, with artificial pinning sites or perhaps pinning produced by irradiation, that have high J_c.

Chapter 7

Concluding Comments and Future Work

In Chapter 1, two questions were proposed that this thesis aimed to answer. First, can nanocrystalline HTS become a class of useful, commercial material? The short answer to this question is no; the transport critical current density of these materials are too low to be commercially useful. Second, by studying nanocrystalline HTS and grain boundaries, what insights could we gain into the potential improvement of other classes of commercial superconductors? Results have shown that, with the exception of microcrystalline Bi-2212, low critical current density in polycrystalline, untextured materials is to be expected and effort should continue to be directed towards texturing samples and removing the grain boundaries. Large grained Bi-2212 is the only HTS material studied in this work for which cheaper, untextured polycrystalline route that has high J_c may yet be possible, by improving pinning.

This thesis has described an approach for measuring the grain boundary resistivity in bulk, not intentionally textured polycrystalline superconductors. The grain boundaries in these materials are very different to the grain boundary resistivity of well-defined, stress-free bicrystals in literature, which are not representative of the complex grain boundary network in a realistic, bulk polycrystalline material with randomly oriented grains. Using the calculated grain boundary resistivity, we were able to go beyond the qualitative description of weak-links in literature, and quantitatively determine the order of magnitude of suppression in the transport critical current density due to local depairing current density.

The grain boundary resistivity in nanocrystalline HTS is simply too high, and causes the depairing current density across the grain boundary to fall by several orders of magnitude, which is sufficient to explain the decrease in the measured transport critical current density.

In order for nanocrystalline HTS materials to be commercially useful, the grain boundary resistivity needs to be decreased by at least an order of magnitude. Current methods of grain boundary engineering which may reduce the resistivity, such as preferential doping at the grain boundaries, are probably insufficient to produce an order of magnitude reduction, but the work in this demonstrate how important such improvements would be. We suggest a breakthrough in grain boundary engineering would be required for grain boundary engineering to be successful. Based on current technology, the most promising direction is to remove grain boundaries in all commercial materials, including LTS such as NbTi and Nb_3Sn. The removal of grain boundaries causes a decrease in the surface pinning of the grains themselves, which should be compensated for by the addition of pinning centres. One such method is to irradiate the superconductors to produce pinning centres. We suggest two directions for new research: i) Research has shown that the choice of irradiation particle, fluence, duration and type of starting superconductor material all affect the type of pinning centre that is produced, and can result in an improvement, degradation, or cause no change at all [281, 282, 285]. A systematic exploration of this parameter space is required to produce optimal results. ii) It would also be interesting to see the concept of a multilayered superlattice with pinning centres aligned along the *ab*-plane and along the *c*-axis, which was used for iron pnictide thin films, applied to other materials. In materials where the grain boundary resistivity is already low and similar to the grain resistivity, for example in microcrystalline $Bi_2Sr_2CaCu_2O_8$ and in certain compositions of Nb_3Sn, it may be interesting to see if irradiation of the grain boundaries can enhance local flux pinning. iii) Microcrystalline $Bi_2Sr_2CaCu_2O_8$ showed high transport J_c and low grain boundary resistivity, which may be due to texturing similar to that seen in Kametani *et al.* [248]. Studies into the tendency of this material to produce texture from a polycrystalline fabrication process, which normally produces randomly aligned crystals, could be of great interest.

The work described in this thesis could greatly benefit from high quality SEM images of the nanocrystalline materials. During the SEM sample preparation process, the samples reacted with liquids that were used for polishing, which caused the surface layer of the samples to flake off. The surface damage was particularly severe in the nanocrystalline materials. If we could solve this problem, high quality SEM data will allow us to obtain valuable information about the material such as texture, chemical composition or phase maps, and even use these to optimise the fabrication process. It may also be possible to determine the grain size of each sample more accurately, and thus determine the relationship between superconducting properties and the grain size more explicitly.

It has been over one hundred years since the discovery of superconductivity. Continuous effort by the entire superconductivity research community has spectacularly increased the critical current density of a range of materials by orders of magnitude during this time. However, the compilation graph of transport critical current density normalized by the depairing current density produced in this thesis (Figure 2.1) has shown that most of these materials are still far from reaching their potential. The author hopes that, armed with a deeper understanding of grain boundaries and the ability to quantitatively determine suppression in critical current density, commercial superconductors may finally reach their full potential, and may bring us one step closer towards commercial fusion energy.

Appendix

The temperature dependence of the depairing current density for a superconductor $(J_{\mathrm{DSc}}(T))$, as listed in Table 4.1, is calculated as shown below. Our approach was broadly either to find expressions for the G-L penetration depth (λ), the G-L coherence length (ξ) and T_{c} directly from the literature or to find the upper critical field $(B_{c2}(T))$ and lower critical field $(B_{c1}(T))$ at any temperature from the literature and use well known temperature dependencies for these critical fields to calculate λ and ξ. In Table 4.1, we have shown values of the critical fields and length scales at 0 K.

A.1 Calculation of J_{DSc}^{ab} in Zero Field

First we consider the Ginzburg-Landau expression for the depairing current density of an anisotropic superconducting material such as YBCO or an isotropic superconductor. When the current is in the ab-plane, J_{DSc}^{ab} is given by:

$$J_{\mathrm{DSc}}^{ab}(T) = \frac{\Phi_0}{3\sqrt{3}\pi\mu_0\lambda_{ab}^2(T)\xi_{ab}(T)}, \tag{A.1}$$

where Φ_0 is the flux quantum, $\lambda_{ab}(T)$ is the G-L penetration depth and $\xi_{ab}(T)$ is the G-L coherence length. Since there is no general theoretical expressions for $B_{c2}(T)$, we use an empirical equation of the form:

$$B_{c2}^c(T) = B_{c2}^c(0)(1 - (T/T_{\mathrm{c}})^\nu). \tag{A.2}$$

Note in equation (A.2) that when the applied magnetic field points in the c-axis direction, the relevant length scale is the G-L coherence length in the ab-plane. We can differentiate equation (A.2) with respect to T to obtain:

$$\left.\frac{\partial B_{\text{c2}}^c(T)}{\partial T}\right|_{T\approx T_{\text{c}}} = -\frac{\nu}{T_{\text{c}}} B_{\text{c2}}^c(0). \tag{A.3}$$

We use the Ginzburg-Landau equation for $B_{\text{c2}}(T)$ (correct only for $T \approx T_{\text{c}}$) [286]:

$$B_{\text{c2}}^c(\text{T}) = \left.\frac{\Phi_0}{2\pi\xi_{ab}^2(T)}\right|_{T\approx T_{\text{c}}}, \tag{A.4}$$

and the Ginzburg-Landau expression for the G-L coherence length $\xi_{ab}(T)$, which is generally taken to be true for all temperatures, of the form:

$$\xi_{ab}(T) = \xi_{ab}(0)\big(1 - (T/T_{\text{c}})\big)^{-1/2}. \tag{A.5}$$

We can differentiate equation (A.4) with respect to T to obtain:

$$\left.\frac{\partial B_{\text{c2}}^c(T)}{\partial T}\right|_{T\approx T_{\text{c}}} = \frac{\Phi_0}{2\pi\xi_{ab}^2(0)}\left(-\frac{1}{T_{\text{c}}}\right). \tag{A.6}$$

From equations (A.3) and (A.6) we have:

$$\xi_{ab}^2(0) = \frac{\Phi_0}{2\pi B_{\text{c2}}^c(0)}\frac{1}{\nu}. \tag{A.7}$$

Substituting this equation into equation (A.5), we have:

$$\xi_{ab}^2(T) = \frac{\Phi_0}{2\pi B_{\text{c2}}^c(0)}\,\frac{1}{\nu}\frac{1}{1-(T/T_{\text{c}})}. \tag{A.8}$$

Substituting equation (A.2) into equation (A.8) leads to:

$$\xi_{ab}^2(T) = \frac{\Phi_0}{2\pi B_{\text{c2}}^c(T)}\,\frac{1}{\nu}\,\frac{1-(T/T_{\text{c}})^\nu}{1-(T/T_{\text{c}})}. \tag{A.9}$$

The temperature dependence of λ in the ab-plane can be calculated in a similar way using:

$$B_{\text{c1}}^c(T) = B_{\text{c1}}^c(0)(1-(T/T_{\text{c}})^\eta), \tag{A.10}$$

where η has been taken to have a value of 2 for all superconductors. This can be differentiated to give:

$$\left.\frac{\partial B_{\text{c1}}^c(T)}{\partial T}\right|_{T\approx T_{\text{c}}} = B_{\text{c1}}^c(0)\left(-\frac{\eta}{T_{\text{c}}}\right). \tag{A.11}$$

We also use the Ginzburg-Landau relation for the G-L penetration depth, valid at all temperatures:

$$\lambda_{ab}(T) = \lambda_{ab}(0)\big(1 - (T/T_{\text{c}})\big)^{-1/2}, \tag{A.12}$$

and the Ginzburg-Landau relation for $B_{c1}^c(T)$ [286]:

$$
\begin{aligned}
B_{c1}^c(T) &= \frac{\Phi_0}{4\pi\lambda_{ab}^2(T)}\left\{\ln\left(\frac{\lambda_{ab}(T)}{\xi_{ab}(T)}\right) + 0.5\right\} \\
&= \frac{\Phi_0}{4\pi\lambda_{ab}^2(T)}\left\{\ln\left(\frac{\lambda_{ab}(0)}{\xi_{ab}(0)}\right) + 0.5\right\},
\end{aligned}
\tag{A.13}
$$

which can be differentiated to give:

$$
\left.\frac{\partial B_{c1}^c(T)}{\partial T}\right|_{T\approx T_c} = \frac{\Phi_0}{4\pi\lambda_{ab}^2(0)}\left(-\frac{1}{T_c}\right)\left\{\ln\left(\frac{\lambda_{ab}(0)}{\xi_{ab}(0)}\right) + 0.5\right\}.
\tag{A.14}
$$

Combining equations (A.11) and (A.14) leads to:

$$
\lambda_{ab}^2(0) = \frac{\Phi_0}{4\pi\eta B_{c1}^c(0)}\left\{\ln\left(\frac{\lambda_{ab}(0)}{\xi_{ab}(0)}\right) + 0.5\right\}.
\tag{A.15}
$$

Combining Equations (A.10), (A.12) and (A.15) gives $\lambda_{ab}(T)$:

$$
\lambda_{ab}^2(T) = \frac{\Phi_0}{4\pi\eta}\frac{1-(T/T_c)^\eta}{B_{c1}^c(T)\big(1-(T/T_c)\big)}\left\{\ln\left(\frac{\lambda_{ab}(0)}{\xi_{ab}(0)}\right) + 0.5\right\}.
\tag{A.16}
$$

Equations (A.9) and (A.16) can be substituted into equation (A.1) to calculate $J_{\mathrm{Dsc}}^{ab}(T)$.

A.2 Calculation of J_{DSc}^c in Zero Field

For anisotropic materials, we can also calculate the depairing current density when the current is flowing in the c-axis direction (J_{DSc}^c), given by:

$$
J_{\mathrm{DSc}}^c(T) = \frac{\Phi_0}{3\sqrt{3}\pi\mu_0\lambda_c^2(T)\xi_c(T)}.
\tag{A.17}
$$

Using the general result for anisotropic superconductors [175]:

$$
\lambda_{ab}\xi_{ab} = \lambda_c\xi_c,
\tag{A.18}
$$

we have:

$$
J_{\mathrm{DSc}}^c(T) = J_{\mathrm{DSc}}^{ab}(T)\frac{\lambda_{ab}(0)}{\lambda_c(0)} = J_{\mathrm{DSc}}^{ab}(T)\frac{\xi_c(0)}{\xi_{ab}(0)}.
\tag{A.19}
$$

The Ginzburg-Landau relation for $B_{c2}^{ab}(T)$ is [286]:

$$
B_{c2}^{ab}(T) = \frac{\Phi_0}{2\pi\xi_c(T)\xi_{ab}(T)}\bigg|_{T\approx T_c},
\tag{A.20}
$$

and the scaling with temperature is given by:

$$B_{c2}^{ab}(T) = B_{c2}^{ab}(0)(1 - (T/T_c)^\nu). \tag{A.21}$$

Similar to the methods described above for current flowing in the ab-plane, by combining the derivatives of equations (A.20) and (A.21) we find:

$$\xi_c(0) = \frac{\Phi_0}{2\pi B_{c2}^{ab}(0)\xi_{ab}(0)}\frac{1}{\nu} = \frac{\Phi_0}{2\pi B_{c2}^{ab}(T)\xi_{ab}(0)}\frac{1}{\nu}\left(1 - \left(\frac{T}{T_c}\right)^\nu\right), \tag{A.22}$$

where $\xi_{ab}(0)$ can be obtained from equation (A.7), and $\xi_c(T)$ can be found using:

$$\xi_c(T) = \xi_c(0)(1 - (T/T_c))^{-1/2}. \tag{A.23}$$

Finally, $\lambda_c(T)$ can be found given $\xi_{ab}(T)$, $\xi_c(T)$ and $\lambda_{ab}(T)$ using equation (A.18). Hence we can calculate the values necessary to produce (A.17), Table 4.1 and Figure 4.1.

A.3 Rietveld Refinement

The diffractometer used was a Bruker D8 Advance Diffractometer. The sample powder were secured onto Si slides using small amounts of Vaseline. The instrument peak broadening was corrected for by obtaining the XRD pattern for large-grained CeO_2 powder.

XRD data were analysed using TOPAS Academic software and Rietveld refinement. The Crystallographic Information File (CIF) for possible phases are used for the initial refinement step. For example, for Y2MHA(1), CIFs used include: $YBa_2Cu_3O_7$ (nominal), Y_2BaCuO_5 (nominal), CeO_2 (nominal), WC (from milling media), Co (from milling media), Al (from powder handling), Nb (from HIP), NbO (from HIP), Ag (from annealing), AgO_2 (from annealing) and various secondary phases such as CuO, $Ba(OH)_2$ and Y-124. Any phases with a negligible weight percentage is then removed from the refinement process. An example of the refinement during this step for the Y1P sample can be found in Figure A.1. Y_2BaCuO_5 and WC phases had weight percentages of $<1\%$ and were therefore removed from the refinement process after this step. Using only the relevant phases, the data was then refined neglecting grain size (i.e. instrument broadening only) in order to refine for the peak positions. All lattice parameters were fixed except for c-lattice parameter which was refined, as the c-lattice parameter is dependent on the oxygen content. After the peak positions are found, all lattice parameters are then fixed, and only the background and grain sizes are refined, typically for 2000 iterations.

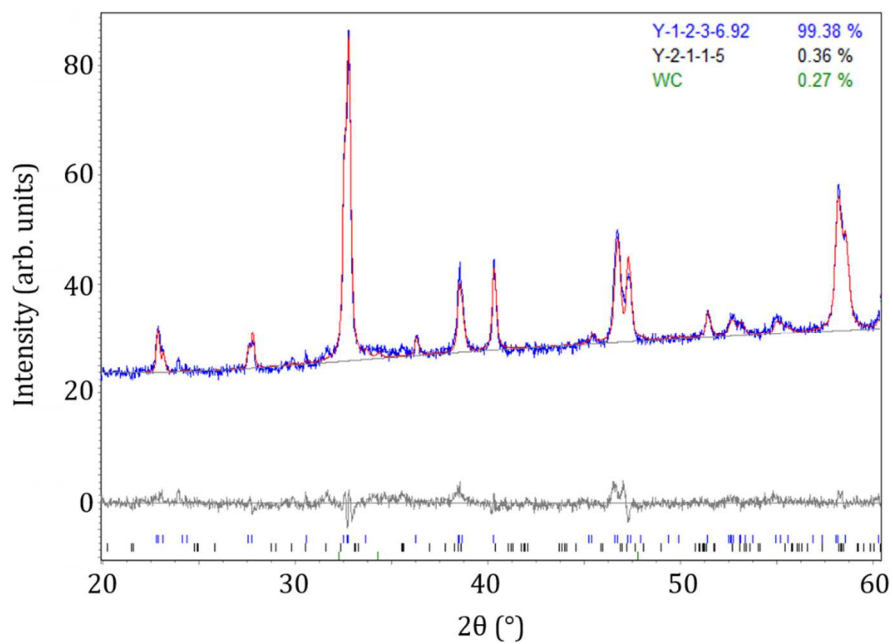Figure A.1: Example of Rietveld refinement using TOPAS Academic software, for the Y1P sample. Blue curve shows raw data, red curve shows fitted data, light grey curve shows the fitted background and dark grey curve shows the difference between raw and fitted data. The phases $YBa_2Cu_3O_{6.92}$, Y_2BaCuO_5 and WC are used in the refinement, the respective weight percentages and peak positions are also shown.

References

[1]   H. K. Onnes, "Further Experiments with Liquid Helium. G On the Electrical Resistance of Pure Metals, etc VI. On the Sudden Change in the Rate at which the Resistance of Mercury Disappears," *Communications from the Physical Laboratory of the University of Leiden,* vol. 124C, pp. 21-26, 1911.

[2]   D. M. J. Taylor, M. Al-Jawad, and D. P. Hampshire, "A new paradigm for fabricating bulk high-field superconductors," *Superconductor Science & Technology,* vol. 21, p. 125006, 2008.

[3]   H. J. Niu and D. P. Hampshire, "Disordered Nanocrystalline Superconducting $PbMo_6S_8$ with Very Large Upper Critical Field," *Physical Review Letters,* vol. 91, p. 027002, 2003.

[4]   H. J. Niu and D. P. Hampshire, "Critical parameters of disordered nanocrystalline superconducting Chevrel phase $PbMo_6S_8$," *Physical Review B,* vol. 69, p. 174503, 2004.

[5]   Y. Sun, X. Song, D. Yu, S. Ran, and A. Xia, "Disordered nanocrystalline superconducting magnesium diboride: A significant improvement in in-field critical current density," *Scripta Materialia,* vol. 70, pp. 55-58, 2014.

[6]   M. J. Raine and D. P. Hampshire, "Characterization of the Low Temperature Superconductor Niobium Carbonitride," *IEEE Transactions on Applied Superconductivity,* vol. 21, pp. 3138-3141, Jun 2011.

[7]   M. J. Raine, "Thesis: High field superconductors for fusion energy applications " *University of Durham* 2015.

[8]   M. K. Wu, J. R. Ashburn, C. J. Torng, P. H. Hor, R. L. Meng, L. Gao*, et al.*, "Superconductivity at 93 K in a new mixed-phase Y-Ba-Cu-O compound system at ambient pressure," *Physical Review Letters,* vol. 58, pp. 908-910, 1987.

[9]   H. Maeda, Y. Tanaka, M. Fukutomi, and T. Asano, "A New High-T_c Oxide Superconductor without a Rare Earth Element," *Japanese Journal of Applied Physics,* vol. 27, pp. L209-L210, 1988.

[10]   D. Dimos, P. Chaudhari, and J. Mannhart, "Superconducting transport properties of grain boundaries in $YBa_2Cu_3O_7$ bicrystals," *Physical Review B,* vol. 41, pp. 4038-4049, 1990.

[11]   SuperPower-Furukawa, "SuperPower 2G HTS Coated Conductors," *www.superpower-inc.com/content/2g-hts-wire*, 2013.

[12]   H. K. Onnes, "The liquefaction of helium," *Proc. Roy. Acad. Amsterdam,* vol. 11, p. 168, 1908.

[13]   H. K. Onnes, *Through Measurement to Knowledge - The Selected Papers of Heike Kamerlingh Onnes 1853-1926*, 1 ed.: Springer Netherlands, 1991.

[14]   W. Meissner and R. Ochsenfeld, "Ein neuer Effekt bei Eintritt der Supraleitfähigkeit," *Naturwissenschaften,* vol. 21, pp. 787-788, 1933.

[15]   F. London and H. London, "The electromagnetic equations of the supraconductor," *Proc Roy Soc (London),* vol. A149, pp. 71-88, 1935.

[16]   V. L. Ginzburg and L. D. Landau, "On the Theory of Superconductivity," *Zhurnal Eksperimentalnoj i Teoreticheskoj Fiziki,* vol. 20, pp. 1064-1082, 1950.

[17]   J. Bardeen, L. N. Cooper, and J. R. Schrieffer, "Theory of Superconductivity," *Physical Review,* vol. 108, pp. 1175-1204, 1957.

[18]   J. G. Bednorz and K. A. Muller, "Possible High-T_c Superconductivity in the Ba-La-Cu-O System," *Zeitschrift Fur Physik B-Condensed Matter,* vol. 64, pp. 189-193, 1986.

[19]   L. Gao, Y. Xue, F. Chen, Q. Xiong, R. Meng, D. Ramirez*, et al.*, "Superconductivity up to 164 K in $HgBa_2Ca_{m-1}Cu_mO_{2m+2+d}$ ($m = 1$, 2, and 3) under quasihydrostatic pressures," *Physical Review B,* vol. 50, pp. 4260-4263, 1994.

[20]   C. W. Chu, L. Gao, F. Chen, Z. J. Huang, R. L. Meng, and Y. Y. Xue, "Superconductivity above 150 K in $HgBa_2Ca_2Cu_3O_8$ at high pressures," *Nature,* vol. 365, pp. 323-325, 1993.

[21]   A. P. Drozdov, M. I. Eremets, I. A. Troyan, V. Ksenofontov, and S. I. Shylin, "Conventional superconductivity at 203 kelvin at high pressures in the sulfur hydride system," *Nature,* vol. 525, pp. 73-76, 2015.

[22]   H. Fröhlich, "Theory of the Superconducting State. I. The Ground State at the Absolute Zero of Temperature," *Physical Review,* vol. 79, pp. 845-856, 1950.

[23]   E. Maxwell, "Isotope effect in the superconductivity of mercury," *Physical Review,* vol. 78, p. 477, 1950.

[24] S. Chakravarty, A. Sudbø, P. W. Anderson, and S. Strong, "Interlayer Tunneling and Gap Anisotropy in High-Temperature Superconductors," *Science,* vol. 261, pp. 337-340, 1993.

[25] P. Monthoux and D. Pines, "Spin-Fluctuation-Induced Superconductivity in the Copper Oxides: A Strong Coupling Calculation," *Physical Review Letters,* vol. 69, pp. 961-964, 1992.

[26] A. A. Abrikosov, "On the magnetic properties of superconductors of the second group," *Soviet Physics JETP,* vol. 5, pp. 1174-1182, 1957.

[27] E. H. Brandt, "Precision Ginzburg-Landau Solution of ideal vortex lattices for any induction and symmetry," *Physical Review Letters,* vol. 78, pp. 2208-2211, 1997.

[28] M. M. Doria, J. E. Gubernatis, and D. Rainer, "Virial theorem for Ginzburg-Landau theories with potential applications to numerical studies of type-II superconductors," *Physical Review B,* vol. 39, pp. 9573-9575, 05/01/ 1989.

[29] C. P. Bean, "Magnetization of high-field superconductors," *Reviews of Modern Physics,* vol. 36, pp. 31-39, 1964.

[30] M. Sborchia, E. Barbero Soto, R. Batista, B. Bellesia, A. Bonito Oliva, E. Boter Rebollo*, et al.*, "Overview of ITER Magnet System and European Contribution," *IEEE/NPSS 24th Symposium on Fusion Engineering,* pp. 1-8, 2011.

[31] CERN. (2013, accessed Aug 2017). *The superconducting magnet of the big european bubble chamber (BEBC) http://cds.cern.ch/record/850617/files/.*

[32] E. Spooner and B. J. Chalmers, "DC motors with high-critical-temperature superconducting field winding and slotless armature," *IEE Proc. Electr. Power Appl.,* vol. 141, pp. 135-143, 1994.

[33] W. Hassenzahl, "Will superconducting magnetic energy storage be used on electric utility systems?," *IEEE Transactions on Magnetics,* vol. 11, pp. 482-488, 1975.

[34] N. Mitchell, D. Bessette, R. Gallix, C. Jong, J. Knaster, P. Libeyre*, et al.*, "The ITER magnet system," *IEEE Transactions on Applied Superconductivity,* vol. 18, pp. 435-440, Jun 2008.

[35] T. Schild, G. Aubert, C. Berriaud, P. Bredy, F. P. Juster, C. Meuris*, et al.*, "The Iseult/Inumac Whole Body 11.7 T MRI Magnet Design," *IEEE Transactions on Applied Superconductivity,* vol. 18, pp. 904-907, 2008.

[36]   P. Lebrun, "Advanced Technology from and for Basic Science: Superconductivity and Superfluid Helium at the Large Hadron Collider http://cds.cern.ch/record/1064354/files/," CERN CERN-AT-2007-030, 2007.

[37]   K. Sawada, "Development of magnetically Levitated High Speed Transport System in Japan," *IEEE Transactions on Magnetics,* vol. 32, pp. 2230-2235, 1996.

[38]   K. Sawada, "Outlook of the Superconducting Maglev," *Proceedings of the IEEE,* vol. 97, pp. 1881-1885, 2009.

[39]   C. C. Torardi, M. A. Subramanian, J. C. Calabrese, J. Gopalakrishnan, E. M. McCarron, K. J. Morrissey*, et al.*, "Structures of the superconducting oxides $Tl_2Ba_2CuO_6$ and $Bi_2Sr_2CuO_6$," *Physical Review B,* vol. 38, pp. 225-231, 1988.

[40]   S. A. Sunshine, T. Siegrist, L. F. Schneemeyer, D. W. Murphy, R. J. Cava, B. Batlogg*, et al.*, "Structure and physical properties of single crystals of the 84-K superconductor $Bi_{2.2}Sr_2Ca_{0.8}Cu_2O_{8+d}$," *Physical Review B,* vol. 38, pp. 893-896, 1988.

[41]   M. A. Subramanian, c. c. Torardi, J. Gopalakrishnan, P. L. Gai, J. C. Calabrese, T. R. Askew*, et al.*, "Bulk Superconductivity up to 122 K in the Tl-Pb-Sr-Ca-Cu-O System," *Science,* vol. 242, pp. 249-252, 1988.

[42]   S. Chu and M. E. McHenry, "Growth and characterization of $(Bi, Pb)_2Sr_2Ca_2Cu_3O_x$ single crystals," *Journal of Materials Research,* vol. 13, pp. 589-595, 1998.

[43]   A. K. Saxena, *High-Temperature Superconductors*: Springer, Berlin, 2010.

[44]   S. R. Dharwadkar, V. S. Jakkal, J. V. Yakhmi, I. K. Gopalakrishnan, and R. M. Iyer, "X-ray diffraction coupled thermogravimetric investigations of $YBa_2Cu_3O_{7-x}$," *Solid State Communications,* vol. 64, pp. 1429-1433, 1987.

[45]   M. F. Yan, R. L. Barns, H. M. Obryan, P. K. Gallagher, R. C. Sherwood, and S. Jin, "Water Interaction with the Superconducting $YBa_2Cu_3O_7$ Phase," *Applied Physics Letters,* vol. 51, pp. 532-534, 1987.

[46]   R. L. Barns and R. A. Laudise, "Stability of superconducting $YBa_2Cu_3O_7$ in the presence of water," *Applied Physics Letters,* vol. 51, pp. 1373-1375, 1987.

[47]   B. Vignolle, D. Vignolles, D. LeBoeuf, S. Lepault, B. Ramshaw, R. Liang*, et al.*, "Quantum oscillations and the Fermi surface of high-temperature cuprate superconductors," *Comptes Rendus Physique,* vol. 12, pp. 446-460, 2011.

[48]   R. Liang, D. A. Bonn, and W. N. Hardy, "Evaluation of CuO_2 plane hole doping in $YBa_2Cu_3O_{6+x}$ single crystals," *Physical Review B,* vol. 73, p. 180505, 2006.

[49]   P. Benzi, E. Bottizzo, and N. Rizzi, "Oxygen determination from cell demensions in YBCO superconductors," *Journal of Crystal Growth,* vol. 269, pp. 625-629, 2004.

[50]   S. J. Hagen, T. W. Jing, Z. Z. Wang, J. Horvath, and N. P. Ong, "Out-of-plane conductivity in single-crystal $YBa_2Cu_3O_7$," *Physical Review B,* vol. 37, pp. 7928-7931, 1988.

[51]   T. Fujii, T. Watanabe, and A. Matsuda, "Comparative study of transport properties of $Bi_2Sr_2Ca_2Cu_3O_{10+\delta}$ and $Bi_2Sr_2CaCu_2O_{8+\delta}$ single crystals," *Physica C: Superconductivity,* vol. 357–360, Part 1, pp. 173-176, 2001.

[52]   J. Z. Wu, P. Y. Hsieh, A. V. McGuire, D. L. Schmidt, L. T. Wood, Y. Shen*, et al.,* "Anisotropic properties of the high-quality epitaxial $YBa_2Cu_3O_{7-d}$ (110) thin film," *Physical Review B,* vol. 44, pp. 12643-12646, 1991.

[53]   P. Chaudhari, J. Mannhart, D. Dimos, C. C. Tsuei, J. Chi, M. M. Oprysko*, et al.,* "Direct Measurement of the Superconducting Properties of Single Grain Boundaries in $YBa_2Cu_3O_{7-d}$," *Physical Review Letters,* vol. 60, pp. 1653-1656, 1998.

[54]   D. Dimos, P. Chaudhari, J. Mannhart, and F. K. LeGoues, "Orientation Dependence of Grain-Boundary Critical Currents in $YBa_2Cu_3O_{7-d}$ Bicrystals," *Physical Review Letters,* vol. 61, pp. 219-222, 1988.

[55]   B. D. Josephson, "Supercurrents through barriers," *Advances in Physics,* vol. 14, pp. 419-450, 1965.

[56]   E. Shimizu and D. Ito, "Critical current density obtained from particle-size dependence of magnetization in $YBa_2Cu_3O_{7-\delta}$ powders," *Physical Review B,* vol. 39, pp. 2921-2923, 1989.

[57]   G. Deutscher, "Origin of weak-link behavior of grain boundaries in superconducting cuprates and pnictides," *Applied Physics Letters,* vol. 96, p. 122502, 2010.

[58]   S. Graser, P. J. Hirschfeld, T. Kopp, R. Gutser, B. M. Anderson, and J. Mannhart, "How grain boundaries limit supercurrents in high-temperature superconductors," *Nature Physics,* vol. 6, pp. 609-614, 2010.

[59]   A. Gurevich and E. A. Pashitskii, "Current transport through low-angle grain boundaries in high-temperature superconductors," *Physical Review B,* vol. 57, pp. 13878-13893, 1998.

[60]   N. D. Browning, J. P. Buban, P. D. Nellist, D. P. Norton, M. F. Chisholm, and S. J. Pennycook, "The atomic origins of reduced critical currents at [001] tilt grain

boundaries in $YBa_2Cu_3O_{7-\delta}$ thin films," *Physica C: Superconductivity,* vol. 294, pp. 183-193, 1998.

[61]   G. Deutscher, O. Entin-Wohlman, S. Fishman, and Y. Shapira, "Percolation description of granular superconductors," *Physical Review B,* vol. 21, pp. 5041-5047, 1980.

[62]   V. S. Sergey, K. M. Maria, and S. Kamel, "Microscopic origins of the grain boundary effect on the critical current in superconducting copper oxides," *Superconductor Science and Technology,* vol. 12, p. 1071, 1999.

[63]   M. F. Chisholm and D. A. Smith, "Low-angle tilt grain boundaries in $YBa_2Cu_3O_7$ superconductors," *Philosophical Magazine A,* vol. 59, pp. 181-197, 1989.

[64]   E. Sarnelli, M. Adamo, S. D. Nicola, S. Cibella, R. Leoni, and C. Nappi, "Amplitude sensitive experiment of pairing symmetry in d_0–d_0 submicron Y–Ba–Cu–O bicrystal grain boundary junctions," *Superconductor Science and Technology,* vol. 26, p. 105013, 2013.

[65]   J. H. Durrell, M. J. Hogg, F. Kahlmann, Z. H. Barber, M. G. Blamire, and J. E. Evetts, "Critical Current of $YBa_2Cu_3O_{7-d}$ Low-Angle Grain Boundaries," *Physical Review Letters,* vol. 90, p. 247006, 2003.

[66]   J. H. Durrell, C. B. Eom, A. Gurevich, E. E. Hellstrom, C. Taratini, A. Yamamoto*, et al.*, "The behaviour of grain boundaries in the Fe-based superconductors," *Reports on Progress in Physics,* vol. 74, p. 124511, 2011.

[67]   A. Palau, J. H. Durrell, J. L. MacManus-Driscoll, S. Harrington, T. Puig, F. Sandiumenge*, et al.*, "Crossover between Channeling and Pinning at Twin Boundaries in $YBa_2Cu_3O_7$ Thin Films," *Physical Review Letters,* vol. 97, p. 257002, 2006.

[68]   R. A. Brown, "A dislocation model of grain boundary electrical resistivity," *Journal of Physics F: Metal Physics,* vol. 7, p. 1477, 1977.

[69]   J. Mannhart and H. Hilgenkamp, "Possible influence of band bending on the normal state properties of grain boundaries in high-T_c superconductors," *Materials Science and Engineering: B,* vol. 56, pp. 77-85, 1998.

[70]   H. Hilgenkamp and J. Mannhart, "Grain boundaries in high-T_c superconductors," *Reviews of Modern Physics,* vol. 74, pp. 485-549, 2002.

[71]   J. Mannhart and H. Hilgenkamp, "Interfaces involving complex superconductors," *Physica C: Superconductivity,* vol. 317–318, pp. 383-391, 1999.

[72]   H. J. H. Smilde, H. Hilgenkamp, G. J. Gerritsma, D. H. A. Blank, and H. Rogalla, "Realization and properties of ramp-type YBa$_2$Cu$_3$O$_{7-\delta}$/Au/Nb junctions," *Physica C: Superconductivity,* vol. 350, pp. 269-275, 2001.

[73]   C. H. Cheng and Y. Zhao, "Repair of grain boundary by preferential-doping in YBa$_2$Cu$_3$O$_{7-y}$," *Physica C: Superconductivity and its Applications,* vol. 463–465, pp. 174-177, 2007.

[74]   C. H. Cheng and Y. Zhao, "Enhancement of J_c by doping silver in grain boundaries of YBa$_2$Cu$_3$O$_y$ polycrysts with solid-state diffusion method," *Journal of Applied Physics,* vol. 93, pp. 2292-2294, 2003.

[75]   Y. Zhao and C. H. Cheng, "Grain boundary doping effect on critical current density in YBa$_2$Cu$_3$O$_7$ polycrystalline materials," *Physica C: Superconductivity,* vol. 386, pp. 286-291, 2003.

[76]   C. H. Cheng, X. T. Zhu, and Y. Zhao, "Chemical preferential doping in grain boundaries of melt textured YBa$_2$Cu$_3$O$_y$ superconductors," *Superconductor Science and Technology,* vol. 16, p. 130, 2003.

[77]   A. Schmehl, B. Goetz, R. R. Schulz, C. W. Schneider, H. Bielefeldt, H. Hilgenkamp, *et al.*, "Doping-induced enhancement of the critical currents of grain boundaries in YBa$_2$Cu$_3$O$_{7-d}$," *Europhys. Lett.,* vol. 47, pp. 110-115, 1999.

[78]   G. Hammerl, A. Schmehl, R. R. Schultz, B. Goetz, H. Bielefeldt, C. W. Schneider, *et al.*, "Enhanced supercurrent density in polycrystalline YBa$_2$Cu$_3$O$_{7-d}$ at 77K from calcium doping of grain boundaries," *Nature,* vol. 407, pp. 162-164, 2000.

[79]   D. P. Norton, C. Park, C. Prouteau, D. K. Christen, M. F. Chisholm, J. D. Budai, *et al.*, "Epitaxial YBa$_2$Cu$_3$O$_7$ films on rolled-textured metals for high-temperature superconducting applications," *Materials Science and Engineering: B,* vol. 56, pp. 86-94, 1998.

[80]   J. H. Durrell, "Importance of low-angle grain boundaries in YBCO coated conductors," *Superconductor Science & Technology,* vol. 22, p. 013001, 2009.

[81]   A. Godeke, A. den Ouden, A. Nijhuis, and H. H. J. ten Kate, "State of the art powder-in-tube niobium-tin superconductors," *Cryogenics,* vol. 48, pp. 308-316, 2008.

[82]   B. A. Glowacki, M. Majoros, M. Vickers, J. E. Evetts, Y. Shi, and I. McDougall, "Superconductivity of powder-in-tube MgB$_2$ wires," *Superconductor Science and Technology,* vol. 14, p. 193, 2001.

[83]   Y. Yamada, M. Mogi, and K. Sato, "Examples and Future Prospects of High-Temperature Superconductor Products," *Sei Technical Review,* vol. 65, pp. 51-59, 2007.

[84]   D. C. Larbalestier, J. Jiang, U. P. Trociewitz, F. Kametani, C. Scheuerlein, M. Dalban-Canassy*, et al.*, "Isotropic round-wire multifilament cuprate superconductor for generation of magnetic fields above 30 T," *Nature Materials,* vol. 13, pp. 375-381, 2014.

[85]   D. Cardwell, "Processing and properties of large grain (RE)BCO," *Mat Sci and Eng,* vol. B53, pp. 1-10, 1998.

[86]   W. K. Yeoh, S. K. Pathak, Y. Shi, A. R. Dennis, D. A. Cardwell, N. H. Babu*, et al.*, "Improved Flux Pinning in Y-Ba-Cu-O Superconductors Containing Niobium Oxide," *IEEE Transactions on Applied Superconductivity,* vol. 19, pp. 2970-2973, 2009.

[87]   H. T. Ren, L. Xiao, Y. L. Jiao, and M. H. Zheng, "Processing and characterization of YBCO superconductors by top-seeded melt growth method in batch process," *Physica C: Superconductivity,* vol. 412–414, Part 1, pp. 597-601, 2004.

[88]   Y. Shi, N. Hari Babu, K. Iida, W. K. Yeoh, A. R. Dennis, S. K. Pathak*, et al.*, "Batch-processed GdBCO–Ag bulk superconductors fabricated using generic seeds with high trapped fields," *Physica C: Superconductivity,* vol. 470, pp. 685-688, 2010.

[89]   J. H. Durrell, A. R. Dennis, J. Jaroszynski, M. D. Ainslie, K. G. B. Palmer, Y. H. Shi*, et al.*, "A trapped field of 17.6 T in melt-processed, bulk Gd-Ba-Cu-O reinforced with shrink-fit steel," *Superconductor Science and Technology,* vol. 27, p. 082001, 2014.

[90]   C. Suryanarayana, "Mechanical Alloying and Milling," *Progress in Materials Science,* vol. 46, pp. 1-184, 2001.

[91]   W. Cao, (accessed Aug 2017), "Synthesis of Nanomaterials by High Energy Ball Milling," *http://www.understandingnano.com/nanomaterial-synthesis-ball-milling.html*.

[92]   J. K. Tien, J. C. Borofka, B. C. Hendrix, T. Caulfield, and S. H. Reichman, "Densification of oxide superconductors by hot isostatic pressing," *Metallurgical Transactions A,* vol. 19, pp. 1841-1847, 1988.

[93]   M. A. Imam, A. K. Singh, K. Sadananda, and M. Osofsky, "Preparation of dense bulk high T_c superconducting materials using hot isostatic pressing," *IEEE Transactions on Magnetics,* vol. 25, pp. 2010-2013, 1989.

[94]   T. Asano, Y. Tanaka, M. Fukutomi, and H. Maeda, "Method for manufacturing oxide high-temperature superconductor," Google Patents, patent number US 5145829 A, 1992.

[95]   Y. Park, H.-J. Shin, Y.-G. Kim, Y. K. Oh, and H. Lee, "Effects of melting diffusion and annealing in oxygen on superconducting characteristics of GdBCO coated conductors: preliminary results," *IEEE Transactions on Applied Superconductivity,* vol. 23, p. 6600804, 2013.

[96]   H. S. Kim, J. B. Song, N. Y. Kwon, K. L. Kim, and H. G. Lee, "The influence of heat-treatment and oxygenation annealing on the superconducting properties of YBCO coated conductors," *Superconductor Science and Technology,* vol. 22, p. 125016, 2009.

[97]   H. Gleiter, "Nanocrystalline materials," *Progress in Materials Science,* vol. 33, pp. 223-315, 1989.

[98]   T. P. Orlando, E. J. McNiff, S. Foner, and M. R. Beasley, "Critical fields, Pauli paramagnetic limiting, and material parameters of Nb_3Sn and V_3Si," *Physical Review B,* vol. 19, pp. 4545-4561, 1979.

[99]   J. Y. Xiang, C. Fleck, and D. P. Hampshire, "Bulk nanocrystalline superconducting $YBa_2Cu_3O_{7-x}$," *Journal of Physics: Conference Series,* vol. 97, p. 012237, 2008.

[100]   D. P. Hampshire and H. J. Niu, "Patent - Nanocrystalline superconductors," International patent number WO03/094251 A2, 2002.

[101]   D. Larbalestier, L. Cooley, M. Rikel, A. Polyanskii, J. Jiang, S. Patnaik, *et al.,* "Strongly linked current flow in polycrystalline forms of the superconductor MgB_2," *Nature,* vol. 410, pp. 186-189, 2001.

[102]   A. Gumbel, O. Perner, J. Eckert, G. Fuchs, K. Nenkov, K. H. Muller, *et al.,* "High density nanocrystalline MgB_2 bulk superconductors with improved pinning," *IEEE Transactions on Applied Superconductivity,* vol. 13, pp. 3064-3067, 2003.

[103]   S. Li, T. White, J. Plevert, and C. Q. Sun, "Superconductivity of nano-crystalline MgB_2," *Superconductor Science and Technology,* vol. 17, p. S589, 2004.

[104]   B. Sangita and A. Pushan, "A review of finite size effects in quasi-zero dimensional superconductors," *Reports on Progress in Physics,* vol. 77, p. 116503, 2014.

[105]   C.-Y. Wu, H.-M. Lin, H.-F. Lin, M.-F. Tai, C.-R. Wang, C.-K. Lin, *et al.,* "Preparation and characterization of nanocrystalline Nb_3Al alloy," *Scripta Materialia,* vol. 44, pp. 1967-1971, 2001.

[106]   P. Mondal, M. Manekar, A. K. Srivastava, and S. B. Roy, "Bulk critical state and fundamental length scales of superconducting nanocrystalline Nb_3Al in Nb-Al matrix," *Physical Review B,* vol. 80, p. 024502, 2009.

[107]   M. Simoneau, G. L'Esperamce, and R. Schulz, "Formation by ball milling and recrystallization of Y-Ba-Cu-O nanocrystalline phases," *Journal of Applied Physics,* vol. 76, p. 136, 1994.

[108]   F. Lavallée, M. Simoneau, G. L'Espérance, and R. Schulz, "Order-disorder transitions and metastable phases produced by mechanical deformations in the $YBa_2Cu_3O_{7-x}$ superconducting system," *Physical Review B,* vol. 44, pp. 12003-12008, 1991.

[109]   S. K. Hasanain, N. Akhtar, and A. Mumtaz, "Particle size dependence of the superconductivity and ferromagnetism in YBCO nanoparticles," *Journal of Nanoparticle Research,* vol. 13, pp. 1953-1960, 2011.

[110]   A. Gomathi, A. Sundaresan, and C. N. R. Rao, "Room-temperature ferromagnetism in nanoparticles of superconducting materials," *Solid State Communications,* vol. 142, pp. 685-688, 2007.

[111]   Z. Zhu, D. Gao, C. Dong, G. Yang, J. Zhang, J. Zhang*, et al.*, "Coexistence of ferromagnetism and superconductivity in YBCO nanoparticles," *Physical Chemistry Chemical Physics,* vol. 14, pp. 3859-3863, 2012.

[112]   X. L. Xu, J. D. Guo, Y. Z. Wang, and A. Sozzi, "Synthesis of nanoscale superconducting YBCO by a novel technique," *Physica C-Superconductivity and Its Applications,* vol. 371, pp. 129-132, 2002.

[113]   H. Jin, W. C. Zhao, F. M. Lou, K. Zhang, K. Q. Ruan, C. Y. Wang*, et al.*, "Correlation of grain size and ac susceptibility in the $Bi_2Sr_2CaCu_2O_8$ system," *Physica C: Superconductivity,* vol. 282–287, Part 2, pp. 843-844, 1997.

[114]   W. Zhao, H. Jin, M. Tian, K. Ruan, L. Yang, and L. Cao, "Nanocrystalline-grained Bi-Sr-Ca-Cu-O and its superconducting property," *Applied Physics A,* vol. 66, pp. 451-454, 1998.

[115]   W. Schauer and W. Schelb, "Improvement of Nb_3Sn High Field Critical Current by a Two-stage Reaction," *IEEE Transactions on Magnetics,* vol. 17, pp. 374-377, 1981.

[116]   G. J. Carty and D. P. Hampshire, "Visualising the mechanism that determines the critical current density in polycrystalline superconductors using time-dependent Ginzburg-Landau theory," *Physical Review B,* vol. 77, p. 172501, 2008.

[117]   J. W. Ekin, A. I. Braginski, A. J. Panson, M. A. Janocko, D. W. Capone, N. J. Zaluzec, *et al.*, "Evidence for weak link and anisotropy limitations on the transport critical current in bulk polycrystalline $Y_1Ba_2Cu_3O_x$," *Journal of Applied Physics,* vol. 62, pp. 4821-4828, 1987.

[118]   J. H. T. Ransley, S. H. Mennema, K. G. Sandeman, G. Burnell, E. J. Tarte, J. E. Evetts, *et al.*, "The normal-state resistivity of grain boundaries in $YBa_2Cu_3O_{7-\delta}$," *Applied Physics Letters,* vol. 84, pp. 4089-4091, 2004.

[119]   G. J. Carty and D. P. Hampshire, "The critical current density of an SNS junction in high magnetic fields," *Superconductor Science and Technology,* vol. 26, p. 065007, 2013.

[120]   K. K. Likharev, "Superconducting weak links," *Reviews of Modern Physics,* vol. 51, pp. 102-159, 1979.

[121]   S. E. Babcock and J. L. Vargas, "The nature of grain boundaries in the high-T_c superconductors," *Annual Review of Materials Science,* vol. 25, pp. 193-222, 1995.

[122]   R. B. Dinner, A. P. Robinson, S. C. Wimbush, J. L. MacManus-Driscoll, and M. G. Blamire, "Depairing critical current achieved in superconducting thin films with through-thickness arrays of artificial pinning centers," *Supercond. Sci. and Technol.,* vol. 24, p. 055017, 2011.

[123]   P. J. Lee and D. C. Larbalestier, "On-Line Master J_c Plots," *(accessed Aug 2017),* *http://www.magnet.fsu.edu/magnettechnology/research/asc/plots.html*.

[124]   A. Gauzzi, J. Le Cochec, G. Lamura, B. J. Jönsson, V. A. Gasparov, F. R. Ladan, *et al.*, "Very high resolution measurement of the penetration depth of superconductors by a novel single-coil inductance technique," *Review of Scientific Instruments,* vol. 71, pp. 2147-2153, 2000.

[125]   L. J. Neuringer and Y. Shapira, "Effect of Spin-Orbit Scattering on the Upper Critical Field of High-Field Superconductors," *Physical Review Letters,* vol. 17, pp. 81-84, 1966.

[126]   D. K. Finnemore, J. E. Ostenson, S. L. Bud'ko, G. Lapertot, and P. C. Canfield, "Thermodynamic and Transport Properties of Superconducting $Mg^{10}B_2$," *Physical Review Letters,* vol. 86, pp. 2420-2422, 2001.

[127]   L. Lyard, P. Samuely, P. Szabo, C. Marcenat, T. Klein, K. H. P. Kim, *et al.*, "Upper critical magnetic fields in single crystal MgB_2," *Superconductivity Science and Technology,* vol. 16, pp. 193-198, 2003.

[128]   D. Zheng, A. Campbell, J. Johnson, J. Cooper, F. Blunt, A. Porch, *et al.*, "Magnetic susceptibilities, critical fields, and critical currents of Co- and Zn-doped YBa$_2$Cu$_3$O$_7$," *Physical Review B,* vol. 49, pp. 1417-1426, 1994.

[129]   T. Sekitani, N. Miura, S. Ikeda, Y. H. Matsuda, and Y. Shiohara, "Upper critical field for optimally-doped YBa$_2$Cu$_3$O$_{7\text{-}d}$," *Physica B,* vol. 346-347, pp. 319-324, 2004.

[130]   H. C. Ri, R. Gross, F. Gollnik, A. Beck, R. P. Huebener, P. Wagner, *et al.*, "Nernst, Seebeck, and Hall effects in the mixed state of YBa$_2$Cu$_3$O$_{7\text{-}d}$ and Bi$_2$Sr$_2$CaCu$_2$O$_{8+x}$ thin films: A comparative study," *Physical Review B,* vol. 50, pp. 3312-3329, 1994.

[131]   A. I. Golovashkin, O. M. Ivanenko, Y. B. Kudasov, K. V. Mitsen, A. I. Pavlovsky, V. V. Platonov, *et al.*, "Low temperature direct measurements of H_{c2} in HTSC using megagauss magnetic fields," *Physica C: Superconductivity,* vol. 185–189, Part 3, pp. 1859-1860, 1991.

[132]   Q. Li, M. Suenaga, J. Gohng, D. K. Finnemore, T. Hikata, and K. Sato, "Reversible magnetic properties of c-axis-oriented superconducting Bi$_2$Sr$_2$Ca$_2$Cu$_3$O$_{10}$," *Physical Review B,* vol. 46, pp. 3195-3198, 1992.

[133]   I. Matsubara, H. Tanigawa, T. Ogura, H. Yamashita, M. Kinoshita, and T. Kawai, "Upper critical field and anisotropy of the high-T_c Bi$_2$Sr$_2$Ca$_2$Cu$_3$O$_x$ phase," *Physical Review B,* vol. 45, pp. 7414-7417, 1992.

[134]   D. C. Larbalestier, A. Gurevich, D. M. Feldmann, and A. Polyanskii, "High-T_c superconducting materials for electric power applications," *Nature,* vol. 414, pp. 368-377, 2001.

[135]   Y. Ando, G. S. Boebinger, A. Passner, L. F. Schneemeyer, T. Kimura, M. Okuya, *et al.*, "Resistive upper critical fields and irreversibility lines of optimally doped high-T_c cuprates," *Physical Review B,* vol. 60, pp. 12475-12479, 1999.

[136]   B. Chen, W. P. Halperin, P. Guptasarma, D. G. Hinks, V. F. Mitrovic, A. P. Reyes, *et al.*, "Two-dimensional vortices in superconductors," *Nat Phys,* vol. 3, pp. 239-242, 2007.

[137]   M. J. Raine, S. A. Keys, and D. P. Hampshire, *"Characterisation of the Transport Critical Current Density for Conductor Applications" in "Handbook of Superconducting Materials"*: Taylor and Francis, Oxfordshire, To be published.

[138]   T. S. Lee, I. Jenkins, E. Surrey, and D. P. Hampshire, "Optimal design of a toroidal field magnet system and cost of electricity implications for a tokamak using high temperature superconductors " *Fusion Engineering and Design,* vol. 98-99, pp. 1072–1075, 2015.

[139]   P. Sunwong, J. S. Higgins, Y. Tsui, M. J. Raine, and D. P. Hampshire, "The critical current density of grain boundary channels in polycrystalline HTS and LTS superconductors in magnetic fields," *Superconductivity Science and Technology,* vol. 26, p. 095006, 2013.

[140]   F. J. Ridgeon, M. J. Raine, and D. P. Hampshire, "The critical current density of NbTi in the strands used for the ITER poloidal field coils," *Private communication,* 2017.

[141]   X. F. Lu, S. Pragnell, and D. P. Hampshire, "Small reversible axial-strain window for critical current in both compression and tension for a high performance Nb_3Sn superconducting strand," *Applied Physics Letters,* vol. 91, p. 132512, 2007.

[142]   D. M. J. Taylor and D. P. Hampshire, "The scaling law for the strain dependence of the critical current density in Nb_3Sn superconducting wires," *Superconductor Science and Technology,* vol. 18, pp. S241-S252, 2005.

[143]   S. A. Keys, N. Koizumi, and D. P. Hampshire, "The strain and temperature scaling law for the critical current density of a jelly-roll Nb_3Al strand in high magnetic fields," *Superconductor Science and Technology,* vol. 15, pp. 991-1010, 2002.

[144]   D. P. Hampshire, H. Jones, and E. W. J. Mitchell, "An in-depth characterisation of $(NbTa)_3Sn$ filamentary superconductor," *IEEE Transactions on Magnetics,* vol. 21, pp. 289-292, 1985.

[145]   N. Cheggour, M. Decroux, Ø. Fischer, and D. P. Hampshire, "Irreversibility Line and Granularity in Chevrel Phase Superconducting Wires," *Journal of Applied Physics,* vol. 84, pp. 2181-2183, 1998.

[146]   G. Z. Li, M. D. Sumption, J. B. Zwayer, M. A. Susner, M. A. Rindfleisch, C. J. Thong*, et al.*, "Effects of carbon concentration and filament number on advanced internal Mg infiltration-processed MgB_2 strands," *Superconductor Science and Technology,* vol. 26, p. 095007, 2013.

[147]   W. Si, J. Zhou, Q. Jie, I. Dimitrov, V. Solovyov, P. D. Johnson*, et al.*, "Iron-chalcogenide $FeSe_{0.5}Te_{0.5}$ coated superconducting tapes for high field applications," *Applied Physics Letters,* vol. 98, p. 262509, 2011.

[148]   C. Tarantini, F. Kametani, S. Lee, J. Jiang, J. D. Weiss, J. Jaroszynski*, et al.*, "Development of very high J_c in $Ba(Fe_{1-x}Co_x)_2As_2$ thin films grown on CaF_2," *Scientific Reports,* vol. 4, p. 7305, 2014.

[149]   S. J. Williamson, "Bulk Upper Critical Field of Clean Type-II Superconductors: V and Nb," *Physical Review B,* vol. 2, pp. 3545-3556, 1970.

[150]   D. N. Zheng, H. D. Ramsbottom, and D. P. Hampshire, "Reversible and irreversible magnetization of the Chevrel-phase superconductor $PbMo_6S_8$," *Physical Review B,* vol. 52, pp. 12931-12938, 1995.

[151]   K. Laby, *Tables of Physical & Chemical Constants (16th Edition)*: Middlesex, England: The National Physical Laboratory, 1995.

[152]   A. Godeke, M. C. Jewell, C. M. Fischer, A. A. Squitieri, P. J. Lee, and D. C. Larbalestier, "The upper critical field of filamentary Nb_3Sn conductors," *Journal of Applied Physics,* vol. 97, p. 093909, 2005.

[153]   V. Guritanu, W. Goldacker, F. Bouquet, Y. Wang, R. Lortz, G. Goll*, et al.*, "Specific heat of Nb3Sn: The case for a second energy gap," *Physical Review B,* vol. 70, p. 184526, 2004.

[154]   M. Xu, H. Kitazawa, Y. Takano, J. Ye, K. Nishida, H. Abe*, et al.*, "Anisotropy of superconductivity from MgB_2 single crystals," *Applied Physics Letters,* vol. 79, pp. 2779-2781, 2001.

[155]   J. Hänisch, K. Iida, F. Kurth, E. Reich, C. Tarantini, J. Jaroszynski*, et al.*, "High field superconducting properties of $Ba(Fe_{1-x}Co_x)_2As_2$ thin films," *Scientific Reports,* vol. 5, p. 17363, 2015.

[156]   D. Wu, N. Barišić, N. Drichko, P. Kallina, A. Faridian, B. Gorshunov*, et al.*, "Superfluid density of from optical experiments," *Physica C: Superconductivity,* vol. 470, pp. Supplement 1, S399-S400, 2010.

[157]   D. Braithwaite, G. Lapertot, W. Knafo, and I. Sheikin, "Evidence for Anisotropic Vortex Dynamics and Pauli Limitation in the Upper Critical Field of $FeSe_{1-x}Te_x$," *Journal of the Physical Society of Japan,* vol. 79, p. 053703, 2010.

[158]   M. Bendele, S. Weyeneth, R. Puzniak, A. Maisuradze, E. Pomjakushina, K. Conder*, et al.*, "Anisotropic superconducting properties of single-crystalline $FeSe_{0.5}Te_{0.5}$," *Physical Review B,* vol. 81, p. 224520, 2010.

[159]   S. Mitra, J. H. Cho, W. C. Lee, D. C. Johnston, and V. G. Kogan, "Magnetic field penetration depth of polycrystalline $(Y,Gd)Ba_2Cu_3O_7$, grain-aligned $YBa_2Cu_3O_7$, and single-crystal $Bi_2Sr_2CaCu_2O_8$," *Physical Review B,* vol. 40, pp. 2674-2677, 1989.

[160]   L. Miu, P. Wagner, U. Frey, A. Hadish, D. Miu, and H. Adrian, "Vortex unbinding and layer decoupling in epitaxial $Bi_2Sr_2Ca_2Cu_3O_{10+\delta}$ films," *Physical Review B,* vol. 52, pp. 4553-4558, 1995.

[161] Y. Shi, T. Hasan, N. Babu, F. Torrisi, S. Milana, A. Ferrari, *et al.*, "Synthesis of YBa$_2$Cu$_3$O$_{7-d}$ and Y$_2$BaCuO$_5$ Nanocrystalline Powders for YBCO Superconductors Using Carbon Nanotube Templates," *ACS Nano,* vol. 6, pp. 5395-5403, 2012.

[162] W. Zhai, Y. Shi, J. H. Durrell, A. R. Dennis, Z. Zhang, and D. A. Cardwell, "Processing and Properties of Bulk Y−Ba−Cu−O Superconductors Fabricated by Top Seeded Melt Growth from Precursor Pellets Containing a Graded CeO$_2$ Composition," *Crystal Growth & Design,* vol. 15, pp. 907-914, 2015.

[163] R. B. Schwarz and R. R. Petrich, "Calorimetry study of the synthesis of amorphous Ni-Ti alloys by mechanical alloying," *Journal of the Less Common Metals,* vol. 140, p. 171, 1988.

[164] A. Hamrita, Y. Slimani, M. K. Ben Salem, E. Hannachi, L. Bessais, F. Ben Azzouz, *et al.*, "Superconducting properties of polycrystalline YBa$_2$Cu$_3$O$_{7-d}$ prepared by sintering of ball-milled precursor powder," *Ceramics International,* vol. 40, p. 1461, 2014.

[165] J. Sestak, "Phase-Diagrams in CuO$_x$ Based Superconductors," *Pure and Applied Chemistry,* vol. 64, pp. 125-136, 1992.

[166] A. Vajpei and G. Upadhyaya, *Powder processing of high T$_c$ oxide superconductors.* Switzerland: Trans Tech Publication Ltd, 1992.

[167] T. Aselage and K. Keefer, "Liquidus relations in Y–Ba–Cu oxides," *Journal of Materials Research,* vol. 3, pp. 1279-1291, 1988.

[168] Quantum Design, "PPMS Resistivity Option User's Manual," in *PPMS Hardware and Options Manual*, ed San Diego: Quantum Design, 2004.

[169] EM Electronics, "DC Nanovolt Amplifier Model A10," *http://www.emelectronics.co.uk/a10.html,* 19 September 2016.

[170] P. Vanderbemden, R. Cloots, M. Ausloos, R. A. Doyle, A. D. Bradley, W. Lo, *et al.*, "Intragranular and intergranular superconducting properties of bulk melt-textured YBCO," *IEEE Transactions on Applied Superconductivity,* vol. 9, pp. 2308-2311, 1999.

[171] Quantum Design, "PPMS ACMS User's manual," in *PPMS Hardware and Options Manual*, ed San Diego: Quantum Design, 2004, pp. 1-3.

[172] E. Pusceddu and D. P. Hampshire, "Nanocrystalline superconducting islands of Nb$_3$Ge in a resistive grain boundary matrix with a bulk critical temperature of 12 K," *Superconductor Science and Technology,* vol. 25, p. 115014, 2012.

[173]   D. Shoenberg, *Superconductivity*: Cambridge University Press, 1952.

[174]   P. Seidel, M. Grajar, A. Plecenik, and R. Hlubina, "Superconducting parameters of YBCO and BSCCO from 'tunneling' spectroscopy," *Physica B,* vol. 218, pp. 224-227, 1996.

[175]   J. R. Clem, "Anisotropy and two-dimensional behaviour in the high-temperature superconductors," *Superconductor Science and Technology,* vol. 11, pp. 909-914, 1998.

[176]   R. A. Klemm and J. R. Clem, "Lower critical field of an anisotropic type-II superconductor," *Physical Review B,* vol. 21, pp. 1868-1875, 1980.

[177]   C. P. Poole, H. A. Farach, and R. J. Creswick, *Superconductivity*. San Diego, California: Academic Press Inc, 1995.

[178]   B. B. Straumal, A. A. Mazilkin, S. G. Protasova, S. V. Stakhanova, P. B. Straumal, M. F. Bulatov*, et al.*, "Grain boundaries as a source of ferromagnetism and increased solubility of Ni in nanograined ZnO," *Rev. Adv. Mater. Sci,* vol. 41, pp. 61-71, 2015.

[179]   B. B. Straumal, S. G. Protasova, A. A. Mazilkin, E. Goering, G. Schütz, P. B. Straumal*, et al.*, "Ferromagnetic behaviour of ZnO: the role of grain boundaries," *Beilstein Journal of Nanotechnology,* vol. 7, pp. 1936-1947, 2016.

[180]   A. M. Campbell, "The response of pinned flux vortices to low-frequency fields," *Journal of Physics C - Solid State Physics,* vol. 2, pp. 1492-1501, 1969.

[181]   G. Deutscher, *"Nanostructured Superconductors" in "The Physics of Superconductors: Vol. II: Superconductivity in Nanostructures, High-T_c and Novel Superconductors, Organic Superconductors"*: Springer, Berlin, 2004.

[182]   J. W. Loram, K. A. Mirza, J. R. Cooper, W. Y. Liang, and J. M. Wade, "Electronic specific heat of $YBa_2Cu_3O_{6+x}$ from 1.8 to 300 K," *Journal of Superconductivity,* vol. 7, pp. 243-249, 1994.

[183]   Y. M. Gerbstein, N. E. Timoshchenko, and F. A. Chudnovskii, "Measurement of electron density of states at the Fermi level in YBCO by means of an "oxygen pump"," *Physica C: Superconductivity,* vol. 162, pp. 961-962, 1989.

[184]   N. C. Yeh, C. T. Chen, C. C. Fu, P. Seneor, Z. Huang, C. U. Jung*, et al.*, "Investigating the pairing state of cuprate superconductors via quasiparticle tunneling and spin injection," *Physica C: Superconductivity,* vol. 367, pp. 174-180, 2002.

[185] K. H. J. Buschow, *Concise Encyclopedia of Magnetic and Superconducting Materials*: UK: Elsevier Science, 2005.

[186] T. Y. Hsiang and D. K. Finnemore, "Superconducting critical currents for thick, clean superconductor-normal-metal-superconductor junctions," *Physical Review B,* vol. 22, pp. 154-163, 1980.

[187] V. Lacquaniti, S. Gonzini, S. Maggi, E. Monticne, R. Steni, and D. Andreone, "Nb-based SNS junctions with Al and TaO_x barriers for a programmable Josephson voltage standard," *Applied Superconductivity, IEEE Transactions on,* vol. 9, pp. 4245-4248, 1999.

[188] R. F. Wang, S. P. Zhao, G. H. Chen, and Q. S. Yang, "Magnetic penetration depth in Nb/Al and Nb/Cu superconducting proximity bilayers," *Physical Review B,* vol. 62, pp. 11793-11801, 2000.

[189] J. Clarke, "Supercurrents in Lead-Copper-Lead Sandwiches," *Proceedings of the Royal Society of London A: Mathematical, Physical and Engineering Sciences,* vol. 308, pp. 447-471, 1969.

[190] F. Bedard and H. Meissner, "Measurements of Contact Resistance between Normal and Superconducting Metals," *Physical Review,* vol. 101, pp. 26-30, 1956.

[191] M. G. Forrester, J. Talvacchio, J. R. Gavaler, M. Rooks, and J. Lindquist, "Fabrication and characterization of $YBa_2Cu_3O_7$/Au/$YBa_2Cu_3O_7$ Josephson junctions," *IEEE Transactions on Magnetics,* vol. 27, pp. 3098-3101, 1991.

[192] Y. Tsui, E. Surrey, and D. P. Hampshire, "Soldered Joints - an essential component of demountable high temperature superconducting fusion magnets," *Supercond. Sci. and Technology,* vol. 290, p. 075005, 2016.

[193] L. Edman, B. Sundqvist, E. McRae, and E. Litvin-Staszewska, "Electrical resistivity of single-crystal graphite under pressure: An anisotropic three-dimensional semimetal," *Physical Review B,* vol. 57, pp. 6227-6230, 1998.

[194] Entegris. (Accessed Aug 2017), Properties and Characteristics of Graphite For the semiconductor industry [Online]. Available: https://www.entegris.com/resources/assets/6205-7329-0513.pdf

[195] Y. Zhu, M. Suenaga, Y. Xu, R. L. Sabatini, and A. R. Moodenbaugh, "Observation of twin boundary layers in pure and alloyed $YBa_2Cu_3O_{7-\delta}$," *Applied Physics Letters,* vol. 54, pp. 374-376, 1989.

[196]   N. W. Ashcroft and N. D. Mermin, *Solid State Physics*: Sanders College Publishing Philadelphia, 1976.

[197]   R. G. Mark, C. J. Adkins, B. Haim, and R. Ralph, "Experimental study of the Ioffe-Regel criterion for amorphous indium oxide films," *Journal of Physics: Condensed Matter,* vol. 10, p. 809, 1998.

[198]   E. W. Collings, *Applied superconductivity, metallurgy, and physics of titanium alloys. Volume 1: fundamentals.* New York: Plenum Press, 1986.

[199]   J. A. Woollam and S. A. Alterovitz, "Electronic Properties of $PbMo_6S_8$ and $Cu_xMo_6S_8$," *Physical Review B,* vol. 19, pp. 749-761, 1979.

[200]   C. Ferdeghini, V. Ferrando, G. Grassano, W. Ramadan, E. Bellingeri, V. Braccini*, et al.*, "Growth of *c*-oriented MgB_2 thin films by pulsed laser deposition: structural characterization and electronic anisotropy," *Superconductor Science and Technology,* vol. 14, p. 952, 2001.

[201]   R. K. Kremer, B. J. Gibson, and K. Ahn. (2001). *Heat Capacity of MgB_2: Evidence for Moderately Strong Coupling Behaviour*   [arXiv:cond-mat/0102432v2 [cond-mat.supr-con]].

[202]   A. Plecenik, Š. Beňačka, P. Kúš, and M. Grajcar, "Superconducting gap parameters of MgB_2 obtained on MgB_2/Ag and MgB_2/In junctions," *Physica C: Superconductivity,* vol. 368, pp. 251-254, 2002.

[203]   C. P. Poole, *Handbook of superconductivity*, first ed.: Academic press, 2000.

[204]   B. Jamtveit and P. Meakin, *Growth, Dissolution, and Pattern Formation in Geosystems Pauli is quoted as saying "God made the bulk; surfaces were invented by the devil"*: Springer, Netherlands, 1999.

[205]   I. F. Tsu, J.-L. Wang, D. L. Kaiser, and S. E. Babcock, "A comparison of grain boundary topography and dislocation network structure in bulk-scale [001] tilt bicrystals of $Bi_2Sr_2CaCu_2O_{8+x}$ and $YBa_2Cu_3O_{7-d}$," *Physica C: Superconductivity,* vol. 306, pp. 163-187, 1998.

[206]   S. Lee, C. Tarantini, P. Gao, J. Jiang, J. D. Weiss, F. Kametani*, et al.*, "Artificially engineered superlattices of pnictide superconductors," *Nature Materials,* vol. 12, pp. 392-396, 2013.

[207]   J. D. Weiss, C. Taratini, J. Jiang, F. Kametani, A. A. Polyanskii, D. C. Larabalestier*, et al.*, "High Intergrain critical current density in fine-grain $(Ba_{0.6}K_{0.4})Fe_2As_2$ wires and bulks," *Nature Materials,* vol. 11, pp. 682-685, 2012.

[208]   N. Tomoyuki, S. Tomohisa, and F. Hiroyuki, "Trapped magnetic field and vortex pinning properties of MgB_2 superconducting bulk fabricated by a capsule method," *Superconductor Science and Technology,* vol. 25, p. 095012, 2012.

[209]   M. Muralidhar, A. Ishihara, K. Suzuki, Y. Fukumoto, Y. Yamamoto, and M. Tomita, "Optimization of the fabrication process for high trapped field MgB_2 bulks," *Physica C: Superconductivity,* vol. 494, pp. 85-88, 2013.

[210]   M. Kambara, N. H. Babu, E. S. Sadki, J. R. Cooper, H. Minami, D. A. Cardwell*, et al.,* "High intergranular critical currents in metallic MgB_2 superconductor," *Superconductor Science and Technology,* vol. 14, p. L5, 2001.

[211]   A. Palenzona, A. Sala, C. Bernini, V. Braccini, M. R. Cimberle, C. Ferdeghini*, et al.,* "A new approach for improving global critical current density in $Fe(Se_{0.5}Te_{0.5})$ polycrystalline materials," *Superconductor Science and Technology,* vol. 25, p. 115018, 2012.

[212]   T. Ozaki, K. Deguchi, Y. Mizuguchi, Y. Kawasaki, T. Tanaka, T. Yamaguchi*, et al.,* "Fabrication of binary FeSe superconducting wires by diffusion process," *Journal of Applied Physics,* vol. 111, p. 112620, 2012.

[213]   B. T. Matthias, T. H. Geballe, S. Geller, and E. Corenzwit, "Superconductivity of Nb_3Sn " *Physical Review,* vol. 95, p. 1435, 1954.

[214]   J. E. Kunzler, "Superconductivity in high magnetic fields at high current densities " *Review of Modern Physics* vol. 33, pp. 501-509, 1961.

[215]   J. Evetts, *Concise Encyclopedia of Magnetic and Superconducting Materials*: Pergamon, Netherlands, 1992.

[216]   M. B. King, "Mechanically milled bulk nanocrystalline NB3Sn with imprfov ed superconducting properties in high magnetic fields," PhD Thesis: Durham University 2006.

[217]   J. Xiang, M. B. King, and D. Hampshire, "Private communication - Unpublished," 2010.

[218]   F. Rullier-Albenque and Y. Quere, "An experimental argument - in Nb3Ge - for the Labbe-Barisic-Friedel theory of A-15 superconductors," *Physics Letters A,* vol. 81, pp. 232-234, 1981.

[219]   N. Cheggour and D. P. Hampshire, "The unified strain and temperature scaling law for the pinning force density of bronze-route Nb_3Sn wires in high magnetic fields," *Cryogenics,* vol. 42, pp. 299 - 309, 2002.

[220]   S. A. Keys and D. P. Hampshire, "A scaling law for the critical current density of weakly and strongly-coupled superconductors, used to parameterise data from a technological Nb₃Sn strand," *Superconductor Science and Technology,* vol. 16, pp. 1097-1108, 2003.

[221]   R. A. Ogg, "Superconductivity in Solid Metal-Ammonia Solutions," *Physical Review,* vol. 70, pp. 93-93, 1946.

[222]   D. K. C. MacDonald, K. Mendelssohn, and A. J. Birch, "Conductivity of Sodium-Ammonia Solutions," *Physical Review,* vol. 71, pp. 563-564, 1947.

[223]   K. Mendelssohn, "Low temperature physics," *Reports on Progress in Physics,* vol. 12, p. 270, 1949.

[224]   É. A. Pashitskiĭ, "Did Ogg really observe high-temperature superconductivity in metal-ammonia solutions?," *Low Temperature Physics,* vol. 24, pp. 835-836, 1998.

[225]   X. Cai, R. Joynt, and D. C. Larbalestier, "Experimental evidence for granular superconductivity in Y-Ba-Cu-O at 100 to 160 K," *Physical Review Letters,* vol. 58, pp. 2798-2801, 1987.

[226]   C. Politis, J. Geerk, M. Dietrich, B. Obst, and H. L. Luo, "Superconductivity above 100 K in multi-phase Y−Ba−Cu−O," *Zeitschrift für Physik B Condensed Matter,* vol. 66, pp. 279-282, 1987.

[227]   J. T. Chen, L. E. Wenger, C. J. McEwan, and E. M. Logothetis, "Observation of the Reverse ac Josephson Effect in Y-Ba-Cu-O at 240 K," *Physical Review Letters,* vol. 58, pp. 1972-1975, 1987.

[228]   J. F. Riley, W. S. Sampath, K. Y. Lee, N. Mate, and J. W. Blake, "Meissner effect up to 300 K in microscopic regions of Y-Ba-Cu-O," *Physical Review B,* vol. 37, pp. 559-561, 1988.

[229]   B. Gao, L. Liu, X. Liu, and J. Kang, "Resistive switching characteristics in HfOₓ layer by using current sweep mode," *Microelectronic Engineering,* vol. 94, pp. 14-17, 2012.

[230]   L. Song-Lin, G. Jian-Lei, L. Jie, C. Hai-Feng, and Z. Dong-Ning, "Reproducible low-voltage resistive switching in a low-initial-resistance $Pr_{0.7}Ca_{0.3}MnO_3$ junction," *Journal of Physics D: Applied Physics,* vol. 41, p. 185409, 2008.

[231]   D. S. Kim, Y. H. Kim, C. E. Lee, and Y. T. Kim, "Colossal electroresistance mechanism in a $Au/Pr_{0.7}Ca_{0.3}MnO_3/Pt$ sandwich structure: Evidence for a Mott transition," *Physical Review B,* vol. 74, p. 174430, 2006.

[232] N. A. Tulina, "Colossal electroresistance and electron instability in strongly correlated electron systems," *Physics-Uspekhi,* vol. 50, p. 1171, 2007.

[233] A. Sawa, T. Fujii, M. Kawasaki, and Y. Tokura, "Interface resistance switching at a few nanometer thick perovskite manganite active layers," *Applied Physics Letters,* vol. 88, p. 232112, 2006.

[234] R. Waser and M. Aono, "Nanoionics-based resistive switching memories," *Nature Materials,* vol. 6, pp. 833-840, 2007.

[235] P. W. Anderson and J. M. Rowell, "Probable Observation of the Josephson Superconducting Tunneling Effect," *Physical Review Letters,* vol. 10, pp. 230-232, 1963.

[236] L. P. Rokhinson, X. Liu, and J. K. Furdyna, "The fractional a.c. Josephson effect in a semiconductor-superconductor nanowire as a signature of Majorana particles," *Nature Physics,* vol. 8, pp. 795-799, 2012.

[237] A. Rogachev, A. T. Bollinger, and A. Bezryadin, "Influence of High Magnetic Fields on the Superconducting Transition of One-Dimensional Nb and MoGe Nanowires," *Physical Review Letters,* vol. 94, p. 017004, 2005.

[238] *Low Level Measurements Handbook 7th Edition, Section 4.4, (accessed Aug 2017).* Available:
http://www.tek.com/sites/tek.com/files/media/document/resources/LowLevelHandbook_7Ed.pdf

[239] J. Gutierrez, A. Llordes, J. Gazquez, M. Gibert, N. Roma, S. Ricart*, et al.,* "Strong isotropic flux pinning in solution-derived $YBa_2Cu_3O_{7-x}$ nanocomposite superconductor films," *Nature Materials,* vol. 6, pp. 367-373, 2007.

[240] T. Amrein, L. Schultz, B. Kabius, and K. Urban, "Orientation dependence of grain-boundary critical current densities in high-T_c bicrystals," *Physical Review B,* vol. 51, p. 6792, 1995.

[241] A. Attenberger, J. Hanisch, B. Holzapfel, and L. Schultz, "Electrical transport properties of Bi2223 [001] tilt grain boundary junctions," *Physica C,* vol. 372-376, pp. 649-651, 2002.

[242] D. Y. Vodolazov, "Effect of surface defects on the first field for vortex entry in type-II superconductors," *Physical Review B,* vol. 62, pp. 8691-8694, 2000.

[243] G. J. Carty, M. Machida, and D. P. Hampshire, "Numerical studies on the effect of normal metal coatings on the magnetisation characteristics of type-II superconductors," *Physical Review B,* vol. 71, p. 144507, 2005.

[244] J. R. Clem, "Two-dimensional vortices in a stack of thin superconducting films: A model for high-temperature superconducting multilayers," *Physical Review B,* vol. 43, pp. 7837-7846, 1991.

[245] G. Blatter, M. V. Feigelman, V. B. Geshkenbein, A. I. Larkin, and V. M. Vinokur, "Vortices in high-temperature superconductors," *Reviews of Modern Physics,* vol. 66, pp. 1125-1388, 1994.

[246] A. Piriou, Y. Fasano, E. Giannini, and Ø. Fischer, "Doping-dependence of the vortex phase diagram of $Bi_2Sr_2Ca_2Cu_3O_{10+\delta}$," *Physica C: Superconductivity and its Applications,* vol. 460, pp. 408-409, 2007.

[247] C. Senatore. (2016, Presented at ASC2016 Conf., Denver, Sept 2016). *30 years to HTS - Status and Perspectives. Available: http://snf.ieeecsc.org/abstracts/rp78-30-years-hts-status-and-perspectives (accessed Aug 2017).*

[248] F. Kametani, J. Jiang, M. Matras, D. Abraimov, E. E. Hellstrom, and D. C. Larbalestier, "Comparison of growth texture in round Bi2212 and flat Bi2223 wires and its relation to high critical current density development," *Scientific Reports,* vol. 5, p. 8285, 2015.

[249] G. Wang, M. J. Raine, and D. P. Hampshire, "How Resistive Must Grain-Boundaries be to Limit J_C in Polycrystalline Superconductors?," *Accepted by Super. Sci. and Tech.,* 2017.

[250] J. Beille, H. Dupendant, O. Laborde, Y. Lefur, M. Perroux, R. Tournier*, et al.,* "Pressure effects, anisotropic transport properties and upper critical fields of $Bi_2Sr_2CaCu_2O_{8+x}$ single crystals - characterization of needle-like Bi-Sr-Ca-Cu-O crystals," *Physica C: Superconductivity,* vol. 156, pp. 448-454, 1988.

[251] G. Yildirim, A. Varilci, and C. Terzioglu, "Anisotropic nature and scaling of thermally activated dissipation mechanism in Bi-2223 superconducting thin film," *Journal of Alloys and Compounds,* vol. 554, pp. 327-334, 2013.

[252] B. Hensel, G. Grasso, and R. Flükiger, "Limits to the critical transport current in superconducting $(Bi,Pb)Sr_2Ca_2Cu_3O_{10}$ silver-sheathed tapes: The railway-switch model," *Physical Review B,* vol. 51, pp. 15456-15473, 1995.

[253] K. Heine, J. Tenbrink, and M. Thoner, "High-field critical current densities in $Bi_2Sr_2Ca_1Cu_2O_{8+x}/Ag$ wires," *Applied Physics Letters,* vol. 55, pp. 2441-2443, 1989.

[254] E. Noritsugu, K. Hiroyuki, U. Naoki, K. Hiroaki, T. Kazumasa, and W. Kazuo, "The High Field Magnetic Dependence of Critical Current Density at 4.2 K for Ag-Sheathed $Bi_2Sr_2CaCu_2O_y$ Superconducting Tape," *Japanese Journal of Applied Physics,* vol. 29, p. L447, 1990.

[255] T. Hikata, K. Sato, and H. Hitotsuyanagi, "Ag-sheathed Bi-Pb-Sr-Ca-Cu-O superconducting wires with high critical current density," *Japanese Journal of Applied Physics,* vol. 28, p. 82, 1989.

[256] K. Osamura, S. Machiya, H. Suzuki, S. Ochiai, H. Adachi, N. Ayai*, et al.*, "Improvement of Reversible Strain Limit for Critical Current of DI-BSCCO Due to Lamination Technique," *IEEE Transactions on Applied Superconductivity,* vol. 19, pp. 3026-3029, 2009.

[257] K. Osamura, S. Machiya, and D. P. Hampshire, "Mechanism for the uniaxial strain dependence of the critical current in practical REBCO tapes," *Superconductor Science & Technology,* vol. 29, p. 065019, Jun 2016.

[258] J. Oberteuffer, "Magnetic separation: A review of principles, devices, and applications," *IEEE Transactions on Magnetics,* vol. 10, pp. 223-238, 1974.

[259] D. P. Matheis, S. T. Misture, and R. L. Snyder, "Melt-texture processing and high-temperature reactions of Bi-2212 thick films," *Physica C: Superconductivity,* vol. 217, pp. 319-324, 1993.

[260] K. Przybylski and T. Brylewski, "The formation of superconducting oxide phases in the (Bi,Pb)−Sr−Ca−Cu−O System," *Journal of Thermal Analysis,* vol. 45, pp. 1135-1143, 1995.

[261] M. Masaaki, E. Hozumi, T. Jun, K. Naoto, S. Akihiko, and O. Yasuo, "Superconductivity of $Bi_2Sr_2Ca_2Cu_3Pb_xO_y$ ($x = 0.2, 0.4, 0.6$)," *Japanese Journal of Applied Physics,* vol. 27, p. L1225, 1988.

[262] Y. L. Chen, R. Stevens, W. Lo, and Y. S. Zhen, "Synthesis and characterization of 110 K superconducting phase in Bi(Pb)-Sr-Ca-Cu-oxide," *Journal of Materials Science: Materials in Electronics,* vol. 1, pp. 185-191, 1990.

[263] P. Majewski, "Materials Aspects of the High-temperature Superconductors in the System Bi_2O_3–SrO–CaO–CuO," *Journal of Materials Research,* vol. 15, pp. 854-870, 2000.

[264] P. Nandi, P. P. Chattopadhyay, S. K. Pabi, and I. Manna, "Solid state synthesis of Al-based amorphous and nanocrystalline Al-Cu-Nb alloys," *Materials Science and Engineering A,* vol. 359, pp. 11-17, 2003.

[265] X. H. Chen, M. Yu, K. Q. Ruan, S. Y. Li, Z. Gui, G. C. Zhang, *et al.*, "Anisotropic resistivities of single-crystal $Bi_2Sr_2CaCu_2O_{8+d}$ with different oxygen content," *Physical Review B,* vol. 58, pp. 14219-14222, 1998.

[266] T. Naruaki, T. Yutaka, M. Minoru, and I. Yoichi, "The Superconducting Properties of [001] Twist Boundaries in a Bi-Sr-Ca-Cu-O Superconductor," *Japanese Journal of Applied Physics,* vol. 31, p. L942, 1992.

[267] M. Dogruer, Y. Zalaoglu, A. Varilci, C. Terzioglu, G. Yildirim, and O. Ozturk, "A Study on Magnetoresistivity, Activation Energy, Irreversibility and Upper Critical Field of Slightly Mn Added Bi-2223 Superconductor Ceramics," *Journal of Superconductivity and Novel Magnetism,* vol. 25, pp. 961-968, 2012.

[268] W. J. Carr and G. R. Wagner, "Surface current and hysteresis in fine filament NbTi superconductors," *Journal of Applied Physics,* vol. 60, pp. 342-345, 1986.

[269] M. F. Laguna, D. Domínguez, and C. A. Balseiro, "Transport properties and structures of vortex matter in layered superconductors," *Physical Review B,* vol. 62, pp. 6692-6698, 2000.

[270] S. Nagata and M. Nakajima, "Averaging effect of the anisotropy of the electrical resistivity in a polycrystalline sample," *Physica B,* vol. 192, p. 228, 1993.

[271] A. Junod, A. Erb, and C. Renner, "Specific heat of high temperature superconductors in high fields at T_c: from BCS to the Bose–Einstein condensation," *Physica C: Superconductivity,* vol. 317–318, pp. 333-344, 1999.

[272] N. Okazaki, T. Hasegawa, K. Kishio, K. Kitazawa, A. Kishi, Y. Ikeda, *et al.*, "Specific-heat anomaly near T_c of the (Bi,Pb)-Sr-Ca-Cu-O superconductor T_c=107 K)," *Physical Review B,* vol. 41, pp. 4296-4301, 1990.

[273] G. Narsinga Rao, P. Molinie, M. Ganne, and D. S. Babu, "Magnetic Relaxation, lower critical field and irreversibility line of W-doped (Bi,Pb)-2223 Superconductor," *Modern Physics Letters B,* vol. 09, pp. 1387-1396, 1995.

[274] B. Mayer, L. Alff, T. Trguble, and R. Gross, "Superconducting transport properties of $Bi_2Sr_2CaCu_2O_{8+x}$ bicrystal grain boundary junctions," *Applied Physics Letters,* vol. 63, pp. 996-998, 1993.

[275] U. Frey, H. Meffert, P. Haibach, K. Üstüner, G. Jakob, and H. Adrian, "Transport properties of $Bi_2Sr_2Ca_2Cu_3O_{10+d}$ Bicrystal Grain Boundary Josephson Junctions and SQUIDs," *J. Phys. IV France,* vol. 6, pp. C3-277-C3-282, 1996.

[276] K. Ohbayashi, H. Fujii, A. Kuzuhara, T. Ohtsuki, M. Inoue, A. Fujimaki, *et al.*, "Fabrication of $Bi_2Sr_2Ca_2Cu_3O_x$ thin film grain boundary junctions," *IEEE Transactions on Applied Superconductivity,* vol. 5, pp. 2816-2819, 1995.

[277] H. Kumakura, K. Togano, K. Tachikawa, Y. Yamada, S. Murase, E. Nakamura, *et al.*, "Synthesis of Nb_3Ga and Nb_3Al Superconducting Composites by Laser-Beam Irradiation," *Applied Physics Letters,* vol. 48, pp. 601-603, 1986.

[278] H. Kumakura, K. Togano, K. Tachikawa, S. Tsukamoto, and H. Irie, "Fabrication of Nb_3Al and $Nb_3(Al,Ge)$ Superconducting Composite Tapes by Electron-Beam Irradiation," *Applied Physics Letters,* vol. 49, pp. 46-48, 1986.

[279] Y. Bugoslavsky, L. Cohen, G. Perkins, M. Polichetti, T. Tate, R. Willam, *et al.*, "Enhancement of the high-magnetic-field critical current density of superconducting MgB_2 by proton irradiation," *Nature,* vol. 411, pp. 561-562, 2001.

[280] H. Bauer, E. J. Saur, and D. G. Schmeitzer, "Effect of neutron irradiations on superconductiong properties of A-15 compunds undoped and doped with ^{10}B and ^{235}U," *Journal of Low Temperature Physics,* vol. 19, p. 171, 1975.

[281] A. Nishimura, T. Takeuchi, S. Nishijima, G. Nishijima, T. Shikama, K. Ochiai, *et al.*, "Neutron irradiation effects on superconducting wires and insulating materials," *Fusion Engineering and Design,* vol. 84, pp. 1425-1428, 2009.

[282] E. Mezzetti, B. Minetti, D. Andreone, R. Cherubini, L. Gherardi, and P. Metra, "Critical currents and dissipative effects in proton-irradiated ceramic YBCO and BISCO," *Journal of Superconductivity,* vol. 5, pp. 185-189, 1992.

[283] G. Fuchs, K. Nenkov, G. Krabbes, R. Weinstein, A. Gandini, R. Sawh, *et al.*, "Strongly enhanced irreversibility fields and Bose-glass behaviour in bulk YBCO with discontinuous columnar irradiation defects," *Superconductor Science and Technology,* vol. 20, p. S197, 2007.

[284] D. Behera, K. Patnaik, and N. C. Mishra, "Irradiation-induced inter- and intra-granular modifications by 120 MeV S Ions in $YBa_2Cu_3O_7$ thick films," *Modern Physics Letters B,* vol. 15, pp. 69-80, 2001.

[285] M. Eisterer, R. Fuger, M. Chudy, F. Hengstberger, and H. W. Weber, "Neutron irradiation of coated conductors," *Superconductor Science and Technology,* vol. 23, p. 014009, 2010.

[286] G. Burns, "Superconducting Properties," in *High-temperature Superconductivity*, ed: Academic Press Limited, London, 1992, pp. 156-157.